

Geodätisch-geophysikalische Arbeiten in der Schweiz

(Fortsetzung der Publikationsreihe
«Astronomisch-geodätische Arbeiten in der Schweiz»)

herausgegeben von der

Schweizerischen Geodätischen Kommission
(Organ der Akademie der Naturwissenschaften Schweiz)

Einundneunzigster Band
Volume 91

GNSS Meteorology
in Spatially Dense Networks

Fabian Peter Hurter

2014

Adresse der Schweizerischen Geodätischen Kommission:

Institut für Geodäsie und Photogrammetrie
Eidg. Technische Hochschule Zürich
ETH Zürich
8093 Zürich
Switzerland

Internet: <http://www.sgc.ethz.ch>

ISBN 978-3-908440-37-6

Redaktion des 91. Bandes:
Dr. F.P. Hurter, J. Müller-Gantenbein, Prof. A. Geiger
Druck: Print-Atelier ADAG, Zürich

VORWORT

Die sogenannte GNSS-Meteorologie erlangte in den letzten Jahren zunehmende Bedeutung im Kontext der Atmosphärenforschung und Wetterprognostik. Zudem hat die Installation von kontinuierlich arbeitenden GNSS-Messstationen in engmaschigen Messnetzen die Anwendung satellitengeodätischer Methoden in Forschung und Praxis begünstigt. In dieser Arbeit wurden die am Institut für Geodäsie und Photogrammetrie der ETH Zürich entwickelten Lösungsansätze zur Bestimmung der Wasserdampfverteilung in der Atmosphäre an Hand von GNSS Messungen weiterentwickelt und detailliert untersucht.

Die hauptsächlichen Methoden umfassen tomographische Ansätze sowie parametrisierte Modellschätzungen mit stochastischer 4D Interpolation. Die Arbeit zeichnet sich zusätzlich aus durch ausführliche und detaillierte Untersuchungen in einem speziell dafür konzipierten, verdichteten, alpinen Messnetz und weiteren Verifikationen und Analysen mit Hilfe des numerischen Wettermodells COSMO-2 der MeteoSchweiz. Es ist zu bemerken, dass der Bericht sowohl ausführliche theoretische Aspekte zur Datenkorrelation als auch deren Anwendung auf die konkret vorliegenden Meteo- und GPS-Daten beschreibt. Insbesondere hat Herr Hurter mit dem Testnetz ‚Zermatt‘ eine auch international einzigartige Datengrundlage erarbeitet.

Viele im Bereich der GNSS-Meteorologie angesiedelte Fragen werden fundiert erörtert und beantwortet. So greift der Autor zum Beispiel ein sehr interessantes, weil bisweilen etwas umstrittenes Thema auf, nämlich der Vergleich von Radiosondenmessungen mit GPS Resultaten. Er kann zeigen, dass auch Radiosonden im Gebrauch nicht unproblematisch sind und ihr Offset gegenüber GPS (Pathdelay Bestimmung) zum Teil durch die Radiosonden selber zu erklären sind.

Die Arbeiten reihen sich ein in die GNSS-Meteorologie-Aktivitäten des Institutes für Geodäsie und Photogrammetrie der ETH Zürich und der Schweizerischen Geodätischen Kommission (SGK). Wir danken dem Verfasser, Herrn Dr. Hurter, für den wertvollen Beitrag zur Geodäsie. Der MeteoSchweiz, armasuisse und der swisstopo danken wir für die aktive Unterstützung, insbesondere wären derartige Studien nicht möglich, ohne deren qualitativ hochwertigen Daten. Ebenso danken wir dem CCES (Competence Center Environment and Sustainability des ETH Bereichs), das im Rahmen des Projektes APUNCH einen Teil der Projektfinanzierung übernommen hat.

Der SCNAT danken wir für die Übernahme der Druckkosten.

Prof. Dr. M. Rothacher
Institut für Geodäsie und Photogrammetrie
ETH Zürich

Prof. Dr. A. Geiger
ETH Zürich
Präsident der SGK

PREFACE

Durant ces dernières années la technique appelée GNSS-Météorologie a pris une importance croissante dans le contexte de la recherche sur l'atmosphère et de la prévision du temps.

De nouveaux récepteurs GNSS, en fonctionnement continu, récemment installés en un réseau dense de stations de mesures a permis des applications des méthodes de la géodésie par satellites à la recherche et à la pratique. Dans le présent travail les méthodes développées à l'institut de géodésie et photogrammétrie de l'EPFZ pour la détermination du contenu en vapeur d'eau de l'atmosphère par GNSS sont étudiées et analysées en détails. Les principales méthodes consistent en une approche tomographique avec estimations des paramètres du modèle à l'aide d'une interpolation stochastique en quatre dimensions.

De plus ce travail se distingue par des investigations détaillées sur un réseau alpin de mesures, spécialement conçu à cet effet, dans lesquelles des vérifications et des analyses ont été menées à l'aide du modèle numérique du temps de « MétéoSwiss », COSMO-2. Il est important de mentionner que ce rapport contient aussi bien d'extensifs aspects théoriques sur les corrélations de données que des applications concrètes sur des données météorologiques et GNSS disponibles.

En particulier, grâce à son réseau « Zermatt » l'auteur a établi un ensemble international unique de données.

Plusieurs questions relatives à la météorologie GNSS sont discutées en profondeur et leurs réponses formulées. Par exemple, l'auteur s'est focalisé sur l'intéressant problème, parfois débattu, de la comparaison entre les résultats obtenus par les ballons sondes et ceux obtenus par GNSS.

Monsieur Hurter a montré que les ballons sondes ne sont pas sans une utilisation problématique et que leurs différences relatives avec le GNSS (Path Delay estimation) doivent être attribuées, en partie du moins, aux radiosondes elles-mêmes.

Le présent travail fait partie d'une série de travaux en météorologie GNSS de l'institut de géodésie et photogrammétrie de l'EPFZ et de la Commission Géodésique Suisse. Nous remercions son auteur, Monsieur le docteur F. Hurter, pour cette très importante contribution à la géodésie. Nos remerciements vont aussi à MétéoSuisse, à ArmaSuisse ainsi qu'au service topographique fédéral (SwissTopo) pour leurs supports actif et particulièrement pour leur mise à disposition de leurs données, de très haute qualité, sans lesquelles cette étude n'aurait pas pu être conduite. De même nous exprimons notre gratitude au CCES (Competence Center Environment and Sustainability du domaine des EPF) qui, dans le cadre du projet APUNCH a pris à sa charge une partie du financement de ce travail

Nous remercions l'Académie Suisse des Sciences Naturelles (SCNAT) pour avoir pris à sa charge les coûts d'impression du présent manuscrit.

Prof. Dr. M. Rothacher
Institut de Géodésie et Photogrammétrie
ETH Zürich

Prof. Dr. A. Geiger
ETH Zürich
Président de la CGS

FOREWORD

Over the recent years the so-called GNSS-Meteorology has experienced an increasing importance within the context of the atmospheric research and weather forecasting. Newly installed, continuously running, and densely distributed GNSS receivers brought forward the applications of satellite geodetic methodologies in research and practice. The approaches and methods, devised at the institute of geodesy and photogrammetry of ETHZ, for the determination of water vapor concentration in the atmosphere by GNSS have been further developed and analyzed in detail in the present report.

Main methods consist of tomographic approaches and parameterized estimations with stochastic 4D interpolation. In addition the work features extensive and detailed investigations in an especially designed, dense alpine measurement network, where verifications and analyses with meteoswiss' numerical weather model COSMO-2 were carried out. It has to be mentioned that this report contains as well extensive theoretical aspects of data correlation as its application to the concretely available meteo- and GNSS data. In particular with his test network 'Zermatt' Mr. Hurter has established an internationally unique data set.

Many questions affiliated with topics of GNSS-meteorology have soundly been discussed and answered. For example the author picks up the very interesting, sometimes debated theme on the comparison of balloon soundings and GNSS results. He is able to show that the balloon soundings are not of unproblematic use and there offsets to GNSS (path delay estimations) might be at least partially attributed to the soundings themselves. The presented work is part of a series of activities in GNSS meteorology at the Institute of Geodesy and Photogrammetry at ETH Zürich and of the Swiss Geodetic Commission. Thanks go to the author, Dr Fabian Hurter, for his valuable contribution to geodesy and meteorology. Thanks are given to Meteo Swiss, armasuisse and swisstopo for their active support, particularly for their high-quality data. We express our gratitude also to the Competence Center Environment and Sustainability of the ETH Domain (CCES) for partially funding the project in the frame of the project APUNCH and to the Swiss Academy of Sciences for covering the printing costs of this volume.

Prof. Dr. M. Rothacher
Institute of Geodesy and Photogrammetry
ETH Zurich

Prof. Dr. A. Geiger
ETH Zurich
President of SGC

Abstract

Two basic products from GNSS meteorology have been investigated in detail: (a) the Zenith Total Delay (ZTD) and, (b) wet refractivity fields reconstructed from Zenith Wet Delays (ZWD). The thesis aims at quantifying the accuracies of GNSS-derived ZTDs and refractivities and at characterizing their temporal and spatial resolution. In a first study using operational radiosondes and Global Navigation Satellite System (GNSS) data from the Swiss meteorological station in Payerne, the following uncertainty figures are obtained: With respect to the radiosonde, the GNSS-derived ZTD has a 1–3 mm dry bias. Annual systematic variations of the comparison are found to have an amplitude of 1–2 mm. Removal of most systematic effects from the GNSS minus radiosonde ZTD time series plus a thorough budget of the radiosonde uncertainties allows the derivation of the random GNSS uncertainties. In the winter half-year, the standard deviation is shown to be 2.5–3.5 mm, during the summer half-year we obtain 3.5–5.0 mm.

In a further study in the western part of Switzerland, wet refractivities have been derived on the basis of interpolated ZWDs from the Automatic GNSS Network for Switzerland (AGNES). The employed interpolation algorithm is termed least-squares collocation. It makes use of a deterministic function to describe the general parametric field and a correlation function describing the spatial and temporal correlations between the zenith wet delays. Corresponding wet refractivities show accuracies superior to results from tomographic reconstructions of a similar data set. Further inclusion of ground meteorological measurements of temperature and water vapour pressure improve the derived refractivities in the lowest 2 km of the troposphere. Radio occultations are added to the reconstruction. The data combination enables the extension of the radio occultation profiles down to the ground. It is also shown that the GNSS data largely contributes to the profile quality above the atmospheric boundary layer. Transformation of the wet refractivities to humidity values with temperature profiles from a radiometer in Payerne show accuracies of a similar order of magnitude to those from numerical weather prediction analysis. Hence, application of the algorithm in nowcasting of rain or investigating boundary layer processes are envisaged.

The third part of the thesis investigates the results from a campaign network of 34 geodetic-grade receivers. They were deployed close to and around Zermatt (Switzerland) for one month in summer 2010. The stations were spaced at distances of a few kilometers from each other and at heights between 1600–3500 m above mean sea level. The mountainous region provides an excellent natural laboratory to investigate the influences affecting the accuracy of the ZTD. Additionally, the Alpine region is prone to small-scale fluctuations in the troposphere. Thus, the spatial and temporal variability of the ZTD has been investigated. The influences of satellite obstructions, antenna and receiver types and a number of processing strategies on the estimated ZTD are analysed and validated with measurements from radiosondes launched during the campaign. The analysis suggests that 1 hour temporal resolution should not be undercut for estimated ZTDs. A temporal resolution of 30 minutes introduces more noise without better following the tropospheric fluctuation. The horizontal variability observed in ZTDs indicates correlation scale lengths of a few kilometers. From comparison with radiosondes, the ZTD uncertainty is shown to have 4–6 mm standard deviation. Some stations show signs of systematic effects caused by multipath and low-quality antenna patterns. Through the GNSS-inherent negative correlation of height with zenith delay, both parameters are similarly affected by these systematic influences. The performance of the numerical weather prediction model COSMO-2 is characterized in terms of integrated atmospheric state. The analysis yields preliminary recommendations on the assimilation of zenith total path delays into weather models in regions of highly complex topography such as the Swiss Alps.

Zusammenfassung

Diese Arbeit befasst sich mit zwei Basisprodukten der GNSS-Meteorologie: (a) der Zenit-Pfadverzögerung und (b) den Feuchtrefraktivitäten, die man aus den Pfad-Verzögerungen rekonstruieren kann. Insbesondere geht es darum, die Genauigkeiten der beiden Parameter zu eruieren und deren räumliche und zeitliche Auflösung zu charakterisieren. In einer ersten Studie wird die aus GNSS-Daten geschätzte Pfadverzögerung mit Daten von Radiosonden verglichen. Es handelt sich dabei um Messungen der operationellen Radiosonden-Station der MeteoSchweiz in Payerne. Folgende Genauigkeiten sind zu beobachten: Ein konstanter Offset von der Radiosonde beläuft sich auf 1–3 mm. Die GNSS-Pfadverzögerung zeigt dabei im Durchschnitt zu tiefe Werte. Systematische Abweichungen der zenitalen Pfadverzögerung zeigen ein jährliches Signal mit einer Amplitude von 1–2 mm. Mit dem jährlichen Signal und der konstanten Abweichung ist ein grosser Anteil der systematischen Einflüsse beschrieben. Die verbleibenden Differenzen zwischen Radiosonde und GNSS können nun mit einer detaillierten Analyse in zufällige Messunsicherheiten der Radiosonde und in solche vom GNSS aufgeteilt werden. Demnach belaufen sich die Standardabweichungen der Zenit-Pfadverzögerung auf 2.5–3.5 mm im Winterhalbjahr und 3.5–5.0 mm im Sommerhalbjahr.

Atmosphärische Pfadverzögerungen des AGNES-Netzes wurden in einer weiteren Studie für den Westen der Schweiz zu Feuchtrefraktivitäts-Felder verarbeitet. Die Refraktivitäten wurden aus interpolierten Pfadverzögerungen bestimmt. Der verwendete Algorithmus nennt sich Kollokation mit der Methode der kleinsten Quadrate. Dabei wird die räumliche Verteilung und das zeitliche Verhalten der Zenit-Pfadverzögerung mit einem funktionalen und einem stochastischen Anteil beschrieben. Die erreichten Genauigkeiten sind deutlich besser als Resultate, die bei früheren Arbeiten mit tomographischen Ansätzen erzielt wurden. Durch zusätzliches Einbinden von Temperatur- und Wasserdampf-Messwerten von meteorologischen Bodenmessstationen konnte die Genauigkeit des rekonstruierten Refraktivitätsfeldes weiter gesteigert werden. Ebenfalls hat der Algorithmus eine Weiterführung von Radio-Okkultationsprofilen, die typischerweise 1–2 km oberhalb der Erdoberfläche aufhören, bis zur Erdoberfläche ermöglicht. Dies wurde durch die gemeinsame Kollokation des GNSS-Datensatzes, der Messwerte der meteorologischen Stationen und der Radio-Okkultationsprofile erreicht. Mit Hilfe von Temperatur-Profilen eines in Payerne stationierten Radiometers wurden die Feuchtrefraktivitäten zu relativer Feuchte umgerechnet. Das Ergebnis war von ähnlicher Genauigkeit, wie Feuchte-Profile aus numerischen Wettervorhersage-Modellen. Eine mögliche Anwendung der Kollokation ist die kurzzeitigen Vorhersage von Regenfällen oder Analysen von Prozessen, die in der atmosphärischen Grenzschicht ablaufen.

Der dritte Teil der Arbeit befasst sich mit einem Kampagnen-Netzwerk von 34 geodätischen GNSS-Empfängern. Es wurde im Sommer 2010 während der Dauer eines Monats in und um Zermatt (Schweiz) betrieben. Die Stationen waren nur wenige Kilometer voneinander entfernt und befanden sich zwischen 1600–3500 m über mittlerem Meeresspiegel. Die hochalpine Region stellte ein exzellentes Versuchsfeld für die Untersuchung von Fehlereinflüssen auf die Zenit-Pfadverzögerung dar. Es waren auch kleinräumige und schnelle zeitliche Fluktuation des atmosphärischen Zustandes zu erwarten. Der Einfluss von Abschattungen, unterschiedlicher Empfänger und Antennentypen und verschiedener Verarbeitungsstrategien auf die Bestimmung der Pfadverzögerung konnte somit genauestens studiert werden. Zur Validierung der Pfadverzögerungen wurden Radiosondierungen durchgeführt. Die Analyse lässt darauf schliessen, dass ein Parameter-Intervall von einer Stunde die beste Schätzung der Pfadverzögerung aus GNSS ermöglicht. Ein Intervall von 30 Minuten hat mehr zufällige Unsicherheiten in der Lösung generiert und keinen Gewinn für die zeitliche Auflösung gebracht. Die Pfadverzögerungen zeigten räumliche Korrelationen von wenigen Kilometern.

Die Vergleiche mit den Radiosonden-Daten ergaben Genauigkeiten von 4–6 mm. Mehrweg-Effekte und schlecht bestimmte Antennen-Phasenzentren verursachten bei einigen Stationen merkliche systematische Abweichungen. Durch die theoretisch bekannte Verschränkung von Stationshöhe und Zenit-Pfadverzögerung wurden diese Einflüsse in beiden Parametern festgestellt. Die Kampagnen-Daten lassen auch eine Analyse des Wettermodells COSMO-2 im alpinen Gebiet zu. Die Performanz in Bezug auf integrierte Zustandswerte in der Atmosphäre konnte quantifiziert werden und eine mögliche Vorgehensweise zur Assimilation von Zenit-Pfadverzögerungen in topographisch komplexen Regionen wird vorgeschlagen.

Contents

Abbreviations	vii
1 Introduction	1
1.1 Review of GNSS meteorology	1
1.2 Potential synergies with other water vapour measurements	6
1.3 Challenges in GNSS meteorology	8
1.4 Objectives and structure of the thesis	9
2 Theory	11
2.1 Refractivity and path delay in the atmosphere	11
2.2 Collocation with the software COMEDIE	13
2.2.1 Collocation of ZWDs with COMEDIE	13
2.2.2 Combined collocation of ZWDs and wet refractivities	15
2.2.3 Lagrange interpolation	16
2.2.4 Norm induced by a symmetric, positive definite Kernel	18
2.2.5 Lagrange interpolation solution as subspace of the Reproducing Kernel Hilbert Space	23
2.2.6 Minimum norm property of the pure collocation solution	25
2.2.7 Kernel interpreted as covariance function	26
2.2.8 Synthetic experiment to illustrate minimum norm property of Lagrange interpolation	29
2.2.9 Parameter estimation from empirical autocorrelations	33
2.2.10 Collocation interpreted as a solution to an integral equation	36
2.2.11 Appropriate station sampling for collocation	38
2.2.12 Recipe for collocation	40
2.3 Water vapour tomography software AWATOS2	41
3 Comparison of zenith path delays from GNSS and radiosonde measurements	43
3.1 Data description	43
3.1.1 Radiosonde data	43
3.1.2 GNSS data	44
3.1.3 Ground meteorological data	44
3.2 Formal uncertainties of ZTD estimates from GNSS	45
3.3 Comparison of ZTDs	47
3.4 Influence of processing strategy on GNSS ZTDs	52
3.5 2nd and 3rd order ionospheric effects	55
3.6 Comparison of ZWDs	55
3.7 Formal uncertainty of radiosonde-derived ZTDs	56
3.7.1 Methodology	57
3.7.2 Estimates of radiosonde formal uncertainty	64
3.8 Derivation of random GNSS ZTD uncertainty	64
3.9 Correlation between GNSS heights and ZTDs	64
3.10 Discussion	69
3.11 Conclusion	70

4	Payerne profile study	73
4.1	Abstract	73
4.2	Introduction	74
4.3	Description of data sets	75
4.3.1	GNSS zenith path delays	75
4.3.2	Meteorological ground stations	76
4.3.3	Radiosonde profiles in Payerne	76
4.3.4	Radio occultations	77
4.3.5	Ground-based microwave radiometer for temperature profiling	78
4.4	Processing	78
4.5	Results	81
4.5.1	Wet refractivity profiles	82
4.5.2	Humidity profiles	87
4.6	Discussion	90
4.7	Conclusions	92
5	Geodetic water vapor campaign in Zermatt	93
5.1	Data description and processing	93
5.1.1	GNSS Measurement Network	94
5.1.2	Ground meteorological stations	100
5.1.3	Radiosonde measurements	100
5.1.4	NWP model	105
5.1.5	Bernese GNSS software processing	105
5.1.6	Station coordinate repeatability	109
5.2	Troposphere results	115
5.2.1	Time resolution of the troposphere parameter	115
5.2.2	Network versus Precise Point Positioning solution	122
5.2.3	Mapping function	122
5.2.4	ZTD accuracy and up component repeatability	126
5.2.5	Horizontal spatial variability of GPS ZTDs	128
5.2.6	Comparison to NWP models	132
5.3	Conclusions	136
6	Conclusions	139
7	Outlook	141
	Bibliography	141
A	Design of AWATOS2	153
A.1	An introductory example	153
A.2	Modular layout	153
A.3	General object-oriented design	155
A.4	Other design patterns used	156
B	Model fits to empirical autocorrelation functions	165
C	Zenith Wet Delay comparison to Payerne radiosonde	167
D	Statistics of Zermatt troposphere results	169
E	Station repeatability of network solution	175
F	Skyplots of Zermatt campaign stations	179
G	ZTD time series of campaign stations	183

Abbreviations

AERI Atmospheric Emitted Radiance Interferometer

AGNES Automatic GNSS Network for Switzerland

amsl above mean sea level

CAPE Convective Available Potential Energy

COMEDIE Collocation of Meteorological Data for Interpolation and Estimation of Tropospheric Path Delays

GPT Global Pressure Temperature

DST Daylight Saving Time

GLONASS Russian Global Navigation Satellite System

GMF Global Mapping Function

GNSS Global Navigation Satellite System

GPS Global Positioning System

IFK Fredholm integral equation of the first kind

IGS International GNSS Service

IQR Inter Quartile Range

ISK Fredholm integral equation of the second kind

ITRF International Terrestrial Reference Frame

IWV Integrated Water Vapor

NWP Numerical Weather Prediction

PCV Phase Center Variation

PCO Phase Center Offset

p.d. positive definite

RKHS Reproducing Kernel Hilbert Space

RMS Root Mean Square

PPP Precise Point Positioning

PW Precipitable Water

PWV Precipitable Water Vapor

STD Slant Total Delay

SWV Slant Water Vapor

TEC Total Electron Content

ZDD Zenith Dry Delay

ZTD Zenith Total Delay

ZWD Zenith Wet Delay

Chapter 1

Introduction

1.1 Review of GNSS meteorology

Remote sensing of the atmosphere with the microwave signal of the Global Navigation Satellite Systems (GNSS) has become a well-established field of research with its major application in meteorology. The primary use of the microwave signals is obviously the positioning of receiving antennas on or within several 100 km around the earth. But the waves passing the atmosphere are affected by the concentration of free electrons in the ionosphere and by the air density in the lower stratosphere and the troposphere. These atmospheric influences can be retrieved to a certain degree in the processing of the GNSS data with sophisticated software. We will focus on the troposphere and discuss the possible parameters to be retrieved from the GNSS data. The following compilation summarizes the today's GNSS meteorology products that are of interest to the meteorological community and outlines their application.

Zenith total delay

The basic tropospheric parameter in present GNSS software is the Zenith Total Delay (ZTD) that describes the signal delay in zenith direction above the receiver. It results from the mapping of the delays to each individual satellite into the zenith direction with appropriate mapping functions (Boehm et al., 2006a,b; Niell, 2000). The mapping functions take the earth's curvature into account and assume horizontal and isotropic layering of the atmosphere around the station. The zenith delay is the combination of all these mapped delays into one parameter. It is therefore an average over all elevation angles and azimuths of the satellites in view and as such a spatial average over a certain part of the atmosphere.

The ZTD's horizontal scale of an exponential correlation function was shown for a study in Japan to be 644 ± 120 km (Shoji et al., 2004), where the scale was defined as the distance at which the correlation coefficient becomes $1/e$. Usually, the zenith path delays are also temporally averaged. For example, the Bernese GNSS software models the troposphere between ZTD parameters as piece-wise linear functions (Dach et al., 2007). The ZTD is traditionally either separated into a dry and wet part, called the Zenith Dry Delay (ZDD) and the Zenith Wet Delay (ZWD), or into a hydrostatic and non-hydrostatic (also termed: wet) part. The hydrostatic and dry part are much larger in amplitude but less varying in time. They are of the order of 2.30 m at sea level. The non-hydrostatic or wet part is more variable but smaller in amplitude, typically 0.0–0.40 m (e.g., Walpersdorf et al., 2001). The hydrostatic delay can be inferred from surface pressure (e.g., Brenot et al., 2013b) without any correction for the water vapor included therein. The dry delay additionally needs measurements of ground water vapor pressure (Troller, 2004). Depending on the research groups, the one or the other formulation is used. Note that GNSS software packages model the dry or hydrostatic delay with the corresponding mapping function as a priori given delays, whereas the wet or non-hydrostatic part is estimated (Dach et al., 2007). Such a procedure is recommended due to the strong similarities between the dry and wet mapping functions. Az-

initially dependent mappings have been investigated with Numerical Weather Prediction (NWP) model ray-traced slant factors by Urquhart et al. (2012). They conclude that “estimation of troposphere gradient parameters along with the use of the Vienna mapping function (VMF1)” produce better coordinate repeatability than their slant-factor approach.

The ZTD from ground-based Global Positioning System (GPS) receivers has become a routinely assimilated observation in some NWP models. In Bennitt and Jupp (2012), the results from several years of assimilation at the UK met office are presented. They see a mild improvement in forecasting clouds due to a general increase in relative humidity through the assimilated ZTDs.

IWV and PWV

Integrated Water Vapor (IWV) (in kg/m^2) and Precipitable Water Vapor (PWV) (in mm) are two equivalent terms and denote a parameter describing the column integrated water vapor in the atmosphere. The PWV is equivalent to the IWV scaled by the density of water. They are not considered a GPS observable as such, but can be derived from ZTD, ground pressure and mean atmospheric temperature (Bevis et al., 1994). Mean atmospheric temperature can be approximately inferred from surface temperature (Bevis et al., 1992) or determined from NWP models (Bevis et al., 1994). Compared to water vapor radiometer measurements as reference method, Duan et al. (1996) show that GPS can recover PWV with an Root Mean Square (RMS) uncertainty of 1.0–1.5 mm. These values have been confirmed by many other investigators (e.g., Van Baelen et al., 2005). An interesting use-case of IWV was shown by Champollion et al. (2009a). They investigate the urban-rural water cycle in an urban heat island setting over Paris.

Zenith delay gradients

In addition to the ZTD, the gradients of the zenith delay can be estimated for a ground-based GNSS station. The gradients measure the tilt of the atmosphere in north-south and east-west direction with the zenith delay being the center of the imaginary surface of the local gradient. Shoji et al. (2004) determines the horizontal scale (at which the correlation becomes $1/e$) of delay gradients to be 62 ± 23 km. Gradients are therefore affected by rather local atmospheric conditions. In general, gradients are poorly understood with respect to their actual tropospheric representativity. Urquhart et al. (2012) note a weak correlation of around 0.44 between gradients from ray-traced delays across a NWP model and those estimated in a Precise Point Positioning (PPP) campaign. Furthermore, gradients are often not estimated in the processing due to their strong correlation to other parameters. For example, Miyazaki et al. (2003) show that there are correlations between site coordinates and delay gradients, or between the gradient’s north component and the estimated ZTD. Still, estimating gradients improves position accuracy not only in the horizontal, but also in the vertical (Miyazaki et al., 2003). Despite the correlations to other parameters, several indications are given in the literature that estimated gradient parameters contain information on the tilt in the atmospheric layering (e.g., Shoji et al., 2004; Chen and Herring, 1997; Walpersdorf et al., 2001; Iwabuchi et al., 2003) and on general atmospheric anisotropy associated with initiation of deep convection (Brenot et al., 2013a). Unlike the case of ZTD, where dry and wet delays considerably differ in magnitude, dry and wet gradient components are of similar order of magnitude. They both have values of some centimeters (Walpersdorf et al., 2001), where gradients are defined in the GPS analysis package GAMIT (version 9.92) as delay differences on slant paths at 10° elevation in opposite directions, projected into the E–W and the N–S plane.

Residual delay

Whatever does not fit the model in the processing is dumped into the residuals. A common assumption is that the residuals from GNSS processing also contain unmodeled parts of the neutral atmosphere, i.e. the lower stratosphere and the troposphere. It is often called the non-isotropic part and should reflect local heterogeneities in the atmosphere. The atmospheric information contained in the residuals remains poorly understood. Many other errors such as multipath, clock errors or higher order ionospheric terms can end up in the residuals and can thus be misinterpreted as

tropospheric influences. Additionally, a commonly used processing strategy has been shown to lead to erroneous retrievals of the residual information under certain circumstances (Elósegui and Davis, 2004). A thorough analysis of postfit residuals has been attempted by Shoji et al. (2004), where the effect of multipath is removed with time-averaged postfit residuals, so-called multipath maps. Azimuthal errors from phase center variations are also corrected for. They infer a scale-length of 2–3 km for an exponential correlation function. Furthermore, from a selection of only the portion of postfit residuals that are larger than 3 mm, they note an increase in correlation in the first 10 km around each station, suggesting that severe local weather phenomena increase atmospheric inhomogeneity and that this increase is manifest in the residuals.

Slant total delay (STD)

When the ZTD is mapped back onto the satellites in view, the resulting delays are called STD. Depending on the processing strategy, the gradient parameters and the residuals are added to the STD. In case the STD is calculated with gradients and residuals, it shows directional variations in the atmospheric water vapour content. For example, the GFZ processing center provides STDs in near real-time that are then processed with a tomographic software to get the distribution of atmospheric water vapour in space and time (Bender et al., 2009, 2011). An example of a validation study of Slant Total Delay (STD) is given in Bender et al. (2008). They compare GPS STDs to radiometer measurements. Mapped to the zenith direction, the mean bias between the two measurement types is found to be 1.18 mm and the RMS is 6.0 mm. In an extensive study, simulated and real Slant Water Vapor (SWV) values have been assimilated into a NWP model (de Haan and van der Marel, 2008). They observe a slight improvement by assimilating the SWV instead of the IWV only. They mention two major advantages of SWV over IWV: (a) information on atmospheric gradients and non-isotropic delays and, (b) the part of the atmosphere sampled by the slant is exactly known.

Refractivity fields in space and time

The STD and ZTD are all integral measures of the atmospheric state. With a receiver network, the integral measures can be reconstructed into a time-varying 3D field of refractivity. Frequently, the ZTD is reduced by the dry part. The reconstruction then yields wet refractivity fields. Wet refractivity depends on both atmospheric temperature and humidity. The spatial resolution of such a field strongly depends on the number of stations that are deployed. In regions with complex topography, where the terrain allows stations to be placed at various heights above mean sea level, it is possible to retrieve vertical information on the wet refractivity field in the available vertical range. Above these stations, the horizontal and to a very limited extent the vertical variation of the wet refractivity can also be determined with tomographic techniques (Champollion et al., 2005; Nilsson and Gradinarsky, 2006; Perler et al., 2011). All these authors demonstrate a certain capability of ground-based tomography to retrieve vertical structures above the top station. In addition, Nilsson and Gradinarsky (2006) and Perler et al. (2011) show the theoretical possibility, to detect an inversion or spike layer, respectively. This is due to the earth’s curvature, but requires many and accurate measurements of the slant delay. Another investigation with theoretical considerations was published by Bender et al. (2009). They characterize the tomography geometry with various proxis that influence the quality of a tomographic reconstruction. Examples of their proxis are: number of ray intersection points for several tomographic grid configurations, distributions of satellite elevations and azimuths with time, percentage of empty grid cells, and histogram of crossing angles between intersecting rays.

The capability of tomography to investigate the diurnal cycle of water vapor in a coastal area is shown by Bastin et al. (2007). Bender et al. (2011) demonstrate that near real-time processing of a large GNSS station network in Germany with a dedicated tomography software is possible and show a qualitative comparison to a NWP model analysis. Another study assesses the uncertainty of the tomographic reconstruction of wet refractivity at Payerne for a one year study period (Perler, 2011). In contrast to other workers that first estimate the tropospheric parameters with a GNSS processing software and invert those delays in a separate tomography, Nilsson and

Gradinarsky (2006) use an alternative approach. They show in a simulation study the feasibility to invert the refractivity structure directly from raw GNSS observations, but with station coordinates being known beforehand. In Nilsson et al. (2007a), their approach is then proven to work also in a campaign setup with real data. In Notarpietro et al. (2011), a tomographic reconstruction is achieved with the aim, to get improved line of sight integrals from retrieved wet refractivity fields. Such an approach has been chosen to calibrate SAR or Interferometric-SAR observations for land remote sensing. A cross-validation of the delays and comparisons to ECMWF are carried out, but the aim of SAR calibration is neither investigated nor further discussed. It presents an overview of attempted tomographic techniques by other authors and their used setups.

The use of a robust Kalman filter approach is tested in Rohm et al. (2013). On the basis of a truncated singular value decomposition and removal of linearly strongly dependent observations, they try to arrive at a better conditioned model matrix. In an iterative procedure, they additionally weigh observations down that show a posteriori residuals above a certain threshold. This step should further improve robustness of the Kalman filter. The latter operation shows to have the largest impact and effectively removes outliers from simulated data. The paper by Xia et al. (2013) investigates a two-step procedure for the reconstruction of ground-based integrated slant water vapor determined from a PPP. For the first step, COSMIC radio occultation profiles provide the a priori values. A generalized inverse solution with the SWV data results in a 3D field of water vapor density. This field serves as input to the iterative algebraic reconstruction technique of the second step. Due to the use of radio occultation data as a priori values, tomography output is only created at the occurrence time of occultations. They obtain RMS differences to radiosonde data of 1.78 g/m^3 below 2.5 km and 0.44 g/m^3 above.

In the framework of better understanding convective initiation, an instructive comparison between GPS tomography, Raman Lidar and Atmospheric Emitted Radiance Interferometer (AERI) measurements have been carried out by Champollion et al. (2009b). In the GPS tomography, radiosonde profiles at 3–6 hourly intervals are included. Thus, it does not come as a surprise that the tomography results are amazingly good. The cloud mask product from the Lidar is nicely coinciding with regions of high relative humidity from the tomography (temperature from nearby radiosondes). Another study concentrates on the use of GPS tomography together with weather radar in a convective orographically-induced precipitation setting (Van Baelen et al., 2011). They are able to separate and explain two convection processes: water vapour blockage at the mountain ridge and a valley outflow with subsequent convection triggered by a hill. The same use-case is investigated with a multi-technique approach in Labbouz et al. (2013). GPS tomography supports the findings from the other techniques: The orography from the Vosges mountain range created moisture flux convergence as a prerequisite for convective initiation. For the effective convective initiation, the small scale orography of some hills inside the valley shows to play a major role.

The beneficial use of water vapor tomography in the Swiss Alps has been demonstrated by Lutz et al. (2010). Their tomographic results from two dense campaign networks yield wet refractivity fields, which are in good agreement with radiosonde measurements taken during the campaigns. Some of the most recent studies about tropospheric tomography with GNSS focus on meteorologically interesting case studies. These studies use tomography as additional means to characterize convective initiation processes in Belgium (Brenot et al., 2013a), or analyse water vapor with precipitation fields from rain radars on the Mediterranean coast and over the Cévennes-Vivarais range (Brenot et al., 2013b), or investigate thunderstorm development in Australia (Manning et al., 2013, 2012).

The densification of GNSS networks has reached an impressive level in Europe. For tomographic applications, it has been hypothesized that further densification is needed, which is obviously costly. Hence, Deng et al. (2009) developed an approach to use single-frequency receivers inside a dual-frequency receiver network. They show an agreement of $\approx 3 \text{ mm}$ RMS between collocated single-frequency and double-frequency receivers (see also Deng, 2012).

Turbulence parameters

A dense ground-based GPS network has been used by Nilsson et al. (2009) to derive information on atmospheric turbulence. The ZTDs from the network are displayed in the form of structure functions. Analytical functions of structure functions from Kolmogorov turbulence theory are fitted to the data and corresponding parameters are determined. Baselines present in the network range from tens of meters up to a few hundred kilometers. The authors consider this baseline distribution to be sufficient in order that most variations can be attributed to turbulence and not to variations such as the passage of weather fronts. Their results show strongly seasonal dependence of this so-derived turbulence parameter and they demonstrate that the retrieved values are mostly in accordance with Kolmogorov theory.

A different route is taken by Kleijer et al. (2004). They fit a variety of stochastic models to the postfit residuals to separate between turbulence from the atmosphere and any other random observation noise. Their models in the horizontal are based on refractivity structure functions that obey a power law, as predicted by Kolmogorov theory. For the vertical correlations, they investigate three different types of models. As they do not have any external validation of their retrievals, their conclusions are of a qualitative character.

Radio occultation measurements

Radiooccultation retrievals of the atmosphere have become a well-established use of space-based GNSS receivers. Excess phase delay and further derived products such as bending angles and refractivity profiles are widely assimilated into Numerical Weather Prediction (NWP) models (Anthes, 2011). The profiling nature and global coverage have made it an important data input, especially in the southern hemisphere. A comprehensive description of the technical aspects concerning radio occultation retrievals is given in Hajj et al. (2002). The quality of the wetPrf product of COSMIC, also used in this thesis, has been evaluated under very strict matching conditions to radiosonde profiles by Wang et al. (2013a). They determine a global mean temperature bias of -0.09 K at 925–10 hPa and a standard deviation of 1.72 K with respect to global radiosonde data. Specific humidity bias is determined to be -0.012 g/kg at 925–200 hPa with a standard deviation of 0.666 g/kg, but these values are strongly height dependent. Characteristics of radio occultation measurements, especially with respect to the tangent point trajectory, are studied with synthetic data by Foelsche et al. (2011). The combination of ground- and space-based GNSS products for atmospheric sciences in a thorough ray-tracing approach has been tentatively investigated in Foelsche and Kirchengast (2001). With the present-day coverage of ground-based GNSS stations in Europe and the many occultations from the COSMIC satellites (launched in April 2006), revisiting this approach is a vital option to mitigate the ill-posedness of the tropospheric water vapor tomography.

Vertical refractivity profiles from single ground-based GNSS stations

Vertical refractivity profiling from single ground-based GPS stations has been investigated by Lowry et al. (2002), Wu et al. (2010), Lin et al. (2012), and Wu et al. (2014). The most comprehensive study is given in Lowry et al. (2002), where they use a simplified refractivity profile to determine the height of the ducting layer, which is frequently observed at their investigation site in San Diego, California. The model of Lowry et al. (2002) has been slightly extended by Wu et al. (2010), showing on synthetic tests the successful retrieval of refractivity profiles. Promising results were shown by Wu et al. (2014) for synthetic tests and real data with a receiver in Beijing. They apply an extensive search algorithm and reduce their search space with five years of COSMIC radio occultation data. Only elevations between 3 – 5° are considered, due to mainly three stated reasons (personal communication with Wu et al.; date: 9 Jan 2014):

1. Their ray tracing algorithm does not account for atmospheric gradients. They demonstrate that the simulated path delays with data from radiosondes and concurrent GPS slant delays considerably differ at elevations $< 3^\circ$. Other effects that are difficult to model, such as multipath, might add to the discrepancies at low elevations.

2. The path delays used for the inversion are back mapped ZTDs and no postfit residuals are added. They thus have to rely on data that does not catch well the refractivity structure below 3° .
3. Some of the low-elevation observations in the south direction are blocked by a building next to their site.

The approach used by Lin et al. (2012) using a relevance vector machine to determine the profiles from differences in STD at various elevations offers an interesting alternative to classical inversion methods. I envisage that the relevance vector machine could also work well in conjunction with radar ground clutter maps that contain information about refractivity gradients in the boundary layer.

Other weather-related parameters

In de Haan (2006), a relationship between a measure of atmospheric stability and a convection parameter derived from GPS observables is sought. The connection is established between Convective Available Potential Energy (CAPE), a commonly used parameter by forecasters to characterize the atmospheric stability, and the power of the non-isotropic GPS path-delay signal, that is, the slant delay minus the isotropic part of the delay. In fact, the temporal frequency content of the postfit-residuals is analysed. The paper shows that there exists a correlation between the total power of this Fourier spectrum and CAPE. The residuals used in the study are double-differenced, and thus, the zero-mean assumption is necessary to get them on a single satellite-receiver basis. That reduces the available elevation angles to $> 50^\circ$, due to the concerns raised by Elósegui and Davis (2004). As the connection between CAPE and residual power is established by the relationship between the refractivity gradient and the Brunt-Väisälä frequency, the reduction to high elevation angles is unfortunate. A more meaningful analysis would probably build on the excess phase path delays at very low elevations. Additionally, the spatial frequency content is not considered at all in the paper. On a very preliminary basis and qualitatively, this latter aspect has been discussed in Brenot et al. (2013b).

From tomographic reconstruction of path delays into wet refractivity during a severe weather event in Australia, Manning et al. (2012) calculate an average refractive index above the boundary layer. This index is used to describe the evolution of the thunderstorm and serves as a proxy of atmospheric stability. It has originally been derived for atmospheric stability characterization with total refractivity measurements from radio occultation measurements (Sharma et al., 2009).

1.2 Potential synergies with other water vapour measurements

GNSS meteorology as shown in Sect. 1.1 has two major targets in mind:

1. It improves the data basis for more accurate fields of atmospheric state variables, such as temperature and relative humidity. Measurements of the state variables have a direct influence on the performance of NWP model predictions. They help solving the initial and boundary value problems of the differential equations inherent in NWP models.
2. In turn, a more accurate description of the atmosphere helps in modeling the atmospheric contribution to the positioning error in GNSS measurements. If improved NWP model output is available, dedicated mapping functions such as the Vienna mapping function, ray-traced slant delays and ray-traced slant-factors (Urquhart et al., 2012) become even more standard in high-precision positioning.

The chance to reach the targets depends on the capability to combine measurements from many methods and thus to profit from the complementary strengths of them. Suitable measurement types to combine with GNSS meteorology data have networks of a similar coverage to the GNSS

networks, are available shortly after being acquired and deliver measurements under most, if not all, weather conditions. There are a number of measurement devices and methods that meet these requirements. The following list mentions the techniques, which are considered by the author to be the most suitable ones for combination on a quantitative level.

ground meteorological measurements: Obvious and elementary data sets are the pressure, temperature and humidity measurements from ground meteorological stations. The potential combination with GNSS meteorology has been mentioned and simulated many times but hardly ever put into practice. It should be noted that ground meteorological measurements are point measurements. In the data combination, they should be treated as such. By no means should they be used to directly calculate ZTDs in a processing software.

satellite-based: A very vital source of water vapour and temperature profiles from satellites are delivered by the Infrared Atmospheric Sounding Interferometer (IASI) on-board the MetOp satellites. Examples of accuracies provided by the instrument are given in Pougatchev et al. (2009) and Masiello et al. (2013). The latter determine an approximate relative accuracy in the lower troposphere of 10 % water vapour amount in layers of 2 km width. They also claim that, unlike the very accurate IASI instrument, the presently most advanced passive microwave sounding units on-board the MetOp satellites 1 to 3 are too limited in accuracy and vertical resolution to have a large impact upon assimilation into NWP models.

weather radar near-surface refractivity: The basic publication that triggered a large effort to determine near-surface refractivity values from weather radar was Fabry et al. (1997). Their use of static ground-based obstacles causing ground echoes in the radar beam has been developed further by several radar groups. It has for example been put into operational use in the UK (Nicol et al., 2011), where they adapt parts of the algorithms to account for their transmitters. Their transmitters' frequency stability is poorer than those investigated in the original study by Fabry et al. (1997). Hence, they determine refractivity changes with respect to some reference epoch, which is not far from the measured epoch's time (typically some hours). In view of making the refractivity retrieval from phase changes also operational in the French radar network, improvements in the retrieval are investigated by Besson and Parent du Châtelet (2013). Quantification of noise in phase measurements due to variable ground target heights and near surface propagation conditions is attempted in an extensive simulation study by Park and Fabry (2010). The application of the method has already yielded intriguing results. Fabry (2006) evaluate the influence of small scale temperature and humidity variability in the boundary layer on storm initiation. Humidity variability is quantified with the variability of the refractivity field from the radar. Their data indicate that temperature variability on scales of 50 km is more important for convective initiation than on small scales of a few kilometers, whereas humidity and updraft velocity are probably the dominant factors on small scales.

refractivity gradient from weather radar: In addition to refractivity values, ground echoes of scanning weather radars can sense the near-surface refractivity gradient dN/dh (Park and Fabry, 2011). Validation procedures compare the radar vertical refractivity gradient dN/dh with measurements of the Atmospheric Emitted Radiance Interferometer (AERI) and with radiosonde observations. They note a generally good agreement between low-level dN/dh from the sonde, the AERI measurements and the radar's amount of ground echo coverage, but also see a discrepancy between the representativeness of radar estimates and the point measurements of the validation observations.

attenuation effects in wireless communication network measurements: Another interesting measurement of near-surface water vapour comes from measuring attenuation effects on microwave links between base stations of cellular networks (David et al., 2009). The type of data is available in many parts of the world, including regions of complex terrain such as the Alps, and could theoretically be retrieved at almost any time resolution. One example in David et al. (2009) performs fairly well with an RMS difference of 1.8 g/m^3 with respect to measurements from a ground meteorological station. The second example shows an RMS difference of 3.4 g/m^3 and a weaker correlation due to reasons they can only speculate about.

There are many more techniques available to combine with GNSS measurements of water vapour. They will definitely gain in importance, if extensive station networks are built. Further vital options for the near future are Raman Lidar and microwave radiometer networks. After all, one last technique is mentioned for oddity: Determination of humidity profiles with a wind-profiling radar and a Radio Acoustic Sounding System (RASS) has been demonstrated by Furumoto et al. (2007).

1.3 Challenges in GNSS meteorology

We have seen that GNSS meteorology has advanced a lot in the past 10 years. Today, many different products are derived from GNSS measurements. Each product senses some sort of meteorological state. The most prevalent product is the ZTD. Some people might object and claim the STD to be the most important GNSS meteorological product. The STD seems to be a more basic or direct measurement of the atmospheric state. It also seems to be independent from some simplified atmospheric model, such as a mapping function approach. Is this true? Yes and no. Let us forget for a moment the ionosphere, the multipath and many other error-causing influences. If you had a perfect and absolute position of a GNSS antenna in an earth-fixed reference frame and if the receiver clock were without drift, the answer would be yes. You could fix the position and clock parameters in the adjustment of a single GNSS station and determine the tropospheric delays between the station and each individual satellite. Without a perfect position and clock, we need to estimate the position, the clock, and the tropospheric delay in a common adjustment. Here, we always rely on some sort of simplified atmosphere model. If we estimated an individual tropospheric delay to each satellite, a strongly under-determined system would result, with clock errors directly correlating with the estimated delays. Hence, simplification is needed and some mapping functions have proven to be very good simplifications of the tropospheric structure. Eventually, the mapping functions enable us to describe the tropospheric delay with one parameter, which is the ZTD.

Since we prefer to have a delay to each individual satellite instead of one averaging parameter, the ZTD is commonly used to reconstruct the STDs. Optionally, one introduces gradient parameters into the GNSS estimation process and uses the gradients to obtain some of the azimuthal asymmetry that must be present in STDs. Residuals might in a large part contain tropospheric delays and thus, might be added to the reconstruction, too. In the end, we get an amalgam of three values, which have undergone many processing steps. We call it the STD and consider it to be a direct measurement of the tropospheric state by GNSS. The situation further complicates, if the processing is carried out in double-difference mode due to the fact that residuals must be reconstructed into zero-difference residuals with additional assumptions. In an attempt to characterize the STD, it has been compared to measurements from microwave radiometers, or the STD has been introduced into tomographic software and resulting refractivities have been compared to radiosondes. The general agreement of these investigations: Residuals and gradient parameters increase the discrepancy of the GNSS STDs to the validation data (e.g., Kačmařík et al., 2012). In conclusion, the STD is by far not as direct and simple a measurement of the troposphere as it seems in the first place.

Presently, the STD is considered to be the GNSS observation of choice for assimilation into NWP models. A measurement should be equipped with its accuracy. Now recall that the STD is to a large part composed of the back-mapped ZTD. Hence, in order to quantify the STD accuracy, we foremost need to assess the ZTD accuracy. Naturally, uncertainty in the gradients and the residuals lower the STD accuracy and would need to be assessed in a further step. There are three major challenges that arise from the need to determine the ZTD's accuracy:

1. Lack of a validation data set from a measurement technique whose ZTDs are clearly more accurate than the GNSS ZTDs
2. The correlation of the ZTD to other parameters in the GNSS processing

3. Incomplete or poor knowledge of unmodeled parts in the GNSS processing and their influences on the ZTD.

These are the challenges a geodesist is mostly faced with. From a meteorologist’s viewpoint, further challenges arise:

1. How does the measurement from the “real” world fit into the model world with its own model orography?
2. How to meld the many scales influencing a measurement in reality with the few scales considered by a NWP model?
3. Is the “real-world” accuracy assigned to the measurement in agreement with the accuracy of the assimilated measurement in the incomplete model-world?

It is the aim of the presented thesis to help resolving some of the stated geodetic challenges and to start a bridge to the meteorological challenges. The author hopes that future projects can finally bridge the knowledge gap between geodesy and meteorology.

1.4 Objectives and structure of the thesis

After having caught a glimpse of many topics in GNSS meteorology, it has been decided to write the thesis on the basis of three objectives:

1. A primary objective is the characterization and quantification of the GNSS ZTD accuracy. Since measurements from radiosondes are used to evaluate the ZTD accuracy, a thorough uncertainty budget of the radiosonde is a prerequisite. Furthermore, the ZTDs calculated from radiosonde data are known to have accuracies, which are not considerably better than those from GNSS. An attempt has therefore been undertaken, to assign observed differences between GNSS and radiosonde ZTDs to either technique.
2. Some of the weaknesses recognized in GNSS ZTD measurements have lead to a second objective: Further development of an existing interpolation methodology to incorporate different measurement types. The question is, if some of the inaccuracy present in ZTDs can be compensated for with other measurements and still lead to accurate measurements of atmospheric humidity.
3. The small-scale variability of ZTDs in complex terrain is another objective. The problem statement requires data from a dedicated station network, with many stations placed at short distances and at many different heights in a mountainous region. Due to the effort needed to run a highly dense network in mountainous terrain, the idea of a permanent network had to be given up in favour of a campaign setup. Thus, the objective includes the planning, realization, processing and data analysis of a GNSS campaign in the Swiss Alps.

Accordingly, the thesis contains three major chapters that focus each on one of the objectives. Following Chap. 2, which explains mathematical aspects of GNSS meteorology and introduces the interpolation method to combine the different measurement types, the ZTD accuracies of GNSS and radiosondes are investigated in Chap. 3. The reconstruction of humidity profiles from several techniques and their validation with radiosonde data is contained in Chap. 4. The third objective leads to a spatially dense campaign network in the Swiss Alps. The network description, the data processing and analysis are presented in Chap. 5. Eventually, the conclusions in Chap. 6 and the outlook in Chap. 7 set the findings into each other’s perspective.

Chapter 2

Theory

The first section of the theory chapter introduces the most important equations and concepts of GNSS meteorology. The second section provides an extensive description of least-squares collocation, a method to interpolate measurements. It starts with the equations that are directly needed to understand the methodology of Chap. 4. The following theoretical treatment reviews the properties of collocation. Several literature sources that deal with the topic from different viewpoints, have been summarized and put together. Some of the properties of collocation are illustrated with numerical experiments and examples. The experiments with synthetic data are meant to provide rules of thumb how to apply collocation in practice. A short section about the water vapor tomography and simulation software AWATOS2 completes the theory chapter.

2.1 Refractivity and path delay in the atmosphere

The propagation of radio waves from the GNSS satellite to the ground receiver across the atmosphere is affected by the free electron content in the ionosphere and by the air in the electrically neutral atmosphere. Both influences are described in terms of the refractive index. In the sequential, we will only deal with the neutral atmosphere. The corresponding refractive index, n , and the atmospheric refractivity $N_{\text{tot}} = (n - 1) \cdot 10^6$ in $\frac{\text{mm}}{\text{km}}$, are described by the meteorological parameters air pressure p , air temperature T and partial water vapor pressure e according to Essen and Froome (1951):

$$N_{\text{tot}} = N_{\text{dry}} + N_{\text{wet}} = k_1 \cdot \frac{p_{\text{dry}}}{T} + k_2 \cdot \frac{e}{T} + k_3 \cdot \frac{e}{T^2} \quad (2.1)$$

with the two contributions to total refractivity N_{tot} being the dry refractivity N_{dry} and the wet refractivity N_{wet} :

$$N_{\text{dry}} = k_1 \cdot \frac{p_{\text{dry}}}{T} \quad (2.2)$$

$$N_{\text{wet}} = k_2 \cdot \frac{e}{T} + k_3 \cdot \frac{e}{T^2} \quad (2.3)$$

and with p_{dry} given as

$$p_{\text{dry}} = p - e. \quad (2.4)$$

$$\begin{aligned}
k_1 &= 77.6890 \text{ K hPa}^{-1} \\
k_2 &= 71.2952 \text{ K hPa}^{-1} \\
k_3 &= 375463 \text{ K}^2 \text{ hPa}^{-1} \\
p &: \text{total air pressure [hPa]} \\
p_{\text{dry}} &: \text{dry air pressure [hPa]} \\
e &: \text{water vapour pressure [hPa]} \\
T &: \text{air temperature [K]}
\end{aligned}$$

The empirically determined coefficients k_1 , k_2 , and k_3 have been reported by many researchers. For our investigations, we use the values given by Rüeiger (2002). Since p_{dry} , e , and T are functions of position and time, also N_{tot} depends on position and time. For reasons of simplicity, we will always assume $N_{\text{tot}} = N_{\text{tot}}(\underline{x}, t)$ with \underline{x} being a vector of coordinates in cartesian space.

The integral of the refractive index along the signal path between satellite r and station p determines the slant delay

$$\Delta\rho_p^r = \int_p^r (n - 1) ds = 10^{-6} \int_p^r N ds \quad (2.5)$$

that adds, among other influences, to the geometrical distance between satellite and receiver. In the discrete case, we get

$$\begin{aligned}
\Delta\rho_p^r &\approx \sum_{i=1}^k \frac{N_{i+1} + N_i}{2} \cdot \Delta s_i \\
\Delta s_i &= |\underline{x}_{i+1} - \underline{x}_i|
\end{aligned} \quad (2.6)$$

where we have

$$\begin{aligned}
\Delta s_i &: \text{linear space segment} \\
\underline{x}_i, \underline{x}_{i+1} &: \text{vectors of coordinates in cartesian space} \\
N_i, N_{i+1} &: \text{refractivity values at positions } \underline{x}_i, \underline{x}_{i+1} \\
i &: \text{index denoting discrete position/refractivity pairs} \\
k &: \text{number of discrete linear segments between satellite } r \text{ and station } p.
\end{aligned} \quad (2.7)$$

The refractivity N either stands for N_{tot} , N_{dry} and N_{wet} , resulting in a total, dry or wet delay, respectively. Corresponding delays in the zenith direction are the ZTD, the ZDD and the ZWD.

For the calculation of coordinates from GNSS data, the slant delay $\Delta\rho_p^r$ is usually modeled with appropriate mapping functions $m(z_p^r)$ as a function of the observation zenith angle z_p^r (90° minus the elevation angle) and the delays in the zenith direction. Since the mapping functions of the dry and the wet part are not identical, they need to be separately modeled:

$$\Delta\rho_p^r = \text{ZDD} \cdot m_{\text{dry}}(z_p^r) + \text{ZWD} \cdot m_{\text{wet}}(z_p^r). \quad (2.8)$$

In GNSS processing packages, it is common practice to provide an approximate ZDD. The ZWD is the parameter that is eventually estimated. This procedure is justified since the dry and the wet mapping functions are too similar to allow a proper estimation of both, the ZDD and the ZWD.

If we require the total path delay to be calculated from ground meteorological values only and not taking into account the refractivities along the ray path or, if we need to provide an a priori zenith delay, the Saastamoinen formula (Saastamoinen, 1973) is commonly used by setting the zenith angle $z_p^r = 0$:

$$\Delta\rho_{\text{tot}, \text{Saasta}}(z_p^r) = \frac{a_1}{\cos(z_p^r)} \left(p + \left(\frac{a_2}{T} + a_3 \right) \cdot e - B \cdot \tan^2(z_p^r) \right) + \delta_R \quad (2.9)$$

with the following coefficients:

$$\begin{aligned} z_p^r &: \text{zenith angle} \\ a_1 &= 0.002279 \text{ hPa}^{-1} \text{ m} \\ a_2 &= 1153 \text{ K} \\ a_3 &= 0.074 \end{aligned} \tag{2.10}$$

where the coefficients a_1 , a_2 , and a_3 were derived using the coefficients k_1 , k_2 and k_3 defined in Eq. (2.1) and applying them to Saastamoinen's formula. The derivation of the coefficients a_1 , a_2 , and a_3 from the k_1 , k_2 and k_3 is shown in Troller (2004). The B and the δ_R term are additional terms that depend on the station height. For this thesis, none of the two terms is taken into account and the formula is always used in the zenith direction. Hence, the formula simplifies to

$$\Delta\rho_{tot,Saasta,zenith} = a_1 \cdot \left(p + \left(\frac{a_2}{T} + a_3 \right) \cdot e \right) \tag{2.11}$$

The Saastamoinen formula can be split up into a dry and wet part following Troller (2004):

$$\Delta\rho_{dry,Saasta} = \frac{a_1}{\cos(z_p^r)} \left(p - a'_3 \cdot e - B \cdot \tan(z_p^r)^2 \right) + \delta_R \tag{2.12}$$

$$\Delta\rho_{wet,Saasta} = \frac{a_1}{\cos(z_p^r)} \left(\frac{a_2}{T} + a''_3 \right) \cdot e \tag{2.13}$$

with

$$\begin{aligned} a_1 &= 0.002279 \text{ hPa}^{-1} \text{ m} \\ a_2 &= 1153 \text{ K} \\ a'_3 &= 0.155500 \\ a''_3 &= 0.229425 \end{aligned} \tag{2.14}$$

The expression in Eq. (2.12) for $z_p^r = 0$ will be frequently used in this thesis to calculate the ZDD. Likewise, the B and the δ_R terms will be omitted.

2.2 Collocation with the software COMEDIE

There are a number of applications, where we need to know the atmospheric state at various locations that do not coincide with actual measurement locations. To interpolate and extrapolate such quantities to arbitrary locations from real meteorological measurement stations, the software package Collocation of Meteorological Data for Interpolation and Estimation of Tropospheric Path Delays (COMEDIE) was developed at the Geodesy and Geodynamics Lab at ETH Zurich, Switzerland (e.g., Eckert et al., 1992a,b; Hirter, 1998; Troller, 2004). COMEDIE is equipped with a least-squares collocation algorithm. Originally, the algorithm has been introduced to geodesy for the interpolation of gravity anomalies from various types of different measurements, such as the gravitational potential differences, the gravitational force or the deflection of the vertical (Moritz, 1978). Several processing steps in this thesis rely on COMEDIE. Above all, the reconstruction of wet refractivity profiles at Payerne from ZWDs. In a more advanced version of the algorithm, wet refractivities are reconstructed from a combination of ZWDs with N_{wet} from point measurements. A theoretical description of the least-squares collocation is given in the following sections.

2.2.1 Collocation of ZWDs with COMEDIE

We have measurements l (Fig. 2.1) that are adjusted in the least-square sense to a deterministic part $f(\mathbf{u}, \mathbf{x}, t)$, and to stochastic parts s and n (modified after Troller, 2004):

$$l = f(\mathbf{u}, \mathbf{x}, t) + s(\mathbf{C}_{ss}, \mathbf{x}, t) + n \tag{2.15}$$

where:

l :	measurement
$f(\mathbf{u}, \mathbf{x}, t)$:	function describing general field of measured values
\mathbf{u} :	unknown parameters
\mathbf{x}, t :	coordinates in space and time
$s(\mathbf{C}_{ss}, \mathbf{x}, t)$:	stochastic parameter $s \sim \mathcal{N}(0; \mathbf{C}_{ss})$
n :	stochastic parameter $n \sim \mathcal{N}(0; \mathbf{C}_{nn})$

The deterministic part $f(\mathbf{u}, \mathbf{x}, t)$ is a function that describes the general trend of the measurements (Fig. 2.1). We employ the following deterministic functions for total air pressure p , water vapour pressure e and ZWD:

$$p(x, y, z, t) = [p_0 + a_p(x - x_0) + b_p(y - y_0) + c_p(t - t_0)] \cdot e^{-\frac{z}{H_p}} \quad (2.16)$$

$$e(x, y, z, t) = [e_0 + a_e(x - x_0) + b_e(y - y_0) + c_e(t - t_0)] \cdot e^{-\frac{z}{H_e}} \quad (2.17)$$

$$\text{ZWD}(x, y, z, t) = [\text{ZWD}_0 + a_{\text{ZWD}}(x - x_0) + b_{\text{ZWD}}(y - y_0) + c_{\text{ZWD}}(t - t_0)] \cdot e^{-\frac{z}{H_{\text{ZWD}}}} \quad (2.18)$$

x_0, y_0, t_0 :	coordinates of reference point and reference time
x, y, z, t :	cartesian coordinates and time
p_0, e_0, ZWD_0 :	pressure, water vapour pressure and ZWD at reference position and time
H, a, b, c :	scale height, and gradient parameters in x, y , and time, respectively. Subscripts denote their affiliation to p, e and ZWD

The covariance matrix \mathbf{C}_{ss} of the stochastic parameter s is described by an analytical covariance function showing spatial and temporal dependencies between measurements. In the literature, it is also termed the signal part of the measurements. The henceforth used covariance function is a function of the distance between the measurements, how much they differ in time and, a scaling factor that increases the correlation length with height above ground (Hirter, 1998).

$$\mathbf{C}_{ss}(\text{ZWD}_k, \text{ZWD}_l) = \frac{\sigma_{\text{signal}}^2}{q} \quad (2.19)$$

where we have for q :

$$q = 1 + \left[\left(\frac{x_k - x_l}{\Delta x_0} \right)^2 + \left(\frac{y_k - y_l}{\Delta y_0} \right)^2 + \left(\frac{z_k - z_l}{\Delta z_0} \right)^2 + \left(\frac{t_k - t_l}{\Delta t_0} \right)^2 \right] \cdot e^{-\frac{z_k + z_l}{2z_0}} \quad (2.20)$$

σ_{signal}^2 :	a priori covariance of signal
x_k, y_k, z_k, t_k :	cartesian coordinates and time of observation k
x_l, y_l, z_l, t_l :	cartesian coordinates and time of observation l
z_0 :	scale height modifying the correlation lengths as a function of height
$\Delta x_0, \Delta y_0, \Delta z_0, \Delta t_0$:	correlation lengths of space and time

The stochastic parameter n is described by the covariance matrix \mathbf{C}_{nn} containing the noise of the individual measurements in the diagonal elements and with all off-diagonal elements being zero.

The collocation eventually estimates in a least-squares sense the parameters \mathbf{u} of the deterministic function (the field-specific parameters p_0, e_0 and ZWD_0 and the parameters a, b, c, H for the respective fields) and the signal and noise part of each measurement. The collocation also allows the interpolation of the deterministic and the signal parts to the points where no measurements are available (Fig. 2.1).

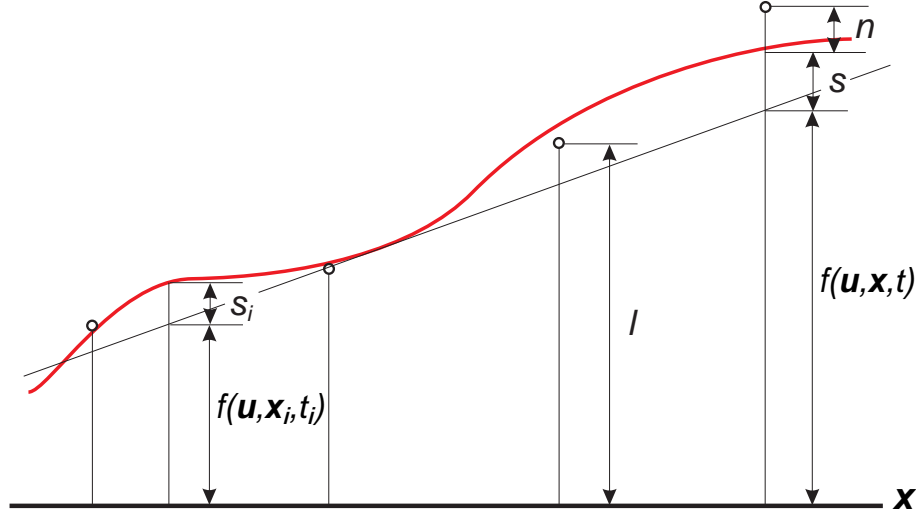


Figure 2.1: Principle of collocation (Troller, 2004). The circles are the measurements l , which are comprised of a deterministic part $f(\mathbf{u}, \mathbf{x}, t)$, of signal s and noise n . The interpolated values are noise-filtered and hence, contain the deterministic part $f(\mathbf{u}, \mathbf{x}_i, t_i)$ at the interpolation point (position \mathbf{x}_i and time t_i) plus the signal s_i .

2.2.2 Combined collocation of ZWDs and wet refractivities

For the combined collocation, we need to describe the relationship between the two measurements. Since N_{wet} is the derivative of the ZWD in zenith direction (Eq. 4.2), the two observation equations become:

$$l_{\text{ZWD}} = f(\mathbf{u}, \mathbf{x}, t) + s(\mathbf{C}_{ss}, \mathbf{x}, t) + n \quad (2.21)$$

$$l_{N_{\text{wet}}} = D(f(\mathbf{u}, \mathbf{x}, t) + s(\mathbf{C}_{ss}, \mathbf{x}, t) + n) \quad (2.22)$$

with

l_{ZWD} :	ZWD measurement
$l_{N_{\text{wet}}}$:	N_{wet} measurement
$f(\mathbf{u}, \mathbf{x}, t)$:	function describing general ZWD field
\mathbf{u} :	unknown parameters of ZWD field
\mathbf{x}, t :	coordinates in space and time
$s(\mathbf{C}_{ss}, \mathbf{x}, t)$:	signal part with respect to ZWD
n :	noise part with respect to ZWD
D :	differential operator relating ZWD to refractivity N_{wet}

and where D :

$$D = -\frac{\partial}{\partial z}. \quad (2.23)$$

Applying the differential operator to the deterministic part of the ZWD (Eq. 2.18), we obtain

$$\begin{aligned} N_{\text{wet}}(x, y, z, t) &= DZWD(x, y, z, t) \\ &= \frac{1}{H_{\text{ZWD}}} [\text{ZWD}_0 + a_{\text{ZWD}}(x - x_0) + b_{\text{ZWD}}(y - y_0) + c_{\text{ZWD}}(t - t_0)] \cdot e^{-\frac{z}{H_{\text{ZWD}}}} \end{aligned} \quad (2.24)$$

Application of the differential operator to the signal of the stochastic part leads to two different covariance matrices. In the first case, the covariance between ZWD and N_{wet} is derived. In a second case, we seek the covariance between two refractivities $N_{\text{wet},k}$ and $N_{\text{wet},l}$:

Case 1:

$$\begin{aligned} \mathbf{C}_{ss}(N_{\text{wet}}, \text{ZWD}) &= \mathbf{C}_{ss}(\text{ZWD}, N_{\text{wet}}) \\ &= \frac{\sigma_{\text{signal}}^2}{q^2} \left[\frac{2 \cdot (-z_{\text{ZWD}} + z_{N_{\text{wet}}})}{(\Delta z_0)^2} \cdot e^{-\frac{z_{N_{\text{wet}}} + z_{\text{ZWD}}}{2z_0}} + \frac{1-q}{2z_0} \right] \end{aligned} \quad (2.25)$$

Case 2:

$$\begin{aligned} \mathbf{C}_{ss}(N_{\text{wet},k}, N_{\text{wet},l}) &= \mathbf{C}_{ss}(N_{\text{wet},k}, N_{\text{wet},l}) \\ &= \frac{2\sigma_{\text{signal}}^2}{q^2} \left[\frac{e^{-\frac{z_k+z_l}{2z_0}}}{(\Delta z_0)^2} + \frac{(q-1)(q-2)}{8qz_0^2} - \frac{4(z_k-z_l)^2}{q(\Delta z_0)^4} \cdot e^{-\frac{z_k+z_l}{z_0}} \right] \end{aligned} \quad (2.26)$$

The uncorrelated noise n of the ZWD becomes the uncorrelated noise of the N_{wet} measurements under the influence of the differential operator.

2.2.3 Lagrange interpolation

Lagrange interpolation is the term found in some mathematical literature to describe the simplest form of collocation. It considers the signal part only. Neither observation noise nor any deterministic model are included in the mathematical model and there are no functionals such as Eq. (2.23) applied to the observations. Despite being very basic, it provides us with some notion of the behaviour of collocation. It will allow us to derive the minimum norm property of collocation. In a special case, the minimum error variance property will also be introduced. The properties will eventually help us to give recommendations on the choice of the covariance function and corresponding parameters, such as the correlation length.

Lagrange interpolation has been nicely compiled in Iske (2011), whose presentation of the method has been summarized here, largely following the notation therein. Let us start with multivariate scattered data sampled at a finite number of discrete points $X = \{x_1, \dots, x_n\} \subset \mathbb{R}^d$, $d \geq 1$ from an unknown function $f : \mathbb{R}^d \rightarrow \mathbb{R}$:

$$f_X = (f(x_1), \dots, f(x_n))^T \in \mathbb{R}^n \quad (2.27)$$

Lagrange interpolation requires a perfect match of the interpolant $s : \mathbb{R}^d \rightarrow \mathbb{R}$ with the unknown function f at the sampled data points:

$$s(x_k) = f(x_k), \quad \text{for all } 1 \leq k \leq n \quad (2.28)$$

In a standard approach, one represents the interpolant s with a linear combination of n basis functions $\mathcal{B} = \{s_1, \dots, s_n\}$:

$$s = \sum_{j=1}^n c_j s_j \quad (2.29)$$

where n corresponds to the number of sampled data points given by the set X . Each s represented by the finite sum in Eq. (2.29) is an element of a finite dimensional linear function space with basis \mathcal{B} . Given n data points and the basis functions, the interpolation problem becomes according to Eq. (2.28):

$$s(x_k) = \sum_{j=1}^n c_j s_j(x_k) = f(x_k), \quad \text{for all } 1 \leq k \leq n \quad (2.30)$$

or in matrix notation, with $V_{\mathcal{B},X} = (s_j(x_k))_{1 \leq j, k \leq n} \in \mathbb{R}^{n \times n}$:

$$V_{\mathcal{B},X} \cdot c = f_X \quad (2.31)$$

where we have to solve for the unknown coefficients c_j in $c = (c_1, \dots, c_n)^T \in \mathbb{R}^n$. Now let us assume we take n data points and then shift them randomly around on \mathbb{R}^d . As the data is shifted, a new set X and thus, another f_X is produced. Independently of the chosen set X and its corresponding f_X , we always want the linear equation system Eq. (2.30) to have a solution. That is, $V_{\mathcal{B}, X}$ should never become singular. In Iske (2011), it is shown with the Mairhuber-Curtis theorem that if we use the above defined basis $\mathcal{B} = \{s_1, \dots, s_n\}$ for $n \geq 2$ data points of dimension $d \geq 2$, there is always a point set $X = \{x_1, \dots, x_n\}$ causing the matrix $V_{\mathcal{B}, X}$ to become singular. Therefore, if we want to interpolate many n -point data sets of type X (where $d \geq 2$), we cannot rely on the single basis $\mathcal{B} = \{s_1, \dots, s_n\}$. Instead, we need a basis that depends on the sets of type X . A straightforward choice is the following:

$$s_j \equiv K(x_j, x) \quad \text{for all } 1 \leq j \leq n \quad (2.32)$$

for some continuous function $K : \mathbb{R}^d \times \mathbb{R}^d \rightarrow \mathbb{R}$. With the new basis $\mathcal{B} = \{K(x_j, x) : 1 \leq j \leq n\}$, equations Eq. (2.30) and Eq. (2.31) become:

$$s(x_k) = \sum_{j=1}^n c_j K(x_j, x_k) = f(x_k), \quad \text{for all } 1 \leq k \leq n \quad (2.33)$$

and in matrix notation, with $A_X = (K(x_j, x_k))_{1 \leq j, k \leq n} \in \mathbb{R}^{n \times n}$:

$$A_X \cdot c = f_X \quad (2.34)$$

Also here, we have to make sure that for any X , the symmetric matrix A_X does never become singular (note that a regular matrix A_X implies a unique solution of Eq. (2.34), as a regular matrix has no null-space). To ensure that A_X is a regular matrix, we would just need to require that all its eigenvalues are non-zero. However, we will focus on a certain class of regular matrices. We require them to be symmetric and positive definite (p.d.) for any X , as this imposes nice properties on the solution to the interpolation problem. Symmetric and p.d. matrices have only positive eigenvalues and are thus regular.

If we want to interpolate to function values of $f \notin f_X$, we need analytical expressions for the basis functions in $\mathcal{B} = \{K(x_j, x) : 1 \leq j \leq n\}$. Since the symmetric matrix A_X is derived from this basis, the functions $K(x_j, x)$ are required to be

- (a) symmetric, i.e. $K(x, y) = K(y, x)$ for all $x, y \in \mathbb{R}^d$
- (b) positive definite (p.d.) functions

Definition 1. A symmetric function $K : \mathbb{R}^d \times \mathbb{R}^d \rightarrow \mathbb{R}$ is said to be positive definite on \mathbb{R}^d , if and only if the matrix $A_X = (K(x_j, x_k))_{1 \leq j, k \leq n}$ is positive definite for all possible choices of finite point sets $X \subset \mathbb{R}^d$. The symmetric matrix A is positive definite, if for any vector x of the associated vector space we have (e.g., Nef, 1966, p.191):

$$x^T A x > 0, \quad \text{and } x^T A x = 0 \text{ if and only if } x = 0. \quad (2.35)$$

Hence, if we do a Lagrange interpolation with symmetric and p.d. basis functions $\mathcal{B} = \{K(x_j, x) : 1 \leq j \leq n\}$, we obtain a continuous interpolant

$$s(x) = \sum_{j=1}^n c_j K(x_j, x) \quad (2.36)$$

that matches the function values f_X exactly.

Remark 1. In Moritz (1978), he uses a formalism very similar to Lagrange interpolation to set the grounds for collocation. He uses the term *Least-squares interpolation* for Lagrange interpolation. *Least-squares collocation* is then viewed as a generalization of the interpolation problem. In pure or simple collocation, not only the function values f_X are exactly reproduced, but also linear functionals thereof.

2.2.4 Norm induced by a symmetric, positive definite Kernel

In order to characterize the interpolation properties imposed by the symmetric and p.d. function K , we use the theory of linear normed vector spaces. We first proceed with some definitions:

Definition 2. *A linear vector space contains elements called vectors that support two types of operations: addition of vectors (denoted by \oplus) and multiplication by scalars (denoted by \otimes). The vectors of some space \mathcal{V} have to obey the following axioms (for any element u, v, w and the zero element $0_{\mathcal{V}}$ of the vector space, and scalars α, β belonging to the field over which also the associated vector space is defined):*

- *associative law:* $(u \oplus v) \oplus w = u \oplus (v \oplus w)$
- *commutative law:* $u \oplus v = v \oplus u$
- *inverse law:* $u \oplus (\ominus u) = 0_{\mathcal{V}}$
- *identity laws:*

$$0_{\mathcal{V}} \oplus u = u$$

$$1 \otimes u = u$$

- *distributive laws:*

$$\alpha \otimes (\beta \otimes u) = (\alpha \otimes \beta) \otimes u$$

$$(\alpha \oplus \beta) \otimes u = \alpha \otimes u \oplus \beta \otimes u$$

Note that the vectors do not need to be of finite dimension. Furthermore, the elements of a vector space can even be functions. Functions can be viewed as generalizations of vectors. From here on, a vector space of functions will always be called a function space.

The next two definitions of a normed space and of an inner product space are taken from the introductory chapter of Moritz (1980) and are adapted to the notation used in **Definition 2**.

Definition 3. *On a vector or function space we can define a norm to make it a normed space with the properties*

- *positivity:* $\|u\| \geq 0$
- *homogeneity:* $\|\alpha \otimes u\| = |\alpha| \otimes \|u\|$
- *triangle inequality:* $\|u \oplus v\| \leq \|u\| \oplus \|v\|$
- $\|u\| = 0$ if and only if $u = 0_{\mathcal{V}}$

Definition 4. *An inner product space is a vector or function space with the following properties:*

- $\langle u, v \rangle$ is a real number,
- *symmetry:* $\langle u, v \rangle = \langle v, u \rangle$
- *distributivity:* $\langle u_1 \oplus u_2, v \rangle = \langle u_1, v \rangle \oplus \langle u_2, v \rangle$
- *homogeneity:* $\langle \alpha \otimes u, v \rangle = \alpha \otimes \langle u, v \rangle$
- $\langle u, u \rangle \geq 0$ and zero if and only if $u = 0_{\mathcal{V}}$

From these definitions, it is easy to see that we can always define a norm on an inner product space and thus, create a normed space. The norm would then be defined according to (e.g., Moritz, 1980):

$$\|u\|^2 := \langle u, u \rangle. \quad (2.37)$$

Before we continue to specify suitable inner products for vector and function spaces, the concept of completeness of a linear normed space is introduced. To illustrate the concept, take any number $\alpha \in \mathbb{R}$, say $\alpha = 0.333$. There exists a sequence of numbers in \mathbb{R}

$$\begin{aligned}\alpha_1 &= 0.3 \\ \alpha_2 &= 0.33 \\ \alpha_3 &= 0.333\end{aligned}$$

that comes infinitely close to α . The sequence is called a Cauchy sequence as it satisfies the Cauchy criterion:

$$\begin{aligned}\text{given any } \epsilon > 0, \text{ there is an integer } N \text{ such that} \\ \|f_n - f_m\| < \epsilon \quad \text{for all } n, m > N\end{aligned}\tag{2.38}$$

where the f_n, f_m are elements of the sequence (Moritz (1980), p. 41). If the limit of the Cauchy sequence is an element of the same space as the elements f_n and f_m , then the space is called complete. For example, take the Cauchy sequence

$$\begin{aligned}\alpha_1 &= 1.4 \\ \alpha_2 &= 1.41 \\ \alpha_3 &= 1.414 \\ &\dots\end{aligned}$$

with its limit $\alpha_\infty = \sqrt{2} \in \mathbb{R}$. All α_n and the limit α_∞ are elements of \mathbb{R} . It is thus complete. Since the Cauchy-sequence is also in space \mathbb{Q} , but its limit is not, the space \mathbb{Q} is called incomplete. The elements in Eq. (2.38) do not need to be numbers, but can be vectors or functions. For the function space, we need to define closeness of a Cauchy sequence f_n with respect to a function f :

$$\|f - f_n\| := \max |f - f_n(t)| \quad \text{for any } t \in [a, b].\tag{2.39}$$

The function f takes the place of $\alpha_\infty = \sqrt{2}$ in the above example of \mathbb{R} . If the Cauchy sequence f_n comes infinitely close to f and if f and the entire Cauchy sequence belong to the same function space, the space is said to be complete.

The properties of **Definition 4** allow the definition of an arbitrary number of inner products for a vector space. The inner product however, needs to have the following form:

Definition 5. *If we have a symmetric (hermitian) and positive definite matrix A , we can define an inner product of a vector space by*

$$\langle u, v \rangle_A = u^T A v\tag{2.40}$$

or for the hermitian matrix A :

$$\langle u, v \rangle_A = u^* A v.\tag{2.41}$$

We can check with **Definition 4** that such an inner product obeys all properties needed to create an inner product vector space. Specifically, the last property of **Definition 4** trivially explains why matrix A has to be positive definite, as the property is equivalent to the definition of a p.d. matrix. If A is equal to the identity matrix, the well-known Euclidian norm results.

For a function space, let us derive an equivalent definition. If matrix A were viewed as a linear continuous operator and the operator were termed $K(x, y)$, then one would expect an inner product of a function space to be:

$$\langle u, v \rangle_K \stackrel{?}{=} \int_a^b \int_a^b u(x)K(x, y)v(y) dx dy\tag{2.42}$$

where the operator $K(x, y)$ is defined on a square area $a \leq x \leq b$, $a \leq y \leq b$. Additionally, we require $K(x, y)$ to be a symmetric and p.d. function as specified in **Definition 1**. From here on, we will call $K(x, y)$ a kernel. To check if Eq. (2.42) is a reasonable definition, we need to introduce some more notions about kernels of type $K(x, y)$. The following theorem is formulated for positive definite kernels, but it has originally been written down for both, positive and negative definite kernels $K(x, y)$ (Mercer, 1909).

Theorem 1. (*Mercer's Theorem*) *If K is a continuous symmetric non-negative definite kernel, then there is an orthonormal basis $\{\varphi_i\}$ of square integrable functions on the interval $[a, b]$ consisting of eigenfunctions of the integral equation*

$$\varphi(x) = \lambda \int_a^b K(x, y)\varphi(y) dy \quad (2.43)$$

such that the corresponding sequence of eigenvalues $\{\lambda_i\}$ is non-negative. The eigenfunctions corresponding to non-zero eigenvalues are continuous on $[a, b]$ and K has the representation

$$K(x, y) = \sum_{i=1}^{\infty} \frac{\varphi_i(x)\varphi_i(y)}{\lambda_i} \quad (2.44)$$

where the convergence is absolute and uniform.

There is a mess of notations in the literature, but most authors use the notation in Eq. (2.43) to specify the eigenvalue problem of kernel functions of integral equations. It is noteworthy that the notation is not equal to the same problem in linear algebra:

$$\lambda u = Au \quad (2.45)$$

as has been pointed out by Smirnov (1973). With the help of **Theorem 1**, another important theorem can be formulated (Courant and Hilbert, 1968):

Theorem 2. (*Entwicklungssatz, Hilbert-Schmit theorem*) *Given that a Kernel $K(x, y)$ can be written in the form Eq. (2.44), where the series uniformly converges for both x and y , then each function $u(x)$ of the form*

$$u(x) = \int_a^b K(x, y)v(y) dy \quad (2.46)$$

where $v(y)$ is continuous or piecewise continuous, can be written as the series

$$u(x) = \sum_{i=1}^{\infty} u_i \varphi_i(x), \quad u_i = \langle u, \varphi_i \rangle = \langle v, \varphi_i \rangle \frac{1}{\lambda_i} \quad (2.47)$$

The inner product in (2.47) is defined as

$$\langle u, \varphi_i \rangle = \int_a^b u(x)\varphi_i(x) dx.$$

Remark 2. *In Smirnov (1973) (p. 58f), it is shown that a real and symmetric kernel only contains real eigenvalues and that two eigenfunctions belonging to non-identical eigenvalues are orthogonal to each other:*

$$\int_a^b \varphi_1(x)\varphi_2(x) dx = 0. \quad (2.48)$$

These facts will considerably simplify subsequent derivations.

From Eq. (2.47), we see that $u(x)$ consists of infinitely many base elements. Mercer's theorem tells us that the base elements, i.e. the orthonormal basis, are square integrable functions, which are complete. Eq. (2.42) also suggests that there is an inner product, yet to be specified, for the

functions of type u and, following Eq. (2.37), the function space is also normed. A complete, inner-product space of infinite dimension is called a Hilbert space \mathcal{H} . If we can find an inner-product definition with respect to a symmetric and p.d. kernel function $K(x, y)$ that obeys the property

$$K(x, \cdot) \in \mathcal{H} \quad (2.49)$$

$$u(z) = \langle u(x), K(x, z) \rangle_K \quad \text{for all } u \in \mathcal{H} \quad (2.50)$$

then the functions of type u belong to a Reproducing Kernel Hilbert Space (RKHS) \mathcal{H}_K , since Eq. (2.50) is called the reproducing property, for obvious reasons. The dot in $K(x, \cdot)$ means that the kernel function is an element of \mathcal{H} with respect to one function argument at a time.

We have now acquired all needed definitions and theorems to define a specific function space that we will need to illustrate collocation properties. We see right away from Eq. (2.44) that not only u and v are elements of a Hilbert space \mathcal{H} , but also $K(x, \cdot)$ and all its linear combinations and hence, property Eq. (2.49) is satisfied for our function space. Applying Eq. (2.44) and Eq. (2.47) to Eq. (2.42) yields:

$$\begin{aligned} \langle u, v \rangle_K &= \int_a^b \int_a^b u(x) K(x, y) v(y) \, dx \, dy \\ &= \int_a^b \int_a^b \sum_{i=1}^{\infty} u_i \varphi_i(x) \sum_{j=1}^{\infty} \frac{\varphi_j(x) \varphi_j(y)}{\lambda_j} \sum_{k=1}^{\infty} v_k \varphi_k(y) \, dx \, dy \\ &= \int_a^b \sum_{i=1}^{\infty} u_i \varphi_i(x) \sum_{j=1}^{\infty} \left(\frac{\varphi_j(x)}{\lambda_j} v_j \int_a^b \varphi_j(y) \varphi_j(y) \, dy \right) \, dx \\ &= \int_a^b \sum_{i=1}^{\infty} u_i \varphi_i(x) \sum_{j=1}^{\infty} \left(\frac{\varphi_j(x)}{\lambda_j} v_j \right) \, dx \\ &= \sum_{i=1}^{\infty} \left(\frac{u_i v_i}{\lambda_i} \int_a^b \varphi_i(x) \varphi_i(x) \, dx \right) = \sum_{i=1}^{\infty} \frac{u_i v_i}{\lambda_i} \end{aligned} \quad (2.51)$$

where we used:

$$\int_a^b \varphi_i(x) \varphi_j(x) \, dx = \begin{cases} 1 & \text{if } i = j \text{ (orthonormality)} \\ 0 & \text{otherwise} \end{cases}$$

Does the inner-product according to Eq. (2.51) make our Hilbert space a RKHS? We check this with the reproducing property (2.50) and note:

$$k_i(z) = \int_a^b K(y, z) \varphi_i(y) \, dy = \frac{\varphi_i(z)}{\lambda_i} \quad (2.52)$$

and therefore

$$\langle u, K \rangle_K = \sum_{i=1}^{\infty} \frac{u_i k_i(z)}{\lambda_i} = \sum_{i=1}^{\infty} \frac{1}{\lambda_i^2} u_i \varphi_i(z) = u(z) \sum_{i=1}^{\infty} \frac{1}{\lambda_i^2} \neq u(z) \quad (2.53)$$

does not yield the reproducing property, as we cannot guarantee that $\sum_{i=1}^{\infty} \frac{1}{\lambda_i^2}$ is equal to 1. Only an upper bound for this sum can be given, as shown in Courant and Hilbert (1968) (p. 110):

$$\int \int K(x, y)^2 \, dx \, dy \geq \sum_{i=1}^{\infty} \frac{1}{\lambda_i^2} \quad (2.54)$$

However, a small change in Eq. (2.51) yields the desired property and we can make our function space a RKHS:

Definition 6. The inner product of a reproducing kernel Hilbert space \mathcal{H}_K with a symmetric and p.d. kernel $K(x, y)$ is defined by:

$$\langle u, v \rangle_K = \sum_{i=1}^{\infty} \lambda_i u_i v_i. \quad (2.55)$$

It is easily verified that this yields the reproducing property:

$$\langle u, K \rangle_K = \sum_{i=1}^{\infty} \lambda_i u_i k_i(z) = \sum_{i=1}^{\infty} \lambda_i \frac{1}{\lambda_i} u_i \varphi_i(z) = u(z) \quad (2.56)$$

From the symmetry of the Kernel, we get the property:

$$\langle K(x, y), K(y, z) \rangle_K = \sum_{i=1}^{\infty} \lambda_i k_i(x) k_i(z) = \sum_{i=1}^{\infty} \lambda_i \frac{\varphi_i(x) \varphi_i(z)}{\lambda_i^2} = K(x, z) \quad (2.57)$$

We now have constructed a function space, whose properties we are going to exploit. Before we continue, we look at a special case that is encountered in Moritz (1980) (e.g., p. 197):

$$K(x, y) = \sum_{i=1}^{\infty} \varphi_i(x) \varphi_i(y) \quad \text{if } \lambda_i = 1 \text{ for all } i = 1, \dots, \infty \quad (2.58)$$

where φ_i with $i = 1, \dots, \infty$ is a complete orthonormal system. Such a representation of the Kernel function would also imply that the eigenvalue problem (2.43) becomes

$$\varphi(x) = \int_a^b K(x, y) \varphi(y) dy \quad (2.59)$$

which is not a valid integral equation, as is stated in Smirnov (1973) (p. 6). Further support for $K(x, y)$ in Eq. (2.58) not being a valid Kernel for a RKHS comes from a proof in Courant and Hilbert (1968) (p. 97, or more refined on p. 110f), where they show that

Theorem 3. Each eigenvalue has finite multiplicity.

This statement contradicts what Eq. (2.58) tells us: the eigenvalue $\lambda_i = 1$ has infinite multiplicity. We can still define an inner product in accordance with **Definition 6**:

$$\Rightarrow \langle u, v \rangle = \sum_{i=1}^{\infty} 1 \cdot u_i v_i \equiv \int_a^b u(x) v(x) dx \quad (2.60)$$

which defines a Hilbert space on the square integrable functions L^2 . The inner product (2.60) builds no RKHS since (2.58) is not a valid definition of a symmetric and p.d. Kernel.

Remark 3. The property (2.60) is the so-called duality relation between the vector space l^2 (represented by u_i and v_i) and the function space L^2 (represented by $u(x)$ and $v(x)$). The duality-relation demonstrates the isomorphism and isometry of the two spaces. We have already used the duality relation in our derivations without having it explicitly mentioned. An example is given in Eqs. (2.52) and (2.53).

From the above considerations, we see that a symmetric and p.d. Kernel function $K(x, y)$, together with a suitable inner-product definition, fully defines a RKHS.

Remark 4. Putting together Eq. (2.34) and Eq. (2.33), the Lagrange interpolation problem can be formulated following Moritz (1978):

$$f(x) = (C_{x,1} \quad C_{x,2} \quad \cdots \quad C_{x,n}) \begin{pmatrix} C_{1,1} & C_{1,2} & \cdots & C_{1,n} \\ C_{2,1} & C_{2,2} & \cdots & C_{2,n} \\ \vdots & \vdots & & \vdots \\ C_{n,1} & C_{n,2} & \cdots & C_{n,n} \end{pmatrix}^{-1} \begin{pmatrix} f_1 \\ f_2 \\ \vdots \\ f_n \end{pmatrix}$$

with $C_{x,k} = K(x, x_k)$ and $C_{j,k} = K(x_j, x_k)$, $1 \leq j, k \leq n$

For $n \rightarrow \infty$, one could expect this matrix equation to result in an integral equation of the form

$$f(x) = \int K^*(x, y) f(y) dy$$

which was shown in the previous paragraph to contradict **Theorem 3**. We conclude that in the limit case $n \rightarrow \infty$, the kernel function K does not serve as a simple weighting in the integral equation. It is the operation of the inner product defined in Eq. (2.55) that does the weighting, where K is just the characteristic and defining function element of this inner product. With the correct inner product, K has been shown to have the reproducing property and thus, recovers the function $f(x)$ in the limit case of $n \rightarrow \infty$.

2.2.5 Lagrange interpolation solution as subspace of the Reproducing Kernel Hilbert Space

The constructed RKHS with the inner product given by **Definition 6** allows a nice derivation of the orthogonal projection properties of the Lagrange interpolation solution presented in Sect. 2.2.3. Let us assume that the interpolant $s(x)$ and the function $f(x)$ belong to our RKHS. $f(x)$ is the true function that we would like to recover as accurately as possible. The orthogonality between $s(x)$ and $(f(x) - s(x))$ in the metric space of the reproducing Kernel is demonstrated in the following. Thus, we need to show

$$\langle s, f - s \rangle_K = \langle s, f \rangle_K - \langle s, s \rangle_K \stackrel{?}{=} 0 \quad (2.61)$$

where distributivity of the inner product from **Definition 4** is used. Applying the inner product of a RKHS yields

$$\langle s, f - s \rangle_K = \sum_{i=1}^{\infty} \lambda_i (f_i s_i - s_i s_i) \quad \text{with } \lambda_i \neq 0 \quad (2.62)$$

Functions f and $s \in \mathcal{H}_K$ are representable as an infinite series of orthonormal base functions (see Eq. (2.47)), where the base functions are the eigenfunctions of K . We further know that the unknown function f and the interpolant s have to coincide at the given data points given in (2.27). Thus, we write Eq. (2.28):

$$\sum_{i=1}^{\infty} s_i \varphi_i(x_k) = \sum_{i=1}^{\infty} f_i \varphi_i(x_k) \quad \text{for } k = 1, \dots, n$$

and obtain

$$\sum_{i=1}^{\infty} (f_i - s_i) \varphi_i(x_k) = 0 \quad (2.63)$$

An expression for the coefficients s_i results from

$$s_i = \int_a^b s(x) \varphi_i(x) dx \quad \text{with } s(x) = \sum_{i=1}^{\infty} s_i \varphi_i(x). \quad (2.64)$$

Combining Eqs. (2.36) and (2.44) with Eq. (2.64):

$$\begin{aligned} s_i &= \int_a^b \sum_{j=1}^n c_j \sum_{k=1}^{\infty} \frac{\varphi_k(x) \varphi_k(x_j)}{\lambda_k} \varphi_i(x) dx = \int_a^b \sum_{j=1}^n \sum_{k=1}^{\infty} \left(c_j \frac{\varphi_k(x) \varphi_k(x_j)}{\lambda_k} \right) \varphi_i(x) dx \\ \Rightarrow s_i &= \sum_{j=1}^n c_j \frac{\varphi_i(x_j)}{\lambda_i}. \end{aligned} \quad (2.65)$$

Inserting s_i into Eq. (2.62) and rearranging:

$$\begin{aligned} \langle s, f - s \rangle_K &= \sum_{i=1}^{\infty} \lambda_i s_i (f_i - s_i) = \sum_{i=1}^{\infty} \lambda_i \sum_{j=1}^n c_j \frac{\varphi_i(x_j)}{\lambda_i} (f_i - s_i) \\ &= \sum_{i=1}^{\infty} \sum_{j=1}^n c_j \varphi_i(x_j) (f_i - s_i) = \sum_{j=1}^n c_j \underbrace{\sum_{i=1}^{\infty} (f_i - s_i) \varphi_i(x_j)}_{=0 \text{ from Eq. (2.63)}} = 0 \quad \blacksquare \end{aligned} \quad (2.66)$$

Remark 5. Note that the solution s is not orthogonal to $(f(x) - s(x))$ in the function space $L2$ with the inner product defined by Eq. (2.60), but at an “acute” angle. They are only orthogonal in the metric space of K . Hence, the usual notion of orthogonality as known from Euclidian geometry does not apply here.

The result from Eq. (2.66) can be stated equivalently as the so-called Pythagoras theorem of the RKHS with Kernel K (Iske, 2011):

$$\|f\|_K^2 = \|s\|_K^2 + \|f - s\|_K^2. \quad (2.67)$$

In a next step, we show that s is the orthogonal projection of f onto the subspace spanned by the basis $\mathcal{B} = \{K(x_j, x) : 1 \leq j \leq n\}$. We recall:

$$s(x_j) = f(x_j) \quad \text{for all } j = 1, \dots, n$$

and expand the equation by the reproducing property of K :

$$\langle K(x, x_j), s(x) \rangle_K = \langle K(x, x_j), f(x) \rangle_K \quad (2.68)$$

$$\langle K(x, x_j), s(x) \rangle_K - \langle K(x, x_j), f(x) \rangle_K = 0 \quad \Rightarrow \quad \langle K(x, x_j), s(x) - f(x) \rangle_K = 0 \quad \blacksquare \quad (2.69)$$

To show the next property, we need to define the notion of best approximation in a RKHS. Best approximation is viewed as (Iske, 2011):

Definition 7. A function s^* that exists on the subspace of the RKHS spanned by $\mathcal{B} = \{K(x_j, x) : 1 \leq j \leq n\}$ is said to be the best approximation to f , if

$$\|s^* - f\|_K < \|s - f\|_K \quad \text{for all } s \in \text{span}\{K(x_j, x) : 1 \leq j \leq n\} \setminus \{s^*\} \quad (2.70)$$

We now state: The solution to the problem statement (2.33) is the best approximation of the function f in the metrics of K . To prove the assertion, we use Eq. (2.69) and take into account that also all linear combinations of K are orthogonal to the difference between f and the solution to Eq. (2.33). The function s is one such possible linear combination, which we can insert for K in Eq. (2.69). Additionally, we denote the solution to Eq. (2.33) by s^* and obtain:

$$\langle s, f - s^* \rangle_K = 0. \quad (2.71)$$

Additionally, we have s^* satisfying Eq. (2.66), and hence, subtracting both sides of Eq. (2.66) from Eq. (2.71) results in:

$$\langle s - s^*, f - s^* \rangle_K = 0 \quad (2.72)$$

From here, we have to show that s^* is indeed satisfying Eq. (2.70). We exactly follow the proof of Iske (2011):

$$\begin{aligned} \|s - f\|_K^2 &= \|s - s^* + s^* - f\|_K^2 = \|s - s^*\|_K^2 + 2 \underbrace{\langle s - s^*, s^* - f \rangle_K}_{=0 \text{ from Eq. (2.72)}} + \|s^* - f\|_K^2 \\ &\Rightarrow \|s^* - f\|_K < \|s - f\|_K \quad \blacksquare \end{aligned} \quad (2.73)$$

2.2.6 Minimum norm property of the pure collocation solution

The minimum norm property is first obtained for the Lagrange interpolation case before it is derived for the more general case of pure or simple collocation. To prove minimum norm of the solution $s(x)$, we show that all functions $g \in \mathcal{H}_K$ that coincide with the unknown function f at the points $x_j, j = 1, \dots, n$ lie in a hyper-plane orthogonal to $s(x)$. As $g \in \mathcal{H}_K$, it can be represented as an infinite series of eigenfunctions of the kernel and we can thus write in analogy to Eq. (2.63):

$$\begin{aligned} f(x_k) &= g(x_k) \quad \text{for all } k = 1, \dots, n \\ \Rightarrow \sum_{i=1}^{\infty} (f_i - g_i) \varphi_i(x_k) &= 0 \end{aligned} \quad (2.74)$$

We get with the help of Eq. (2.65):

$$\begin{aligned} \langle s, f - g \rangle_K &= \sum_{i=1}^{\infty} \lambda_i s_i (f_i - g_i) \\ &= \sum_{j=1}^n c_j \underbrace{\sum_{i=1}^{\infty} (f_i - g_i) \varphi_i(x_j)}_{=0 \text{ from Eq. (2.74)}} = 0 \quad \blacksquare \end{aligned} \quad (2.75)$$

From the fact that all other functions $g(x)$ that obey Eq. (2.74) are in an orthogonal hyperplane to the interpolant $s(x)$, we conclude that $s(x)$ must be the solution with the smallest norm in the metrics of the RKHS. Note that upon inserting s as one possible function g in Eq. (2.75), we get again Eq. (2.66) and from there, the Pythagoras theorem (2.67).

The generalization to collocation follows from the fact that observations can be linear functionals of the unknown function. A functional associates a function to a real or complex number (we will not deal with the complex case in the sequel). In our case, it is a mapping $L^x(\cdot)_{x=x_j} : \mathcal{H}_K \rightarrow \mathbb{R}$, where the superscript x in L^x denotes the action of L onto the variable x of the function enclosed in brackets (\cdot) . Linearity of the functional means:

$$\begin{aligned} L^x(f + g)_{x=x_j} &= L^x(f)_{x=x_j} + L^x(g)_{x=x_j} \quad \text{and} \quad L^x(\alpha f)_{x=x_j} = \alpha L^x(f)_{x=x_j} \\ \text{for all } f, g \in \mathcal{H}_K, \alpha \in \mathbb{R}, x, x_j \in \mathbb{R}^d. \end{aligned}$$

The observations are termed l_k henceforth. Instead of Eq. (2.28) we write:

$$L_k^x(f(x))_{x=x_k} = l_k = L_k^x(s(x))_{x=x_k} \quad (2.76)$$

With L_k^x , we denote a linear functional of type k applied to the domain x of the mapping $L_k^x(\cdot)_{x=x_k} : \mathcal{H}_K \rightarrow \mathbb{R}$. It stresses the fact that some functional L_1 is not necessarily equal to some other functional L_2 . For Eq. (2.33), we have

$$s(x) = \sum_{j=1}^n c_j L_j^y(K(y, x))_{y=x_j}. \quad (2.77)$$

The analogous matrix multiplication to Eq. (2.34) becomes

$$l_k = L_k^x(s(x))_{x=x_k} = \sum_{j=1}^n c_j L_k^x(L_j^y(K(y, x))_{y=x_j})_{x=x_k} \rightarrow A_X \cdot c = l_X \quad (2.78)$$

with $A_X = (L_k^x(L_j^y((K(y, x))_{y=x_j})_{x=x_k}))_{1 \leq j, k \leq n}$. In order to make A_X invertible, we again require that it is symmetric and p.d.. This is for now a sufficient and not necessary requirement. We will see in Sect. 2.2.7, why p.d. is the best choice for most applications. For A_X to be symmetric and p.d., we have to make sure that the operations L_k^x and L_j^y carried out by the linear functionals

on the variables x and y result in p.d. kernel functions. Use of linear functionals in Lagrange interpolation, which is termed simple collocation in Moritz (1978), does not alter the fact of being minimum norm, as is demonstrated by:

$$\text{for Eq. (2.65): } s_i = \sum_{j=1}^n c_j \frac{L_j^x(\varphi_i(x))_{x=x_j}}{\lambda_i} \quad (2.79)$$

$$\text{for Eq. (2.74): } \sum_{i=1}^{\infty} (f_i - g_i) L_k^x(\varphi_i(x))_{x=x_k} = 0 \quad (2.80)$$

$$\begin{aligned} \text{for Eq. (2.75): } \langle s, f - g \rangle_K &= \sum_{i=1}^{\infty} \lambda_i s_i (f_i - g_i) \\ &= \sum_{j=1}^n c_j \underbrace{\sum_{i=1}^{\infty} (f_i - g_i) L_j^x(\varphi_i(x))_{x=x_j}}_{=0 \text{ from Eq. (2.80)}} = 0 \quad \blacksquare \end{aligned} \quad (2.81)$$

2.2.7 Kernel interpreted as covariance function

Let us assume we have a symmetric variance-covariance matrix C_{ss} of some parameters. We would like to know the variance of a linear combination of these parameters, which we calculate according to the law of uncertainty propagation:

$$\text{variance of linear combination} = x^T C_{ss} x \quad (2.82)$$

with x containing the coefficients of the linear combination. As the variance of a random variable needs to be positive by definition, it is necessary to require that C_{ss} is a p.d. matrix according to **Definition 1**. We saw in Sect. 2.2.3 that symmetry and positive definiteness is sufficient to guarantee a unique solution to the problem of Lagrange interpolation and we saw that this implies a number of interesting properties of the interpolation scheme, as e.g., minimum norm in the respective RKHS. If we interpret the kernel function as a covariance function, it becomes a necessary condition that K is a p.d. function due to Eq. (2.82). But how to test if a symmetric kernel is p.d.? For this purpose, we introduce the notation:

$$\begin{aligned} K(x, y) &:= \Phi(r) \\ r &= \|x - y\| \quad \text{for } x, y \in \mathbb{R}^d. \end{aligned} \quad (2.83)$$

Hence, we require the function $\Phi : \mathbb{R}^d \rightarrow \mathbb{R}$ to be even and radially symmetric. Furthermore, the function is normalized according to

$$\Phi(0) = 1 \quad (2.84)$$

For such a function, a modified version of Bochner's theorem, as stated in Iske (2011), can be applied:

Theorem 4. $\Phi : \mathbb{R}^d \rightarrow \mathbb{R}$ is even and continuous. Assume that Φ has a continuous Fourier transform $\hat{\Phi}$ satisfying the Fourier inversion formula

$$\Phi(r) = \frac{1}{\sqrt{2\pi}} \int_{-\infty}^{\infty} \hat{\Phi}(\omega) \exp(-i\omega r) d\omega \quad (2.85)$$

i.e., Φ and $\hat{\Phi}$ are a Fourier pair. If $\hat{\Phi}$ is non-negative on \mathbb{R}^d , then $K(x, y) = \Phi(r)$ is positive definite.

Let us illustrate the theorem with a simplified version of the covariance function (2.19):

$$\Phi(\|z_1 - z_2\|) = \frac{1}{1 + \left(\frac{\|z_1 - z_2\|}{l_z}\right)^2} \quad \text{with } l_z > 0 \text{ and } z_1, z_2 \in \mathbb{R}. \quad (2.86)$$

Normalization and its symmetry with respect to z_1 and z_2 are fulfilled. It is also even and continuous on \mathbb{R} . The corresponding Fourier spectrum is

$$\hat{\Phi}(f) = l_z \cdot \pi \cdot \exp(-2\pi l_z |f|) \quad (2.87)$$

which is non-negative on \mathbb{R} and thus, $K(x, y) = \Phi(\|z_1 - z_2\|)$ is p.d. by Bochner's theorem. As seen in Eq. (2.78), also functionals of the Kernel function can be used for interpolation. If they are to be interpreted as covariance functions of some data, their positive definiteness has to be ascertained. In Eq. (2.25) and Eq. (2.26), there are two examples of covariance functions derived from linear functionals. The simplified covariance functions are:

$$-\frac{\partial \Phi(\|z_1 - z_2\|)}{\partial z_1} = \frac{2l_z^2 \cdot (z_1 - z_2)}{(l_z^2 + r^2)^2} \quad (2.88)$$

$$-\frac{\partial}{\partial z_2} \left(-\frac{\partial \Phi(\|z_1 - z_2\|)}{\partial z_1} \right) = \frac{2l_z^2 (l_z^2 - 3 \cdot r^2)}{(l_z^2 + r^2)^3} \quad (2.89)$$

$$\text{with: } r = \|z_1 - z_2\|$$

From the covariance functions, the three corresponding correlation functions $Cor(z_1, z_2)_{(2.86)}$, $Cor(z_1, z_2)_{(2.88)}$ and $Cor(z_1, z_2)_{(2.89)}$ can be derived:

$$Cor(z_1, z_2)_{(2.86)} = \frac{l_z^2}{l_z^2 + r^2} \quad (2.90)$$

$$Cor(z_1, z_2)_{(2.88)} = \frac{\sqrt{2}(z_1 - z_2)}{\sqrt{l_z^2 - 3r^2}} \quad (2.91)$$

$$Cor(z_1, z_2)_{(2.89)} = \frac{l_z^4 (l_z^2 - 3r^2)}{(l_z^2 + r^2)^3}. \quad (2.92)$$

For illustration, these functions are plotted in Fig. 2.2. We note the half width of Eq. (2.92) to be much smaller than that of Eq. (2.90). Another interesting feature is the zero correlation of Eq. (2.91) at zero distance. The zero correlation at zero distance is probably not reasonable. For example, we would expect wet refractivity and ZWD measured at the same location on the ground to be both high in summer and low in winter. They are thus correlated. This is not represented in the correlation function between wet refractivity and ZWD and hints at an inappropriate description of the signal part. Further investigations are needed to find more appropriate covariance functions for ZWD and wet refractivity.

Note that normalization is not a crucial aspect of the present problem. Since Bochner's theorem as stated here is only applicable to even functions, which is not true for the function in (2.88), we first check Eq. (2.89) for positive definiteness with its fourier transform:

$$\hat{\Phi}_{(2.89)} = l_z \cdot 4\pi^3 f^2 \cdot \exp(-2\pi l_z |f|) > 0. \quad (2.93)$$

Hence, also the double-differential of the kernel results in a p.d. kernel function. Matrix A_X from Eq. (2.78) has the following structure, where the two sub-matrices A_{11} and A_{22} have been checked to be p.d.

$$A_X = \left(\begin{array}{c|c} A_{11} & A_{12} \\ \hline A_{21} & A_{22} \end{array} \right) = \left(\begin{array}{c|c} \Phi(\|z_1 - z_2\|) & -\frac{\partial \Phi(\|z_1 - z_2\|)}{\partial z_1} \\ \hline -\frac{\partial \Phi(\|z_1 - z_2\|)}{\partial z_1} & -\frac{\partial}{\partial z_2} \left(-\frac{\partial \Phi(\|z_1 - z_2\|)}{\partial z_1} \right) \end{array} \right). \quad (2.94)$$

The symmetry of A_X is granted, however, we do not know yet if the two submatrices A_{12} and A_{21} retain the positive definiteness of A_X . Even though intuition tells us that p.d. must be retained, a proof has not been achieved. An idea of an algorithm that does not require to calculate all eigenvalues of matrix A_X is given in the following. The full eigenvalue problem of A_X is:

$$\left[\begin{pmatrix} A_{11} & A_{12} \\ A_{21} & A_{22} \end{pmatrix} - \lambda \cdot I \right] \begin{pmatrix} x_1 \\ x_2 \end{pmatrix} = \begin{pmatrix} A_{11}x_1 + A_{12}x_2 \\ A_{21}x_1 + A_{22}x_2 \end{pmatrix} - \lambda \begin{pmatrix} x_1 \\ x_2 \end{pmatrix} = 0.$$

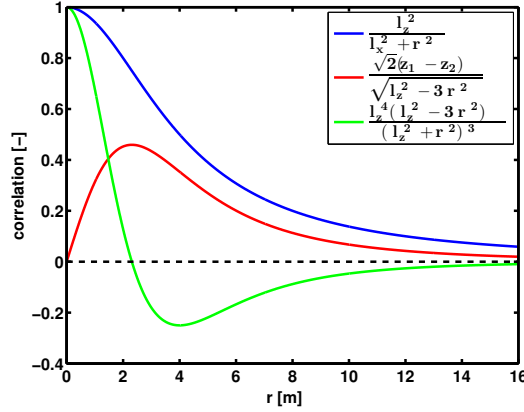


Figure 2.2: The correlation functions in Eq. (2.90), Eq. (2.91) and Eq. (2.92) are plotted with respect to distance $r = \|z_1 - z_2\|$ between two sites. They can be viewed as examples of correlations between two ZWDs (blue), a wet refractivity and a ZWD (red) and between two wet refractivities (green), respectively. The formulas are shown for $l_z = 4$ m.

where the symmetry of A_X is used. Expanding into two equations with two new scalars λ_{x_1} and λ_{x_2} , which are the eigenvalues of $A_{11}x_1 = \lambda_{x_1}x_1$ and $A_{22}x_2 = \lambda_{x_2}x_2$, we get:

$$\begin{aligned} A_{11}x_1 - \lambda_{x_1}x_1 + \lambda_{x_1}x_1 - \lambda_{x_1} + A_{12}x_2 &= 0 \\ A_{22}x_2 - \lambda_{x_2}x_2 + \lambda_{x_2}x_2 - \lambda_{x_2} + A_{12}^T x_1 &= 0. \end{aligned}$$

Hence, $A_{11}x_1 - \lambda_{x_1}x_1 = 0$ and $A_{22}x_2 - \lambda_{x_2}x_2 = 0$ yields:

$$\begin{aligned} A_{12}x_2 &= (\lambda - \lambda_{x_1})x_1 \\ A_{12}^T x_1 &= (\lambda - \lambda_{x_2})x_2 \quad \rightarrow \quad x_2 = \frac{A_{12}^T x_1}{(\lambda - \lambda_{x_2})} \\ \Rightarrow \quad A_{12}A_{12}^T x_1 &= (\lambda - \lambda_{x_1})(\lambda - \lambda_{x_2})x_1 \\ A_{12}A_{12}^T x_1 - \zeta x_1 &= 0 \quad \text{with } \zeta = (\lambda - \lambda_{x_1})(\lambda - \lambda_{x_2}) \end{aligned} \quad (2.95)$$

which is a new eigenvalue problem for the matrix $A_{12}A_{12}^T$. Instead of determining all eigenvalues of A_X and check, if they are positive, we can first determine the eigenvalues ζ of $A_{12}A_{12}^T$. We know that

$$\lambda_{x_1} > 0, \lambda_{x_2} > 0 \quad (2.96)$$

since the submatrices A_{11} and A_{22} are p.d. and thus, their eigenvalues are positive. From Eq. (2.95) and Eq. (2.96), we see that $\zeta < 0$ follows from a positive λ . If eigenvalues $\zeta > 0$ exist, all eigenvalues of A_{11} and A_{22} have to be determined. The possible $\{\zeta, \lambda_{x_1}, \lambda_{x_2}\}$ sets need then to be checked according to:

$$\lambda = \frac{1}{2} \left(\lambda_{x_1} + \lambda_{x_2} \pm \sqrt{(\lambda_{x_1} - \lambda_{x_2})^2 + 4\zeta} \right) \quad (2.97)$$

If every such set yields $\lambda > 0$, then the matrix A_X can be considered to be a valid covariance matrix.

Another question remains to be answered: Why would we like to interpret the kernel function as a covariance function? The answer lies in the following equation for the error variance-covariance matrix E_{ss} of the interpolated data s from known data l . It has been derived in Moritz (1980) (p. 78 and p. 94):

$$E_{ss} = C_{ss} - C_{sl}C_{ll}^{-1}C_{ls} + \left(\bar{C}_{sl}\bar{C}_{ll}^{-1} - C_{sl}C_{ll}^{-1} \right) C_{ll} \left(\bar{C}_{sl}\bar{C}_{ll}^{-1} - C_{sl}C_{ll}^{-1} \right)^T \quad (2.98)$$

with the following matrices:

C_{ss} : “true” covariance between interpolated data points derived from kernel function K

C_{ll} : “true” covariance between known data points from K

\bar{C}_{ss} : covariance of interpolated data points derived from some kernel function \bar{K}

\bar{C}_{ll} : covariance of known data points from some \bar{K}

C_{sl}, \bar{C}_{sl} : covariance between interpolated and known data points from K and \bar{K} , respectively.

The covariance matrices are composed much the same way as matrix A in Eq. (2.34) or in Eq. (2.78). In order to achieve minimum error variance in Eq. (2.98), we need to require that the two functions K and \bar{K} are the same, such that the third term of the equation becomes zero. Thus, with the Kernel interpreted as a covariance function, we arrive at another optimality property of collocation: The correct covariance function allows data interpolation in a statistically optimal way.

The error covariance for noisy data is shown for completeness:

$$E_{ss} = C_{ss} - C_{sl}D^{-1}C_{ls} + \left(\bar{C}_{sl}\bar{D}^{-1} - C_{sl}D^{-1}\right)D\left(\bar{C}_{sl}\bar{D}^{-1} - C_{sl}D^{-1}\right)^T \quad (2.99)$$

$$D = C_{ll} + C_{nn}, \quad \bar{D} = \bar{C}_{ll} + \bar{C}_{nn}$$

C_{nn}, \bar{C}_{nn} : “true” and some arbitrary noise covariance

It can be obtained in close analogy to the derivation of Eq. (2.98).

2.2.8 Synthetic experiment to illustrate minimum norm property of Lagrange interpolation

What are the consequences of Lagrange interpolation being a minimum norm solution? With the following little experiment, the consequences are illustrated. The one-dimensional covariance function

$$C(z_1, z_2) = \frac{\sigma_{signal}^2}{1 + \left(\frac{z_1 - z_2}{l_z}\right)^2} \quad (2.100)$$

with standard deviation $\sigma_{signal} = 2 \text{ m}$ and correlation length $l_z = 4 \text{ m}$, is used to create the signal part s of the synthetic data. A section of the synthetic data series that has a spatial resolution of 0.5 m is shown in dark gray in Fig. 2.3a and serves as reference. The corresponding discrete fourier transform is depicted to the right. Downsampled to 4 m yields the asterisk in the left plot. The downsampled data is then introduced into a Lagrange interpolation using the correct correlation length of $l_z = 4 \text{ m}$. The corresponding signal that is interpolated to a spatial resolution of 0.5 m and its fourier spectrum are shown in light gray in Figs. 2.3a and b, respectively. We observe from the fourier spectra that low frequencies are also well reproduced in the collocated signal. On the other hand, downsampling reduces most of the power in the frequencies close to and above the Nyquist frequency. Those frequencies are not well represented in the coarsely sampled data and as collocation seeks minimum norm, it only fully includes frequencies that are “demanded” by the data. That is to say, the interpolated data has to pass through the data points given by the asterisk (despite all the wiggles, the interpolated lines always pass through the downsampled data points, as is required by Eq. (2.33)). As a side note: The Nyquist frequency does not impose a clear cutoff, but a gradual decrease in reconstructed signal strength.

In Sect. 2.2.5, it was shown that the minimum norm property only applies to the metrics induced by the respective Kernel function. This is illustrated in Fig. 2.4, where the experiment from Fig. 2.3 is repeated, but with correlation lengths for the collocation that are different from the one used to generate the synthetic data. Thus, different minimum norm metrics apply to each row of Fig. 2.4. In all experiments, the value for σ_{signal} has been kept constant and at the true value of the synthetic data. We also note here that for correlation lengths $l_{z,interpolation} \geq l_{z,data}$, amplitudes of frequencies clearly lower than $f_{Nyquist}$ are well reproduced, since the data has to pass

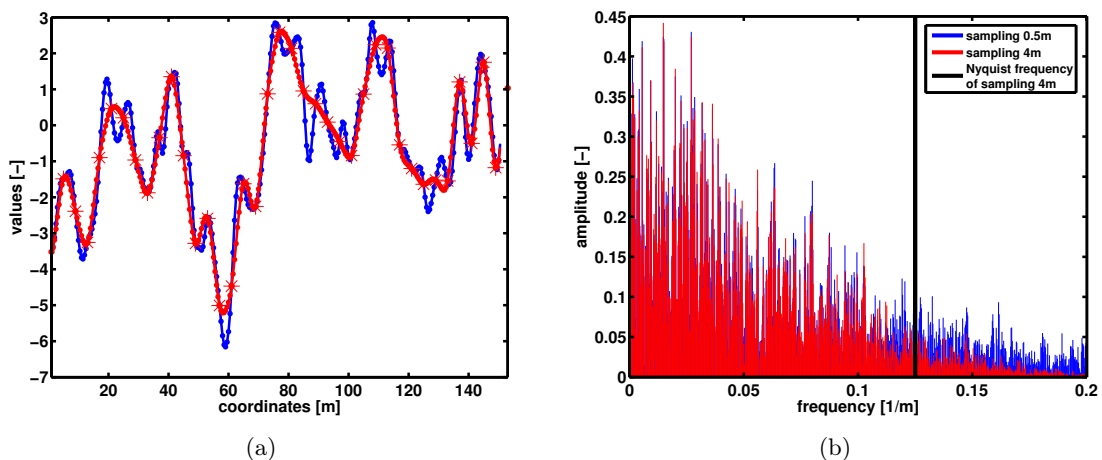


Figure 2.3: (a) The blue line shows a part of the original data at 0.5 m sampling. The entire data set includes 8000 data points. It has been downsampled to 4 m sampling, shown with asterisk. The downsampled data has been introduced into a Lagrange interpolation to arrive at the 0.5 m sampling of the original data and is shown in red. (b) Fourier spectra of the blue and red line of (a). The vertical black line marks the Nyquist frequency of the downsampled data.

through the asterisk. For frequencies close and above f_{Nyquist} , the drop in reconstructed amplitude is different for the different metrics induced by $l_{z,\text{interpolation}}$. It means that the result is not only affected by the data and the fact that all lines have to go through the asterisk, but also obeys the particular metrics. If $l_{z,\text{interpolation}} < l_{z,\text{data}}$, the amplitude drop above f_{Nyquist} becomes even less pronounced than in the case of $l_{z,\text{interpolation}} = l_{z,\text{data}}$, creating spurious results with high-frequency wiggles in the interpolated signal. The wiggles in Figs. 2.4d and notably in 2.4b are accompanied by a loss in low frequency amplitudes with respect to the original data. In Fig. 2.4b, the prominent feature is the hump at frequencies close to 0.25 m^{-1} , which is the sampling frequency of these data. A look at the reconstructed signal explains the feature as a result of the need to pass through the measured data points while obeying the metrics of the correlation length. In addition to poorly reconstructed amplitudes above f_{Nyquist} for short correlation lengths, it is also evident that corresponding phase values become poorly determined. From the illustrative experiment, we conclude that in case of unknown correlation length, the impact on the reconstructed signal is less detrimental, if the choice rather tends to the upper end of still sensible correlation lengths offered by the downsampled data set.

The same conclusion is also reached on a more statistical basis in Figure 2.5. The error covariance matrix E_{ss} has been calculated according to Eq. (2.98), with various correlation lengths $l_{z,\text{interpolation}}$ different from the “true” one ($l_{z,\text{data}} = 4 \text{ m}$) as input to some Kernel function \bar{K} . The average error caused by the interpolation with \bar{K} instead of K has been determined taking the trace of the error covariance matrix and normalized to the trace value at $l_{z,\text{interpolation}} = 1 \text{ m}$. Figure 2.5 demonstrates that the minimum loss of accuracy is achieved, if $l_{z,\text{interpolation}} = l_{z,\text{data}}$.

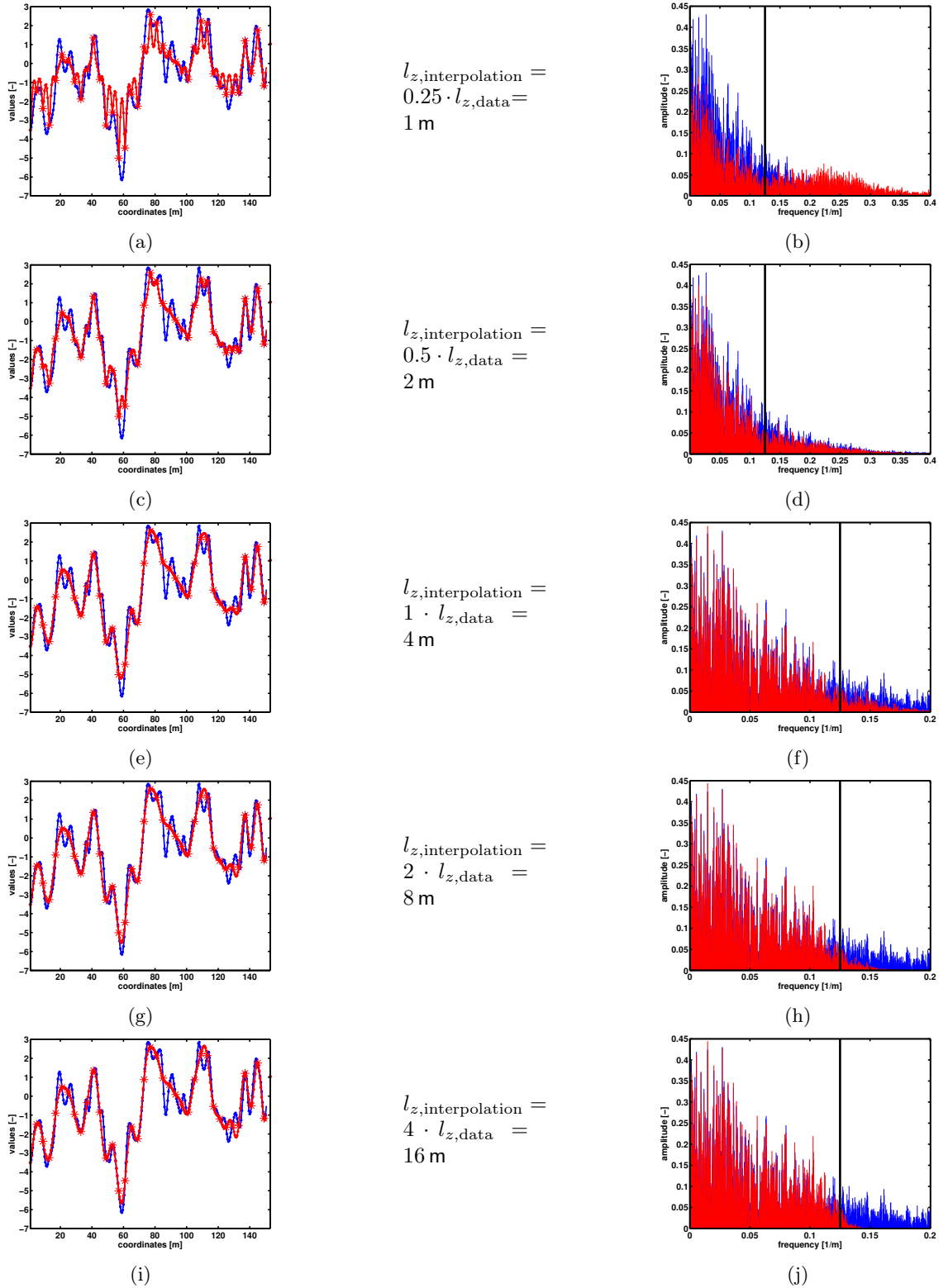


Figure 2.4: Left column: The blue line denotes the true reference data at $l_{z,\text{data}} = 4 \text{ m}$ and the asterisk are the downsampled data. Collocation of the asterisk data is shown as red line. Center column: Configurations of correlation lengths for each collocation experiment. Right column: Discrete fourier spectra of left column. Note that (b) and (d) have another x-axis scaling than the other fourier spectra. The vertical black line marks f_{Nyquist} of the 4 m sampling.

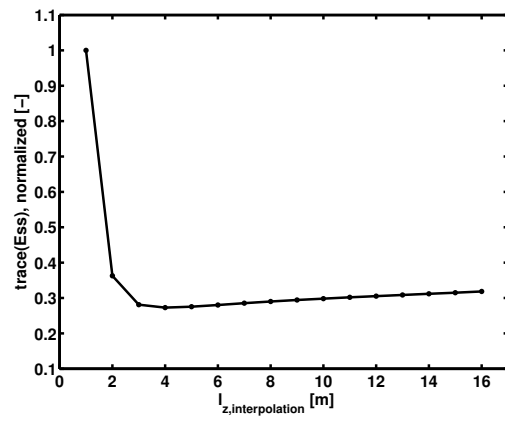


Figure 2.5: Trace of the error covariance matrix E_{ss} , normalized to its value at $l_{z,\text{interpolation}} = 1$ m for various correlation lengths unequal to the “true” one at $l_{z,\text{data}} = 4$ m.

2.2.9 Parameter estimation from empirical autocorrelations

The next synthetic data experiment moves one step closer to the collocation problem of Eq. (2.15). The synthetic data that is analysed includes a signal part s and a noise part n , but the deterministic function f is omitted. We look at the following problem: We would like to collocate some data. Frequently, we do not know the correlation length l_z , the standard deviation of the signal σ_{signal} and the standard deviation of the noise σ_{noise} of the data set. Consequently, they need to be determined from the data. We assume that the data follows a known covariance function and hence, we can determine l_z , σ_{signal} and σ_{noise} by fitting the known covariance function to the data's empirical autocovariance function. As we have seen in Sect. 2.2.8, a correlation length larger than the true one is preferable to an underestimation of this length. In the following experiment, we answer the question, if undersampling of the data causes per se an estimated correlation length l_z that is larger than the true value:

$$l_{z,\text{estimated}} \stackrel{?}{\geq} l_{z,\text{data}}.$$

Hence, the following experiment investigates the effect of undersampling on the retrieval of collocation parameters from the empirical autocovariance of a synthetic data set.

The signal s is produced with the simple covariance function in Eq. (2.100) and the noise n follows a Gaussian distribution. The synthetic data is created with the following parameters:

$$l_{z,\text{data}} = 4 \text{ m}, \quad \sigma_{\text{signal}} = 2, \quad \sigma_{\text{noise}} = 1. \quad (2.101)$$

Since the data fit will be carried out on empirical autocorrelation functions instead of autocovariance functions, we further introduce the parameter a . It enables us to transform the autocorrelation value at station distance $r = 0$, sometimes called the nugget variance, into values for σ_{signal} and σ_{noise} . It is defined as

$$a = \frac{\sigma_{\text{signal}}^2}{\sigma_{\text{signal}}^2 + \sigma_{\text{noise}}^2} \quad (2.102)$$

We assume that $\sqrt{\sigma_{\text{signal}}^2 + \sigma_{\text{noise}}^2} \approx (\text{sample SD of dataset})$, where *sample SD* is the sample standard deviation of the data. We get for the signal and noise standard deviation:

$$\sigma_{\text{signal}} \approx \sqrt{a} \cdot (\text{sample SD of dataset}) \quad (2.103)$$

$$\sigma_{\text{noise}} \approx \sqrt{1-a} \cdot (\text{sample SD of dataset}). \quad (2.104)$$

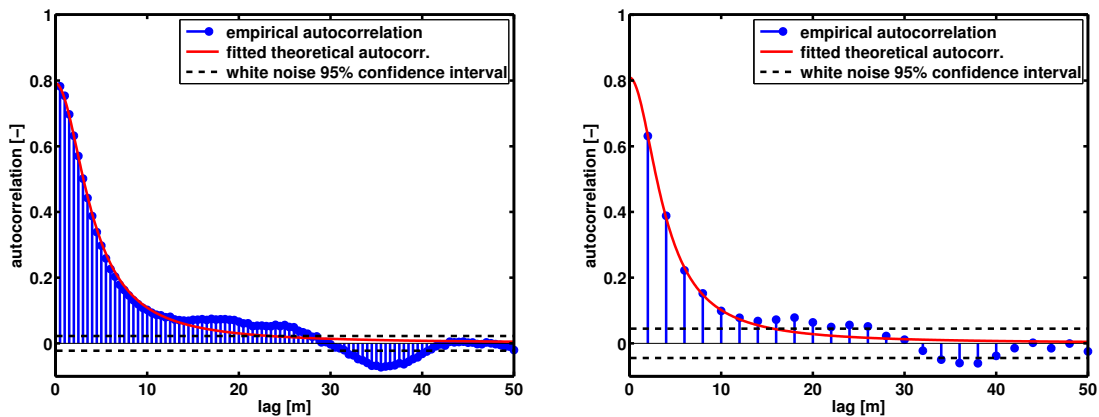
Our experiment's theoretical value of the parameter a is $\frac{2^2}{2^2+1^2} = 0.8$. For the model fit, only the first 5 points of the empirical autocorrelation are used. If 1 or 2 of these 5 points of the empirical autocorrelation fall within the theoretical 95% confidence bounds of a white noise stochastic process, they are rejected. In case of two data points left for fitting, the data series is considered to be useless for the determination of l_z , σ_{signal} and σ_{noise} from the empirical autocorrelation.

Figure 2.6 gives two examples of empirical autocorrelation functions for two different data samplings. They have been created with the parameter values stated in (2.101). The theoretical models fitted to the empirical autocorrelations are shown as light gray lines. Results from several data sampling experiments are summarized in Tab. 2.1. Blank entries in Table 2.1 are a result of the rejection procedure. A minimum number of 3 points are required for the fit to be valid. Table B.1 of Appendix B shows the same values as in Table 2.1, but ordered according to the number of sample stations.

Table 2.1 shows that with coarser sampling, the spread of the estimated correlation length around the true value of 4 m increases. Furthermore, a general underestimation of the estimated correlation length with respect to the correct value is observed. Note that many 1σ standard deviations of the parameters are far from giving reasonable uncertainty bounds. The smaller the number of stations to calculate the empirical autocorrelation, the more pronounced this discrepancy

becomes (Table B.1 of Appendix B). Hence, the rejection procedure still allows an accurate fit, but fewer stations result in an empirical autocorrelation that is less representative for the actual statistics of the original data.

The results from the experiment suggest that the amplitude a and thus, σ_{signal} and σ_{noise} , are seemingly robust parameters to estimate, even for very low sampling. This is surprising, since the two parameters $l_{z,data}$ and a are correlated by as much as $Cor(l_{z,data}, a) = -0.8$ in this specific experiment. Wherever the experiment is repeated on other sections of the synthetic data (not shown here), this robustness is not observed and hence, occurs by chance. Consequently, estimating the correlation length from the data itself is not per se a safe procedure in the sense that the resulting correlation length is always equal or larger than the true value. On the contrary, it may even underestimate the correlation length $l_{z,estimated}$. Due to the negative correlation between a and $l_{z,estimated}$, we can at least resort to rather low a -values (i.e. low σ_{signal} and high σ_{noise} , see Eq. (2.102)), which then results in high values for $l_{z,estimated}$. The choice of high $l_{z,estimated}$ is a safe procedure, as shown in Sect. 2.2.8.



(a) sample spacing: 0.5m, # of samples: 8000, spatial extent: 4000m

(b) sample spacing: 2m, # of samples: 2000, spatial extent: 4000m

Figure 2.6: (a) Estimation of collocation parameters from empirical autocorrelation function of the reference data set. Theoretical values for generating the synthetic data are: $l_{z,data} = 4$ m, $\sigma_{signal} = 2$, $\sigma_{noise} = 1$. (b) Autocorrelation function from a downsampling of the same data set as used in (a). Dashed lines give the 95% confidence bounds for the autocorrelation of white noise. Data between these bounds is considered to be uncorrelated.

Table 2.1: Estimated model parameters and their 1σ standard deviations from fits of Eq. (2.100) to empirical autocorrelation functions. If there are too few points to fit the model, the cell is left blank. Values for σ_{signal} and σ_{noise} are derived according to Eqs. (2.103) and (2.104), respectively.

		Spatial extent [m]						
		4000	1000	500	100	50	30	
Sample spacing [m]	0.5	$l_{z,data}$	3.943 \pm 0.045	4.045 \pm 0.036	3.474 \pm 0.071	2.739 \pm 0.214	2.590 \pm 0.195	1.894 \pm 0.211
		a	0.798 \pm 0.003	0.828 \pm 0.002	0.820 \pm 0.006	0.777 \pm 0.028	0.797 \pm 0.029	0.748 \pm 0.045
		σ_{signal}	2.010	2.199	2.029	1.801	2.055	1.779
		σ_{noise}	1.012	1.003	0.950	0.964	1.036	1.032
	1.0	$l_{z,data}$	3.817 \pm 0.039	3.945 \pm 0.054	3.067 \pm 0.189	2.627 \pm 0.288	3.230 \pm 0.029	
		a	0.805 \pm 0.005	0.837 \pm 0.007	0.859 \pm 0.036	0.793 \pm 0.060	0.746 \pm 0.003	
		σ_{signal}	2.009	2.197	2.072	1.943	2.145	
		σ_{noise}	0.989	0.968	0.839	0.994	1.252	
	2.0	$l_{z,data}$	3.784 \pm 0.077	4.628 \pm 0.370	3.213 \pm 0.175			
		a	0.809 \pm 0.014	0.797 \pm 0.049	0.881 \pm 0.042			
		σ_{signal}	2.047	2.207	2.140			
		σ_{noise}	0.994	1.114	0.785			
3.0	$l_{z,data}$	4.361 \pm 0.504	5.801 \pm 0.991					
	a	0.747 \pm 0.080	0.619 \pm 0.087					
	σ_{signal}	1.947	1.914					
	σ_{noise}	1.134	1.501					

2.2.10 Collocation interpreted as a solution to an integral equation

There is a connection between simple least-squares collocation and integral equations, which we will explore in the following. Two tests are developed from the theory of integral equations to check, if collocation is an appropriate method to interpolate a specific data set. The first test works on the basis of a Fredholm integral equation of the first kind (IFK) and the second on a Fredholm integral equation of the second kind (ISK).

IFK: A sufficient requirement for a physical parameter for use in collocation

Consider a IFK, defined by

$$f(x) = \int_a^b g(x, y)m(y) dy \quad (2.105)$$

where $m(y)$ is the unknown model function to be determined. The so-called representer or data kernel $g(x, y)$ is a known function. The data function $f(x)$ describes some physical parameter that is measured at discrete points in an experiment (and is our collocation target). Furthermore, assume the model $m(y)$ to be discretized by n basis functions $h_j(y) = h(x_j, y)$:

$$m(y) = \sum_{j=1}^n \alpha_j h_j(y) \quad (2.106)$$

with n being the number of given data points, as in Eq. (2.29). Equivalently to $h_j(y)$, let us introduce the notation $g_i(y) = g(x_i, y)$, $i = 1, \dots, n$ for the representers at specific data points and substitute Eq. (2.106) into Eq. (2.105) to arrive at a discretized version of Eq. (2.105) (Aster et al., 2011, p. 133):

$$\begin{aligned} f(x_i) &= \int_a^b g_i(y) \sum_{j=1}^n \alpha_j h_j(y) dy \\ &= \sum_{j=1}^n \alpha_j \int_a^b g_i(y) h_j(y) dy, \quad \text{for all } i = 1, \dots, n. \end{aligned} \quad (2.107)$$

Define the matrix Γ with the elements

$$\Gamma_{i,j} = \int_a^b g_i(y) h_j(y) dy, \quad i, j = 1, \dots, n \quad (2.108)$$

and obtain from Eq. (2.107) the linear system

$$f(x_i) = f_i = \Gamma_{i,j} \alpha_j \quad \text{or:} \quad \Gamma_X \alpha = f_X \quad (2.109)$$

that is equivalent in form to Eq. (2.34), but with Γ_X and α not necessarily equal to A_X and c , respectively. In order to guarantee that Γ_X is symmetric and p.d., the basis functions $h_j(y)$ of the model need to adopt one of two possible forms:

$$h_j(y) = g_j(y), \quad \text{or:} \quad (2.110)$$

$$h_{i,j}(y) = \kappa_{i,j} \cdot g_j(y), \quad (2.111)$$

where $\kappa_{i,j}$ is some arbitrary symmetric and p.d. kernel.

From Eq. (2.110), Eq. (2.111) and Eq. (2.106), we see that the model function $m(y)$ is a linear combination of a subspace of the data representer, the subspace being defined by $g_j(y)$, $j = 1, \dots, n$. The restriction thus put on the basis functions $h_j(y)$ strongly reduces the number of physical problems whose models are reasonably described by Eq. (2.106). In particular, if the number of observations is low, the model has to get by with only a few basis functions that possibly do not describe the model in an adequate manner. With dense data sampling, the severity of the problem is somewhat mediated. As mentioned in Aster et al. (2011) (p. 140), the use of representers as

basis functions guarantees convergence to a solution of the continuous inverse problem. However, they also point out that the increasing number of basis functions worsens the conditioning of the inversion problem, making it more prone to noise in the data. With real data, this approach should thus only be applied, if the representer constitutes a good basis for the model space.

Even though we consider herewith a very limited number of physical problems, it provides us with a sufficient (but not necessary) requirement for a physical parameter to be used in collocation inside a RKHS. In conclusion, data $f(x)$ that are well described by an IFK whose model function is a linear combination of the data representer, can be well approximated using Eq. (2.34), with A_X being p.d. and symmetric. The corresponding functions

$$K(x, z) = \int_a^b g(z, y)g(x, y) dy, \quad \text{or:} \quad (2.112)$$

$$K(x, z) = \int_a^b g(z, y)\kappa(z, x)g(x, y) dy \quad (2.113)$$

are valid kernels to be used in Eq. (2.33).

Remark 6. *The matrix Γ_X in Eq. (2.108) derived from basis function (2.110), is called Gram matrix. A Gram matrix derived in such a way is always symmetric and p.d. (e.g., Aster et al., 2011, p. 312).*

Note that more possibilities for $h(x, y)$ are available than those in Eq. (2.110) and Eq. (2.111), if $g(x, y)$ and $m(y)$ can become complex functions.

ISK: Physics of the data itself

In practice, checking if a linear combination of the representer $g(x, y)$ is an appropriate basis for the model can become very difficult since an analytical solution of $m(y)$ rarely exists. We thus need to bring our physics into a form that makes it easier to decide if collocation can be applied to some measurable data resulting from that physics. Let us for now assume, the physics behind Eq. (2.105) leads to an equivalence between Eq. (2.109) and Eq. (2.33). In such a case, we can indeed say that Eq. (2.109) comprises a collocation problem. Consequently, we can combine Mercer's Theorem from Sect. 2.2.4 with Eq. (2.33), and we see that $f(x)$ is a linear combination of the kernel's eigenfunctions:

$$f(x) = \sum_{j=1}^n c_j K(x_j, x) = \sum_{j=1}^n c_j \sum_{i=1}^{\infty} \frac{\varphi_i(x_j)}{\lambda_i} \cdot \varphi_i(x) \quad (2.114)$$

By definition, eigenfunctions are the result of the homogeneous ISK (repeated from Eq. (2.43)):

$$\varphi(x) = \lambda \int_a^b K(x, y)\varphi(y) dy$$

If $\varphi_1, \varphi_2, \dots$ are various solutions of the homogeneous ISK, then all linear combinations $c_1\varphi_1 + c_2\varphi_2 + \dots$ are solutions thereof (Courant and Hilbert, 1968, p. 96). Hence, $f(x)$ in Eq. (2.114) is a solution to the homogeneous ISK with kernel $K(x, y)$.

Now let us make the connection to a different representation of the ISK. In Gerlach (2009), it is nicely shown that the following inhomogeneous boundary value problem

$$\begin{aligned} \frac{d}{dx}p(x)\frac{d\varphi}{dx} + [q(x) + \lambda\rho(x)]\varphi &= -k(x), & a < x < b \\ \varphi(a) &= d \\ \varphi(b) &= e \end{aligned} \quad (2.115)$$

leads to an ISK of the form

$$\begin{aligned} \varphi(x) &= \lambda \int_a^b G(y, x)\rho(y)\varphi(y) dy \\ &+ p(a)\varphi(a)\frac{dG(y, x)}{dy} \Big|_{y=a} - p(b)\varphi(b)\frac{dG(y, x)}{dy} \Big|_{y=b}. \end{aligned} \quad (2.116)$$

Note that the boundary values are now intrinsic and are not stated explicitly as in Eq. (2.115). The function $G(x, y)$ is called the Green's function, and is the solution to the boundary value problem

$$\begin{aligned} \left[\frac{d}{dx} p(x) \frac{d}{dx} + q(x) \right] G(x, y) &= -\delta(x - y) \\ G(a, y) &= 0 \\ G(b, y) &= 0. \end{aligned} \quad (2.117)$$

In case of an inhomogeneous differential equation with homogeneous boundary values $\varphi(a) = 0$, $\varphi(b) = 0$, or equivalently (as shown in Courant and Hilbert, 1968, p. 236) a homogeneous differential equation

$$\frac{d}{dx} p(x) \frac{d\varphi}{dx} + [q(x) + \lambda \rho(x)] \varphi = 0$$

with inhomogeneous boundary values, the integral equation becomes

$$\varphi(x) = \lambda \int_a^b G(y, x) \rho(y) \varphi(y) dy \quad (2.118)$$

which is our well known eigenvalue problem. Gerlach (2009) lists specific eigenvalue problems to which the solutions are known. For illustrative purposes, one example is shown here:

$$\begin{aligned} \text{boundary value problem: } & \frac{1}{x} \frac{d}{dx} x \frac{d\varphi}{dx} + \left(\lambda - \frac{n^2}{x^2} \right) \varphi = 0 \\ & n = \text{integer, } \varphi \text{ finite at } x = 0, \infty \end{aligned}$$

$$\text{corresponding ISK: } \varphi(x) = \lambda \int_0^\infty G(x, y) u(y) y dy$$

$$G(x, y) = \frac{1}{2n} \begin{cases} \left(\frac{x}{y} \right)^n, & x < y \\ \left(\frac{y}{x} \right)^n, & y < x \end{cases}$$

$$\text{eigenfunctions: } \varphi_n(x) = J_n(\sqrt{\lambda}x); 0 < \lambda < \infty; J_n = \text{Bessel function of order } n$$

From Eq. (2.118) and Eq. (2.43), it is evident that any homogeneous boundary value problem with

$$K(x, y) = G(x, y) \rho(y) = \text{symmetric and p.d. kernel} \quad (2.119)$$

can be solved with simple collocation. Since any linear differential equation can be written as a linear combination of solutions from the homogeneous problem plus a special solution of the boundary value problem, we can conclude that all physical parameters $\varphi(x) = f(x)$ described by Eq. (2.115) and fulfilling Eq. (2.119), are well suited for collocation. In such a case, the inhomogeneous term in Eq. (2.116) takes the place of the deterministic part in Eq. (2.15) and the kernel $K(x, y)$ is interpreted as the covariance function of the signal part.

2.2.11 Appropriate station sampling for collocation

In Sect. 2.2.9, it was shown that the sampling of a physical parameter needs to be very dense and of vast extent in order to allow the determination of the correlation length and nugget variance. Approximate maximum values for station spacing might be one fourth of a presumed correlation length and the spatial extent should also be at least a hundred times this correlation length (see Table 2.1). In the following section, we assume the shape of the correlation function and the correlation length to be given. We ask here, which station network of a fixed number of stations catches most of the structure to be recovered.

We have a continuous signal $s(x)$ that perfectly obeys the normalized covariance function (2.86). We assume that neither a deterministic part nor measurement noise is in the data. If we know the correct correlation function of a continuous signal, the Wiener-Khinchin theorem (e.g., Chatfield,

2003) tells us that the power spectral density and the autocorrelation of the signal form a Fourier transform pair:

$$a(z) = \int_{-\infty}^{\infty} S_{xx}(f) e^{2\pi i z f} df \quad (2.120)$$

$$S_{xx}(f) = \int_{-\infty}^{\infty} a(z) e^{-2\pi i z f} dz \quad (2.121)$$

$S_{xx}(f)$: power spectral density as a function of frequency f

$a(z)$: autocorrelation function of the signal s

Note that the Wiener-Khinchin theorem only applies to correlation functions. Covariance functions need to be normalized according to Eq. (2.84). With the help of the theorem, we arrive at the power spectral density of $s(x)$:

$$\begin{aligned} S_{xx}(f) &= \int_{-\infty}^{\infty} \frac{1}{1 + \left(\frac{\|z_1 - z_2\|}{l_z}\right)^2} \cdot e^{-2\pi i z f} dz \\ &= l_z \cdot \pi \cdot e^{-2\pi l_z |f|} \end{aligned} \quad (2.122)$$

If the signal is perfectly sampled, we can define the total energy Φ_{tot} as to:

$$\Phi_{\text{tot}} = \lim_{f_{\text{top}} \rightarrow \infty} \int_0^{f_{\text{top}}} S_{xx}(f) df = \int_0^{\infty} l_z \cdot \pi \cdot e^{-2\pi l_z |f|} df = \frac{1}{2} \quad (2.123)$$

If we took the lower frequency limit to minus infinity, we would arrive at a value of one, as it should be for a density function.

We recall that $s(x)$ is sampled at specific intervals Δl and covers only data along a spatial extent of L . Frequencies close to and above Nyquist frequency will not be well retrieved. In Sect. 2.2.8, we have seen that the sampling frequency does not impose a clear cutoff, but deriving correct phase information from the measured data will be very uncertain. Hence, the total power density will not be reached. Colloquially and in analogy to Eq. (2.123), we define a partial signal energy recovered by the system

$$\begin{aligned} \Phi_{\text{part}} &= \int_{f_{\text{bot}}}^{f_{\text{top}}} S_{xx}(f) df = \int_{f_{\text{bot}}}^{f_{\text{top}}} l_z \cdot \pi \cdot e^{-2\pi l_z |f|} df \\ &= \frac{1}{2} \left(e^{-2\pi l_z |f_{\text{bot}}|} - e^{-2\pi l_z |f_{\text{top}}|} \right) \end{aligned} \quad (2.124)$$

where the upper and lower bounds of the frequency f are given by

$$f_{\text{bot}} = 0 \quad (2.125)$$

$$f_{\text{top}} = \frac{1}{2 \cdot \Delta l} = \frac{m}{2L} = \text{Nyquist frequency} \quad (2.126)$$

L : spatial extent

Δl : sampling interval

m : number of stations in the network

We search for the station network for which $p\%$ of the spectral energy is recovered:

$$\begin{aligned} f_{\text{bot}} = 0 \quad \rightarrow \quad \frac{\Phi_{\text{part}}}{\Phi_{\text{tot}}} &= 1 - \exp\left(-m\pi \cdot \frac{l_z}{L}\right) = p \\ \Rightarrow \frac{L}{l_z} &= \frac{-m\pi}{\ln(1-p)}, \quad \frac{\Delta l}{l_z} = \frac{-\pi}{\ln(1-p)} \end{aligned}$$

Let us illustrate the formula with a numerical example:

$$m = 100, \quad p = 99\% : \quad \frac{L}{l_z} \approx 68, \quad \frac{\Delta l}{l_z} \approx 0.68$$

Given a known correlation length, 100 stations and the target to recover 99% of the spectral energy, the station network might be chosen according to $\Delta l \approx 0.68 \cdot l_z$.

In Moritz (1980) (p. 175), some remarks are given on the choice of the covariance function and on the determination of its parameters from data. It is observed that 3 parameters are sufficient to describe most covariance functions:

Variance C_0 : The value of the covariance function at station distance $r = 0$, i.e. $C_0 = C(0)$.

Correlation length ξ : Here defined as $r = \xi$, where $C(r) = \frac{1}{2}C_0$ (German: Halbwertsbreite).

Curvature parameter χ : A dimensionless quantity related to the curvature of the covariance curve at zero station distance r .

In test computations, Moritz (1980) (p. 177) confirms that for $r \leq \xi$, various functions with the same 3 parameters C_0 , ξ and χ are practically equivalent. Furthermore, he claims that interpolation is accurate enough only, if station distances are well below ξ , without stating numerical values for his claim. As shown in Sect. 2.2.9, a reasonable number would be $\frac{\Delta l}{\xi} < 0.25$. Such a strict rule is definitely correct, if the correlation function has to be determined from the interpolation data set alone. Hence, values of $\frac{\Delta l}{\xi} = \frac{\Delta l}{l_z} \approx 0.68$ for $m = 100$ (with $\xi = l_z$, see Eq. (2.86)) are restricted to the situation of known correlations. They should be regarded as an upper bound for proper interpolation tasks.

2.2.12 Recipe for collocation

From the theory presented, a procedure for collocating data is established in a recipe-like manner:

1. Find information on the shape of the correlation function. In some cases, the physics may tell you to choose for example a harmonic function, as for the gravitational potential (for ZWD, one could possibly resort to Kolmogorov theory). Optimally, the target parameter can be shown to obey the boundary value problem in Eq. (2.115) with a symmetric and p.d. kernel. The solution to the homogeneous differential equation is assigned to the stochastic signal. The specific solution to the inhomogeneous differential equation is used to derive the deterministic part.
2. Lack of physical reference requires the existence of densely sampled data and data of vast spatial extent. These might come from a high-resolution numerical model. The station spacing should be at least as dense as one fourth of the expected correlation length. From these data, create an empirical autocorrelation and fit some function to it. For the fit, take roughly the first 5 lags into account and definitely avoid fitting to data that are inside the 95% confidence interval of pure noise. If less than 3 lags are outside this interval, use a correlation length that is 4 to 8 times the station spacing. The frequently used value at GGL of twice the station spacing is not appropriate in such a worst-case scenario. Estimating the correlation function is also possible in the Fourier domain for gridded data or from periodograms for ungridded data.
3. Take the upper end of the confidence interval for the estimated correlation length. For the signal variance, use the corresponding lower confidence bound and for the noise variance the upper bound. Overshooting the actual correlation length deteriorates the solution far less than undercutting it.
4. The design of a network should be based on information about the correlation length to be expected. If correlations are well known, use $\Delta l = \frac{-\pi}{\ln(1-p)} \cdot l_z$ to determine the station spacing. Note that this formula does not contradict the above stated 4 to 8 times the station spacing. Application of values of $\Delta l < 4 \cdot l_z$ can only be considered if l_z , σ_{signal} and σ_{noise} are accurately known and are not estimated from the acquired data.

2.3 Water vapour tomography software AWATOS2

AWATOS2 is the acronym for Atmospheric Water Vapor Tomography Software2 and has been programmed by Donat Perler. Its aim is to simulate refractivity and GNSS tropospheric observations in 4D and to invert for refractivity with data from GNSS observations with a tomographic technique and on the basis of a Kalman filter. In Perler et al. (2011) and in Perler (2011), a thorough account of the implemented models and algorithms is given and will not be repeated hereafter. In Appendix A, an entire chapter is dedicated to the software design that lies behind the source code. It explains the design at the conceptual level, i.e. what are the responsibilities of different software parts, and at the specification level, that is, how are the responsibilities fulfilled and how do the parts work together (Shalloway and Trott, 2004). In this thesis, AWATOS2 has been used for the following tasks:

1. Ground meteorological values have been input into AWATOS2 to calculate the ZDD according to Eq. (2.12). The ZDD has then been used to reduce ZTD to ZWD in the Payerne profile study in Chap. 4.
2. Simulate ZTDs from meteorological fields of NWP models. AWATOS2 had to be modified by Fabian Hurter in order to read NWP model output files in netcdf format.

Chapter 3

Comparison of zenith path delays from GNSS and radiosonde measurements

The ZTD is a fundamental parameter in GNSS meteorology. Its accuracy should be well characterized and quantified, before using it as input into NWP models or combining it with other measurement types. The ZTD from GNSS is an integrated measurement, which is often validated with radiosonde measurements. The comparison to radiosonde integrated ZTDs has become an accepted standard, even though the fundamental differences between these measurement types make the comparison notoriously difficult. The following chapter assigns some of the uncertainty present in the GNSS minus radiosonde ZTD differences to either the radiosonde or the GNSS ZTD. The separation is possible to a certain degree because of the availability of a long time series from 2006–2012, which includes different changes in the radiosonde acquisition unit and in the GNSS processing. Day-night and seasonal patterns provide an informative basis for the separation. Additionally, an uncertainty budget of the random effects is prepared for the radiosonde. The random uncertainties from the sonde and the statistics of the ZTD differences, which have been reduced by systematic effects, are eventually used to derive the random part of the GNSS ZTD uncertainty.

3.1 Data description

The comparison study between GNSS and radiosonde ZTDs makes use of three data sets. Firstly, we have radiosonde data from MeteoSwiss at our disposal. Secondly, we have hourly GNSS ZTD data from Swisstopo and thirdly, there is a data set of ground meteorological measurements from the SwissMetNet of MeteoSwiss. The data sets are explained in more detail in the following sections.

3.1.1 Radiosonde data

The available radiosonde data includes measurements of height, pressure, temperature and humidity values from the operational radiosonde in Payerne. The data lasting from 2006–2012 has been provided by MeteoSwiss that operates the Payerne site. The acquisition unit has undergone a number of changes during the years 2009–2012 (Tab. 3.1). The change with the largest effect on the data quality took place in May 2009. The VIZ/Sippican carbon hygistor was replaced by a Rotronic HC2 capacitive polymer sensor. Considerable improvements in relative humidity readings were observed after the change (Philipona et al., 2009). Furthermore, the improvements had a marked influence on the quality of the integral measures of ZTD and ZWD calculated from radiosonde measurements, as will be shown in this chapter.

The data from 2006–2007 has also been analysed in a similar study by Perler (2011), but contains only radiosonde data from the old humidity sensor. Since our data includes several years of data featuring the new humidity sensor, the analysis has been repeated and extended. For the years also analysed by Perler (2011), we only have the radiosonde product TEMP at hand, whereas the data from 2008 onward is available as raw radiosonde data files. The TEMP product denotes data that is reduced to significant pressure levels with some unknown filter procedure and quality-controlled for outliers. It contains roughly 46 lines of data per sounding. The raw sonde data is the direct output from the soundings without any filtering or outlier removal applied. On average, these soundings contain roughly 2000 measurements before the change to 1 second data sampling (Tab. 3.1) and around 6000 afterwards. For the radiosonde raw data, an outlier removal was incorporated into the processing of this study using the following rules for quality control:

1. The first pressure, temperature and humidity readings of each radiosonde ascent was taken to calculate a ZTD with the Saastamoinen formula in Eq. (2.11). The sounding is considered to be an outlier, if

$$|ZTD_{rs,saastamoinen} - ZTD_{rs,integration}| > 0.01m \quad (3.1)$$

where $ZTD_{rs,integration}$ was calculated according to Eqs. (2.1) and (2.6). Outliers are usually associated with humidity values approximately 100% close to the ground. While the first radiosonde value is still well calibrated from the launching procedure and thus yields a reasonable ZTD with the Saastamoinen model, the affected sondes show persistently high values after some seconds of flight. The humidity readings look as if the sensor were clogged. Furthermore, these sondes' ZTDs usually show large discrepancies to GNSS ZTDs. At first sight, the 0.01m criterium seems to be a very strict rule. However, from a total of 161 cases detected by this rule, only 14 stem from the period of the new humidity sensor.

2. Soundings are removed if their ZTD differs by >5 cm from the GNSS value. There are 9 cases affected by this rule.

Additionally to the sonde outliers, ZTDs from GNSS are said to be outliers, if their formal uncertainty is >1.4 mm. Such cases occur, if very little data is observed during a period of 1 day (124 cases affected). Eventually, 280 (gnss-rs) differences were removed from a total of 4267 concurrent GNSS and radiosonde observations, corresponding to 6.6% of all cases.

3.1.2 GNSS data

By courtesy of Swisstopo, the ZTDs were placed at our disposal. They have been processed by Dr. Elmar Brockmann at Swisstopo. In the presented study, only ZTDs from the AGNES station PAYE are considered. Table 3.1 displays the changes in the GNSS hardware (Swisstopo, 2014a) and in the processing of the data (Brockmann and Ineichen, 2008). In May 2008, all except for three (BOUR, FRIC, and SAAN) AGNES stations were equipped with GPS/GLONASS capable receivers (Ineichen et al., 2007 and Swisstopo, 2014c). The GNSS data used in this study was processed with a modified version of Bernese 5.0 according to the processing description given in Tab. 3.2. In all further discussions, GNSS will be used synonymously to GPS/GLONASS. Axis labelling of plots will always use the term GNSS, including also the years 2006–2007 of GPS-only processing.

The change from weekly 7-day sliding window strategy to daily coordinate sets (Tab. 3.1) resulted in 2 ZTD values at the boundaries of the processing batches at midnight. The 2 ZTD values usually differed by a small amount. With a weighted average, one midnight value was obtained. The inverse variance of the formal uncertainty served as weighting.

3.1.3 Ground meteorological data

The ground meteo was used for the calculation of the ZDD according to Eq. (2.12). The ZDD was subtracted from the ZTD to yield GNSS ZWD. Pressure and water vapour measurements were

Table 3.1: Acquisition changes at the operational radiosonde unit in Payerne for the last 3 years (Gonzague Romanens, personal communication, 2013) and at the AGNES GNSS station PAYE (Elmar Brockmann, personal communication, 2014 and Brockmann and Ineichen, 2008).

Date	Radiosonde acquisition
01 May 2009	• Rotronic HC2 replaces VIZ/Sippican relative humidity sensor
11 Jan 2011	• SRS400 (analog) to SRS-C34 (digital) radiosonde migration. Change from radar reflector to GPS for positioning
09 Feb 2011	• SRS-C34 without hypsometer (pressure and altitude from GPS)
16 Apr 2012	• new radiation correction on temperature sensor and change to 1 second data sampling
Date	GNSS acquisition
14 Jun 2007	• receiver at the PAYE GNSS station was changed from a TRIMBLE 4700 to a TRIMBLE NETR5 and the antenna from a Trimble Micro-centered L1/L2 to a Trimble Zephyr Geodetic antenna
24 Feb 2008	<ul style="list-style-type: none"> • change from GPS only to GPS/GLONASS processing • combination of GPS and GLONASS on normal equation level • elevation cutoff decreased from 10° to 3° • troposphere gradients included • use of CODE final GNSS orbits instead of IGS final orbits • change from relative (I01.ATX) to absolute (C05.ATX) antenna calibration and calibration applied to all AGNES antennas • change from weekly (7-day sliding window) to daily coordinate sets • ambiguity resolution of GLONASS with enhanced GNSS Bernese 5.0+ Version (Brockmann and Ineichen, 2008)
17 Apr 2011	• change from International Terrestrial Reference Frame ITRF05 to ITRF08 and change from antenna file C05.ATX to I08.ATX

therefore required at each individual GNSS station. Since these values are commonly not measured at the stations themselves, the pressure and water vapour measurements from the SwissMetNet of MeteoSwiss were collocated to the GNSS stations using COMEDIE (Sect. 2.2). In this chapter, only the values in Payerne are needed. The final reduction from ZTD to ZWD was carried out with AWATOS2 (Sect. 2.3).

3.2 Formal uncertainties of ZTD estimates from GNSS

The formal uncertainties of the estimated ZTD parameters provide us with qualitative information about the ZTDs' accuracies. Even though formal uncertainties are usually too optimistic, ratios of formal uncertainties are a measure of relative accuracy between ZTDs of the same acquisition period.

For example, the formal uncertainty of the estimated ZTD parameters from the Bernese processing have time-varying characteristics (Fig. 3.1). Fast fluctuations at the beginning of 2008 are due to the changing number of available observations. The number of observations increased because of the transition from GPS-only to GPS/GLONASS-combined processing and the decrease of the elevation cutoff from 10° to 3°. Since the formal uncertainty becomes better with the GPS/GLONASS combination, one might also expect an improvement in the quality of other estimated parameters. It is shown in Brockmann and Ineichen (2008) that for example daily coordinates do not benefit from the combination, whereas kinematic coordinates have a great benefit from the GPS/GLONASS solution. Especially for stations with relatively poor visibility, the ad-

Table 3.2: Parameter settings of the Bernese 5.0 processing that remained the same for the entire study period 2006–2011.

Parameter	Settings
processing mode	<ul style="list-style-type: none"> • double-difference processing in a network solution using the ionosphere-free L_3 combination
datum definition	<ul style="list-style-type: none"> • minimum constraint solution on the latest International Terrestrial Reference Frame (ITRF) weekly solution. A no-net-translation condition is imposed on the ITRF station solutions. Net rotation and net scaling are left free
orbit product	<ul style="list-style-type: none"> • final orbits
sampling rate	<ul style="list-style-type: none"> • 30s
baseline strategy	<ul style="list-style-type: none"> • maximum number of observations
a priori troposphere	<ul style="list-style-type: none"> • zenith direction: dry delay Saastamoinen model with standard atmosphere (Dach et al., 2007, p. 243) • mapping function: dry Niell
estimated troposphere	<ul style="list-style-type: none"> • piecewise-linear wet path delays using wet Niell mapping function with 1 hour parameter spacing
observation weighting	<ul style="list-style-type: none"> • elevation-dependent weighting with $1/\cos^2(elev)$

ditional GLONASS satellites improve the kinematic coordinate solutions. The influence on the tropospheric parameters still needs to be more closely investigated and compared to validation data from radiosondes.

Furthermore, there is a long-term negative trend in Fig. 3.1 that can be well attributed to the increasing number of satellites with time, mainly the completion of the GLONASS constellation. The trends have been determined individually for day and night, but they do not significantly differ (Tab. 3.3). On the other hand, the mean value is higher at night than at day. A possible explanation for the difference in the mean between day and night is given by the processing change in February 2008 (Tab. 3.1). Since then, the processing delivers results of daily period instead of the 7-day stacked solution. The daily epochs end at midnight. Hence, the ZTD parameters at midnight are only supported by observations from before or after midnight, whereas at noon the ZTD parameters are constrained by earlier and later observations. Before February 2008, the mean shows no statistically significant difference between night and day (not displayed). This is due to 7-day stacked solutions with one coordinate set calculated for this period (Tab. 3.1) and hence, two consecutive midnight troposphere parameters are combined into one. From Tab. 3.3, we learn that the amplitudes of the yearly period are practically the same during day and night. Not shown are the amplitude and phase of the half-yearly period. Its amplitudes are approximately half the yearly amplitudes, and again, they are practically equal for day and night. Yearly and half-yearly periods are by far the most prominent contributions to the GNSS formal uncertainty and can not be associated to changing numbers of observations. They must be caused by varying complexity of environmental conditions, whereas the model to describe these variations does not change between Feb 2008 and Apr 2011. Possible explanations for annually varying postfit residuals are the higher dynamics of the atmosphere during summer and unmodeled atmospheric and ground-water loading. The reason for the difference in phase shift between day and night remains unexplained.

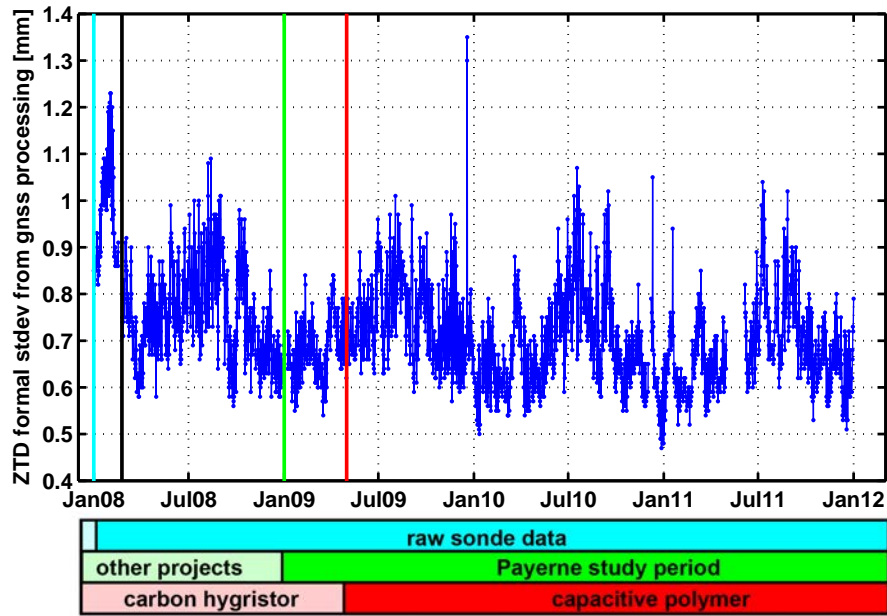


Figure 3.1: Formal 1σ uncertainty of the ZTD parameter from GNSS processing for the station in Payerne (PAYE). Data displayed corresponds to the times when concurrent radiosondes are available, that is, one hour before noon and one hour before midnight. For time guidance, vertical lines are included. They mark important acquisition changes in the radiosonde and in the GNSS acquisition. They are described in Tab. 3.1. The solid black line stands for the processing change to GPS/GLONASS-combined processing and explains the sudden drop in the formal uncertainty at the beginning of 2008. Note that none of the formal uncertainties are above 1.4 mm since larger values have been rejected as outliers.

Table 3.3: Results from fitting a sine with a 365-day period, a mean and a linear trend to the formal ZTD uncertainty from GPS/GLONASS-combined processing shown in Fig. 3.1, once for the day and once for the night values.

Parameter	Unit	Day		Night	
		Value	SD	Value	SD
mean	10^{-1} mm	7.09	0.03	7.36	0.03
trend	10^{-1} mm/year	-0.36	0.03	-0.31	0.02
amplitude	10^{-1} mm	0.52	0.04	0.59	0.03
phase	days	244.9	4.25	226.9	3.52
corr	-	-0.0323		0.0124	
σ_a posteriori	10^{-1} mm	0.9		0.9	

3.3 Comparison of ZTDs

In Fig. 3.2a, the difference between GNSS and radiosonde derived ZTDs is plotted for the entire study period. The time bars below the main figure show acquisition changes in the radiosonde data and mark important dates for the interpretation of the data.

From the time series shown in Fig. 3.2a, it is difficult to assess, if the change from TEMP to raw data changed the quality of the radiosonde-derived ZTDs. We do not observe any harmful influence caused by the use of the TEMP product in place of the raw data. In general, the influences of the individual acquisition changes before May 2009 are not recognizable in the time series. This is

due to the dominance of the signal measured by the old humidity sensor. For example, the change of the GNSS receiver and antenna on the 14 Jun 2007 (dashed line in Figs. 3.2a and b) causes a negative offset in the coordinate time series of the PAYE station of about -1 cm (Brockmann and Ineichen, 2008). Due to the correlation between height and ZTD (Rothacher, 2002), we would expect to also see an offset in the ZTD time series. The time series however does not reveal any sign of an offset on that date.

An obvious change in the time series is caused by the transition from the VIZ/Sippican to the Rotronic HC2 sensor. For better understanding the characteristics of this change, the following seasonal model was fitted to the (gnss-rs) differences in Figs. 3.2a and 3.3a:

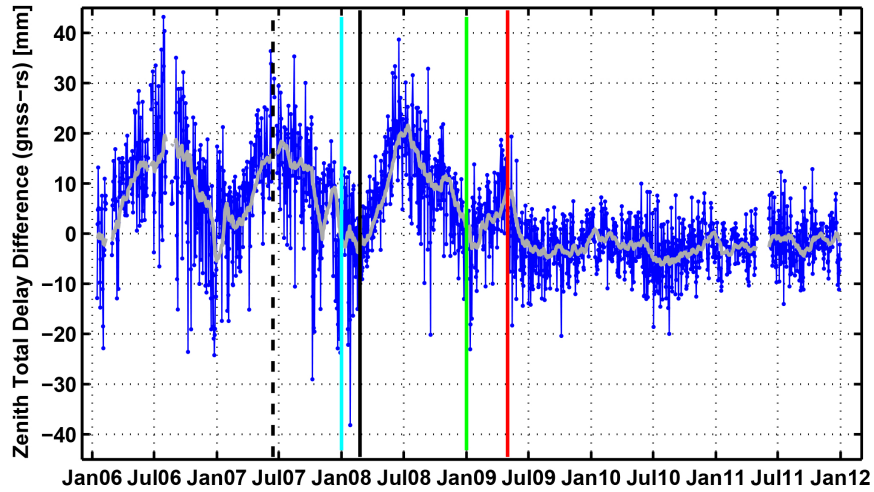
$$\Delta ZTD_{\text{gnss-rs}}(t) = \mu + a \cdot \sin\left(\frac{2\pi}{\tau}(t + \phi)\right) \quad (3.2)$$

- μ : mean over the entire time series
- a : amplitude of yearly period
- ϕ : phase of yearly period
- τ : period of 1 year (365 days)

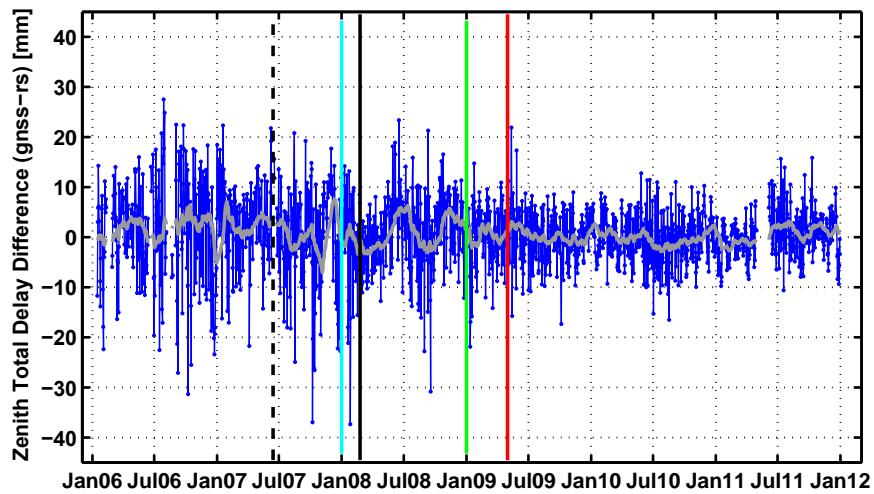
The estimation process is carried out individually for day and night time soundings and the two periods with different humidity sensors (Tab. 3.4). The model in Eq. (3.2) is subtracted from the time series to produce Fig. 3.2b for day time soundings. Equivalent plots for night time are shown in Figs. 3.3a (original difference) and 3.3b (filtered, i.e. with model removed). The GNSS minus sonde differences with the old sensor show a considerably larger mean during day than during night (Tab. 3.4). With the old sensor, the amplitude a of the model is also larger during day than during night. Day-night comparisons show no significant phase changes.

Upon use of the new humidity sensor, the phase changes by approximately half a year with respect to the old sensor. During the years 2006–2009, the maxima are in summer and for 2010–2011, they are in winter. This hints either at a completely different systematic behaviour of the new humidity sensor or at a systematic effect from the GNSS that has been previously hidden by the lower quality of the old humidity sensor. Another interesting feature of the new sensor is the stronger mean offset, stronger amplitude and higher $\sigma_{\text{a posteriori}}$ during night than during day. Whether these numbers are due to GNSS, sonde, or both is difficult to determine. A possible explanation for the higher night $\sigma_{\text{a posteriori}}$ is given in Sect. 3.2. There, the higher GNSS formal uncertainty is due to less observations at the boundaries of the processing batches. The sonde on the other hand, is expected to be less accurate during daytime, as will be discussed in Sect. 3.7. This suggests that the better humidity sensor exposed the weaker estimation quality of the GNSS ZTD at night.

After removal of some systematic effects modeled by Eq. 3.2, we arrive at Figs. 3.2b and 3.3b. For all 5 years, we observe a wider spread during the summer than during the winter half year. Before May 2009, the effect is markedly more pronounced. In Sect. 3.7, this matter will be analysed in detail.



(a) original day



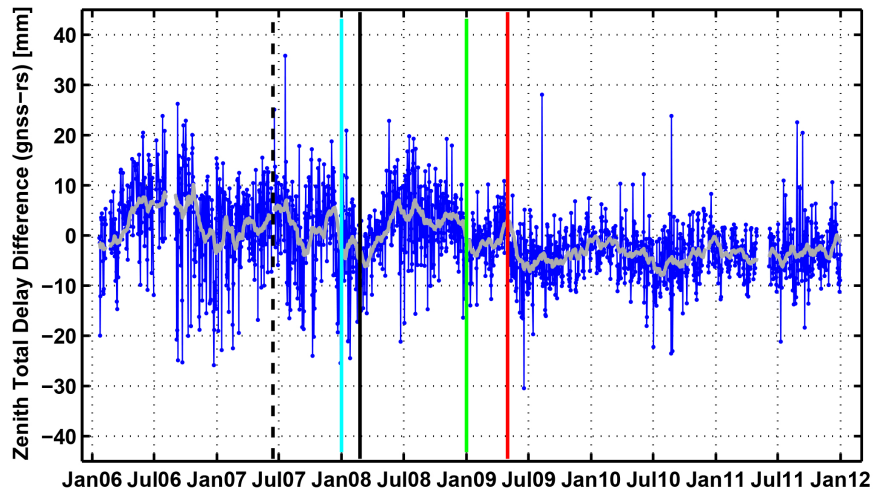
TEMP product	raw sonde data
other projects	Payerne study period
carbon hygistor	capacitive polymer

(b) filtered day

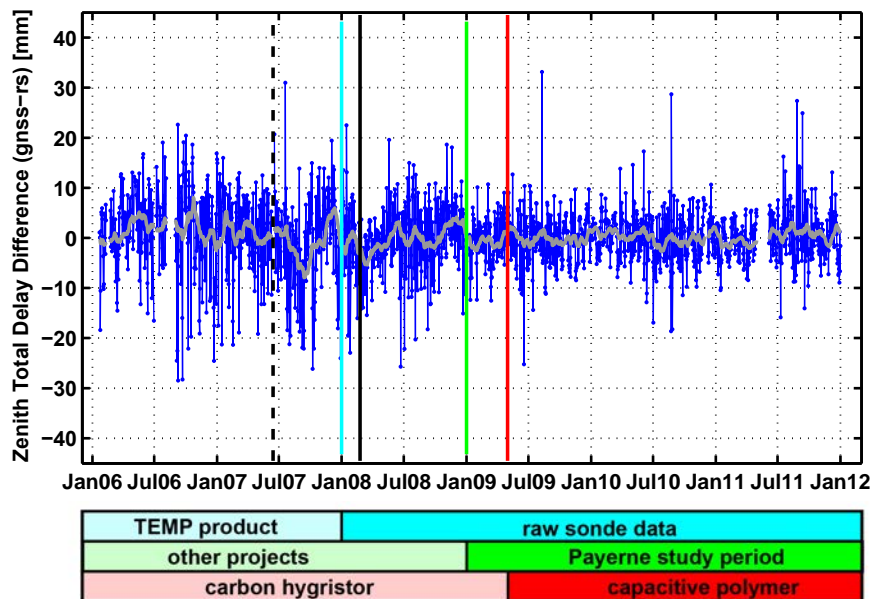
Figure 3.2: (a) Original day (gnss-rs) ZTD time series. (b) Filtered day (gnss-rs) ZTD time series. The light blue and red vertical lines mark important acquisition changes in the radiosonde data. The light green line marks the date after which data is further processed to ZWD and used in Chap. 4. At the date of the dashed black line, the GNSS receiver and antenna in Payerne were exchanged. The solid black line denotes the processing change to GPS/GLONASS-combined processing (Tab. 3.1). The grey line is a 30-day moving average of the data and is plotted for illustrative purposes.

Table 3.4: Estimated parameters from fitting the function in Eq. (3.2) to the (gnss-rs) ZTD differences in Fig. 3.2a. The parameters are separately calculated for day and night data.

Sensor type	Parameter	Unit	Day		Night	
			Value	SD	Value	SD
carbon hygistor (until Apr 2009)	mean	mm	7.4	0.3	1.6	0.2
	amplitude	mm	8.6	0.4	3.2	0.3
	phase	days	264.7	2.6	258.0	6.0
	correlation	-	-0.051		-0.044	
	σ_a posteriori	mm	8.8		7.8	
capacitive polymer (starting May 2009)	mean	mm	-2.5	0.2	-3.8	0.2
	amplitude	mm	1.0	0.2	1.5	0.2
	phase	days	51.7	13.6	84.4	9.0
	correlation	-	-0.013		-0.013	
	σ_a posteriori	mm	4.8		5.0	



(a) original night



(b) filtered night

Figure 3.3: (a) Original night time series (gnss-rs) ZTDs. (b) Filtered night time series (gnss-rs) ZTDs. Other information as for Figs. 3.2a and b.

3.4 Influence of processing strategy on GNSS ZTDs

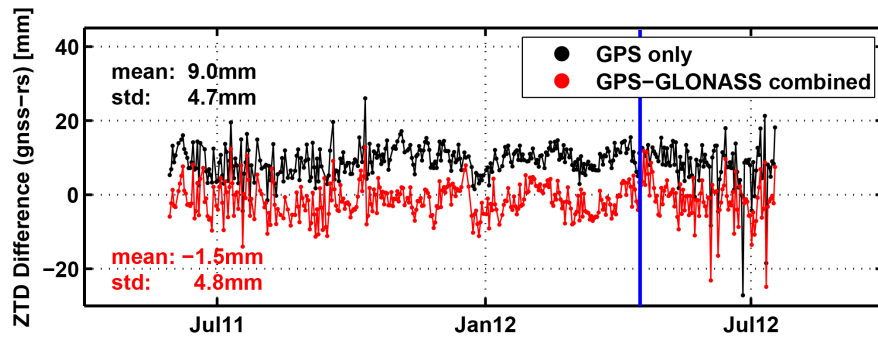
For the period Jun 2011 to Jul 2012, we have both the original processing (before Feb 2008) and the most recent way (after Apr 2011) of processing at hand. For a list of changes, see Tab. 3.1. The original and the most recent solution differ by a mean offset of roughly 10 mm (Fig. 3.4a for noon and Fig. 3.4b for midnight). Thus, the mean of the GNSS ZTD is very sensitive to changes in the processing. The means during day and night differ by 1.4 mm for the original and 1.6 mm for the most recent solutions. In Sect. 3.5, we will discuss if the influence of diurnal variations in the ionosphere onto the GNSS-determined ZTDs is strong enough to explain the 1.4–1.6 mm day-night differences. Figure 3.4 also tells us that the standard deviation of the (gnss-rs) is hardly altered by the new processing, meaning that the variation in ZTD is similarly well captured by both processing strategies. Additionally, the two solutions correlate to a large degree, from which we conclude that the GPS/GLONASS combination does not cause a marked improvement in the estimation of the troposphere parameters. Furthermore, Fig. 3.1 shows that no variation or data offset is caused by the new radiation correction on the temperature sensor of the radiosonde. The stronger spread between the two solutions after this date is likely to be associated with the more dynamic atmosphere during summer time, since a similar behaviour is observed in summer 2011. The new radiation correction differs by ≈ 0.1 K in the troposphere (Kräuchi, 2011), which is of a similar magnitude as the calibration uncertainty of a radiosonde temperature sensor. As will be shown in Sect. 3.7, the influence of such a temperature calibration uncertainty on the ZTD is negligible.

Table 3.5 lists the stations of the AGNES network and the ZTD mean differences between the two solutions. The offset varies around 10 mm. The table shows differing offsets between double stations (e.g., ETHZ/ETH2, BOUR/BOU2, HOHT/HOH2), emphasizing that the variability is probably due to the completely different antenna files I01.ATX and I08.ATX of the two solutions. A further argument for the antenna files to be the major cause comes from the local variability between the offsets. This precludes the change in reference frame from being the major influence. The standard deviation of all stations is small and close to 3 mm, suggesting that both solutions show roughly the same atmospheric variations. Consequently, a new processing strategy can offset the estimated ZTDs by more than 10 mm. Individual stations are unequally affected, which excludes the possibility of applying a standard bias correction to the entire network.

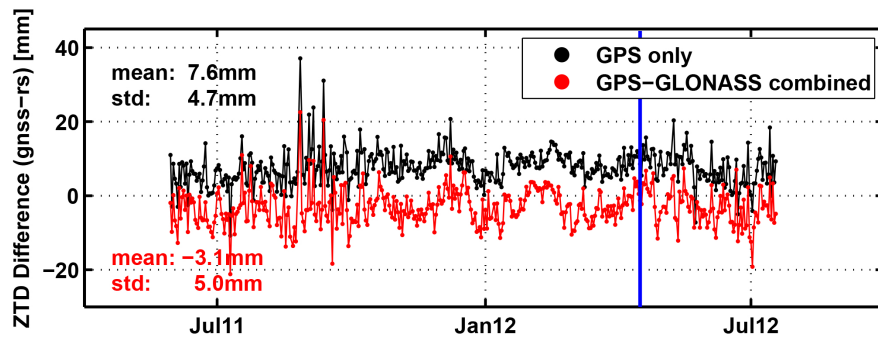
It has been noted in Sect. 3.3 that the GNSS processing in daily batches might have caused the increase in $\sigma_{\text{a posteriori}}$ during the night. Figure 3.4 supports the conjecture, since the GPS only processing with 7-day coordinates and one midnight ZTD parameter of consecutive days keeps the standard deviation with respect to the radiosonde, independent from day or night. In the GPS/GLONASS solution with daily coordinates, a slight increase in standard deviation is observed from day to night. Furthermore, the standard deviation of the GPS-only solution is slightly below the standard deviations of the GPS/GLONASS-combined solution.

The seasonal variation of the GPS/GLONASS-combined solution is lower than of the GPS-only solution (see captions to Figs. 3.4a and b). This indicates that a systematic seasonal component is associated with artefacts of the GNSS processing. Note that the GNSS processing changes in Tab. 3.1 are not directly connected to a yearly signal.

With respect to the radiosonde, the GPS/GLONASS solution shows an improvement of the (gnss-rs) mean with the new antenna phase center variation file I08.ATX. For this to see, compare the values of -1.5 mm and -3.1 mm for day and night from Figs. 3.4a and b, which are closer to zero than corresponding values of -2.5 mm and -3.8 mm in Tab. 3.4



(a) ZTD comparison for the noon soundings. Amplitudes of a sine fit to the data show $1.3 \text{ mm} \pm 0.3 \text{ mm}$ for the GPS-only and $0.6 \text{ mm} \pm 0.4 \text{ mm}$ for the GPS-GLONASS-combined processing.



(b) ZTD comparison for the midnight soundings. Amplitudes of a sine fit show $1.5 \text{ mm} \pm 0.3 \text{ mm}$ for the GPS-only and $0.9 \text{ mm} \pm 0.3 \text{ mm}$ for the GPS-GLONASS-combined processing.

Figure 3.4: Differences between GNSS and radiosonde ZTD for the GPS-only processing before Feb 2008 and the GPS-GLONASS-combined processing after Apr 2011 (Tab. 3.1). The vertical blue line marks the new radiation correction applied to the temperature readings from the sonde. Mean and sample standard deviation of the time series are given inside the plot. (a) noon sondes. (b) midnight sondes, with GPS times corresponding to 1 hour before midnight.

Table 3.5: Mean and sample standard deviation of differences between the GPS-only ZTD solution and the GPS/GLONASS-combined ZTD solution for stations of the AGNES network of Switzerland. They are sorted according to increasing height

Station	Latitude	Longitude	Height [m]	Mean [mm]	SD [mm]	Station	Latitude	Longitude	Height [m]	Mean [mm]	SD [mm]
ENTZ	48 ° 33.0'	7 ° 38.4'	204.2	10.7	3.0	MART	46 ° 7.3'	7 ° 4.2'	644.6	6.9	3.5
STJ9	48 ° 37.3'	7 ° 41.0'	237.1	15.1	2.6	FRI2	47 ° 31.6'	8 ° 6.7'	723.9	12.0	3.1
COMO	45 ° 48.1'	9 ° 5.7'	292.3	10.9	3.0	FRIC	47 ° 31.6'	8 ° 6.7'	725.7	7.1	2.9
TORI	45 ° 3.8'	7 ° 39.7'	310.7	12.4	3.0	FRI3	47 ° 31.6'	8 ° 6.7'	726.9	14.4	2.8
DOMO	46 ° 7.3'	8 ° 17.3'	356.2	9.8	3.1	LUCE	47 ° 26.3'	7 ° 16.1'	741.6	10.9	2.5
BSCN	47 ° 14.8'	5 ° 59.4'	359.5	10.4	2.7	STGA	47 ° 26.5'	9 ° 20.8'	753.7	8.9	2.9
FHBB	47 ° 32.0'	7 ° 38.3'	377.7	11.5	2.9	HUTT	47 ° 8.5'	7 ° 50.1'	779.1	9.9	3.0
BUAN	48 ° 29.2'	5 ° 21.2'	416.3	11.3	2.9	ERDE	46 ° 14.1'	7 ° 17.4'	782.2	10.6	2.4
BLFT	47 ° 37.6'	6 ° 51.5'	416.4	9.3	3.0	VISW	48 ° 4.4'	8 ° 31.6'	790.9	10.4	2.9
STA2	45 ° 51.4'	8 ° 56.5'	417.2	11.4	3.0	CHTL	45 ° 18.2'	6 ° 21.5'	850.2	9.5	2.9
LOMO	46 ° 10.3'	8 ° 47.2'	438.0	9.0	3.0	HCHS	47 ° 42.8'	8 ° 12.3'	889.2	8.8	2.9
EPFL	46 ° 31.3'	6 ° 34.1'	460.4	9.9	2.9	BOUR	47 ° 23.6'	7 ° 13.8'	940.1	6.3	2.8
LIND	47 ° 33.5'	9 ° 42.5'	473.3	11.6	3.2	BOU2	47 ° 23.6'	7 ° 13.8'	942.0	10.8	2.9
AIGE	46 ° 14.9'	6 ° 7.7'	473.8	10.4	3.1	ZIMM	46 ° 52.6'	7 ° 27.9'	956.3	10.8	2.8
KALT	47 ° 13.1'	9 ° 0.5'	477.0	9.9	2.9	ZIM2	46 ° 52.6'	7 ° 27.9'	956.4	11.0	3.0
RAVE	47 ° 47.6'	9 ° 37.5'	503.9	9.9	2.9	HOH2	46 ° 19.2'	7 ° 45.8'	985.7	8.8	3.0
NEUC	46 ° 59.6'	6 ° 56.4'	504.6	8.9	3.1	HOHT	46 ° 19.2'	7 ° 45.8'	985.7	6.9	2.9
STDL	47 ° 32.5'	8 ° 29.7'	510.1	11.3	3.0	PFA2	47 ° 30.9'	9 ° 47.1'	1090.1	14.0	2.9
MARG	46 ° 5.1'	6 ° 30.6'	524.2	10.0	2.8	MABZ	46 ° 41.2'	10 ° 33.1'	1092.0	9.8	2.9
SOND	46 ° 10.2'	9 ° 51.0'	529.1	9.1	3.2	HABG	46 ° 44.9'	8 ° 11.0'	1147.9	7.0	3.2
KREU	47 ° 38.5'	9 ° 9.6'	529.9	12.1	3.1	MODA	45 ° 12.8'	6 ° 42.6'	1182.2	16.1	3.5
SLTB	47 ° 27.3'	7 ° 42.7'	535.0	12.4	3.0	MAKS	47 ° 55.4'	7 ° 1.9'	1237.2	11.0	2.9
TRLK	47 ° 38.4'	8 ° 41.9'	538.5	9.9	2.9	SARG	46 ° 59.0'	9 ° 30.4'	1258.6	8.7	3.2
LUZE	47 ° 4.1'	8 ° 18.0'	542.2	12.9	3.2	BORM	46 ° 28.1'	10 ° 21.8'	1263.3	13.5	3.0
BLGN	46 ° 10.3'	5 ° 34.5'	544.7	9.6	2.9	FALE	46 ° 48.3'	9 ° 13.8'	1344.1	9.4	2.9
PAYE	46 ° 48.7'	6 ° 56.6'	548.7	10.8	2.8	FCLZ	45 ° 38.6'	5 ° 59.1'	1358.1	4.8	4.5
LFNB	47 ° 35.5'	8 ° 3.4'	555.9	10.3	3.0	SAAN	46 ° 30.9'	7 ° 18.1'	1419.5	6.9	2.7
MIRGT	47 ° 16.3'	7 ° 52.1'	558.1	12.3	3.2	ARD2	46 ° 46.6'	10 ° 12.3'	1546.4	10.0	2.8
WLCH	47 ° 40.1'	8 ° 28.8'	561.4	9.7	2.7	ARDE	46 ° 46.6'	10 ° 12.3'	1546.6	6.9	2.8
MTTI	47 ° 22.1'	7 ° 10.1'	570.2	11.6	2.8	DAV2	46 ° 48.8'	9 ° 50.6'	1645.3	10.0	2.8
FLDK	47 ° 13.9'	9 ° 34.8'	570.3	8.9	2.9	DAVO	46 ° 48.8'	9 ° 50.6'	1645.6	11.0	2.8
HGGL	47 ° 23.5'	8 ° 15.6'	570.5	12.3	3.3	SANB	46 ° 27.8'	9 ° 11.1'	1702.2	8.2	3.4
THYN	47 ° 45.1'	8 ° 44.0'	594.6	9.3	2.9	SAME	46 ° 31.8'	9 ° 52.7'	1759.2	9.9	3.0
BZBG	47 ° 30.3'	8 ° 10.0'	594.7	8.8	2.8	LECH	47 ° 13.4'	10 ° 8.3'	1822.8	9.8	2.6
ETH2	47 ° 24.4'	8 ° 30.6'	594.8	9.8	2.8	ZERM	46 ° 0.1'	7 ° 43.9'	1931.2	10.3	3.6
ETHZ	47 ° 24.4'	8 ° 30.6'	594.8	10.5	2.5	SIMP	46 ° 14.4'	8 ° 1.2'	2012.8	11.3	2.7
WAB2	46 ° 55.4'	7 ° 27.9'	611.2	10.1	2.3	KRBG	47 ° 8.8'	10 ° 37.6'	2258.0	9.7	2.7
WAB1	46 ° 55.4'	7 ° 27.9'	611.2	13.6	2.4	ANDE	46 ° 39.2'	8 ° 37.0'	2367.7	8.9	3.0
EXWI	46 ° 57.1'	7 ° 26.3'	626.9	12.1	2.5	WEHO	46 ° 22.9'	7 ° 28.4'	2966.9	11.4	2.3
SCHA	47 ° 44.2'	8 ° 39.4'	638.2	9.9	3.0	HOGR	45 ° 58.9'	7 ° 40.3'	3515.0	10.7	2.7
MAR2	46 ° 7.3'	7 ° 4.2'	644.1	10.1	3.6	JUJO	46 ° 32.9'	7 ° 59.1'	3634.6	-3.7	3.3

3.5 2nd and 3rd order ionospheric effects

Section 3.4 concludes that the GNSS processing strategy can have a considerable influence on the mean offset, but most of the day-night differences and seasonal systematics remained unexplained. Possible suspects are the ionospheric effects that are not completely removed by the ionosphere-free linear combination during the GNSS processing with Bernese. The aim of this section is to acquire the order of magnitude of the higher order ionospheric terms, especially their diurnal and seasonal variations. It serves us as a basis to better judge the day-night differences observed in the data.

Mathias Fritsche kindly granted us to use data from the first reprocessing project (Steigenberger et al., 2006) and provided the ZTD data sets. Two data sets are placed at our disposal:

- Q1:* Tropospheric ZTD parameters of 2001–2003 for all reprocessed stations. The classical approach of ionosphere-free linear combination processing without higher order ionospheric terms is used. The GPS only solution is calculated for daily processing batches and the ZTD parameters have a 2-hour resolution. The adjustment includes all relevant parameters such as satellite orbits, Earth rotation parameters and tropospheric zenith delays.
- Q2:* Observations are corrected for second and third order ionospheric terms. The terms are modelled according to Fritsche et al. (2005). The subsequent adjustment is equivalent to the Q1 processing.

Major results from these data are presented in Fritsche et al. (2005). From the many globally available stations, the station ZIMM is selected, as it is the closest station to the Payerne radiosonde and GNSS site. The ZTD values of the two solutions Q1 and Q2 have been differenced and are displayed in Fig. 3.5. Additionally, the mean global vertical Total Electron Content (TEC) in $\text{TECU}=10^{16} \text{ m}^{-2}$, i.e. the number of free electrons per square meter (e.g., Schaer, 1999, p. 94; data obtained by Dr. Michael Meindl ETH Zurich) is plotted below to underline the connection between higher-order ionosphere and their influence on the ZTD parameter adjustment. We see that 2001–2003 are years of strong solar activity (Ball, W. T. et al., 2012) with the peak of the 11–13 years solar cycle around 2002.

Since we would like to check, if the diurnal and seasonal variations in the (gnss-rs) ZTD time series are due to unmodeled higher-order ionospheric terms, a sine function of a 364.8-day period was fitted to the day and night data of Fig. 3.5. Table 3.6 is a compilation of the sine fit. The half-yearly period sine fit was added to the table because it had a similar amplitude to the yearly period, which is not true for our (gnss-rs) ZTD data in Fig. 3.2a. The yearly period from the higher-order ionospheric effect is an order of magnitude smaller than the yearly variation of the (gnss-rs) ZTDs observed in Sect. 3.3 or Sect. 3.4. The same is true for diurnal variations in the mean, represented by the differences in mean for day and night. Systematic day-night and seasonal differences between GNSS and radiosonde are thus very unlikely to stem from ionospheric effects not being accounted for in the GNSS processing.

3.6 Comparison of ZWDs

Reduction of ZTDs to ZWDs is accomplished with pressure and water vapor pressure values from ground meteo sensors collocated at the GNSS stations. The available ground meteo data lasts from 2009 till beginning of 2012, which is the so-called Payerne study period (see e.g., Figure 3.2b). As there is very little data from the old humidity sensor, the seasonal model of Eq. (3.2) is only applied to data after May 2009. The results are shown in Tab. 3.7. Corresponding original and filtered time series are included in Appendix C (Figs. C.1a and b for day sondes; Figs. C.2a and b for night sondes).

Note that the day-night difference remains stable during the reduction process. This is to be expected, since the reduction is mostly governed by the pressure whose calibration uncertainty does not vary with the time of day. Except for the mean, all values remain similar to those determined from the ZTD time series (Tab. 3.4). Thus, the dry delays determined from the ground meteo measurements approximate the seasonal dependence to a large degree. However, the mean is offset

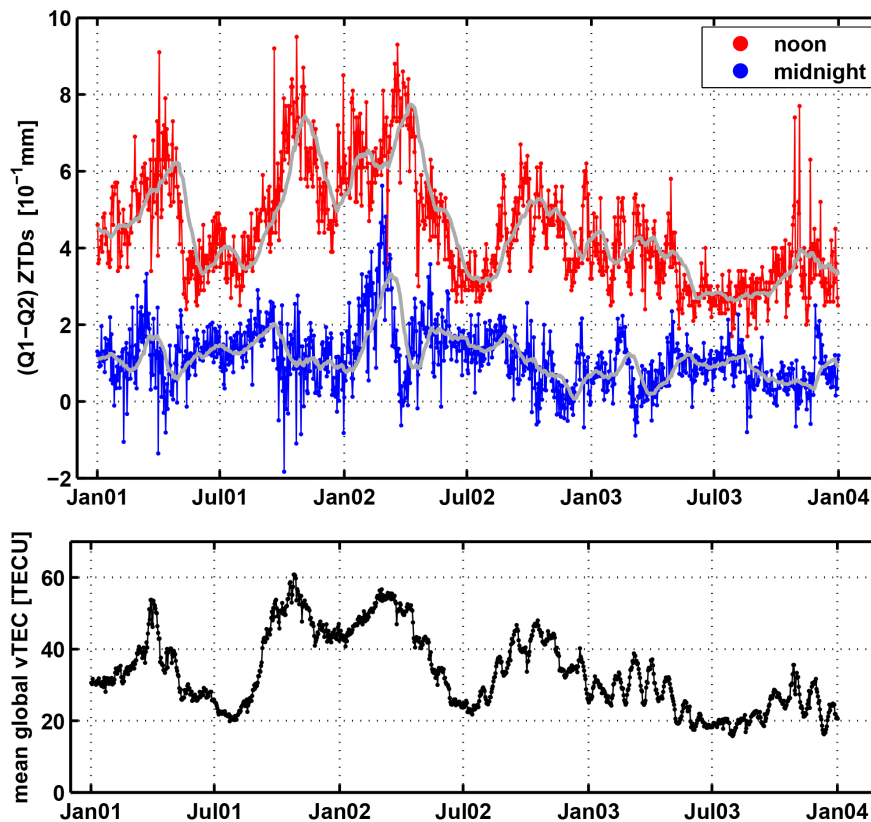


Figure 3.5: For the station of Zimmerwald (ZIMM) and the years 2001–2003, the top figure shows the differences between the Q1 and the Q2 tropospheric ZTD parameters at noon (red) and at midnight (blue). Q1 includes only first order approximation of the ionospheric effect. Additionally, Q2 corrects for second and third order ionosphere according to Fritsche et al. (2005). The bottom figure displays the mean global vertical TEC (Schaer, 1999) in number of free electrons per square meter: $\text{TECU} = 10^{16} \text{ m}^{-2}$. The two midnight values of consecutive days are combined into one by a weighted average, with weights taken from the formal uncertainty.

by more than 3 mm. It is a likely consequence of the use of ground measurements to describe an integral measure across the entire atmospheric column. For the years 2006–2007, Perler (2011) obtains ZWD mean differences of $\mu = 3.5 \text{ mm}$ for noon and $\mu = -5.1 \text{ mm}$ for midnight if his model describing systematic effects is transformed to Eq. (3.2). For ZTD mean differences, he obtains $\mu = 6.1 \text{ mm}$ for noon and $\mu = -1.6 \text{ mm}$ for midnight. The day-night difference in ZWD determined with the old humidity sensor is thus similar to this study (see carbon hygistor in Tab. 3.4). Furthermore, both studies show a decrease of μ by roughly 3 mm when going from ZTD to ZWD, i.e. $\mu_{\text{ZTD}} - \mu_{\text{ZWD}} \approx 3 \text{ mm}$. The latter statement merely confirms that processing the GNSS ZTD to ZWD has been carried out in the same manner and with the same software as in Perler (2011). Observed discrepancies between the here presented result and the result from Perler (2011) are due to different radiosonde data and another time period processed. Hence, the strong negative offset of GNSS with respect to radiosonde in Tab. 3.7 is a combination of an inaccurate reduction process from ZTD to ZWD and either a wet bias of the new humidity sensor or a dry bias of GNSS.

3.7 Formal uncertainty of radiosonde-derived ZTDs

In the following, the random components of the radiosonde uncertainty are described. In a second step, their individual contributions to the total uncertainty of the radiosonde zenith delays are

Table 3.6: Results from fitting a mean, linear trend and sine functions to (Q1–Q2) ZTDs displayed in Fig. 3.5. The yearly and half yearly periods of the noon data are fitted after a dominant long-wavelength period of 875.6 days has been removed. No significant year or half-year period is found for midnight data.

Period	Parameter	Unit	Day		Night	
			Value	SD	Value	SD
	mean	10^{-1} mm	4.48	0.04	1.13	0.02
	trend	10^{-1} mm/year	-0.79	0.05	-0.26	0.03
182.4 days	amplitude	10^{-1} mm	0.79	0.04	-	-
	phase	days	135.3	1.64	-	-
	corr	-	0.0019			
	σ_a posteriori	10^{-1} mm	1.0			
364.8 days	amplitude	10^{-1} mm	0.73	0.04	-	-
	phase	days	80.7	3.08	-	-
	corr	-	-0.0027			
	σ_a posteriori	10^{-1} mm	0.9			

Table 3.7: Estimated parameters from fitting the function (3.2) to the (gnss–rs) ZWD differences. The corresponding time series are Fig. C.1a in Appendix C for day data and Fig. C.2a in Appendix C for night data. For the carbon hygristor, there is not enough ZWD data available to derive representative parameters.

Sensor type	Parameter	Unit	Day		Night	
			Value	SD	Value	SD
capacitive polymer (starting May 2009)	mean	mm	-5.8	0.2	-7.3	0.2
	amplitude	mm	0.8	0.2	1.5	0.2
	phase	days	53.6	17.4	82.3	9.5
	corr	-	-0.0168		-0.0116	
	σ_a posteriori	mm	5.1		5.1	

quantified. In conjunction with the previously shown differences between GNSS and radiosonde, the random GNSS uncertainty is eventually assessed.

3.7.1 Methodology

In Figs. 3.2a and b, we have seen that the calculation of the path delay is not visibly affected by using either the TEMP radiosonde product or the raw data. This is not true for the calculation of the formal uncertainty, since the sensor uncertainties are only available for raw data readings. The filtering procedure of the TEMP product cannot be taken into account in the calculation due to a lack of information about the exact filtering procedure. The formal uncertainty investigations are thus restricted to the raw sonde data from the period 2008–2011.

Table 3.8 gives an overview of the values considered to derive the radiosonde’s formal uncertainty in the zenith path delay calculation. Each contribution is treated independently from the other, assuming no correlation between them.

Table 3.8: Overview of the components of the formal radiosonde uncertainty described in Sect. 3.7.1.

Name of component	Short description
integration	random measurement uncertainty of p/T/f sensors during flight
top Saastamoinen	random component of mostly p sensor uncertainty, creating a delay uncertainty at the profile top
relative position	erroneous height position of p/T/f sensors due to uncertainty in GPS position
calibration 1	calibration uncertainty on the ground of p/T/f sensors
calibration 2	effect of erroneous p calibration onto the delay uncertainty at the profile top

Integration

This component is traditionally considered by the law of uncertainty propagation from sensor uncertainties to zenith path delays. The following formulas are used to calculate the uncertainty of the radiosonde-derived refractivities, assuming no correlation between the sensors:

$$\begin{aligned}\sigma_{N_{\text{dry}}} &= \sqrt{\left(\frac{\partial N_{\text{dry}}}{\partial p} \cdot \Delta p\right)^2 + \left(\frac{\partial N_{\text{dry}}}{\partial T} \cdot \Delta T\right)^2 + \left(\frac{\partial N_{\text{dry}}}{\partial k_1} \cdot \Delta k_1\right)^2} \\ \sigma_{N_{\text{wet}}} &= \sqrt{\left(\frac{\partial N_{\text{wet}}}{\partial f} \cdot \Delta f\right)^2 + \left(\frac{\partial N_{\text{wet}}}{\partial T} \cdot \Delta T\right)^2 + \left(\frac{\partial N_{\text{wet}}}{\partial k_2} \cdot \Delta k_2\right)^2 + \left(\frac{\partial N_{\text{wet}}}{\partial k_3} \cdot \Delta k_3\right)^2} \\ \sigma_{N_{\text{tot}}} &= \sqrt{\left(\frac{\partial N_{\text{tot}}}{\partial p} \cdot \Delta p\right)^2 + \left(\frac{\partial N_{\text{tot}}}{\partial T} \cdot \Delta T\right)^2 + \left(\frac{\partial N_{\text{tot}}}{\partial f} \cdot \Delta f\right)^2 + \left(\frac{\partial N_{\text{tot}}}{\partial k_1} \cdot \Delta k_1\right)^2 + \left(\frac{\partial N_{\text{tot}}}{\partial k_2} \cdot \Delta k_2\right)^2 + \left(\frac{\partial N_{\text{tot}}}{\partial k_3} \cdot \Delta k_3\right)^2}\end{aligned}$$

where

$\Delta p, \Delta T, \Delta f$: random uncertainty component of the pressure, temperature and relative humidity sensor

$\Delta k_1, \Delta k_2, \Delta k_3$: uncertainties of the coefficients k_1, k_2 and k_3 (see Eq. (2.1))

The dry, wet and total refractivities are given by Eq. (2.2), Eq. (2.3) and Eq. (2.1), respectively. It is important to note that the pressure sensor measures the total pressure p and not p_{dry} . Corresponding uncertainties in Tab. 3.9 apply to total pressure only. We will need dry refractivity in the form:

$$N_{\text{dry}} = k_1 \cdot \frac{p - e(T)}{T}. \quad (3.3)$$

For the transformation from relative humidity f to water vapor pressure e , the formula by Hyland and Wexler (1983) is used:

$$e(T) = \frac{f}{100} \cdot \exp(q(T)) \quad (3.4)$$

with $q(T)$ being a function of temperature:

$$\begin{aligned}
q(T) = & -0.58002206 \cdot 10^4 \cdot \frac{1}{T} \\
& + 0.13914993 \cdot 10^1 \\
& - 0.48640239 \cdot 10^{-1} \cdot T \\
& + 0.41764768 \cdot 10^{-4} \cdot T^2 \\
& - 0.14452093 \cdot 10^{-7} \cdot T^3 \\
& + 0.65459673 \cdot 10^1 \cdot \ln(T)
\end{aligned} \tag{3.5}$$

Temperature T is given in K and the resulting water vapor pressure e in units of Pa. Any inaccuracy of the numeric factors in the transformation formula (3.5) is considered negligible. Standard deviations of the uncertainties of sensors and coefficients k_1 , k_2 , and k_3 are given in Tab. 3.9. The partial derivatives of total refractivity with respect to relative humidity is obtained according to:

$$\frac{\partial N_{\text{tot}}}{\partial f} = \frac{\partial N_{\text{dry}}}{\partial f} + \frac{\partial N_{\text{wet}}}{\partial f} = \frac{1}{100} \cdot \left(-\frac{k_1}{T} + \frac{k_2}{T} + \frac{k_3}{T^2} \right) \cdot \exp(q(T)) \tag{3.6}$$

Justification to use relative humidity instead of water vapor pressure for the primary humidity parameter comes from the fact that the resistive hygistor and the capacitive polymer humidity sensors are directly sensitive to relative humidity. The former in a very non-linear and the latter in an almost linear way (Philipona et al., 2009, p. 14). The partial derivative with respect to temperature is obtained by:

$$\begin{aligned}
\frac{\partial N_{\text{tot}}}{\partial T} &= \frac{\partial N_{\text{dry}}}{\partial T} + \frac{\partial N_{\text{wet}}}{\partial T} \\
&= k_1 \cdot \frac{-p - \frac{\partial e}{\partial T} \cdot T + e}{T^2} + k_2 \cdot \frac{\frac{\partial e}{\partial T} \cdot T - e}{T^2} + k_3 \cdot \frac{\frac{\partial e}{\partial T} \cdot T^2 - 2 \cdot e \cdot T}{T^4}.
\end{aligned} \tag{3.7}$$

$$\frac{\partial e}{\partial T} = e \cdot \frac{\partial(q(T))}{\partial T}$$

where $q(T)$ is given by Eq. (3.5). With Eq. (3.7), the effect of temperature uncertainty on the transformation from relative humidity to water vapor pressure is taken into account.

With the assumption that the uncertainties between refractivities at different height levels are uncorrelated, the integration component is then calculated according to the law of uncertainty propagation of equation Eq. (2.6) in zenith direction:

$$\begin{aligned}
\sigma_{\text{zenithdelay,integration}} &= \sqrt{\sum_{i=1}^k \sigma_{\hat{N}_i}^2 \cdot \Delta h_i^2} \\
\Delta h_i &= |h_{i+1} - h_i| \\
\hat{N}_i &= \frac{N_{i+1} + N_i}{2}
\end{aligned} \tag{3.8}$$

where k is the height index at profile top. Note that correlations between $\hat{N}_i, \hat{N}_{i+1}, \dots$ are not taken into account. This has to be reconsidered in the future. Furthermore, icing of the sensor during cloud passage will lead to correlations between refractivities of consecutive height levels that are not accounted for in this study. From some figures in Philipona et al. (2009), it can be concluded that these correlations were still large for the VIZ/Sippican humidity sensor, but strongly decreased when the Rotronic HC2 sensor was emplaced. As the correlation is expected to be positive (icing causes detention of the sensor to adjust to the changing atmosphere), the integration component might be underestimated in those cases.

Calibration

Uncertainty resulting from the calibration procedure propagates from the bottom to the top of the profile. The calibration component of the ZTD uncertainty is modelled as if the error caused

during calibration persists throughout the entire profile and with the same positive or negative sign. The calibration uncertainty of pressure is of relative size with respect to the pressure reading. It therefore decreases with height, whereas the other sensors are modeled with a constant calibration uncertainty. In the current implementation, the effect of the pressure sensor is linearly modelled. Furthermore, each sensor calibration is considered independently from the others:

$$\sigma_{ZTD, \text{calib}, \Delta p} = \sum_{i=1}^k \left(\left(\frac{\partial N(p(h), T(h), f(h))}{\partial p} \right)_{h=\frac{h_i+h_{i+1}}{2}} \cdot \Delta p_{i, \text{calib}} \right) \cdot \Delta h_i \quad (3.9)$$

$$\Delta p_{i, \text{calib}} = \Delta p_{\text{calib}, \text{bottom}} + \frac{(h_i - h_{\text{bottom}})}{(h_{\text{top}} - h_{\text{bottom}})} \cdot (\Delta p_{\text{calib}, \text{top}} - \Delta p_{\text{calib}, \text{bottom}})$$

$$\sigma_{ZTD, \text{calib}, \Delta T} = \sum_{i=1}^k \left(\left(\frac{\partial N(p(h), T(h), f(h))}{\partial T} \right)_{h=\frac{h_i+h_{i+1}}{2}} \cdot \Delta T_{\text{calib}} \right) \cdot \Delta h_i \quad (3.10)$$

$$\sigma_{ZTD, \text{calib}, \Delta f} = \sum_{i=1}^k \left(\left(\frac{\partial N(p(h), T(h), f(h))}{\partial f} \right)_{h=\frac{h_i+h_{i+1}}{2}} \cdot \Delta f_{\text{calib}} \right) \cdot \Delta h_i \quad (3.11)$$

where we have:

$$\Delta h_i = \frac{h_{i+1} - h_i}{2}$$

$\Delta p_{\text{calib}, \text{bottom}}, p_{\text{calib}, \text{top}}$: calibration uncertainty of pressure sensor at profile bottom and top (15 km amsl)

$\Delta T_{\text{calib}}, \Delta f_{\text{calib}}$: calibration uncertainty of temperature and relative humidity sensor.

The total calibration uncertainty of the ZTD becomes:

$$\sigma_{ZTD, \text{calib}, \text{total}} = \sqrt{\sigma_{ZTD, \text{calib}, \Delta p}^2 + \sigma_{ZTD, \text{calib}, \Delta T}^2 + \sigma_{ZTD, \text{calib}, \Delta f}^2} \quad (3.12)$$

In analogy to the integration component, the refractivity is either wet, dry or total. Hence, Eqs. (3.9), (3.10) and (3.11) equally apply to ZWD, ZDD and ZTD. Note that even though calibration introduces a systematic effect across the refractivity profile, the resulting error in the ZTD is of random nature. Calibrations of sondes 12 hours apart are considered to be uncorrelated.

At the top of the profile to be taken at 15 km amsl, the Saastamoinen formulas Eq. (2.11), Eq. (2.12), and Eq. (2.13) without the additional terms B and δ_R are deployed to determine the remaining part of the path delay. Corresponding uncertainties in calibration associated with the Saastamoinen term are added to the calibration components of Eqs. (3.9), (3.10) and (3.11). Here, the expressions are shown for the ZTD:

$$\begin{aligned} \sigma_{ZTD, \text{Saasta calib}, \Delta p} &= \left(\frac{\partial \Delta \rho_{\text{dry}, \text{Saasta}}}{\partial p} + \frac{\partial \Delta \rho_{\text{wet}, \text{Saasta}}}{\partial p} \right) \cdot \Delta p_{\text{calib}, \text{top}} \\ &= (a_1 + 0) \cdot \Delta p_{\text{calib}, \text{top}} \end{aligned} \quad (3.13)$$

$$\begin{aligned} \sigma_{ZTD, \text{Saasta calib}, \Delta T} &= \left(\frac{\partial \Delta \rho_{\text{dry}, \text{Saasta}}}{\partial T} + \frac{\partial \Delta \rho_{\text{wet}, \text{Saasta}}}{\partial T} \right) \cdot \Delta T_{\text{calib}, \text{top}} \\ &= \left(-a_1 \cdot a'_3 \cdot \frac{\partial e}{\partial T} - a_1 \cdot a_2 \cdot \frac{e}{T^2} + a_1 \cdot \left(\frac{a_2}{T} + a''_3 \right) \cdot \frac{\partial e}{\partial T} \right) \cdot \Delta T_{\text{calib}, \text{top}} \end{aligned} \quad (3.14)$$

$$\begin{aligned} \sigma_{ZTD, \text{Saasta calib}, \Delta f} &= \left(\frac{\partial \Delta \rho_{\text{dry}, \text{Saasta}}}{\partial f} + \frac{\partial \Delta \rho_{\text{wet}, \text{Saasta}}}{\partial f} \right) \cdot \Delta f_{\text{calib}, \text{top}} \\ &= \left(-a_1 \cdot a'_3 + a_1 \cdot \left(\frac{a_2}{T} + a''_3 \right) \right) \cdot \frac{\partial e}{\partial f} \cdot \Delta f_{\text{calib}, \text{top}} \end{aligned} \quad (3.15)$$

Pressure produces by far the strongest contribution at this height. Thus, $\Delta p_{\text{calib}, \text{top}}$ is the dominating term. With the value $\Delta p_{\text{calib}, \text{top}} = 1.0 \text{ hPa}$ from Tab. 3.9, we get $\sigma_{ZTD, \text{topsaastacalib}} \approx a_1 \cdot \Delta p_{\text{calib}, \text{top}} \approx 0.3 \text{ mm}$, which could practically be omitted.

Top Saastamoinen

For quantifying the effect of random measurement uncertainty at profile top, simple uncertainty propagation of the Saastamoinen formula is applied. Exemplary, the formula is shown for ZTD:

$$\sigma_{\text{ZTD,top Saasta}} = \left[\left(\frac{\partial \Delta \rho_{\text{dry,Saasta}}}{\partial p} + \frac{\partial \Delta \rho_{\text{wet,Saasta}}}{\partial p} \right)^2 \cdot (\Delta p_{\text{calib,top}})^2 + \left(\frac{\partial \Delta \rho_{\text{dry,Saasta}}}{\partial T} + \frac{\partial \Delta \rho_{\text{wet,Saasta}}}{\partial T} \right)^2 \cdot (\Delta T_{\text{calib,top}})^2 + \left(\frac{\partial \Delta \rho_{\text{dry,Saasta}}}{\partial f} + \frac{\partial \Delta \rho_{\text{wet,Saasta}}}{\partial f} \right)^2 \cdot (\Delta f_{\text{calib,top}})^2 \right]^{1/2}$$

Corresponding derivatives are shown in Eqs. (3.13), (3.14) and (3.15). Note that the pressure uncertainty of the sensor has linearly decreased towards the profile top (Tab. 3.9), but is still almost a factor of 10 larger than the calibration pressure uncertainty at 15 km height. Unlike the Saastamoinen contribution to the uncertainty in calibration, it will be separately displayed in the result plots.

After 09 Feb 2011 (Tab. 3.1), pressure is determined from GPS. Since the absolute position uncertainty of GPS is of the order of 10 m corresponding to ≈ 1 hPa pressure difference, $\Delta p_{\text{calib,top}}$ is kept fixed throughout the entire study period.

Relative position

The random relative position uncertainties of adjacent $\Delta h_i = |h_{i+1} - h_i|$ are highly negatively correlated. It is therefore assumed that the integration offsets the individual random positioning uncertainties against each other and approximately sum up to zero. A systematic offset in relative positioning however will not cancel and needs to be accounted for. The approach chosen to approximate this error uses Eq. (2.6) in the zenith direction. $\Delta H_{\text{absolute}}$ is the absolute height uncertainty at the top of the profile integration and is evenly distributed across all Δh_i :

$$\begin{aligned} \Delta \rho + \Delta(\Delta \rho) &= \sum_{i=1}^k \hat{N}_i \cdot \left(\Delta h_i + \frac{\Delta H_{\text{absolute}}}{h_{\text{top}} - h_{\text{bottom}}} \cdot \Delta h_i \right) \\ &= \sum_{i=1}^k \hat{N}_i \cdot \Delta h_i + \underbrace{\frac{\sum_{i=1}^k \hat{N}_i \cdot \Delta h_i}{h_{\text{top}} - h_{\text{bottom}}}}_{N_{\text{average}}} \cdot \Delta H_{\text{absolute}} \end{aligned} \quad (3.16)$$

$$\hat{N}_i = \frac{N_{i+1} + N_i}{2}$$

If $\Delta H_{\text{absolute}}$ is taken to be the standard deviation of the absolute height uncertainty, we obtain an approximation of the relative positioning component of the ZTD uncertainty:

$$\sigma_{\text{ZTD,relative position}} \approx N_{\text{average}} \cdot \Delta H_{\text{absolute}} \quad (3.17)$$

with N_{average} being either wet, dry or total average atmospheric refractivity between ground and maximum integration height.

Before 2011, height was derived from integrating the hydrostatic pressure equation. If there was a ground calibration uncertainty in pressure and temperature, this caused a systematic height error. A dry atmosphere with a constant temperature gradient up to the tropopause at 11 km and a constant stratospheric temperature up to the integration height of 15 km is used to estimate the systematic height offset at the top associated with the use of pressure and temperature readings and the hydrostatic pressure equation for height determination (e.g., Jacobson, 2005):

$$z = \frac{T_{\text{bot}}}{\Gamma} \left[1 - \left(\frac{p_{\text{tropo}}}{p_{\text{bot}}} \right)^{\frac{\Gamma R}{g}} \right] + \frac{T_{\text{strato}} R}{g} \ln \left(\frac{p_{\text{tropo}}}{p_{\text{strato}}} \right)$$

and the same equation with calibration uncertainty of pressure Δp_{calib} and temperature ΔT_{calib} :

$$z + \Delta H_{\text{absolute}, \Delta T_{\text{calib}}} = \frac{T_{\text{bot}} + \Delta T_{\text{calib}}}{\Gamma} \left[1 - \left(\frac{p_{\text{tropo}}}{p_{\text{bot}}} \right)^{\frac{\Gamma R}{g}} \right] + \frac{(T_{\text{strato}} + \Delta T_{\text{calib}})R}{g} \ln \left(\frac{p_{\text{tropo}}}{p_{\text{strato}}} \right)$$

$$z + \Delta H_{\text{absolute}, \Delta p} = \frac{T_{\text{bot}}}{\Gamma} \left[1 - \left(\frac{p_{\text{tropo}} + \Delta p_{\text{calib}, \text{top}}}{p_{\text{bot}} + \Delta p_{\text{calib}, \text{bot}}} \right)^{\frac{\Gamma R}{g}} \right] + \frac{T_{\text{strato}}R}{g} \ln \left(\frac{p_{\text{tropo}} + \Delta p_{\text{calib}, \text{top}}}{p_{\text{strato}} + \Delta p_{\text{calib}, \text{top}}} \right)$$

With the help of generic values:

$$T = T_{\text{bot}} - \Gamma \cdot h \quad : \text{ temperature profile from ground to } h = 11 \text{ km}$$

$$T_{\text{bot}} \quad : \text{ temperature at profile bottom } = 285 \text{ K}$$

$$\Gamma \quad : \text{ constant temperature gradient from ground to 11 km } = 6.5 \cdot 10^{-3} \text{ K/m}$$

$$p_{\text{bot}} \quad : \text{ pressure at profile bottom } = 955 \text{ hPa}$$

$$p_{\text{tropo}} \quad : \text{ pressure at tropopause 11 km } = 217 \text{ hPa}$$

$$p_{\text{strato}} \quad : \text{ pressure in stratosphere at 15 km } = 120 \text{ hPa}$$

$$T_{\text{strato}} \quad : \text{ constant stratospheric temperature between 11 km and 15 km}$$

$$g \quad : \text{ acceleration of gravity } \approx 9.8 \text{ m/s}^2$$

$$R \quad : \text{ gas constant of dry air } = 287.04 \text{ m}^3 \text{ Pa}/(\text{kg K})$$

and the calibration uncertainties from Tab. 3.9, the height uncertainty becomes:

$$\Delta H_{\text{absolute}} = \sqrt{(\Delta H_{\text{absolute}, \Delta T_{\text{calib}}})^2 + (\Delta H_{\text{absolute}, \Delta p_{\text{calib}}})^2} \approx 11 \text{ m}$$

where the pressure term clearly dominates the estimate. Tests with radiosondes carrying pressure sensors plus GPS (11 Jan 2011–09 Feb 2011) confirm that this approach is a good approximation for the position error before 2011.

The absolute height uncertainty of GPS corresponds to the height uncertainty of code measurements and is $\approx 10\text{m}$ (Tab. 3.9). It seems a sound assumption that distributing $\Delta H_{\text{absolute}}$ across the profile according to Eq. (3.16) describes the contribution that is not offset by negatively correlated Δh_i , $i = 1 \dots k$. As the data contains no $\Delta h_i < 0$ even though there are many $\Delta h_i < 10 \text{ m}$ in the data, a Kalman filter is expected to drive GPS positioning of the sonde (confirmed by Romanens Gonzague, MeteoSchweiz, personal communication, 2013). Synthetic tests with a Kalman filter and $\Delta H_{\text{absolute}} = 10\text{m}$ show that Eq. (3.17) overestimates the error by roughly a factor of 2. Since the order of magnitude is met, a generic value of $\Delta H_{\text{absolute}} = 10\text{m}$ is kept for the entire study period.

Table 3.9: Compilation of sensor uncertainties (1σ) and uncertainties in coefficients of equation Eq. (2.1). Sources of uncertainty values: (a) Löhnert and Maier, 2012, (b) Vaisala, 2013a, (c) Rüeger, 2002, (d) Philipona et al., 2009, (e) Meteolabor, 2010. Note that some calibration uncertainties are taken from a sonde of comparable sensors (Vaisala RS92) as the Swiss sonde SRS400 and SRS-C34.

Parameter	Unit	Uncertainty	Source	Note
Δp_{bottom}	hPa	2.0	(a)	pressure uncertainty at bottom of profile for a water hypsometer
Δp_{top}	hPa	1.0	(b)	pressure uncertainty at top of profile ($\approx 15'000\text{m}$, $\approx 100\text{ hPa}$)
ΔT	K	0.2	(a)	temperature uncertainty of copper-constantan thermocouples
$\Delta f_{\text{carbon hygistor}}$	%	15.0	(a)	mean uncertainty of a carbon hygistor humidity sensor
$\Delta f_{\text{capacitive polymer}}$	%	7.5	(a)	mean uncertainty of a capacitive polymer humidity sensor
Δk_1	K/hPa	0.013	(c)	uncertainty of best available coefficients
Δk_2	K/hPa	10.5	(c)	uncertainty of best available coefficients
Δk_3	K ² /hPa	3000.0	(c)	uncertainty of best available coefficients
Δv_{ascent}	m/s	0.15	(b),(e)	velocity uncertainty of radiosonde ascent derived from GPS Doppler velocities
$\Delta H_{\text{relative}}$	m/m	0.028		relative distance uncertainty derived from Δv_{ascent} and average balloon velocity in 2008: $v_{\text{balloon}} = 5.3\text{ m/s}$
$\Delta H_{\text{absolute}}$	m	10.0	(b),(e)	approximate vertical GPS code absolute positioning uncertainty (spherical error probability given in (e) is 5m)
$\Delta p_{\text{calib, bottom}}$	hPa	0.204	(b),(e)	calibration uncertainty of pressure sensor at bottom of profile (resolution given in (e) is 0.1 hPa, giving a lower bound for the order of magnitude of the calibration uncertainty)
$\Delta p_{\text{calib, top}}$	hPa	0.153	(b)	calibration uncertainty of pressure sensor at top of profile ($\approx 15'000\text{m}$, $\approx 100\text{ hPa}$)
ΔT_{calib}	K	0.077	(b),(e)	calibration uncertainty of temperature sensor (accuracy given in (e) is $\approx 0.1\text{ K}$ and resolution is given in (e) as 0.01 K)
$\Delta f_{\text{calib,carbon hygistor}}$	%	2.0	(d),(e)	approximate calibration uncertainty of carbon hygistor humidity sensor derived from twin soundings (resolution in (e) is given as 1%, accuracy as 2%)
$\Delta f_{\text{calib,capacitive polymer}}$	%	1.020	(b),(d),(e)	calibration uncertainty of capacitive polymer humidity sensor (resolution in (e) is given as 0.1%, accuracy as 1%)

3.7.2 Estimates of radiosonde formal uncertainty

Figures 3.6a and b display the individual uncertainty contributions of sonde ZTDs for day and night. In both cases, relative humidity calibration and measurement inaccuracies to calculate the top Saastamoinen part constitute major influences. The latter is largely the result of inaccurate pressure measurements. Relative humidity calibration is primarily responsible for seasonal fluctuations in the formal sonde uncertainty. Until May 2009, also the integration component is quite large and with a marked seasonal change. It decreases with the humidity sensor change. Hence, the integration accuracy strongly depends on the accuracy of the humidity sensor. This is especially true for the summer months, when warm air can take up a lot of water vapor. Of minor influence are inaccuracies in pressure calibration and height position. Temperature calibration has negligible effect on the ZTD. Further note that the accuracy is slightly worse during day than during night. With the new sensor, the day-night contrast becomes hardly noticeable.

A slightly different picture is presented in Figs. 3.7a and b for the ZWD. Temperature calibration has become a minor contribution, but neither top Saastamoinen, nor relative position and pressure calibration need to be taken into account. Humidity calibration remains the dominant factor, creating a clear seasonal signal.

3.8 Derivation of random GNSS ZTD uncertainty

After all, we would like to quantify the random uncertainty of GNSS-derived ZTDs. For this purpose, we have the filtered (gnss-rs) differences, the formal GNSS uncertainty (Sect. 3.2) and the sonde contributions (Sect. 3.7) at hand. We combine the latter two in the following way to arrive at a confidence interval for the (gnss-rs) differences:

$$(\text{gnss-rs}) \text{ random uncertainty} = \sigma_{\text{ZTD diff}} = \sqrt{(\alpha \cdot \sigma_{\text{ZTD,gnss}})^2 + (\sigma_{\text{ZTD,rs}})^2} \quad (3.18)$$

Assuming that the formal uncertainty of GNSS and radiosonde are normally distributed, we arrive at:

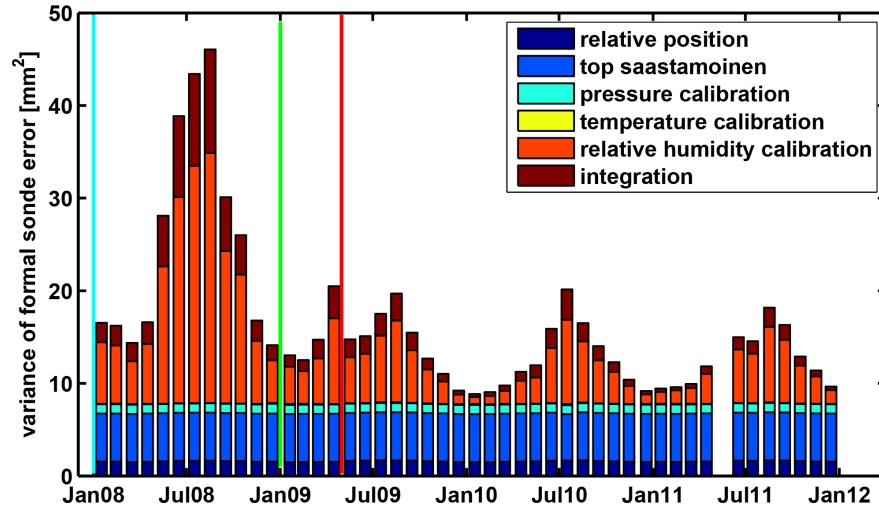
$$95 \% \text{ confidence interval} = \pm 1.96 \cdot \sigma_{\text{ZTD diff}} \quad (3.19)$$

with α to be determined such that 95 % of the (gnss-rs) differences lie within the confidence intervals of Eq. (3.19). The shaded region in the top Fig. 3.8 shows the confidence interval corresponding to the factor $\alpha = 5$, covering 95.03 % of all differences. The individual contributions of GNSS and sonde to the confidence intervals are shown in the bottom plots of the same figure, once as standard deviations and once as stacked barplot of variances. Note that the plots display the GNSS values from Fig. 3.1 multiplied by the factor $\alpha = 5$. After the change of the sonde's humidity sensor, the GNSS and radiosonde contributions are of very similar magnitude. The variance plot exposes a coincidence between sub-annual peaks in radiosonde and GNSS uncertainty. The correlation is not strong but intriguing, since the two values come from two distinctly different sensors.

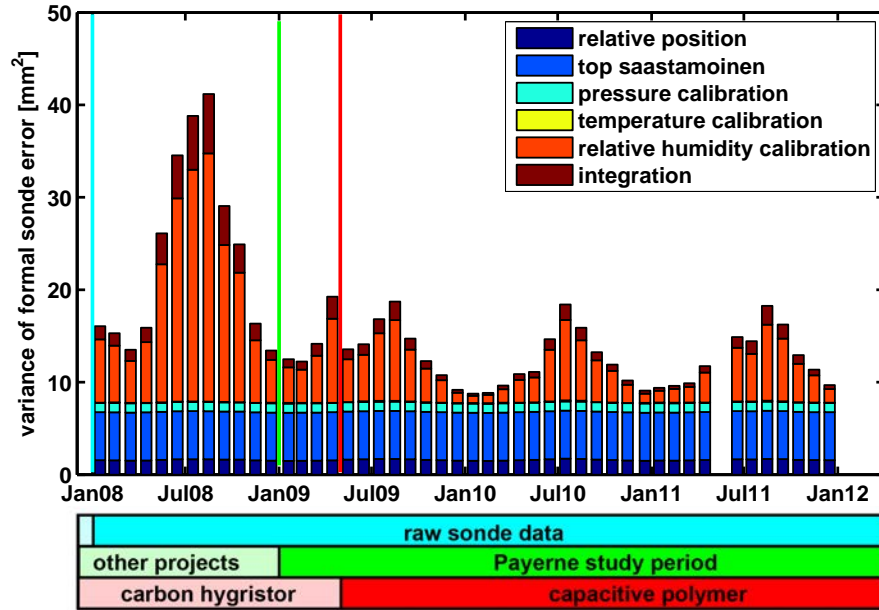
In case of the new humidity sensor, the confidence bounds are overestimating the uncertainty during the winter half year. Hence, the procedure described herein gives conservative uncertainty estimates. According to Fig. 3.8, GNSS ZTD standard deviations are 2.5–3.5 mm during the winter half-year and 3.5–5.0 mm in summer. On very rare occasions, a value of 5 mm is exceeded. Those cases coincide with high radiosonde uncertainty during summer. They are likely to be associated with high humidity values, since high humidity values strongly alter the radiosonde uncertainty. In total, the modeled confidence interval is in good agreement with the actual seasonal variation of the (gnss-rs) differences.

3.9 Correlation between GNSS heights and ZTDs

ZTDs and heights of a GNSS station are highly correlated. If the height and clock parameters are determined in a common parameter estimation, we can approximate the effect of an error in the



(a) day



(b) night

Figure 3.6: Components of the formal radiosonde ZTD uncertainty, (a) for daytime launches and, (b) for nighttime launches. For a description of the individual contributions, see Sect. 3.7.1. Note that temperature calibration has an insignificant influence.

troposphere model according to (Geiger, 1987):

$$\delta z = -\delta r(0) \frac{12}{(1 - \cos(\theta_{\max}))^2} \left(1 + \frac{1}{2} \left(\cot\left(\frac{\theta_{\max}}{2}\right) \right)^2 \ln(\cos(\theta_{\max})) \right) \quad (3.20)$$

$\delta r(0)$: error in ZTD parameter

δz : error in height

θ_{\max} : maximum zenith angle at which satellites are still visible

The use of a horizontal and flat model atmosphere in the derivations by Geiger (1987) does not allow to apply Eq. (3.20) below minimum elevations of $15^\circ - 20^\circ$. Despite not being quite compliant

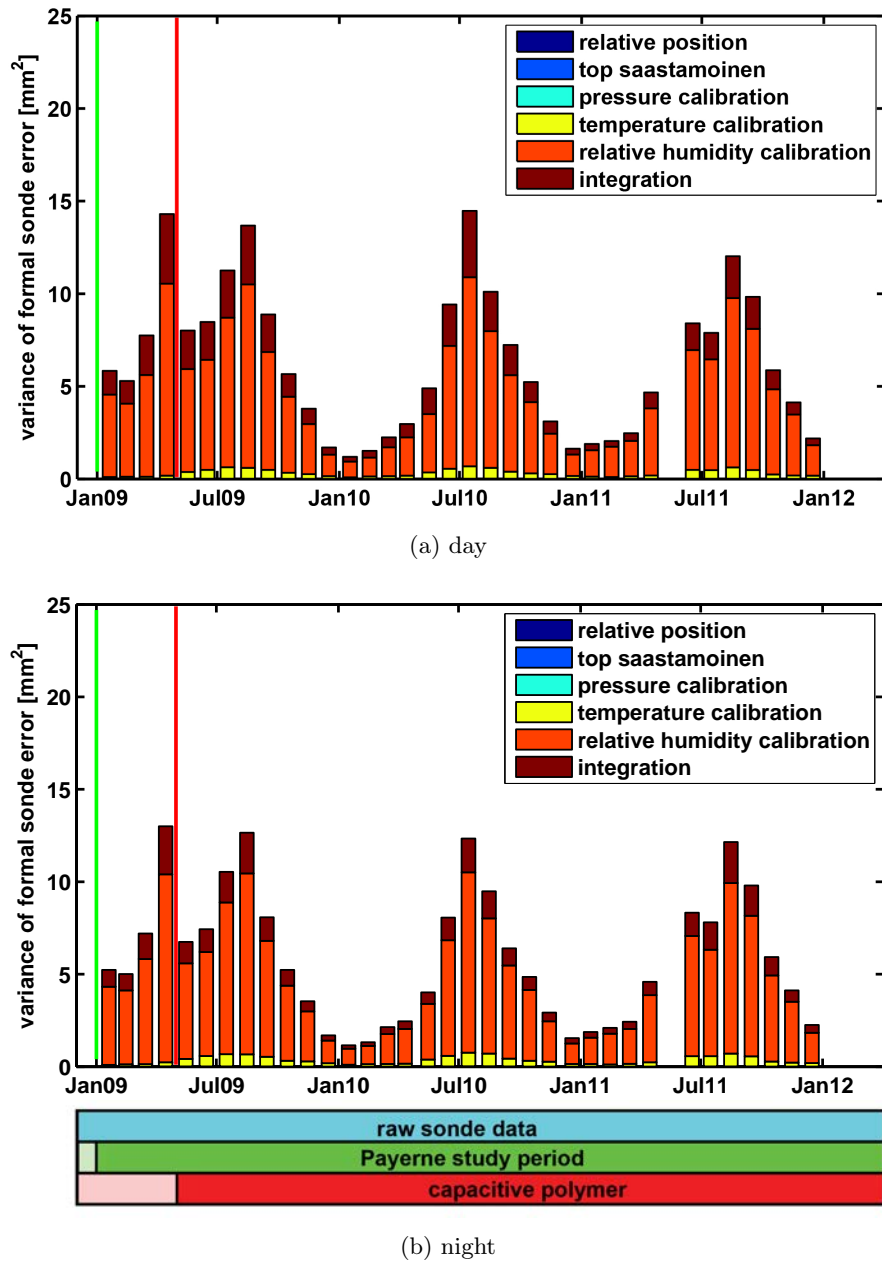


Figure 3.7: Components of the formal radiosonde ZWD uncertainty, (a) for daytime launches and, (b) for nighttime launches. For a description of the individual contributions, see Sect. 3.7.1. Unlike the ZTD uncertainty in Figs. 3.6a and b, the ZWD shows a negligible relative position component.

with our case, it provides us with an order of magnitude of the effect, which is

$$\delta z = 2.7 \cdot \delta r(0) \quad \text{with } \theta_{\max} = 70^\circ. \quad (3.21)$$

According to Eq. (3.21), an error in the ZTD model of +1 mm causes a positive and amplified error of +2.7 mm in the estimated height parameter. However, it is important to note that the shown relationship does not strictly apply to the here presented case, where the ZTD parameter is estimated together with all other parameters. In the scenario of estimating also tropospheric parameters, there is a negative correlation between ZTD and height (Rothacher, 2002). Figure 3.9 shows the daily height-coordinate time series of the GNSS station in Payerne. We observe a pronounced yearly period with maxima in winter. Table 3.10 presents the results of fitting a sine

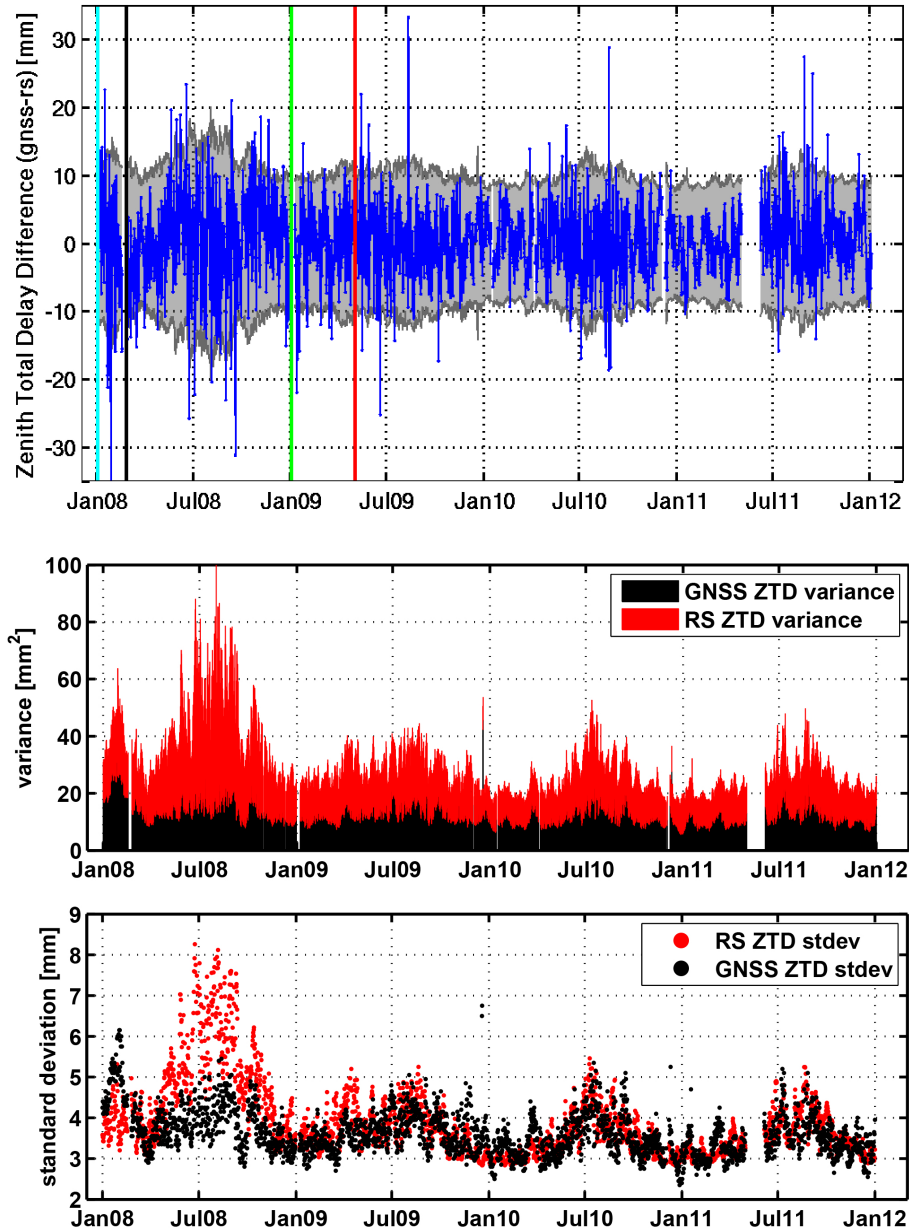


Figure 3.8: ZTD difference between GNSS and radiosonde is shown in the top figure in blue. Grey shading marks the 95 % confidence interval of the difference. The two bottom figures display separate contributions from the GNSS and radiosonde (RS) uncertainties to the uncertainty of the difference (gnss-rs), either as variances or as standard deviations. The black bars in the variance plot show the GNSS-only contribution. On top of the GNSS-only contribution, the radiosonde-only contribution is added as red bars. The tips of the red bars mark the cumulative variance.

with a 365-day period to the coordinate time series. Strikingly, the amplitude of +3.1 mm in the seasonal height fluctuation (Tab. 3.9) complies with the seasonal troposphere fluctuations of 1.0–1.5 mm from Tab. 3.4 and with the rule of thumb of Eq. (3.21). The phase of 68.8 days of Tab. 3.4 is close to the average of the day and night phases of the (gnss-rs) difference (average phase of day and night: 71.6 days \pm 7.5 days). This contradicts the known negative correlation between ZTD and height. According to the negative height to ZTD correlation, we would expect maxima

in summer in the seasonal fluctuations of the (gnss-rs) differences. This rises the question, if the height fluctuations in Payerne represent true height changes. The following physical processes might cause an actual yearly height change:

1. Dilatation of the building and the mounting pole during summer due to higher temperature. Differential yearly height fluctuations of the order of a millimeter are possible as demonstrated by Gschwend (2012) for the ETHZ and ETH2 AGNES double stations. Daily fluctuations due to a temperature range of 21–30 degree Celsius and measured with terrestrial methods caused a 1.6 mm absolute height change of a 9m steel mast in Zimmerwald (Brockmann et al., 2012).
2. Hydrological effects due to surface infiltration of rain water or river infiltration into a ground water aquifer.
3. Unmodeled atmospheric loading effects

The three effects are very unlikely to cause height maxima in the driest and coldest season of Switzerland. The GNSS processing of sidereal day repeating biases, such as multipath and antenna phase center variations, with 24-hour batches are thus thought to have caused the observed height changes. Hence, some of these biases also enter the troposphere, but with reversed polarity. It is therefore hypothesized that the humidity sensor change of the radiosonde created not only a phase shift in its bias, but its amplitude is larger by 1–2 mm than what is visible in the (gnss-rs) differences of Fig. 3.2a.

A comparison of the height minima in summer in Fig. 3.9 reveals that the minimum in summer 2011 is lowered by roughly 4 mm with respect to summer 2009 and summer 2010. The associated positive offset in ZTD would be 1–2 mm. The magnitude of the changes in Apr 2011 are supported by Schaer and Meindl (2011). Thus, the offset between the two processing strategies presented in Sect. 3.4 of 10.5–10.7 mm (Figs. 3.4a and b) are likely attributed to the GNSS processing changes in Feb 2008 and not to the ones in Apr 2011 (Tab. 3.1). It would be consistent with the notion that the change from relative (I01.ATX) to absolute (C05.ATX) antenna corrections is more influential than the change from absolute (C05.ATX) to another absolute (I08.ATX) correction.

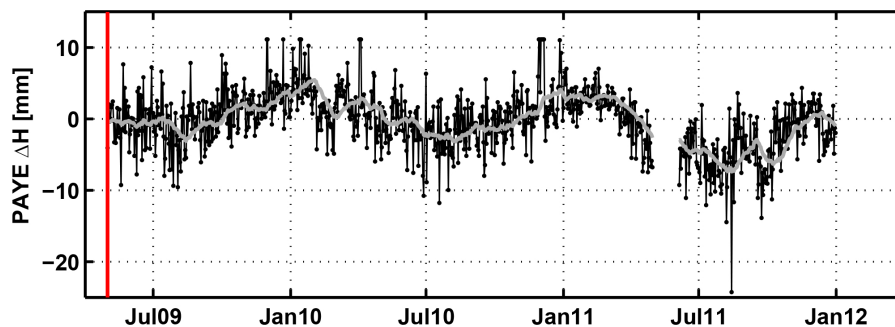


Figure 3.9: Daily coordinate heights at Payerne minus mean height (548.7m ell. height, WGS84). The red vertical line denotes the date when the new humidity sensor was emplanced in the radiosonde.

Table 3.10: Parameters from fitting a mean value and a sine of 365-day period to the daily coordinate heights in Fig. 3.9.

Parameter	Unit	Value	SD
mean	m	548.6898	0.0001
amplitude	mm	3.1	0.2
phase	days	68.8	3.1
corr	-	-0.0266	
$\sigma_{\text{a posteriori}}$	mm	3.6	

3.10 Discussion

The presented study quantifies uncertainty contributions to GNSS- and radiosonde-determined ZTDs. A number of influences affecting the ZTD accuracy are assigned to either GNSS or radiosonde:

- The (gnss-rs) differences reveal a mean offset between GNSS and radiosonde. The offset is shown to strongly depend on the way the GNSS data are processed. Specifically, exchanging the antenna phase center patterns causes offsets of several millimeters in the ZTD. A major part of the offset can be corrected for with accurate and individual antenna calibrations in dedicated chambers (Sect. 3.4). Near-field effects and multipath however will always depend on the surrounding of the antenna and can be regarded as site-dependent antenna patterns.
- Philipona et al. (2009) investigated the new humidity sensor and discovered low sensitivity of the sensor below temperatures of -35°C and below mixing ratios of $0.5\text{ g}/(\text{kg of dry air})$. In Payerne, those values are typically reached around 8 km above ground. From two pre-operational flights in March and two flights in April 2009 with the SRS400, the low sensitivity results in an average dry bias of 2–3 % relative Precipitable Water (PW), corresponding to 0.2–0.3 mm PW or equivalently, $\approx 1.4\text{--}2.1\text{ mm ZWD}$. During the LUAMI campaign with 14 sondes in November 2008 and with the SRS-C34 system using a different temperature sensor setup (Philipona et al., 2009), a wet bias of 2–3 % relative PW is observed. Hence, the sign of the bias might depend on the temperature sensor setup or the humidity profile structure, but the magnitude is likely to reach 1–2 mm.
- Since most of the water vapor resides in the lowermost 5 km of the atmosphere, the top Saastamoinen formula adds a quasi-zero contribution to the radiosonde ZWD. Hence, there is no uncertainty contribution to be expected from the top Saastamoinen term. The GNSS ZWDs are strongly affected by the dry Saastamoinen formula. The ZTD to ZWD reduction causes an increase in the (gnss-rs) offset by $\approx 3\text{ mm}$. Thus, the offset must be caused by the dry Saastamoinen model. This is in accordance with Perler (2011) (p. 79). He obtained a positive bias of 2.6 mm for dry Saastamoinen minus integrated dry refractivity from radiosondes.
- The sine-filter with 365-day period shows a large decrease in amplitude and a strong phase shift by roughly half a year after the new humidity sensor is emplaced. On the basis of the negative correlation between the GNSS height and the ZTD, the remaining 1.0–1.5 mm yearly sine amplitude can be ruled out to be the result of some systematic effect in the GNSS ZTDs. This suggests that the new humidity sensor still causes systematic yearly fluctuations in ZTD, but with a reversed sign compared to the old humidity sensor.
- The old humidity sensor caused most diurnal variations in the mean and the seasonal amplitude of the ZTD data due to a strong and non-linear temperature dependence of its response function (Philipona et al., 2009). With the new humidity sensor, the day-night mean in (gnss-rs) still varies by 1.3 mm. Is this variation assigned to GNSS or to sonde problems? Possible candidates to explain the diurnal variation of the (gnss-rs) mean are:

1. Unmodeled ionospheric effects in the GNSS processing. The day-night difference in the mean and in the sine amplitude from the (gnss-rs) is shown to be marginally affected by unmodeled ionospheric terms. The ionospheric influence on the ZTD is roughly one order of magnitude lower than the actual variation in mean and amplitude.
2. Dilatation of the building and the mounting pole of the GNSS station. Day-night height differences of 1.6 mm of the steel mast in Zimmerwald (Brockmann et al., 2012) would cause a corresponding ZTD variation of roughly half a millimeter, not explaining the observed magnitude in Payerne. In addition, it is expected that the 9 m steel mast in Zimmerwald shows more vertical motion upon temperature variation than the building and the much shorter mounting pole of the Payerne station.
3. Different behaviour of the temperature sensor of the sonde due to presence or absence of solar radiation. Sect. 3.7 demonstrates that feasible systematic temperature offsets of the order of 0.1 K caused by solar radiation (Kräuchi, 2011) are unlikely to produce more than a few tenths of a millimeter diurnal variations in ZTD.
4. Diurnal errors of the sonde’s humidity sensor:
 - (a) Temperature and solar radiation dependent errors. For Vaisala RS92 humidity data, the radiation dry bias correction is quantified by Wang et al. (2013b). They mention that the twin HUMICAPS sensors have a design drawback to its predecessor RS80, lacking a radiation shield. The systematic influence on PW is thus large and reaches 1–2 mm, with a maximum in June and a minimum in December and hence, is also seasonally dependent. The HC2 of the SRS400 or the SRS-C34 of MeteoSwiss has a different design. Its response to solar radiation is unknown to the author.
 - (b) Time lag correction errors that are associated with typical day or night time atmospheric humidity structures. The humidity sensor is indeed capable of producing systematic offsets of the order of a few millimeters in ZTD due to the time lag correction error (Philipona et al., 2009). Temperatures below -35°C , where the sensor sensitivity deteriorates, might be earlier reached during night than during day. The same effect would also show up in winter, with a similar magnitude and the same positive or negative sign.

Hence, both influences (a) and (b) can cause day-night and summer-winter error signals of the order of 1–2 mm and with the maxima during day and summer or during night and winter. This is in contrast to our data, which shows a day-night amplitude of approximately 1.3 mm with maximum during the day and a summer-winter amplitude of roughly 1 mm with maximum in winter.

Despite the contradictory phase information between day-night and summer-winter, the diurnal variation is presumably caused by radiation or time lag errors of the sonde’s humidity sensor. This preliminary conclusion is reached on the basis of the magnitude of the observed (gnss-rs) discrepancies.

- The (gnss-rs) ZTD time series and the calculated formal radiosonde uncertainty demonstrate that the humidity sensor calibration has the strongest influence on the ZTD quality from the sonde. With the new humidity sensor, GNSS and the radiosonde now contribute similarly to the random uncertainty. Both methods exhibit more fluctuations during summer than winter, causing a strong annual signal in the spread of the (gnss-rs) differences. The GNSS ZTD uncertainty is derived to have a 2.5–3.5 mm and 3.5–5.0 mm standard deviation during winter and summer, respectively.

3.11 Conclusion

The analysis of the Payerne time series of GNSS- minus radiosonde-derived ZTDs during the years 2006–2012 yield a detailed picture of the systematic effects present in the data. After introduction of a new humidity sensor in the radiosonde in May 2009, seasonal fluctuations with maxima in winter instead of summer show up in the (gnss-rs) time series. There are strong indications that

the annual signal is still to a large part due to the radiosonde. On the basis of the magnitude of 1.3 mm, day-night systematic offsets are likely to be associated to some radiation dependent effects of the humidity sensor. Final conclusions are not reached due to contradictory phase characteristics of the diurnal and annual systematic signals. The overall mean offset of ≈ -3 mm between the GNSS and the radiosonde time series is impossible to assign to either measurement technique. Both techniques are prone to mean offsets of millimeter magnitude. Removal of the annual signal and the mean offset in the (gnss-rs) time series leaves us with the combined and more or less random measurement uncertainty of the methods. They have been assigned to either GNSS or radiosonde. The resulting standard deviations of GNSS ZTDs are shown to be generally lower than the assumed 5–7 mm of most studies.

On the sonde's side, the humidity sensor calibration should be improved. Additionally, systematic day-night effects of the radiosonde are expected to decrease, if humidity readings are corrected for solar radiation influences. On the GNSS side, unmodeled delays such as multipath, atmospheric loading, higher-order ionospheric terms etc. can create biases in all processing parameters. Due to mutual correlations, the unmodeled parts are partitioned into the station coordinates, the clock and the ZTDs. Since the correlation is inherent and cannot be avoided, further reduction of any possible modeling error is the only way to go. Eventually, if GNSS ZTDs are to be assimilated into NWP models, station-specific bias corrections are indispensable.

Chapter 4

Payerne profile study

Water vapour profiling of the atmosphere is still a hard challenge in meteorology. How well can GNSS meteorology with its integral measure contribute to the task? In Chap. 3, radiosonde-derived refractivities have been integrated to validate the GNSS ZTD. Here, the reverse is done: refractivity values are reconstructed from GNSS ZTDs and compared to radiosonde measurements of refractivity. How accurate are we expecting the refractivities to be? From the accuracy investigations in Chap. 3, it becomes clear that a simple differencing of two ZTDs with $\sigma_{\text{ZTD}} = 2.5\text{--}5\text{ mm}$ located at 200 m vertical distance from each other results at best in

$$\sigma_{N_{\text{tot}}} = \sqrt{2} \cdot \sigma_{\text{ZTD}} \cdot \frac{1000\text{ m}}{200\text{ m}} = 18\text{--}35\text{ ppm}$$

uncertainty for the average refractivity over this 200 m height interval. Note that in the lower troposphere, the 200 m layer width is a commonly used grid spacing of tomography approaches. The little thought experiment demonstrates the fundamental problem: Without further a priori information or accurate refractivity measurements, profiling with GNSS ZTDs will not result in much more than approximate exponential profiles of refractivity. The following study attempts at combining GNSS ZTDs with other data sets to investigate the benefit gained by the data combination. The study largely repeats the material published in Hurter and Maier (2013).

4.1 Abstract

We reconstruct atmospheric wet refractivity profiles for the western part of Switzerland with a least-squares collocation approach from data sets of (a) zenith path delays that are a byproduct of the GNSS processing, (b) ground meteorological measurements, (c) wet refractivity profiles from radio occultations whose tangent points lie within the study area, and (d) radiosonde measurements. Wet refractivity is a parameter partly describing the propagation of electromagnetic waves and depends on the atmospheric parameters temperature and water vapour pressure. In addition, we have got measurements of a lower V-band microwave radiometer at Payerne. It delivers temperature profiles at high temporal resolution, especially in the range from ground to 3000 m above ground level, though vertical information content decreases with height. The temperature profiles together with the collocated wet refractivity profiles provide nearly continuous dew point temperature or relative humidity profiles at Payerne for the study period from 2009 to 2011.

In the validation of the humidity profiles, we adopt a two-step procedure. We first investigate the reconstruction quality of the wet refractivity profiles at the location of Payerne by comparing them to wet refractivity profiles computed from radiosonde profiles available for that location. We also assess the individual contributions of the data sets to the reconstruction quality and demonstrate a clear benefit from the data combination. Secondly, the accuracy of the conversion from wet refractivity to dew point temperature and relative humidity profiles with the radiometer temperature profiles is examined, comparing them also to radiosonde profiles.

For the least-squares collocation solution combining GNSS and ground meteorological measurements, we achieve the following uncertainty figures with respect to the radiosonde reference: the

maximum median of the relative difference in refractivity is -16% and quartiles are 5% to 40% for the lower troposphere. We further added 189 radio occultations that met our requirements. They mostly improved the accuracy in the upper troposphere. The maximum median of the relative difference has decreased from 120% to 44% at 8 km height. Compared to radiosonde dew point values, the uncertainty figures of the collocation-derived dew point temperature profiles are: absolute dew point temperature differences to the radiosonde in the lower troposphere have a maximum median of -2 K and maximum quartiles of 4.5 K . For relative humidity, we get a maximum mean difference of 7.3% , with standard deviations of $12\text{--}20\%$.

We demonstrate in this study that least-squares collocation is capable of combining humidity related data sets such that resulting humidity profiles gain from complementary strengths of the various measurement methods. Since the data sets are operational and available in near real-time, we envisage collocation to be a possible tool for nowcasting of clouds and rain and to understand processes in the boundary layer and at its top.

4.2 Introduction

Up to this date, several techniques have been developed to remotely monitor the atmospheric water vapour, being a key variable in numerical weather prediction models. Among these are e.g., microwave radiometer, differential absorption lidar, raman lidar, solar spectrometer and radio occultation measurements. Furthermore, GNSS (Global Navigation Satellite System) receivers are able to deliver an integral measure of water vapour content at temporal resolution of at least 30 minutes (Bender et al., 2011). This measure is defined by the delay of the electromagnetic wave that travels from the satellite through the atmosphere to the GNSS receiver. It includes the total influence of the atmosphere along its path, also that of the water vapour. With sophisticated software packages, the delay can be retrieved at each GNSS station. To obtain a profile of atmospheric water vapour from the delays, a GNSS receiver network, ground meteorological stations and profiles of atmospheric air temperature are needed. There are many studies that have used a tomographic approach to reconstruct humidity fields from GNSS delays. They either process path delays from stations of permanent GNSS networks (Perler et al., 2011), or from campaign setups, as in the ESCOMPTE experiment in France (Champollion et al., 2005; Nilsson et al., 2007a; Bastin et al., 2007). Further works that exploit the tomographic approach are Nilsson and Gradinarsky (2006), Bender et al. (2009, 2011), Rohm and Bosy (2011), Bosy et al. (2012), Manning et al. (2012) and Rohm (2013).

In this study, the GNSS zenith delays from permanent GNSS stations are taken as the basis to monitor the atmospheric water vapour above Payerne, Switzerland, the MeteoSwiss launch site of operational radiosondes. We motivate our choice for GNSS path delays as primary data set with its good time resolution, its all-weather capability, the stable and high data availability, low maintenance and the fact that financing can be shared with other applications (e.g., GNSS reference networks for positioning). The integral measures of several GNSS receivers are interpolated to profiles of so-called wet refractivity (N_{wet}), which depends on both atmospheric temperature and water vapour pressure. For the interpolation, an algorithm termed least-squares collocation is employed. It incorporates a deterministic trend function and fits this function together with statistical parameters to the data that can be of many different types. Herein, we make use of the integral measures from GNSS and of point measurements from ground meteorological stations, radio occultations and from radiosondes. Temperature profiles from a lower V-band ($51\text{--}58\text{ GHz}$) microwave radiometer (Löhnert and Maier, 2012) in Payerne allow the conversion of wet refractivity profiles into vertical profiles of dew point temperature and relative humidity at the radiometer location.

In Sect. 4.3, we describe the data sets used in this study. Section 4.4 explains how the data is processed and interpolated with collocation to arrive at wet refractivity and at humidity profiles. We then demonstrate in Sect. 4.5 the performance of the collocation algorithm with 3 yr of data that is validated against the radiosonde, whose launch site is in Payerne. We also show the beneficial effect of the data combination. Eventually, Sect. 4.6 sets the findings into the context of other humidity reconstruction and measurement techniques and of numerical weather prediction.

Table 4.1: Overview of data sets used in this study (mwr = microwave radiometer, ro = radio occultation).

Sensor name	Start of data set [UTC]	End of data set [UTC]	Time resolution	Number of stations	Data provider
radiosonde	1 Jan 2009 00:00:00	31 Dec 2011 00:00:00	2 profiles/day at 00:00:00 and 12:00:00 UTC	1	MeteoSwiss
GNSS	28 Dec 2008 00:00:00	31 Dec 2011 00:00:00	1 h	18	Swisstopo
ground meteo	1 Jan 2009 00:00:00	31 Dec 2011 00:00:00	10 min	20	MeteoSwiss
mwr	1 Jan 2009 00:00:00	31 Dec 2011 23:53:20	6 to 7 min	1	MeteoSwiss
ro	1 Jan 2009	21 Dec 2011	189 profiles	–	CDAAC

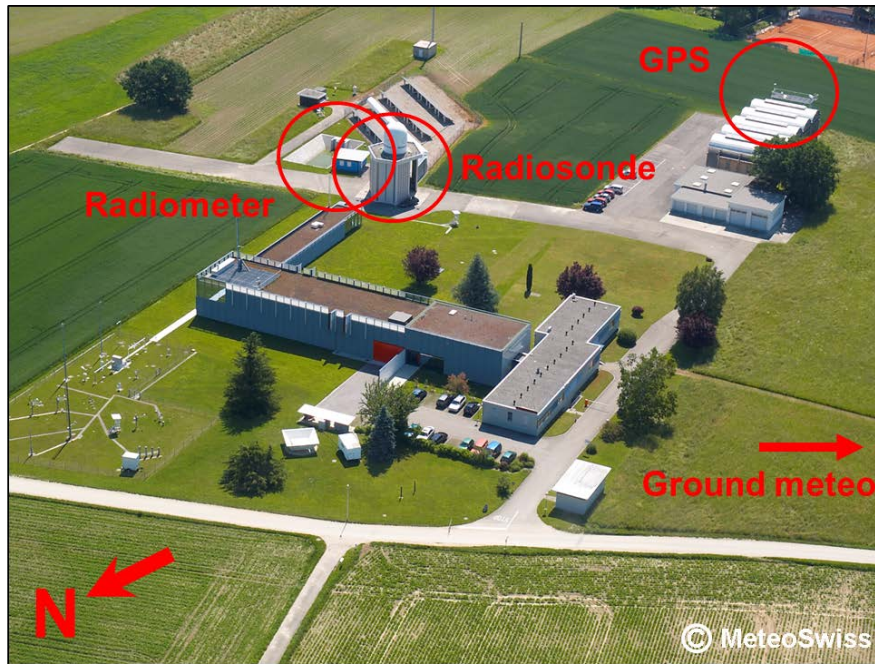


Figure 4.1: Overview of the operational MeteoSwiss radiosonde site in Payerne.

4.3 Description of data sets

This study makes use of data measured at the MeteoSwiss Regional Center of Payerne and locations within approximately 100 km distance and from January 2009 to December 2011 (Tab. 4.1). See Fig. 4.1 for an overview of the Payerne site. The GNSS data, being the main source of information for the spatial distribution of humidity in our study, and further data sets such as ground meteorological data, radio-soundings, radio occultations and vertical temperature profiles from the ground-based microwave radiometer are detailed in the following.

4.3.1 GNSS zenith path delays

GNSS satellites transmit electromagnetic waves in the L-band, which travel from the satellite's orbit position to the receiver on the earth's ground. On its way across the atmosphere, the waves get bent and slowed down, causing a delay in the arrival at the receiver. The parameter called refractivity in Eq. (2.1) describes the propagation of radio waves and can be well determined for the neutral part of the atmosphere from basic thermodynamic parameters at any point in space and time where measurements of these parameters are available. Refractivities are in units of ppm or mm km^{-1} , which expresses the delay caused by the neutral atmosphere per kilometer of propagation path. The integral of the refractivity N_{tot} along the propagation path s from satellite

q to receiver r yields the total propagation delay Δ^{PD} .

$$\Delta^{\text{PD}} = 10^{-6} \int_q^r N_{\text{tot}} ds \quad (4.1)$$

There is such a delay for each satellite-receiver pair. If they were to be estimated individually by a GNSS processing software, the number of unknown parameters would be too large and their correlation to other parameters too strong to be properly handled. Mapping functions are introduced that project all delays for a station onto a common zenith direction. The mapped delays are then averaged producing one atmospheric parameter at a time, the so-called total zenith path delay (ZTD). Traditionally, the total zenith path delay is split into a slowly varying dry (ZDD) and a more variable wet (ZWD) part, corresponding to the integrals of N_{dry} and N_{wet} , respectively. The path integral of the refractivities in zenith direction then becomes the total zenith delay:

$$\begin{aligned} \text{ZTD} &= \text{ZDD} + \text{ZWD} \\ &\approx 10^{-6} \int_{\text{zenith direction}} (N_{\text{dry,average}} + N_{\text{wet,average}}) ds \end{aligned} \quad (4.2)$$

where $N_{\text{dry,average}}$ and $N_{\text{wet,average}}$ represent horizontal averages in a cone around the receiving antenna and temporal averages over the epochs used in the GNSS processing. Apart from 31 Apr 2011 00:00:00 UTC to 4 June 2011 23:50:00 UTC where some problems in storing the data occurred (E. Brockmann, personal communication, 2012), 3 yr of hourly ZTDs were provided by Swisstopo, the Swiss Federal Office of Topography (Tab. 4.1). Figure 4.2a shows the considered GNSS receivers, which belong to the Automated GNSS Network for Switzerland (AGNES). They are distributed over an area of 125 km \times 125 km around Payerne and have an average inter-station distance of 30 km. All stations recorded data from the GPS and the Russian Global Navigation Satellite System (GLONASS). The processing carried out by Swisstopo is described in Sect. 3.1.2. A modified version of Bernese GNSS Software Version 5.0 (Dach et al., 2007) is used. The modifications enable ambiguity resolution for both recorded navigation systems GPS and GLONASS. Mapping functions applied are dry Niell for the a priori part of the troposphere and wet Niell for the estimated part. Together, they form the total zenith path delays that are determined by the software once per hour. In between, the temporal change of the troposphere is modeled with a piecewise linear function. The final orbits from CODE have been used in the processing.

4.3.2 Meteorological ground stations

From the permanent and automatic ground meteorological measurement network called SwissMet-Net of the Swiss Federal Office of Meteorology and Climatology (MeteoSwiss), 14 to 19 stations within the perimeter of study were concurrently measuring pressure, temperature and relative humidity during the 3 yr of our investigation period (Tab. 4.1). Figure 4.2b displays the considered ground meteo stations and Fig. 4.3 the height distribution of these stations, together with the GNSS stations. Uncertainties given in Tab. 4.2 are from general working experience with these sensors and correspond to their achievable measurement uncertainties that have been listed in the CIMO Guide, 2008.

4.3.3 Radiosonde profiles in Payerne

The radiosonde data comprises profiles from 3 yr of continuous radiosonde operation (Tab. 4.1) at the MeteoSwiss Regional Center of Payerne, Switzerland. Most days contain 2 launches that reach the tropopause at 00:00:00 UTC and 12:00:00 UTC, roughly 1 h after launch. Exceptional days include a third sounding at 18:00:00 UTC. The parameters that are important for this study and are contained in the original data are shown in Tab. 4.2. Also shown in Tab. 4.2 are respective sensor uncertainties as given by Löhnert and Maier (2012). They comply with the working experience at MeteoSwiss and with the experience gained from intercomparison with other radiosonde systems (Nash et al., 2011).

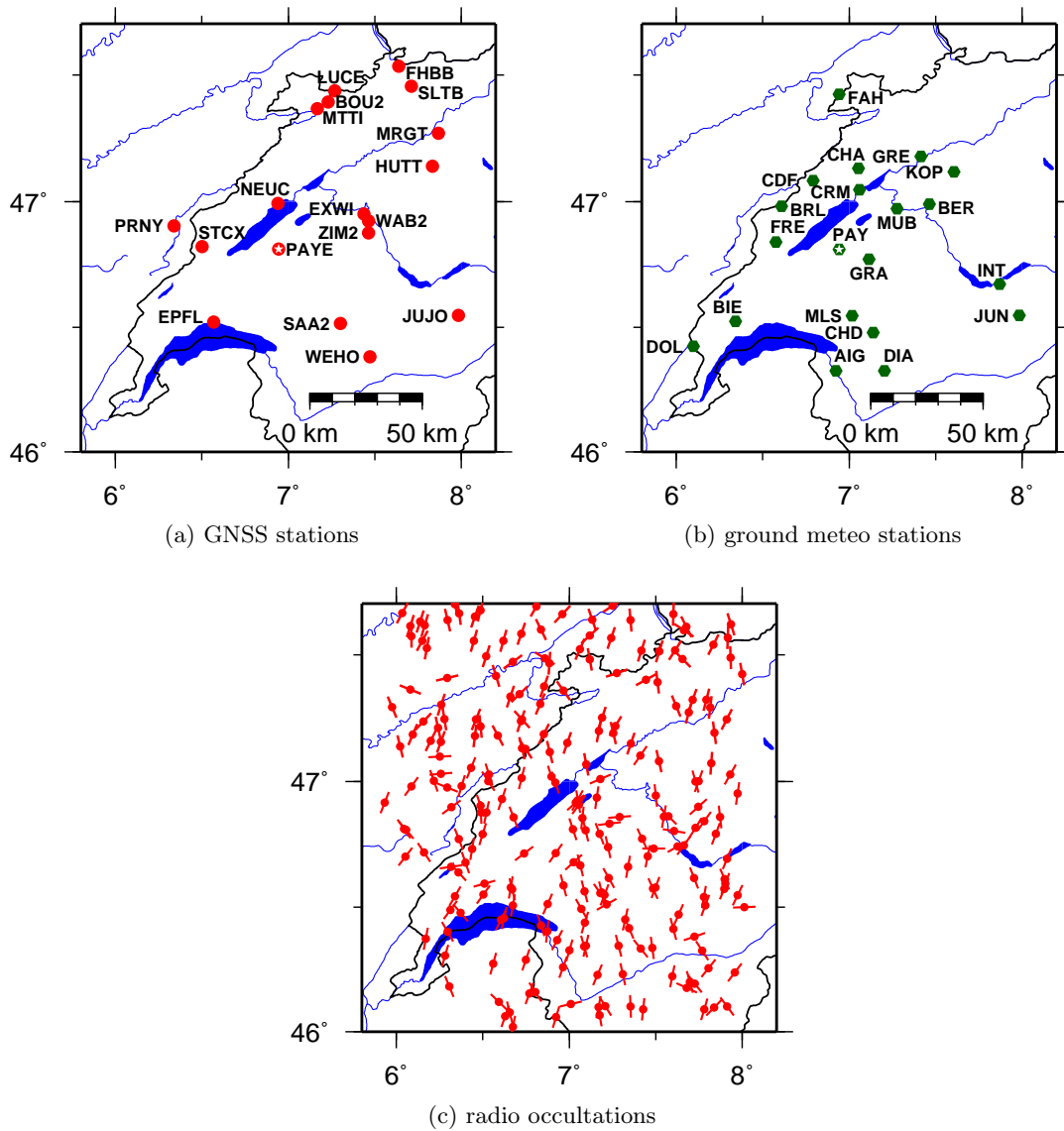


Figure 4.2: (a) GNSS stations whose zenith path delays contribute to this study. They are all stations from the AGNES deployed by the Swiss Federal Office of Topography. White star in Payerne denotes the place of the profile comparison. (b) SwissMetNet (SMN) stations of MeteoSwiss used in this study. (c) radio occultations taking place during the 3 yr of the study. Dots show approximate tangent point positions, when the tangent trajectory is at around 3–5 km amsl. Little lines protruding from the dots mark the direction of the occultations.

4.3.4 Radio occultations

From the COSMIC Data Analysis and Archive Center (CDAAC, Version 4.0), post-processed data products of radio occultations (ro in Tabs. 4.1 and 4.2) taking place during 2009–2011 and restricted to the investigation area were downloaded (Fig. 4.2c). They consist mostly of data from the COSMIC mission, but also occultations from the GRACE, the MetOp-A, the SAC-C and the TerraSar-X missions are included. Processing flow of these data is outlined in Ho et al. (2009) and Kuo et al. (2004). From the data product *wetPrf*, containing water vapour pressure and temperature profile data from a variational analysis of total refractivity (described in VARS Documentation), profiles of wet refractivity (Eq. 2.3) were calculated up to a maximum height of 11 km. For uncertainty measures, the uncertainties from the product *atmPrf* were taken. Approximate

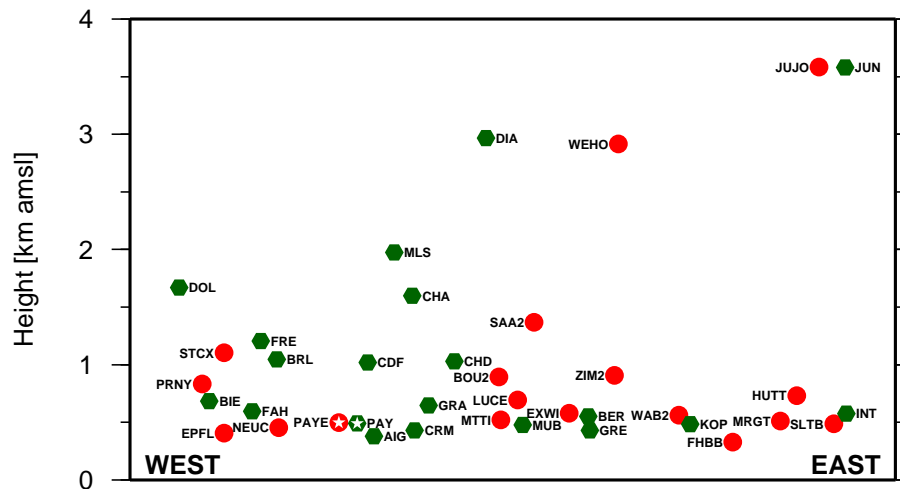


Figure 4.3: Height distribution of the GNSS (red dots) and ground meteorological stations (green hexagons) shown in Figs. 4.2a and b, projected onto a West-East plane. Their longitudinal positions were shifted to improve label readability.

values are given in Tab. 4.2. For the middle to upper troposphere they are consistent with the values given in Kuo et al. (2004) of roughly 0.3–0.5 % or in Scherllin-Pirscher et al. (2011) of roughly 0.5 % relative total refractivity uncertainty. For the lower troposphere, these authors give tentative relative uncertainties of $\approx 5\%$, which do not match the values in *atmPrf*, the latter values being most likely too optimistic. For the region in the lower troposphere, where the formal uncertainties failed to be calculated, a default value of 1 ppm was adopted and needs further refinement in the future. However, all these uncertainties refer to total refractivity, being the sum of dry and wet refractivity according to Eq. (2.1) and hence, are only approximate measures of wet refractivity uncertainty. They are considered to be conservative for at least the middle and the upper troposphere, where the variational analysis is successfully extracting temperature and dry pressure (Scherllin-Pirscher et al., 2011), but probably too optimistic for the lower troposphere. Positions of the occultation profiles have been taken along the longitude and latitude of the tangent points from the operational processing, being a good approximation of the true tangent point trajectories from ray-tracing (Foelsche et al., 2011).

4.3.5 Ground-based microwave radiometer for temperature profiling

Profiles of temperature at Payerne from ground-based microwave radiometry (mwr in Tab. 4.1) have been provided by the CN-MET (Centrale Nucléaire et Météorologie) network of MeteoSwiss. A longer period of maintenance from 8 May 2009 07:10:00 UTC to 17 Sep 2009 12:50:00 UTC (Löhnert and Maier, 2012) and some smaller periods of missing data are the only data gaps in an otherwise complete 3 yr data set. The deployed device is the microwave profiler system HATPRO (Humidity And Temperature PROfiler) whose original data output are brightness temperatures in the V-band with seven channels ranging from 51 to 58 GHz. A detailed description of the system can be found in Löhnert and Maier (2012). All-weather data is used, including precipitation events. Unlike Löhnert and Maier (2012), the bias was removed simply by retrieving a mean temperature difference to radiosonde at each height level for the years 2009–2011 and applying this difference to individual radiometer profiles.

4.4 Processing

The flowchart in Fig. 4.4 gives an overview of the processing steps taken to obtain wet refractivity, dew point temperature and relative humidity profiles at Payerne. Rectangles with corresponding numbers denote processing steps explained in the following.

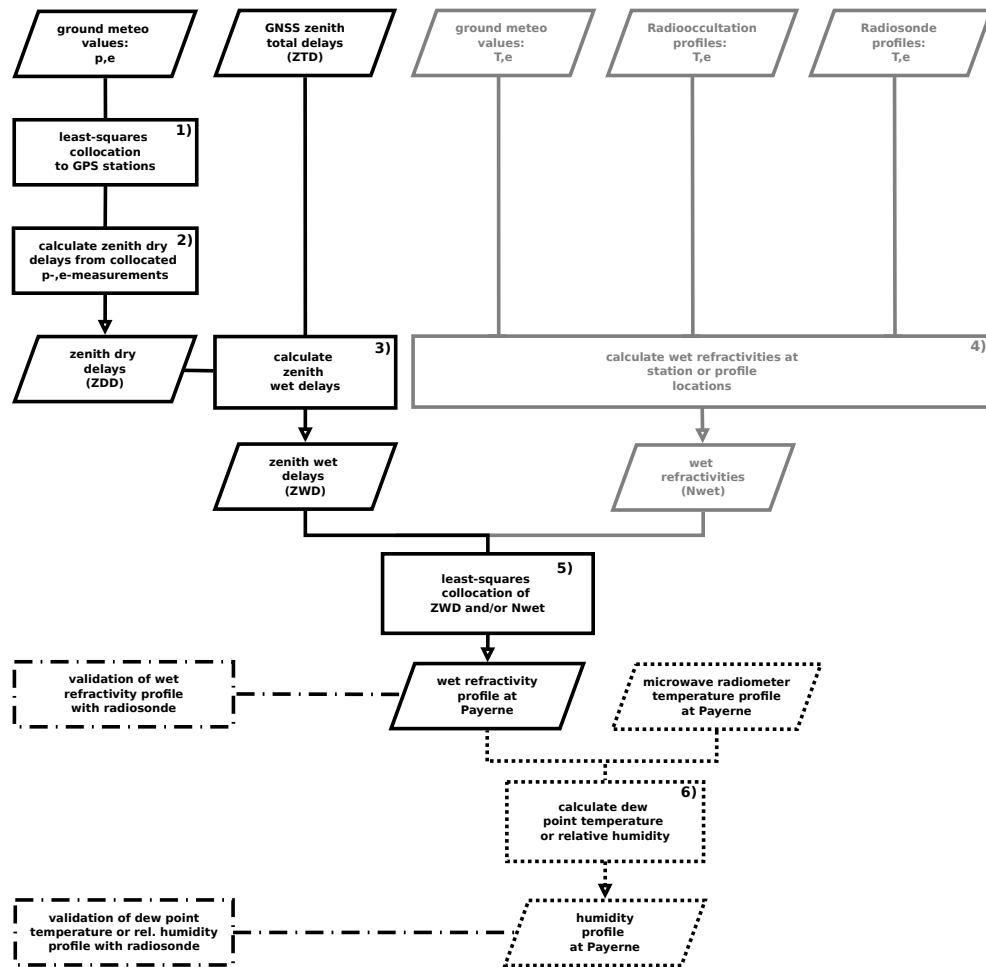


Figure 4.4: Flowchart of the steps carried out to get refractivity or dew point temperature profiles at Payerne. Rectangles stand for processing steps and parallelograms denote data and results from the processing. The numbers in the chart refer to the processing steps explained in Sect. 4.4. The solid lines show the processing that leads to the refractivity profiles. The second part of the study, where humidity profiles in Payerne are produced, is shown with dashed lines.

Table 4.2: Parameters contained in the original data sets and associated sensor uncertainties (^aLöhnert and Maier, 2012, ^bCIMO Guide, 2008, ^cLöhnert and Maier, 2012).

Sensor name	Parameter	Uncertainty	Note
radiosonde ^a	temperature	± 0.2 K	copper-constantan thermocouples
	pressure	± 0.2 % of value $\cong \pm 2$ hPa	water hypsometer
	humidity	± 10 to 20 %	carbon hygristor until April 2009
		± 5 to 10 %	capacitive polymer starting May 2009
gps	total zenith path delay	1.6 mm	average formal uncertainty from GNSS processing of L1/L2 double-frequency geodetic GNSS receivers
ground meteo ^b	temperature	± 0.2 K	achievable measurement uncertainty
	pressure	± 0.15 hPa	achievable measurement uncertainty
	relative humidity	± 3 %	achievable measurement uncertainty
microwave ^c radiometer	temperature	± 0.5 K lower boundary layer ± 1.7 K at 4 km height	standard deviations from comparison with radiosondes
radio occultation	total refractivity	$\approx \pm 1$ ppm at 1.0 km height ± 2 ppm at 4 km height ± 0.03 ppm at 8 km height	average formal uncertainties from operational level2 product

1. We obtain total air pressure and water vapour pressure estimates at the GNSS stations from 20 ground meteorological stations with the individual collocation of the two parameters. We use the methodology and parameter settings outlined in Tab. 4.3 and Hirter (1998). Deterministic functions are given in Eq. (2.16) for pressure and Eq. (2.17) for water vapour pressure.
2. From the collocated air pressure and water vapour pressure values, zenith dry delays (ZDD) are calculated at the locations of the GNSS stations (Lutz, 2009):

$$\text{ZDD} = 0.002277 \cdot (p_1 - 0.155471 \cdot e_1) \quad (4.3)$$

where p_1 is the total air pressure [hPa] and e_1 the partial water vapour pressure [hPa] at the station, yielding ZDD in units of meters. Note that the water vapour pressure, whose collocation is inherently problematic due to its strong spatial and temporal variations, has only a minor influence on the ZDD. This is why we can model the ZDD to millimeter accuracy from collocated ground meteo stations, as was demonstrated in Perler (2011). In a comparison between ZDD calculated from ground meteo (Eq. 4.3) and from radiosonde integration at Payerne, Perler (2011) obtains 1.6 mm standard deviation and a mean offset of 2.6 mm (ground meteo minus radiosonde).

3. The zenith total delays (ZTD) from the GNSS processing are reduced to the zenith wet delays (ZWD) by subtracting easy-to-model dry zenith delays (ZDD) using the results from the previous processing step:

$$\text{ZWD} = \text{ZTD} - \text{ZDD} \quad (4.4)$$

Table 4.3: List of stochastic parameters applied in the least-squares collocation. For the covariance function of the signal part s , see Eq. (2.19).

Observation	σ_{signal}	σ_{noise}	Δx_0	Δy_0	Δz_0	Δt_0	z_0
pressure	6 hPa	0.5 hPa	200 km	150 km	0.50 km	3.8 h	4 km
water vapor pressure	2 hPa	0.5 hPa	75 km	50 km	0.15 km	1.7 h	4 km
ZWD	1.2–5 mm	2 mm	35 km	35 km	1 km	4 h	4 km

The uncertainty of the ZWD is very difficult to assess. It must be above the formal uncertainty given in Tab. 4.2 for the ZTD plus some uncertainty contribution added from the ZDD (see Eq. 4.4). We adopt a rather optimistic and tentative value of 2 mm (Tab. 4.3).

- Wet refractivities are determined with Eq. (2.3) from several sources: ground meteorological data, radio occultations and radiosonde profiles. For ground meteo and radiosonde, uncertainties are calculated from uncertainty propagation of the values in Tab. 4.2, assuming no correlation between temperature and humidity readings. For radio occultations, see Sect. 4.3.4.
- Different combinations of the ZWD and the N_{wet} data sets have been input into a collocation using the methodology of Sect. 2.2.2. The settings for the covariance matrix of the stochastic parameter s are listed in Tab. 4.3. Correlation lengths were set according to a rule of thumb that was derived from tests on synthetic data (Sect. 2.2.9). Stable results were obtained, if correlation lengths were at least 4 times the average sampling in either space or time. Due to the large amount of data, collocations were carried out in batches of 8 h data with 1 h overlap to the next batch to ensure smooth continuation between the batches. Interpolated wet refractivities N_{wet} are output at the heights in Payerne, where also microwave radiometer derived air temperatures are given.
- N_{wet} links the GNSS data to meteorology. From the N_{wet} and the radiometer temperature profiles, both at Payerne, we obtain profiles of water vapour pressure e [hPa] rearranging Eq. (2.3). Dew point temperature T_{dew} [K] is then calculated following (Jacobson, 2005):

$$T_{\text{dew}} = \frac{4880.357 - 29.66 \ln e}{19.48 - \ln e}. \quad (4.5)$$

For reasons of simple comparability with humidity profiles from other techniques, the profiles are also calculated in units of percent relative humidity according to

$$f = \frac{e}{e_{\text{sat}}} \cdot 100[\%] \quad (4.6)$$

with

$$e_{\text{sat}} = 6.112 \cdot \exp\left(\frac{17.67 \cdot (T - 273.15)}{(T - 273.15) + 243.5}\right)$$

where temperature T is given in Kelvin and water vapour pressure e and saturation vapour pressure e_{sat} (Bolton, 1980) are both in units of hPa.

4.5 Results

The results from the least-squares collocation algorithm are compared to radiosonde profiles in Payerne at two stages of the processing (see flowchart in Fig. 4.4). Firstly, we only investigate the profile quality of the wet refractivity profiles, which are the result of processing step 5 in Sect. 4.4. Secondly, profiles of humidity from processing step 6 in Sect. 4.4 are validated with radiosonde

profiles of dew point temperature and relative humidity. Corresponding radiosonde profiles have been calculated using Eqs. (2.3), (4.5), and (4.6). Profiles that result from the COMEDIE processing are short-named “model” to simplify description of the results. The radiosonde profiles are shortnamed “rs”. Since COMEDIE can output a profile at any time and we are mostly interested in the fast varying part of the lower troposphere, the comparison takes place shortly after launch time of the radiosondes, that is, one hour before 00:00 UTC and 12:00 UTC.

4.5.1 Wet refractivity profiles

Fig. 4.5 displays the time series of the difference between model and rs, where we combine the two data sets (GNSS and ground meteo) in a common collocation. A clear seasonal trend is observed with strongly positive values at heights around 2 km during the months June–October. This coincides with large negative values above and below. The clear seasonal pattern suggests that a more elaborate deterministic model would improve the collocation results. The subfigure to the right gives the RMS difference for all 3 yr and is a measure of interpolation quality. The RMS varies between 2 and 7 ppm below the maximum at 2 km and 4–7 ppm above it.

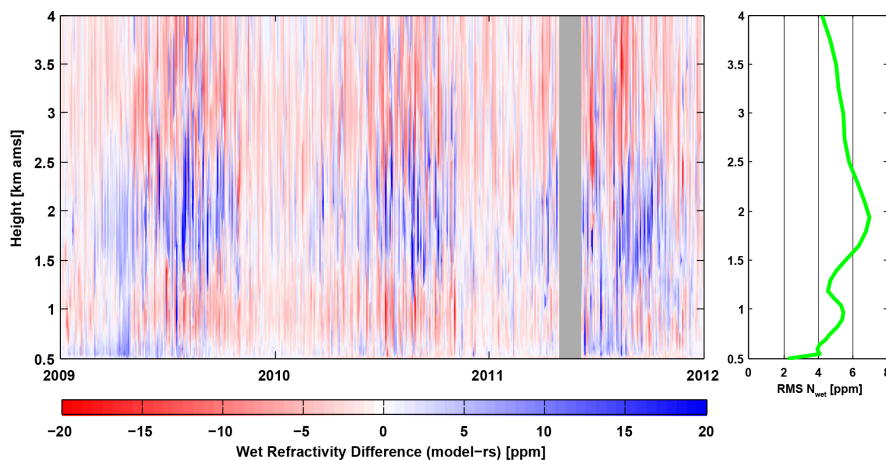


Figure 4.5: Time series showing the difference between the COMEDIE-derived wet refractivities from the GNSS plus ground meteo solution and the radiosonde (grey box: GNSS data gap). The RMS difference for all 3 yr is plotted at the side of the time series.

Figures 4.6a and b show two characteristic October profiles, comparing the COMEDIE solutions with the radiosonde. They are plotted with formal uncertainty bands and for 3 different input data sets. Input data sets include (i) ZWDs only, (ii) ZWDs and N_{wet} from ground meteo and, (iii) ZWDs combined with N_{wet} from ground meteo and from radiosonde derived wet refractivities. Uncertainty bands for the model solutions are calculated a posteriori during the least-squares estimation. We note strong smoothing of the model profiles and underestimation of the actual uncertainty by the interpolation algorithm. The underestimation of the uncertainty is probably due to an inappropriate choice of the correlation lengths in Eq. (2.19). The problem of the choice of the correlation lengths has been discussed in Sects. 2.2.8 and 2.2.9. In case of too few data to determine accurate stochastic parameters from empirical autocorrelation functions, we better reside to large correlation lengths. Hence, the correlation lengths are to some extent a function of the network density. The coarser the network, the larger they have to be chosen to avoid the danger of selecting them too short.

The smoothing is partly responsible for the limited capability to reproduce strong vertical changes in the atmosphere that are frequent during summer and early autumn months. Some deviations of the model from the radiosonde at around 2 km height result from ground meteo values of stations situated around this height. The corresponding stations do not represent the situation above Payerne. We observe this in the comparison between the ZWD only and the ZWD plus N_{wet} solution (e.g., Fig. 4.6b), the latter solution showing a slightly degrading effect from the

inclusion of ground meteo stations. Responsible are the stations DOL, MLS and CHA (Fig. 4.3), which generally show too high values with respect to corresponding heights in Payerne.

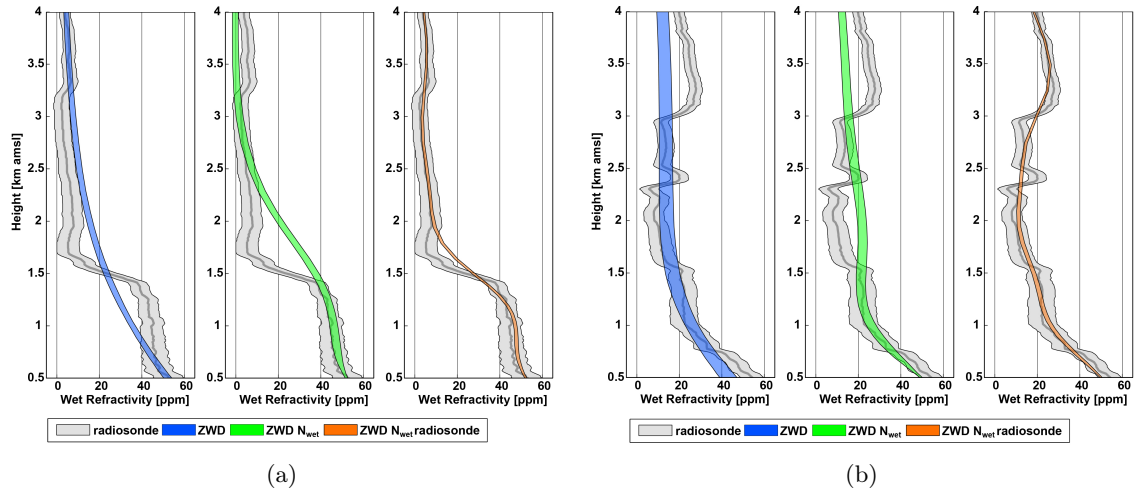


Figure 4.6: Single profiles of wet refractivity for (a) 17 Oct 2011, 12:00 UTC and (b) 28 Oct 2011, 12:00 UTC for different input data sets. The formal 1-sigma uncertainty of the profiles and of the corresponding radiosonde are shown as shaded patches.

On a single profile basis, Figs. 4.7a and b show the difference of the model solution to the radiosonde rs at the same dates as in Figs. 4.6a and b, respectively. Colour coding and naming has been kept consistent with previous plots. In Figs. 4.7a and b, one solution previously not mentioned is shown in black. It represents the solution achieved, if only the deterministic part from the ZWD solution is compared to the radiosonde (see Sect. 2.2.1). The blue line shows, how the solution benefits from the signal part. The improvement from the black to the blue line is especially obvious in Fig. 4.7b. The effect of the aforementioned stations DOL, MLS and CHA and of the smoothing of the applied correlation lengths are again well observed in all solutions shown. The light blue line is the solution including ground meteorological data only. We observe already in Fig. 4.7a that the collocation of ground meteo performs well in the lowest 1 km. Its statistical behaviour will be investigated later in this section.

A rough quantification of the loss in reconstruction quality in case of missing stations in a network is attempted in Fig. 4.8. It shows the RMS difference between the combined solution (GNSS and ground meteo) and the radiosonde for the 3 yr data. The light gray curve includes all measurement stations and is repeated from Fig. 4.5. For the dark gray curve, the GNSS and the meteo stations in Payerne are excluded from the reconstruction. Mostly affected are the refractivities in the lowermost 2 km with an increase in RMS difference of 1–2 ppm. Since both, the AGNES and the SwissMetNet network are not very dense in the region of Payerne, it is expected that the accuracy of wet refractivity reconstruction for all Switzerland is quite well represented with the dark gray curve in Fig. 4.8.

The wet refractivity profiles from our processing have been validated building the difference between model and rs for our data set of 3 yr. Results for the lower troposphere are shown in Figs. 4.9a–c. Figure 4.9a includes only ZWDs in the collocation and demonstrates the quality of reconstruction if we use GNSS data. The median shows a distinct negative offset of -5 ppm at ≈ 1.5 km height. This offset has almost disappeared in Fig. 4.9b. Here, the collocation also includes N_{wet} from ground meteo stations. For the heights 0.5–4 km a.m.s.l., maximum median offsets have been found to be 2.3 ppm and quartiles reach a maximum of 3.8 ppm. The quartiles inside the boundary layer have decreased from ≈ 3.4 ppm (Fig. 4.9a) to ≈ 2.1 ppm (Fig. 4.9b). A clear improvement was achieved for large differences (lines in all boxplots, including roughly 99% of all data assuming normal distribution). In Fig. 4.9b they rarely exceed 10 ppm. In order to quantify the effect of the N_{wet} data set on its own, it was separately included in the collocation (Fig. 4.9c). A clear linear trend of the median is observed that drifts away from the zero line.

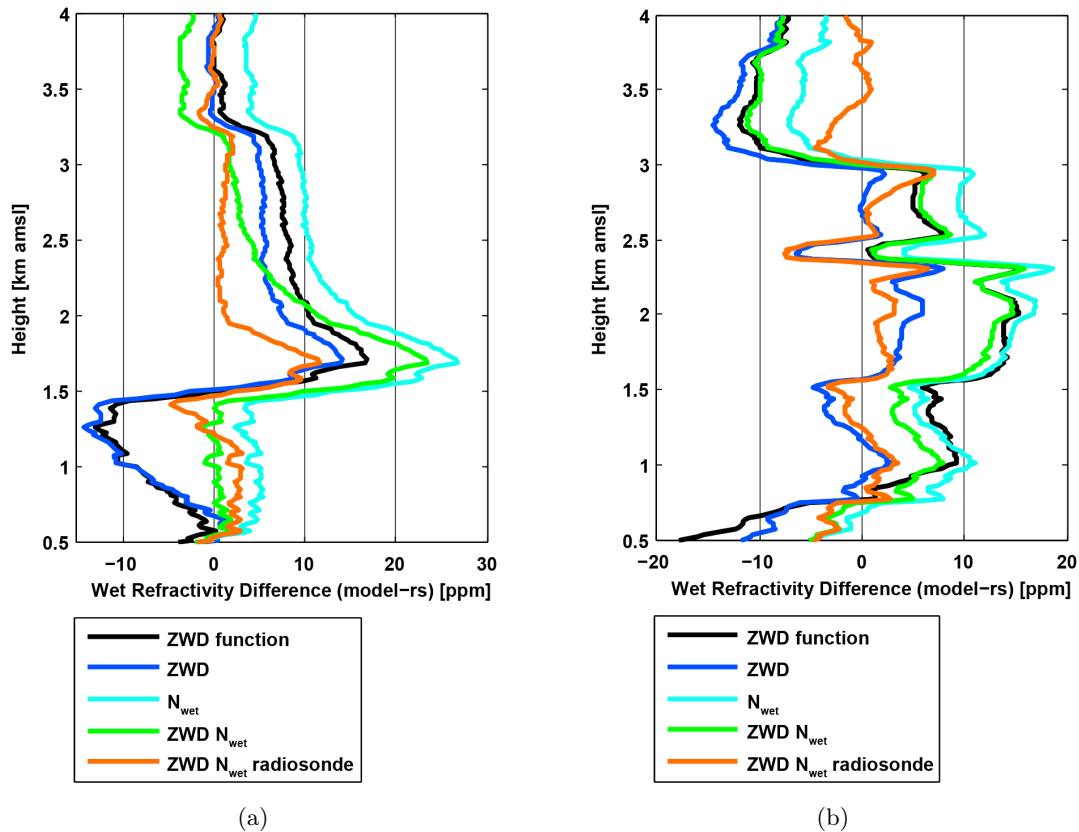


Figure 4.7: Comparison between interpolated refractivity profiles from COMEDIE and the radiosonde profile from the 17 Oct 2011, 12:00 UTC. The ZWD function only takes the deterministic part into account. All other profiles contain also the signal part derived from either ZWD data from GNSS, refractivity data from ground meteorological stations or the radiosonde at Payerne, or a combination of these data sets. (b) Comparison between interpolated refractivity profiles from COMEDIE and the radiosonde profile from the 28 Oct 2011, 12:00 UTC. Other information as for (a).

The spread has also increased with respect to Fig. 4.9b. Hence, a clear benefit comes from the combination of the two data sets.

The comparison of our solutions to the tomographic solution calculated by Perler (2011) is shown in Figs. 4.10, 4.11 and 4.12. The AWATOS2 solution uses the AGNES stations of Switzerland and data from the Payerne radiosonde for validation. The station network of our study has slightly changed since the study by Perler (2011). However, in the surroundings of Payerne, there have been no noteworthy changes. Our GNSS-only solution that has been calculated with ZWDs shows a slightly better performance than the results from tomography. With the help of ground meteo data, we get a definitely superior solution.

Now that the achievable accuracy in terms of absolute wet refractivities has been demonstrated, we continue the statistical analysis with relative differences between model and rs in Figs. 4.13a–c, which correspond to Figs. 4.9a–c. In Fig. 4.13a, the median’s offset at ≈ 1.5 km height amounts to -16% and we observe quartiles of 10% in the boundary layer. The quartiles in Fig. 4.13b have improved to $5\text{--}7.5\%$ relative difference below 1.5 km. Furthermore, the strong asymmetry of the quartiles at heights between 3 km and 4 km of Fig. 4.13a has been greatly reduced in Fig. 4.13b. The same data that is used in Fig. 4.13b, is plotted as time series in Fig. 4.14. Unlike the absolute refractivity differences in Fig. 4.5, the relative differences do not show the seasonal variation in accuracy. This is due to higher refractivity values in summer than in winter. The amount of rela-

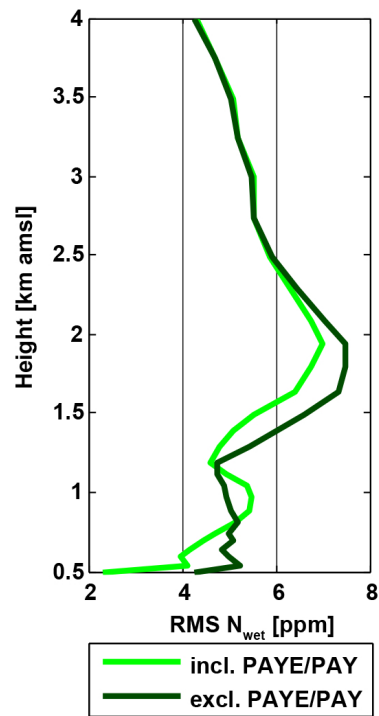


Figure 4.8: RMS of model minus radiosonde difference for a collocation including the GNSS station PAYE and the meteo station PAY (green) and for a collocation without those two stations (dark green). The comparison shows 3yr of data with 2132 radiosonde profiles being evaluated. Note that the light green line corresponds to the right panel of Fig. 4.5, but with another x-axis scale.

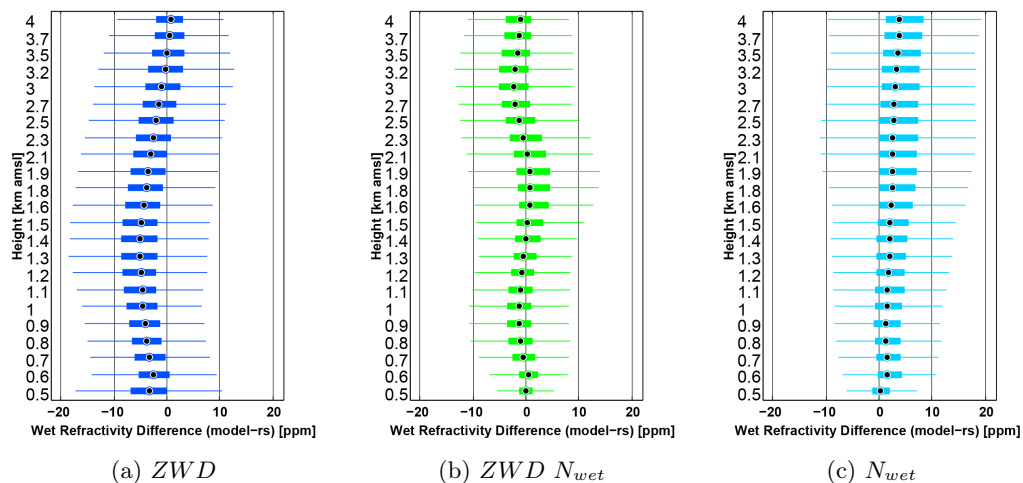


Figure 4.9: (a) Boxplot of the absolute differences between COMEDIE-derived wet refractivities with data from GNSS only and the radiosonde. Data of 3yr have been evaluated. Boxes denote the 25th and 75th percentile. The median is marked inside the boxes. Lines show large offsets and extend from $q_{25\%} - 1.5 \cdot (q_{75\%} - q_{25\%})$ to $q_{75\%} + 1.5 \cdot (q_{75\%} - q_{25\%})$. They cover roughly 99% of the data spread if normal distribution is assumed. Further data is classified as outliers and not shown. Total number of evaluated cases is 2132. (b) As for (a) but with COMEDIE-derived wet refractivities using data from GNSS and ground meteorological stations. (c) As for (a) but using COMEDIE-derived wet refractivities from data of ground meteorological stations only.

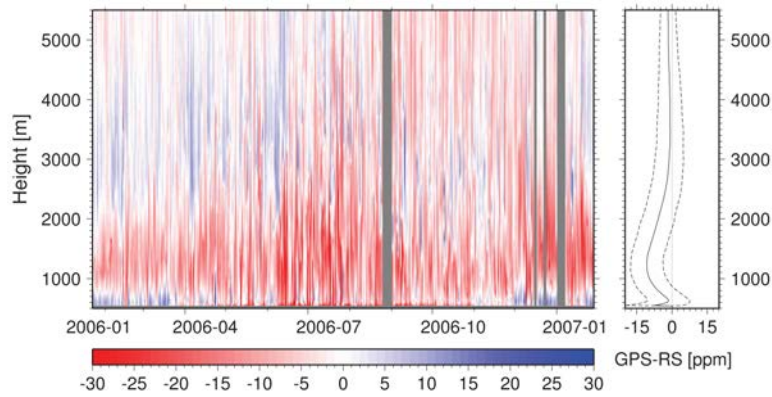


Figure 4.10: Wet refractivity differences between the tomographic solution from AWATOS2 and the operational radiosonde in Payerne. The figure has been taken from Perler (2011). Right hand side shows the mean difference and standard deviation between the AWATOS2 solution and the radiosonde. The solution uses GPS only data. Neither ground meteo nor a GPS/GLONASS combined solution is included.

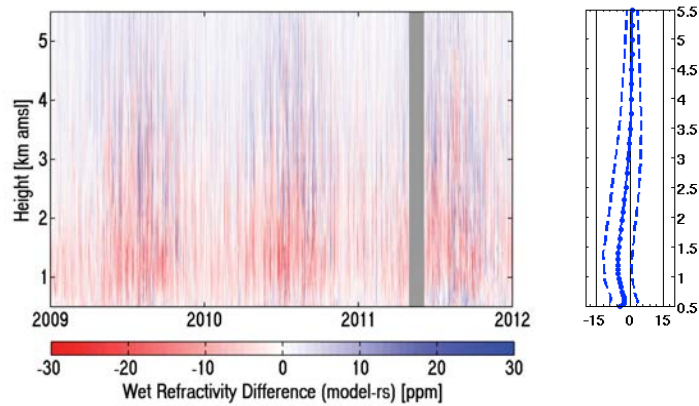


Figure 4.11: The wet refractivity difference from the COMEDIE solution with the GNSS data only. Unlike the solution from AWATOS2 in Fig. 4.10 that reconstructs slant wet delays, our solution operates with zenith path delays. Further note that we process a different time span. The color scaling and the calculation of the mean difference and standard deviation has been kept consistent with the AWATOS2 solution.

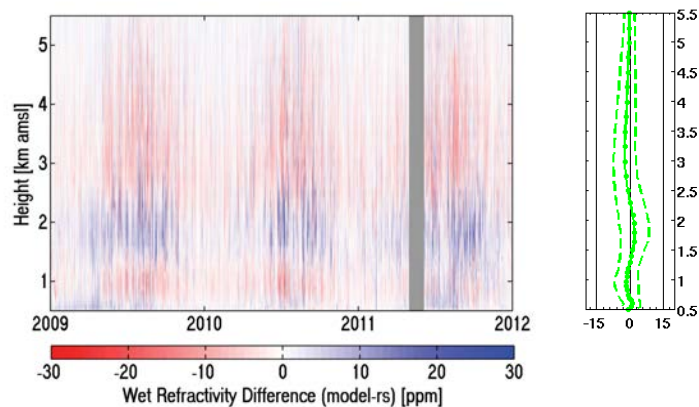


Figure 4.12: Wet refractivity difference from the COMEDIE solution with GNSS data plus ground meteo data. The same data is displayed as in Fig. 4.5 but with another color scaling to remain consistent with Fig. 4.10.

tive differences $> 95\%$ amounts to 7% of all data shown in Fig. 4.14. Note that even though there are time spans with fewer black regions, they are not associated to any particular season of the year.

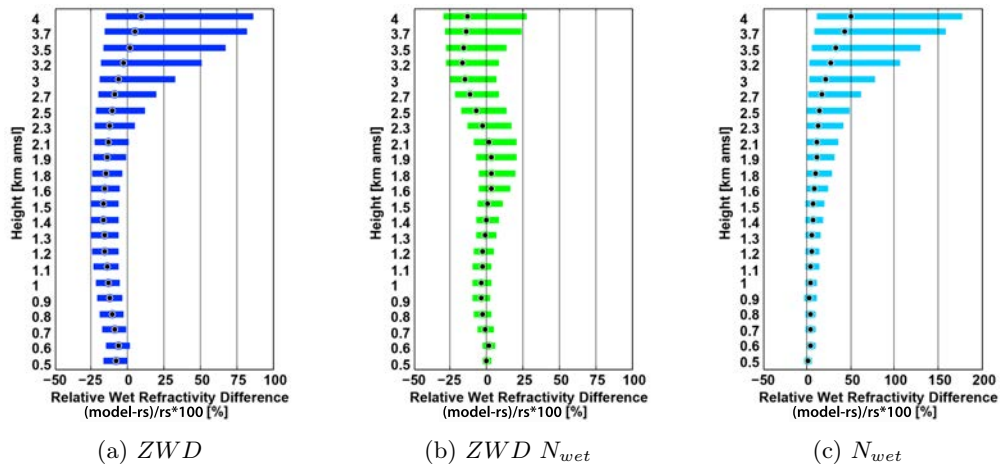


Figure 4.13: (a) Boxplot of the relative differences between COMEDIE-derived wet refractivities with data from GNSS only and the radiosonde. Boxes denote the 25th and 75th percentile and the median is marked inside the boxes. Total number of evaluated cases is 2132. (b) As for (a) but with COMEDIE-derived wet refractivities using data from GNSS and ground meteorological stations. (c) As for (a) but using COMEDIE-derived wet refractivities from data of ground meteorological stations only. Note that the abscissa in (c) is scaled differently to (a) and (b).

Radio occultations deliver an atmospheric product that can be used to calculate point measurements of wet refractivity. They can be included in the collocation approach much the same way as ground meteo measurements of wet refractivity. There are 189 radio occultations available in the investigation area during the 3 yr (Tab. 4.1). Therefore, only a limited number of COMEDIE calculation batches would actually contain one or more occultations in their data set. Eventually, 132 calculation batches could be compared to radiosonde profiles. Their statistics are shown in Fig. 4.15. Figure 4.15a shows the COMEDIE solution without the occultations, but GNSS and ground meteo data, and Fig. 4.15b with the occultations in addition to GNSS and ground meteo. The occultation's influence is practically zero below 1.6 km. In the upper troposphere, however, an improvement in the median offset and reduction in spread is observed.

4.5.2 Humidity profiles

With the additional temperature profiles from the microwave radiometer, the wet refractivity profiles have been converted to dew point temperature. To display dew point temperature and air temperature on a single plot, thermodynamic diagrams called emagrams are shown in Figs. 4.16a and b. Beside the quality of dew point temperature, also the quality of the radiometer temperatures can thus be demonstrated. The figures contain the GNSS plus ground meteo solution from COMEDIE for the previously shown October cases. The smooth nature of the model solution is also noted here. In addition, the incapability to reconstruct the cloud layer between 3–4 km is shown in Fig. 4.16b. This is due to a lack of stations at that height in the vicinity of Payerne (Fig. 4.3).

The same statistical model to rs comparison as in Sect. 4.5.1 has been carried out on the basis of absolute differences of dew point temperature (Figs. 4.17a and b). Similarly to the relative wet refractivity differences in Figs. 4.13a and b, the differences in dew point temperature increase almost uniformly with height. This is due to the increased sensitivity of dew point temperature to uncertainties in wet refractivity with decreasing temperature and hence, with height. In Tab. 4.4 it is shown that the influence of temperature uncertainty on dew point temperature is one order of magnitude lower than the influence of wet refractivity, which means that the microwave radiometer adds very little to the uncertainty figure of the model solution. These sensitivities have been

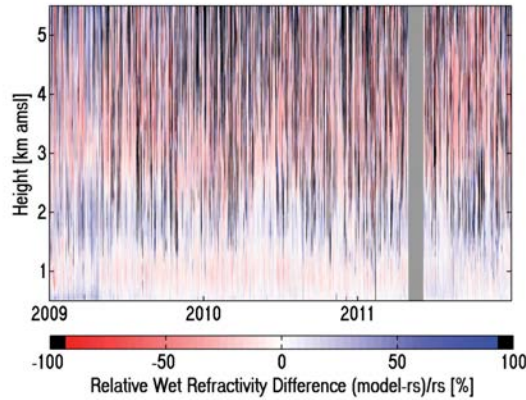


Figure 4.14: Time series of the relative difference between the solution using GNSS and ground meteo data and the radiosonde wet refractivities. Relative differences of more than 95% are shown in black. These regions correspond to 7% of all data points shown in this plot.

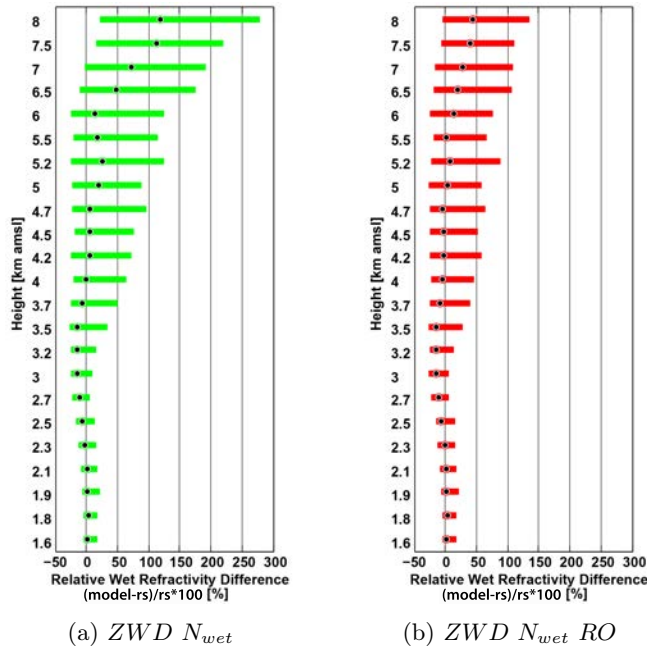


Figure 4.15: Relative wet refractivity differences as boxplots. (a) As for Fig. 4.13b but showing the boxplot for the upper troposphere from 1.6 km to 8 km and including only the 132 cases that would contain radio occultations in their computation batches. (b) Shows the statistics of the 132 interpolation batches that contain the occultations. Data from GNSS, ground meteorological stations and radio occultation profiles of wet refractivity have been included and interpolated.

calculated on the basis of Eqs. (4.5) and (4.6). Water vapour pressure e has been expressed according to Eq. (2.3). The partial derivatives with respect to N_{wet} and T directly yield the respective sensitivities.

The result of including radio occultations in the reconstruction of dew point temperature profiles is shown in Figs. 4.18a and b, where the latter includes the 189 radio occultations from the 3yr period. Note that also here, the behaviour of model minus rs in dew point temperature is similar to the behaviour of the relative wet refractivity differences. The conversion using radiometer temperatures does not considerably change the characteristics of the plots.

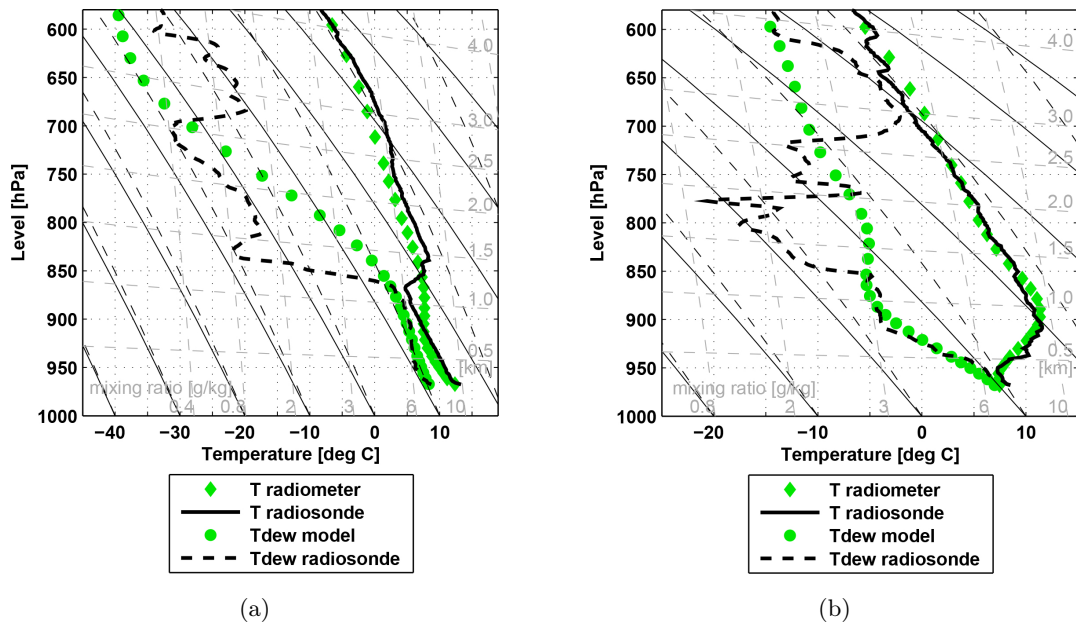


Figure 4.16: Emagrams with dew point temperatures calculated from the COMEDIE solution (GNSS plus ground meteo solution) and radiometer temperatures for (a) 17 Oct 2011 (b) 28 Oct 2011, 12:00 UTC.

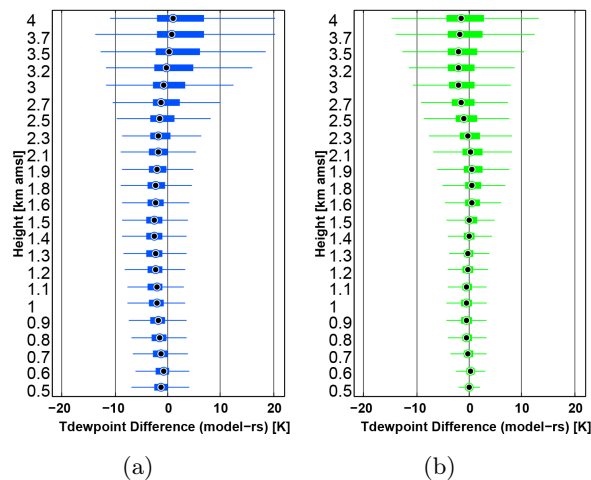


Figure 4.17: (a) Boxplot showing the differences between dew point temperature derived from COMEDIE wet refractivities and radiometer temperatures and dew point temperature entirely calculated with radiosonde data. COMEDIE wet refractivities were calculated using GNSS zenith path delays only. For further information on boxplots, see Fig. 4.9. (b) As for (a), but with wet refractivities from ground meteo stations as additional input data into COMEDIE.

We also calculated profiles of relative humidity (Eq. 4.6) from microwave radiometer temperature and model refractivity of the combined solution of GNSS and ground meteo. Figure 4.19 shows the statistics with respect to the radiosonde data as mean and standard deviation of the difference. Systematic deviations from zero of maximum 7.3% and standard deviations of 12–20.0% are observed for the lower troposphere. Note that contrary to the sensitivity of dew point temperature, where wet refractivity has much more influence on the uncertainty than temperature, relative humidity is similarly affected by temperature and refractivity (Tab. 4.4).

Table 4.4: Sensitivity of dew point temperature and relative humidity to uncertainty in wet refractivity and temperature. Valid for atmospheric values of $N_{\text{wet}} = 10\text{--}50$ ppm and $T = 273\text{--}293$ K.

	10 ppm uncertainty in N_{wet}	1 K uncertainty in temperature
dew point temperature	2–11 K	≤ 0.1 K
relative humidity	10–30 %	1–12 %

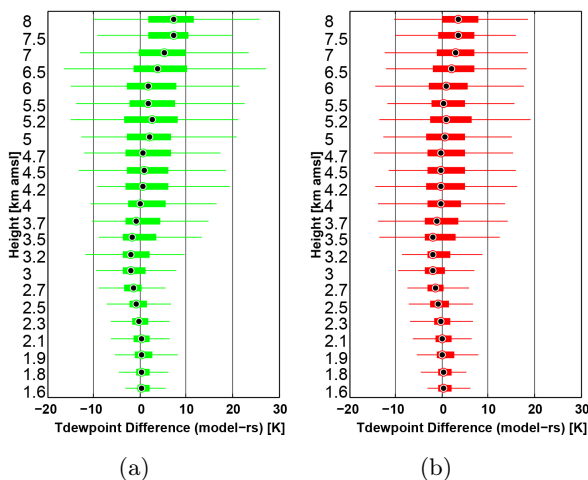


Figure 4.18: (a) As for Fig. 4.17b but showing the boxplot for the upper troposphere from 1.6 km to 8 km and including only the 132 cases that would contain radio occultations in their computation batches. (b) Shows the statistics of the 132 interpolation batches that contain the occultations of the 3 yr investigation period. Data from GNSS, ground meteorological stations and radio occultation profiles of wet refractivity have been included and interpolated.

4.6 Discussion

This study uses an interpolation technique to determine wet refractivity profiles from mainly GNSS zenith path delays. Many other investigators have used the tomographic approach using slant path delays from the GNSS processing to reconstruct wet refractivity fields. The slant paths, if fully recovered during the processing, do not have the averaging nature of zenith path delays and should hence contain information about the heterogeneity of wet refractivity in the atmosphere. The tomographic approach has been statistically validated in Perler (2011) for a one year period in Payerne, Switzerland. He obtains standard deviations of ≈ 10 ppm at ground level, which decrease to ≈ 5 ppm at 4500 m amsl with respect to the radiosonde reference. With another tomographic method, Nilsson et al. (2007a) arrive at 4–5 ppm absolute difference to a radiosonde reference and a relative difference of 10% most of the time for the refractivity in the lower 2 km of the troposphere. The problem of the tomographic approach lies in the fact that path delays from ground-based GNSS stations have very limited capability to recover vertical structures in the atmosphere above the top station as has been shown by Champollion et al. (2005) or Perler et al. (2011). GNSS tomography software with data from ground-based GNSS stations, therefore, rely on information other than actual measurements to retrieve meaningful fields. For example, the tomography might be supported with a priori fields of refractivity or inter-voxel constraints. The collocation approach in the study presented here, relies on a different type of additional information. It divides the data into a signal part of assumed statistical behaviour, a measurement noise part and into a deterministic function that describes the general refractivity field. Hence, collocation imposes a relatively strong parameterization of the refractivity field. The question then arises: Despite working with ZWD and thus lacking azimuthal information, is the collocation approach capable of reconstructing refractivity fields that can compete with tomographic results? Using the

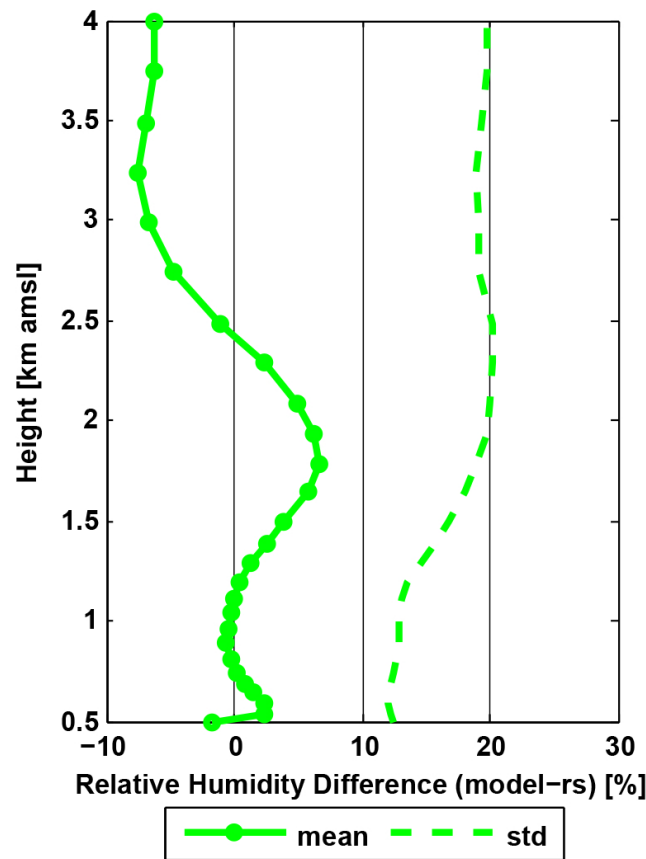


Figure 4.19: Mean and standard deviation of the difference between relative humidity from the combined COMEDIE solution (GNSS and ground meteo) and the radiosonde from the comparison of 2132 radiosonde cases.

GNSS data only, we obtain quartiles of ± 3.4 ppm for the heights 0.5–4 km amsl with a maximum median offset of -5 ppm at around 2 km height. Given that the results are close in accuracy to studies using GNSS tomography for the refractivity reconstruction suggests that, with the currently investigated station networks and reconstruction techniques, slant path delays add little additional information compared to the use of zenith delays only.

The least-squares collocation is capable of including other measurement types. In a first experiment, ground meteo data has been included. Ground meteo data has been previously included into GNSS tomography and its beneficial effect has been shown (Manning et al., 2013) or has been suggested (Bosy et al., 2010). We show that including ground meteo measurements of wet refractivity has a very positive effect on the mean offset with respect to the radiosonde reference, particularly in the region ≤ 2 km. In addition, including N_{wet} profiles from radio occultations has been shown to improve the accuracy in the upper troposphere. Due to the few occultations taking place in the study region during the 3 yr, radio occultations give little support to the overall solution. We demonstrate however that their continuation to the ground with GNSS path delays and ground meteo measurements is feasible. Foelsche and Kirchengast (2001) demonstrate that a thorough ray-tracing approach together with slant delays from ground stations allows the retrieval of the complete information contained in radio occultation delays.

The Raman Lidar is a measurement technique with high vertical resolution. For an operational Raman Lidar at Payerne, Switzerland, Brocard et al. (2012) demonstrate a relative humidity mean difference to the radiosonde of 2% for day-time and 5% for night-time profiles (conversion from mixing ratio to relative humidity with temperatures from radiosonde). They take the radiosonde profiles as their working reference. Standard deviations of this comparison are around 5% (night)

and 7% (day) for most of the lower troposphere. At night, when humidity gradients at 1.5 km above ground are often pronounced, the standard deviation of the lidar minus radiosonde comparison reaches up to 10% at that height. This suggests that lidar profiles are also somewhat smoothed and do not fully catch strong gradients close to the boundary layer top, but far better than the profiles from this study. Compared to the radiosonde, the relative humidity mean difference using collocation is around 5–7%, with standard deviations of 12–20%. For the conversion of N_{wet} to relative humidity, we have temperature values from the microwave profiler at hand, which adds further uncertainty to our retrieval, but is generally available, including times with fog and light rain, and not restricted to heights below cloud base. Exceptions occur in case of strong rain, where the quality of temperature profiles from radiometers have not been sufficiently investigated yet. The easy maintenance, good data reliability and low costs due to shared use with other applications are the strengths of the GNSS data. The collocation of GNSS ZWDs is not a measurement technique as such, but an aggregation of data from a relatively large area (100 km radius). In contrast to the LIDAR that is very precise at one location, the aggregation aims at a certain representativity. Due to costs, a dense radiosonde or LIDAR network would be difficult to setup and maintain. Compared to radiosondes, the temporal resolution of the GNSS data is more suited to follow the evolution of atmospheric humidity on time scales of hours. The smoothed profiles however, do not allow to image strong vertical humidity gradients correctly. The relative humidity uncertainty of the radiosonde is given by 5–10% (Tab. 4.2) with approximately 10 m average vertical resolution. This makes it a suitable reference in case of sharp humidity gradients.

Relative humidity is still one of the most difficult variables to forecast by a numerical weather prediction model. Forecast uncertainties in relative humidity of 10–20% are common (e.g., Wilhelm, 2012) and are thus of the same order of magnitude as our results. Since GNSS, microwave radiometer and ground meteo stations together provide humidity information in near real-time, we expect a benefit from our profiles for applications of cloud and rain nowcasting. The profiles achieve dew point temperature quartiles ≤ 2 K below 2 km height that increase to 4.5 K at 4 km. A possible product could be the calculation of CAPE (convective available potential energy) for thunderstorm detection or other indices related to the occurrence of precipitation events and their severity, before they can be detected and quantified by other means (e.g., weather radar).

4.7 Conclusions

We presented results from an interpolation approach of GNSS zenith wet delays and several data sets of point measurements of wet refractivity to reconstruct wet refractivity profiles. Water vapour profiles have been calculated, where temperature profiles from a microwave radiometer were available. Wet refractivity profiles from our processing are shown to have comparable accuracy to results from investigations that reconstruct refractivity with GNSS tomography. Additional data sets, such as ground meteorological values or radio occultations improve the results. With respect to dew point temperature, a maximum median offset of 2 K and maximum quartiles of 4.5 K were achieved for the lower troposphere, combining the presently available data from a GNSS and a ground meteo network in the western part of Switzerland. Collocation can incorporate a suite of data into a common least-squares framework. Possible further data sets to include would be Lidar profiles, refractivity gradients derived from rain radar clutter maps, differential delays from InSAR interferograms (with topographic phase removed), or troposphere gradients, the latter being a result of the GNSS processing. The combination of many data sets of either integral or point measures of refractivity already available in near real-time could give a valuable contribution to the nowcasting community or for investigations of individual instrument accuracies, profiting from mutually complementary instrumental strengths.

Chapter 5

Geodetic water vapor campaign in Zermatt

In summer 2010, a measurement campaign in the region of Zermatt was set up to investigate the accuracy of GNSS-retrieved ZTDs in a dense alpine test network. The core sensors of the campaign were 34 GNSS (GPS+GLONASS) receivers placed at many different height levels within a region of $10 \text{ km} \times 10 \text{ km}$. For validation of the GNSS meteorological parameters, radiosondes were launched during the campaign. The local scale of the investigation and the dense network was chosen to recover the temporal and spatial representativity of the ZTD parameter. The design of the campaign aimed at answering questions of the sort: How much horizontal variability can be observed in the ZTDs of closely spaced GNSS stations? Is there a clear tradeoff between retrieving ZTDs at better temporal resolution and the accuracy of these delays with respect to in-situ measurements from radiosondes? Does the accuracy of ZTDs change with altitude of the station? And how does a NWP model such as COSMO-2 perform in a complex region of the Alps in terms of ZTDs? What has to be taken care of in the Alps if ZTDs are to be assimilated into a NWP model?

In the following, the acquisition of the GNSS and radiosonde data during the campaign is described. The data processing and validation of GNSS zenith total path delays with respect to integrated path delays from radiosondes are shown. Different GNSS processing strategies are extensively studied and compared to the radiosonde. Further comparison with NWP model fields allow a qualitative description of where and when the NWP models could be supported by GNSS values of ZTD. The chapter contains some of the material published in Hurter et al. (2012) and extends the investigation to a more quantitative level.

5.1 Data description and processing

The campaign was carried out in the surrounding area of Zermatt, located in the Canton of Valais in the South of Switzerland. Its location is shown as inset in Fig. 5.1. Since it is a highly developed skiing and hiking resort, there are abundant cable cars that provided us with a favorable infrastructure, both for accessing the measuring stations at different height levels and for their power supply with batteries. In addition, it is an investigation area of other ETH Zurich research groups, whose collaborations were extremely helpful. One group that helped us with data and work force was the Institute of Environmental Engineering (IfU) lead by Prof. Dr. P. Burlando. They built a sensor transect of mobile rain stations between Zermatt and Trockener Steg (Schäppi, 2013). In addition to rainfall intensity, the sensors measured also temperature and humidity. Their permanent reference station at Trockener Steg close to our GNSS station TROC provided the same data as the mobile stations, but at higher data quality. Further help came from Jan Beutel and his co-workers from the Computer Engineering and Networks Laboratory of ETH Zurich. Their research platform close to the Hörnli alpine hut provided the electricity for the GNSS station

GLAZ. During the campaign that lasted from 15 Jul–12 Aug 2010 (4 weeks), two major data sets were collected:

- (a) GPS and GLONASS data from the campaign network
- (b) radiosonde measurements

We have obtained two additional data sets from MeteoSwiss:

- (c) NWP model fields from COSMO-2
- (d) measurements from ground meteorological stations

The following subsections detail the campaign network, the data acquisition procedures of the radiosonde, and the NWP model data.

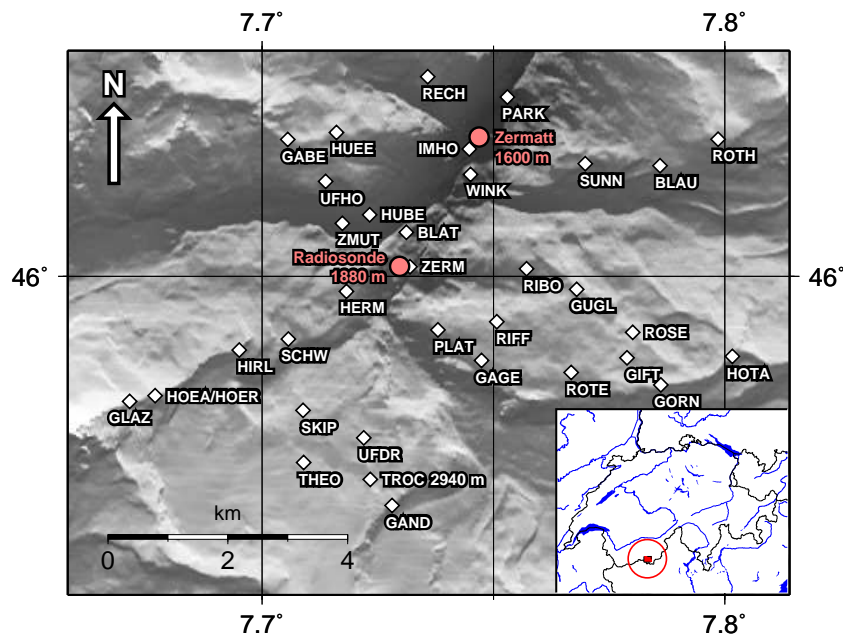


Figure 5.1: Campaign area with GNSS receiver stations marked with white diamonds. The Zermatt village center and the radiosonde launch site are marked red, with their station heights given as m amsl. The inset shows Switzerland with the area of the large map displayed as an encircled true size rectangle in the South of Switzerland at the border to Italy. The stations HOEA and HOER are very close together and thus plotted at the same location. The latter replaced the former after a few days of campaign duration.

5.1.1 GNSS Measurement Network

The campaign network consisted of 33 geodetic GNSS (GPS+GLONASS) receivers and 1 permanent geodetic station from the AGNES network. The 34 geodetic stations with inter-station distances of 1–2 km are shown in Fig. 5.1. The stations covered a height range of 1600–3500 m amsl (Fig. 5.2). The shape of the valley was responsible for the reduced number of stations at lower altitude, causing the funnel-like pattern. As a consequence of the network geometry, the low-altitude stations had a strongly narrowed sky view. The skyplots derived from the digital height model DHM25 (Swisstopo, 2014b) are shown in Figs. F.1–F.3 of Appendix F. They are ordered according to their heights and unmask the poor sky visibility of low-altitude stations. They are expected to perform worse in the processing with respect to coordinate repeatability and troposphere parameter estimation.

The measurement duration in summer 2010 and data gaps of the campaign stations are displayed in Fig. 5.3. Data gaps usually resulted from interruption in power supply or receivers corrupting

the memory cards. The latter error was frequent with the LEICA RX1250TC receivers due to unknown reasons. We were informed by the producer that these receivers were not designed for static longterm measurements. Most stations were deployed with car batteries. The car batteries often showed behaviours different from laboratory tests preceding the campaign. Gaps in power supply mostly happened during the first week of the campaign after which we gained good control over the battery behaviour under real environmental conditions. The battery interchange at station HOEA soon became too laborious. The station was moved to a better accessible location near the Hörnli hut after 4 days of operation. It was renamed HOER from then on. The hut's supervisor allowed us to draw from the hut's power supply making the battery exchange needless. The interruption at IMHO was caused by a problem of power supply. The station being placed on the roof of a school and receiving power from a plug, it was unfortunately switched off when maintenance and cleaning personnel dutifully set the power supply to holiday mode.

The Tabs. 5.1–5.3 portray the campaign stations. In order to achieve the desired network density, we relied on receivers and antennas from a number of institutions. Hence, it was inevitable to use many different receiver and antenna types. On the one hand, this was not advantageous, since it made it difficult to separate between antenna-related issues and other modeling errors. On the other hand, it permitted the characterization of the antenna performance with respect to ZTD retrieval. The following institutions provided us with their receivers:

- Institut Vermessung und Geoinformation, Fachhochschule Nordwestschweiz
- Remote Sensing Laboratories, University of Zurich
- Département Environnement construit et Géoinformation, Haute école d'ingénierie et de gestion du canton de Vaud
- Geodesy and Geodynamics Lab, ETH Zurich
- Geodetic Metrology and Engineering Geodesy, ETH Zurich
- Applied and Environmental Geophysics, ETH Zurich

The antennas were usually mounted on an aluminium pole of 70 cm length with a screw thread on one side and a bolt on the other (e.g., HOEA in Tab. 5.2). An antenna adapter could be easily attached to the bolt and carried the antenna screwed on top. Into the rock, a hole was drilled and an internally threaded sleeve was glued into the hole. The sleeve served as matching part for the screw thread of the pole. Where the aluminium pole was not a mounting option, tripods were used (e.g., BLAU in Tab. 5.1).

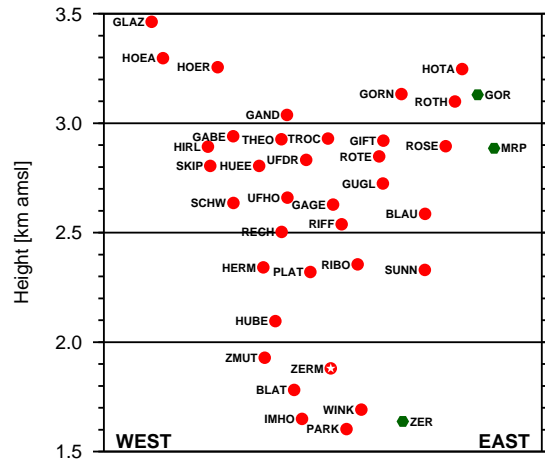


Figure 5.2: Station heights of campaign stations shown in Fig. 5.1, viewed from the South and shown as red dots. Green hexagons with 3-letter station names mark meteorological ground stations from the SwissMetNet of MeteoSwiss (GOR=Gornergrat, MRP=Monte Rosa-Plattje, ZER=Zermatt). Some longitudinal positions were shifted by several hundreds of meters to improve readability. Close to the station of ZERM, the radiosonde launches took place. A white star thus marks this station. It is also the only AGNES station close-by.

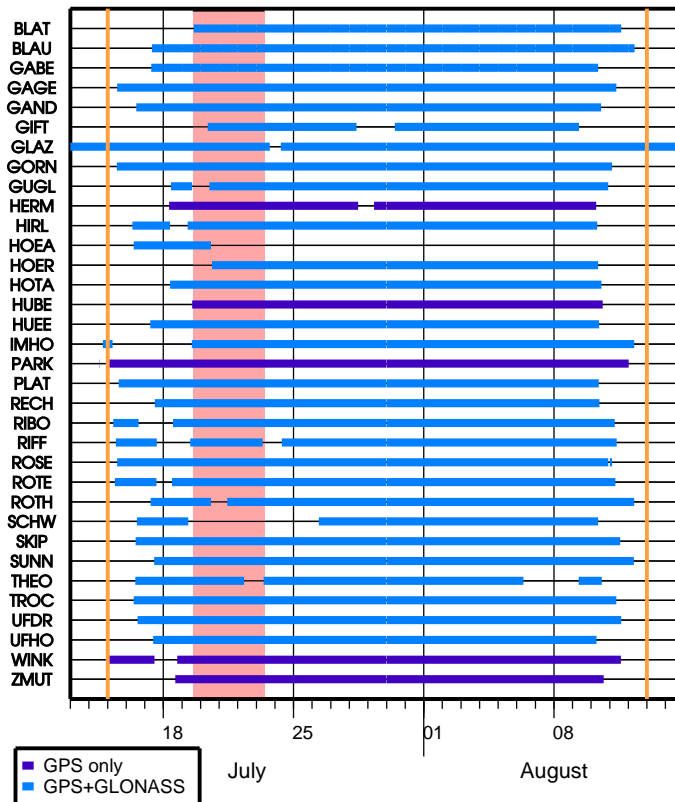


Figure 5.3: Activities of all stations that were installed for the duration of the campaign only. Most stations measured signals from both GPS and GLONASS satellites. Orange vertical lines mark start (15 Jul 2010) and end (12 Aug 2010) of campaign. The red shading between 19 Jul and 23 Aug 2010 denotes the period of the radiosonde measurements.







Table 5.1: Description of the campaign stations in Zermatt. See Fig. 5.1 for their location within the research area. Each description contains the following entries: station name, station name abbreviation, receiver, antenna, antenna dome, latitude, longitude, height [m] (wgs84), Swiss coordinates Easting/Northing/Height [m] (Bessel ellipsoid). The order of stations is kept alphabetically for consistency with most figures.

			
<p>Blatten zum See BLAT JAVAD TRE_G3T DELTA JAV_GRANT-G3T NONE 46° 00' 23.901" 07° 43' 50.995" 1833.658 622634 / 95051 / 1782</p>		<p>Blauherd BLAU LEICA GRX1200+GNSS LEIAR25.R3 LEIT 46° 00' 59.963" 07° 47' 8.457" 2637.630 626878 / 96182 / 2586</p>	
			
<p>Unteres Gabelhorn GABE LEICA GX1230GG LEIAX1202GG NONE 46° 01' 14.197" 07° 42' 18.935" 2991.539 620648 / 96597 / 2940</p>		<p>Gagerhaupt GAGE LEICA GX1230GG LEIAX1202GG NONE 45° 59' 14.439" 07° 44' 49.653" 2679.456 623905 / 92911 / 2627</p>	
			
<p>Gandegg GAND LEICA GX1230GG LEIAX1202GG NONE 45° 57' 55.958" 07° 43' 40.038" 3089.849 622415 / 90482 / 3038</p>		<p>Gifhittli GIFT LEICA RX1250TC LEIAX1230+GNSS NONE 45° 59' 15.861" 07° 46' 42.642" 2972.023 626337 / 92965 / 2920</p>	
			
<p>Glaziologen GLAZ LEICA GX1230GG LEIAX1202GG NONE 45° 58' 52.104" 07° 40' 15.847" 3515.169 618013 / 92201 / 3463</p>		<p>Gornergrat GORN LEICA GRX1200+GNSS LEIAR25.R3 LEIT 45° 59' 1.129" 07° 47' 9.987" 3184.918 626927 / 92512 / 3133</p>	
			
<p>Gugle GUGL LEICA GX1230GG LEIAX1202GG NONE 45° 59' 52.989" 07° 46' 4.864" 2776.455 625519 / 94108 / 2725</p>		<p>Hermettji HERM LEICA SR530 LEIAT502 NONE 45° 59' 51.854" 07° 43' 4.496" 2392.950 621637 / 94058 / 2341</p>	

Table 5.2: Station description continued from previous page.

	 <p>Hirli HIRL LEICA GX1230GG LEIAX1202GG NONE 45° 59' 20.124" 07° 41' 40.914" 2944.841 619842 / 93072 / 2893</p>		 <p>Hörnlihütte 1 HOEA LEICA GX1230GG LEIAX1202GG NONE 45° 58' 55.809" 07° 40' 33.085" 3348.926 618384 / 92316 / 3297</p>
	 <p>Hörnlihütte 2 HOER LEICA GX1230GG LEIAX1202GG NONE 45° 58' 54.893" 07° 40' 36.425" 3307.549 618456 / 92288 / 3256</p>		 <p>Hohtälli HOTA LEICA RX1250TC LEIATX1230GG NONE 45° 59' 16.498" 07° 48' 4.447" 3299.461 628098 / 92992 / 3248</p>
	 <p>Hubelwäng HUBE NOV DL4 NOV600 NONE 46° 00' 33.194" 07° 43' 22.570" 2147.790 622022 / 95336 / 2096</p>		 <p>Hühnerchnubel HUEE LEICA GX1230GG LEIAX1202GG NONE 46° 01' 18.005" 07° 42' 58.040" 2856.422 621489 / 96717 / 2805</p>
	 <p>Schulhaus Imhof IMHO JAVAD TRE_G3T DELTA JAV_GRANT-G3T NONE 46° 01' 8.948" 07° 44' 40.022" 1701.371 623684 / 96446 / 1649</p>		 <p>Parkplatz Central PARK LEICA SR530 LEIAT502 NONE 46° 01' 37.112" 07° 45' 9.721" 1653.914 624319 / 97318 / 1602</p>
	 <p>Plattelen PLAT LEICA RX1250TC LEIATX1230GG NONE 45° 59' 31.015" 07° 44' 15.490" 2371.984 623168 / 93420 / 2320</p>		 <p>Recherten RECH LEICA GX1230GG LEIAX1202GG NONE 46° 01' 48.189" 07° 44' 9.033" 2554.463 623013 / 97655 / 2503</p>
	 <p>Riffelboden RIBO LEICA GRX1200+GNSS LEIAR25.R3 LEIT 46° 00' 3.086" 07° 45' 26.670" 2406.305 624696 / 94416 / 2354</p>		 <p>Riffelberg RIFF LEICA RX1250TC LEIATX1230GG NONE 45° 59' 35.372" 07° 45' 2.594" 2590.029 624181 / 93558 / 2538</p>

Table 5.3: Station description continued from previous page.

			
Rosenritz ROSE LEICA GX1230GG LEIAX1202GG NONE 45° 59' 29.646" 07° 46' 48.281" 2946.097 626456 / 93391 / 2894		Rotenboden ROTE LEICA GRX1200+GNSS LEIAR25.R3 LEIT 45° 59' 7.991" 07° 45' 59.193" 2899.698 625403 / 92718 / 2848	
			
Rothorn ROTH LEICA GRX1200+GNSS LEIAR25.R3 LEIT 46° 01' 14.123" 07° 47' 53.605" 3151.200 627848 / 96623 / 3099		Schwarzsee SCHW LEICA RX1250TC LEIATX1230GG NONE 45° 59' 25.973" 07° 42' 19.312" 2686.905 620667 / 93255 / 2635	
			
Skipiste SKIP LEICA GX1230GG LEIAX1202GG NONE 45° 58' 47.380" 07° 42' 30.785" 2857.186 620919 / 92064 / 2805		Sunnegga SUNN LEICA GRX1200+GNSS LEIAR25.R3 LEIT 46° 01' 4.977" 07° 46' 16.837" 2381.081 625767 / 96332 / 2329	
			
Theodulgletscher THEO LEICA GX1230GG LEIAX1202GG NONE 45° 58' 19.159" 07° 42' 31.273" 2977.986 620932 / 91193 / 2926		Trockener Steg TROC LEICA GX1230GG LEIAX1202GG NONE 45° 58' 9.965" 07° 43' 23.019" 2982.113 622047 / 90913 / 2930	
			
Uf dr Mur UFDR JAVAD TRE_G3T DELTA JAV_GRANT-G3T NONE 45° 58' 32.398" 07° 43' 17.953" 2884.423 621936 / 91605 / 2832		Ufem Hohlicht UFHO LEICA GX1230GG LEIAX1202GG NONE 46° 00' 51.565" 07° 42' 49.477" 2711.503 621308 / 95900 / 2660	
			
Winkelmatte WINK LEICA SR530 LEIAT502 NONE 46° 00' 55.154" 07° 44' 41.009" 1743.611 623707 / 96020 / 1692		Zmutt ZMUT TRIMBLE 5700 TRM39105.00 NONE 46° 00' 24.187" 07° 43' 6.583" 1980.845 621679 / 95056 / 1929	

5.1.2 Ground meteorological stations

Three meteorological ground stations of the SwissMetNet of MeteoSwiss are situated close to the Zermatt region:

GOR: Gornergrat

MRP: Monte Rosa-Plattje

ZER: Zermatt

Their heights are shown in Fig. 5.2. The data include pressure, temperature and water vapor pressure values at 10 min temporal resolution.

5.1.3 Radiosonde measurements

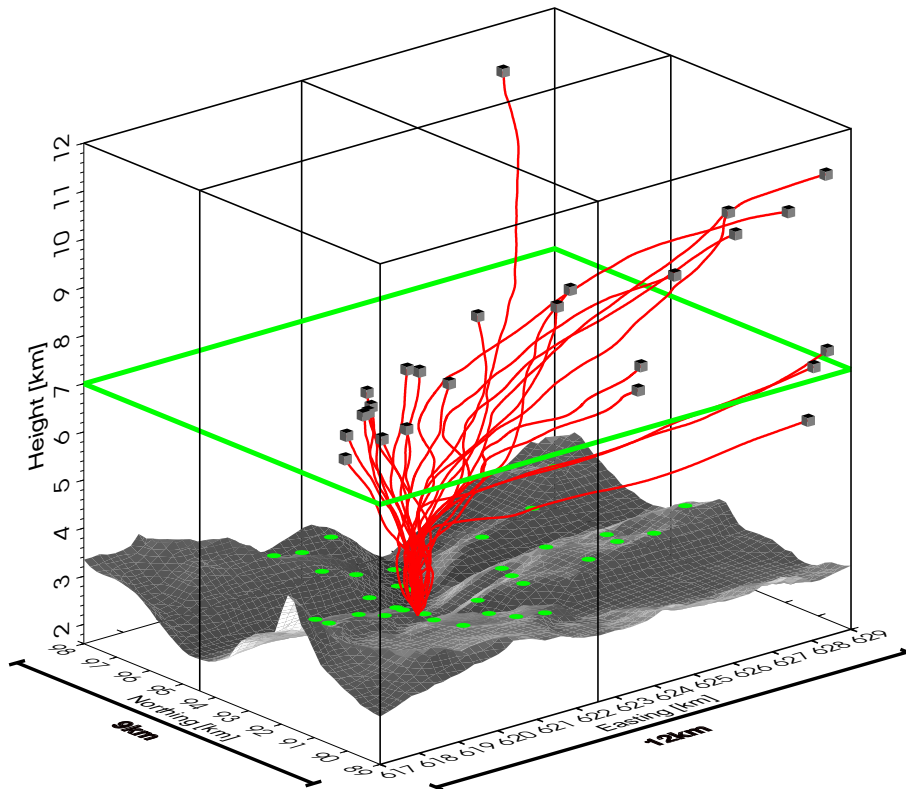
For validation of the water vapor retrieval by GNSS, 25 radiosondes were launched in the center of the investigation area by Andreas Rieder from armasuisse. The launch site at 1880 m amsl is marked in Fig. 5.1. The white star on top of the GNSS station ZERM in Fig. 5.2 denotes the AGNES station of Zermatt, but also the radiosonde site close-by. Four GNSS stations were thus below the launch height. They will be excluded from the direct comparison with the radiosonde data.

Table 5.4 gives an overview of all launches for the duration marked as shaded box in Fig. 5.3. The so-called leaving height of the research area was on average around 6 km. The time it took the sonde to reach 5 km amsl was 15–20 min and to reach the tropopause, it took 40–50 min. We should keep these values in mind, when we compare the radiosonde to the ZTDs from GNSS. They give us an approximate notion of the radiosonde’s temporal resolution with respect to calculated ZTD values.

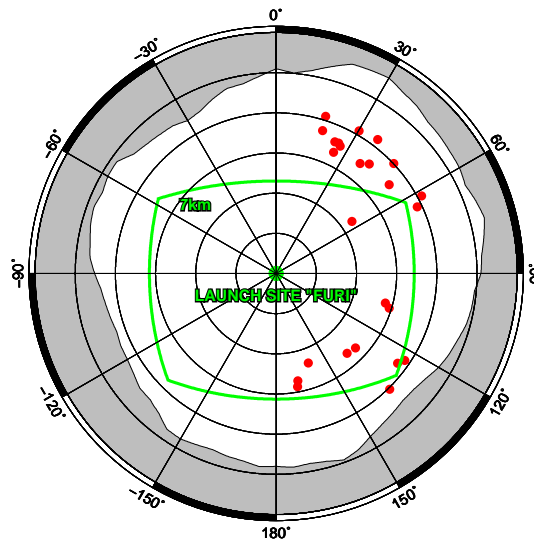
The sonde’s flight tracks are given in Fig. 5.4a. The cube delimits the same area as displayed in Fig. 5.1 and will be called research area hereafter. The positions where the radiosonde leaves the research area are visible as dots in the skyplot of Fig. 5.4b. The more or less arbitrary height of 7 km amsl was marked with a solid line. It demonstrate that the sondes usually leave the area below 7 km. Most water vapour resides in the layer below and largely contributes to the horizontal variability of GNSS-derived ZTDs. Some differences between radiosonde and GNSS-derived ZTDs will thus be attributed to the horizontal variability within and outside the research area. The prevalent west wind direction shows up clearly in the skyplot. All 25 sondes drifted eastwards.

Table 5.4: A list of all radiosonde launches during the campaign. Start date and time are given in local DST, which is UTC+2 hours. Azimuth, elevation and height corresponding to where the sonde leaves the research area are contained in this table. (rec.time=duration of recording a signal from the sonde; tropo. time=radiosonde reaches the tropopause at 11 km amsl; 5 km time=radiosonde reaches 5 km amsl; max. height=no recorded signal after this height amsl; vert. velo.=average vertical velocity during recorded flight time; azim.=azimuth of sonde leaving the investigation area, viewed from the launch site; elev.=elevation of sonde leaving the investigation area; leave hei.=height at which the sonde leaves the investigation area)

#	Date	Start	Rec. time	Tropo. time	5 km time	Max. height	Vert. velo.	Azim.	Elev.	Leave hei.
[-]	[yyyy - mm - dd]	[hh : mm]	[min]	[min]	[min]	[km]	[m/s]	[deg]	[deg]	[km]
1	2010-07-19	14:00	94	67	26	15.9	2.8	135.6	29.4	6.2
2	2010-07-19	15:59	93	49	18	21.3	3.8	124.1	32.1	6.7
3	2010-07-19	17:59	97	49	17	22.0	3.8	126.5	33.6	7.2
4	2010-07-20	08:00	90	44	15	22.5	4.1	169.3	47.0	7.8
5	2010-07-20	10:00	92	53	19	19.5	3.5	168.6	49.1	8.3
6	2010-07-20	12:00	88	43	15	22.2	4.2	160.3	54.5	10.0
7	2010-07-20	14:00	89	47	16	20.9	3.9	138.4	50.2	10.6
8	2010-07-20	16:00	91	46	14	21.5	3.9	107.0	45.9	8.8
9	2010-07-20	18:00	85	44	14	21.2	4.1	105.2	47.7	9.2
10	2010-07-20	20:00	89	48	16	20.3	3.8	133.2	49.4	11.2
11	2010-07-21	08:00	94	49	17	21.2	3.8	37.3	38.3	5.4
12	2010-07-21	10:00	79	42	13	20.3	4.3	25.3	39.9	5.1
13	2010-07-21	12:00	93	65	26	15.9	2.8	46.9	29.9	4.8
14	2010-07-21	14:00	88	44	14	21.3	4.0	51.9	36.3	6.1
15	2010-07-21	16:00	92	42	11	22.8	4.1	64.7	31.8	6.3
16	2010-07-21	18:00	78	26	11	23.3	5.0	55.5	55.7	11.0
17	2010-07-21	20:00	84	44	16	20.5	4.1	61.9	28.4	5.8
18	2010-07-22	08:00	89	42	14	23.0	4.3	17.5	28.5	3.9
19	2010-07-22	10:00	88	42	16	23.0	4.3	24.0	36.2	4.7
20	2010-07-22	12:00	75	42	12	18.8	4.1	26.7	36.8	4.8
21	2010-07-22	14:00	47	44	12	12.2	4.3	30.2	28.4	4.1
22	2010-07-22	16:00	46	-	18	10.4	3.8	37.2	27.2	4.1
23	2010-07-22	18:00	44	44	13	11.3	4.3	18.0	33.9	4.4
24	2010-07-23	08:00	40	-	14	10.8	4.5	40.4	36.3	5.3
25	2010-07-23	10:30	44	-	16	10.6	4.0	25.7	36.0	4.7



(a) Flight tracks of radiosondes.



(b) Skyplot with leaving positions of sondes.

Figure 5.4: (a) Radiosonde tracks calculated from sonde wind information. The tracks start at Furi and leave the research area at the small gray boxes. The additional grid lines are placed at the easting and northing of the launch site at Furi and divide the field into quadrants. The green dots are the campaign’s GNSS stations from Fig. 5.1. The green square denotes the height of 7 km. (b) Skyplot of radiosonde leaving positions. The sonde tracks have been calculated with sonde wind information. Gray shading shows the visibility horizon at Furi calculated from the digital height model DHM25 (Swisstopo, 2014b).

The RS92-SGP radiosondes from Vaisala delivered measurements of pressure, temperature and humidity, and horizontal wind velocity and direction. The vertical resolution of these measurements was 5–10 m. Table 5.5 is a summary of the measurement uncertainties as stated by the Vaisala data sheet (Vaisala, 2013b). Figs. 5.5a–d show the sonde with its helical GPS antenna, the Vaisala Ground Check Set GC25 to calibrate and recondition the humidity sensor, the battery activation and the assembly of all sonde parts. After these preparatory steps, the sonde was attached to a balloon filled with hydrogen (Figs. 5.6a–d). Preparation and launch of the sonde took roughly half an hour, whereas the recording time lasted for one and a half hour. This resulted in the 2 hours interval shown in Tab. 5.4.

Table 5.5: Technical data of the Vaisala RS92-SGP sonde (Vaisala, 2013b). * Total uncertainty in sounding, given as 95% confidence level. ** Standard deviation of differences in twin soundings.

Measurement	Sensor type	Uncertainty in sounding
pressure	micromechanical silicon capacitive sensor	1 hPa for the pressure range 1080–100 hPa *
temperature	capacitive wire	0.5°C *
humidity	thin-film capacitor, heated twin sensor	5% RH *
position		10 m horizontal
wind velocity	code-correlating GPS receiver	0.15 m/s **
wind direction		2 degrees **



(a) From top to bottom: the attachment for the balloon, the sonde with the sensors, battery case and battery.



(b) Calibration set from Vaisala with the sonde being calibrated.



(c) Sonde battery in the water bath for activation.



(d) Assembly of all parts belonging to the sonde.

Figure 5.5: Inside the monitoring car, preparatory steps are taken to initialize the sonde.



(a) Monitoring car and trailer for hydrogen supply.



(b) Inflation of balloon with hydrogen.



(c) The sonde is attached to the balloon.



(d) The sonde is launched.

Figure 5.6: Balloon preparation and launch outside the monitoring car by Andreas Rieder from armasuisse.

5.1.4 NWP model

The NWP model analysis data of pressure, temperature, humidity, wind direction, and wind velocity were provided in netcdf format by the Swiss Federal Office of Meteorology and Climatology at a time resolution of 1 hour. They stem from the COSMO-2 weather model (Doms and Schättler, 2002) whose nominal horizontal resolution is close to 2 km (Fig. 5.7). The model has 60 height levels with the maximum hybrid level at 23588.5m. The analysis data corresponds to the model field after the assimilation cycle. It contains the blending of a starting field from a former model run of a global model (ECMWF model) with the complete model physics from the regional model (COSMO-2) and with all available measurements. The data assimilation is carried out with the nudging technique. The most important data sets assimilated into the operational model are (André Valser, personal communication, Oct 2011):

- rain radar data with latent heat nudging
- data from the Aircraft Meteorological Data Relay (AMDAR)
- surface meteorological data
- radiosonde profiles
- wind profiler measurements

In the topographically complex regions of the Alps only few ground meteo stations are close enough to the model orography to meet the requirements for their data to be assimilated. Neither satellite data nor GNSS IWV data are assimilated. Nonetheless, satellite data enter COSMO-2 via the global model. The global model serves as initial and boundary condition for the regional model. From a model perspective, the analysis field is considered to be the best possible model description of the atmospheric state.

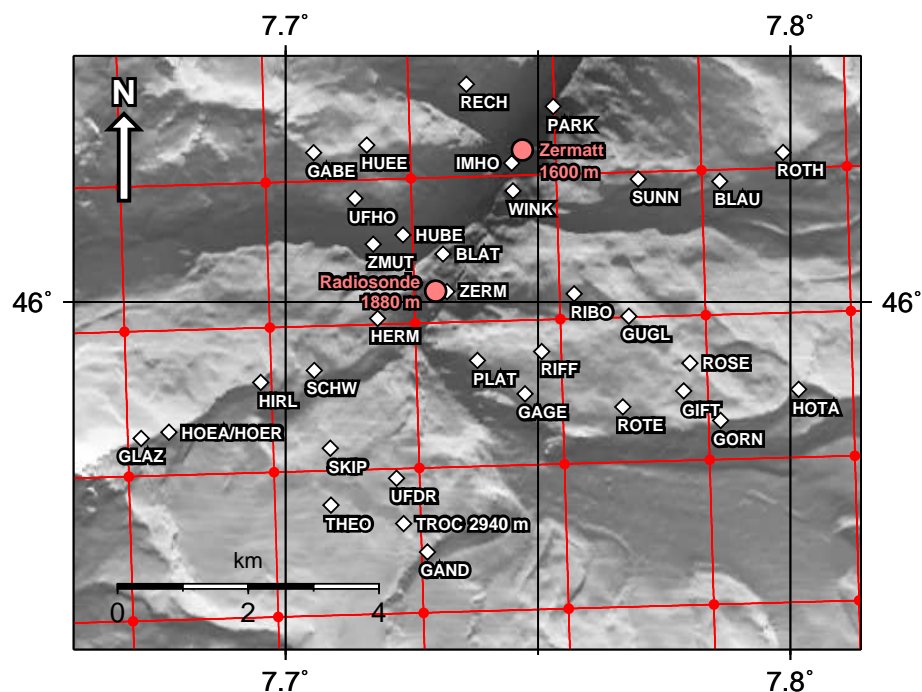


Figure 5.7: The COSMO-2 NWP model grid on top of the research area map.

5.1.5 Bernese GNSS software processing

The GNSS (GPS+GLONASS) data collected during the campaign was processed with a modified version of the Bernese software 5.0 (Dach et al., 2007), including the Vienna Global Mapping

Function (GMF) (Boehm et al., 2006a) for troposphere modelling. Three major final solutions were calculated:

1. Daily coordinates from a PPP solution of the campaign stations (Tab. 5.6) to check the quality of the station coordinates and their repeatability. The resulting coordinates were used as a priori coordinates in the subsequent double-difference solution.
2. Daily double-difference network solution (Tab. 5.7) with a minimum network constraint on the International GNSS Service (IGS) stations (Fig. 5.8a) and on the AGNES stations (Fig. 5.8b) for the best possible daily coordinate solution.
3. Seven-day gliding window double-difference network solution (Tab. 5.8). Troposphere parameters at day boundaries of two subsequent processing periods were combined into one to prevent jumps at day boundaries.

Solutions 1) and 2) are based on the PPP and network processing examples in Dach et al. (2007), respectively. Station selection of IGS and AGNES stations for datum definition of the local campaign network was carried out according to the following criteria:

IGS stations:

- Stations need to be GPS and GLONASS capable.
- Baseline length to ZIM2 < 2000 km, since ambiguities are resolved with the QIF (quasi-ionosphere-free) strategy, whose success rate drops in case of longer baselines (Dach et al., 2007, p. 334)
- available for duration of campaign
- formal 3D station position accuracy < 7 mm of the IGS cumulative solution and for the campaign's duration (extracted from short SINEX file)
- span a large area to decorrelate ZTD estimates between stations in a network solution

AGNES stations:

- Stations need to be GPS and GLONASS capable.
- good station position repeatability (visual inspection of station position repeatabilities available as figures from Swisstopo)
- available for duration of campaign.

Retrospectively, there was no need to include all the AGNES stations shown in Fig. 5.8b. The IGS stations and AGNES station ZIM2 would suffice to ensure a stable datum-definition realization and to span a large area to decorrelate ZTD estimates between the stations. The advantage of having ZIM2 in the network was that it had many common observations with the campaign stations.

From two of the aforementioned processing strategies (Tabs. 5.6 and 5.7), several variations were calculated to quantify how the troposphere parameters are affected by different processing strategies. The following notation will be used to distinguish between strategies:

PPP, NTW	precise point positioning or network solution
300s, 180s, 30s	sampling interval used in the processing
GMF, Niell	Global Mapping Function or Niell mapping function for troposphere modeling
3h, 2h, 1h, 30min	parameter spacing of estimated troposphere zenith wet delay

As an example, take (PPP, 30s, GMF, 1h) being a precise point positioning solution at a sampling interval of 30 seconds. The troposphere is modeled with the Global Mapping Function and a parameter spacing of 1 hour. Since only results from GPS processing are shown in this chapter, we will stick to the term GPS in almost all cases. For denoting specific GPS and GLONASS capable receivers, we will obviously keep the term GNSS.

Table 5.6: Summary of the settings for the precise point positioning solution of the Zermatt campaign data.

Parameter	Settings
processing mode	<ul style="list-style-type: none"> daily coordinates of Zermatt campaign stations from precise point positioning using the ionosphere-free L_3 combination, GPS-only solution
cutoff angle, weighting	<ul style="list-style-type: none"> 3°, elevation-dependent weighting ($1/\cos^2(\text{elev})$)
orbit and clock products	<ul style="list-style-type: none"> IGS final orbits and clocks
sampling rate	<ul style="list-style-type: none"> 300 seconds
a priori troposphere	<ul style="list-style-type: none"> dry GMF, hydrostatic delay with values from the Global Pressure Temperature (GPT) model (Boehm et al., 2007)
estimated troposphere	<ul style="list-style-type: none"> piecewise-linear wet path delays using wet GMF with 2 hours resolution
ambiguities	<ul style="list-style-type: none"> ambiguity-float solution
ocean tides	<ul style="list-style-type: none"> GOT00.2 ocean tide model, long-period tides from FES99, computed on 30 Mar 2011 through the web-service at http://holt.oso.chalmers.se/loading/ (last visit: 15 Mar 2014)
phase center variation	<ul style="list-style-type: none"> absolute antenna phase center variation file derived from I08.ATX
a priori coordinates	<ul style="list-style-type: none"> code solution with phase-smoothed code

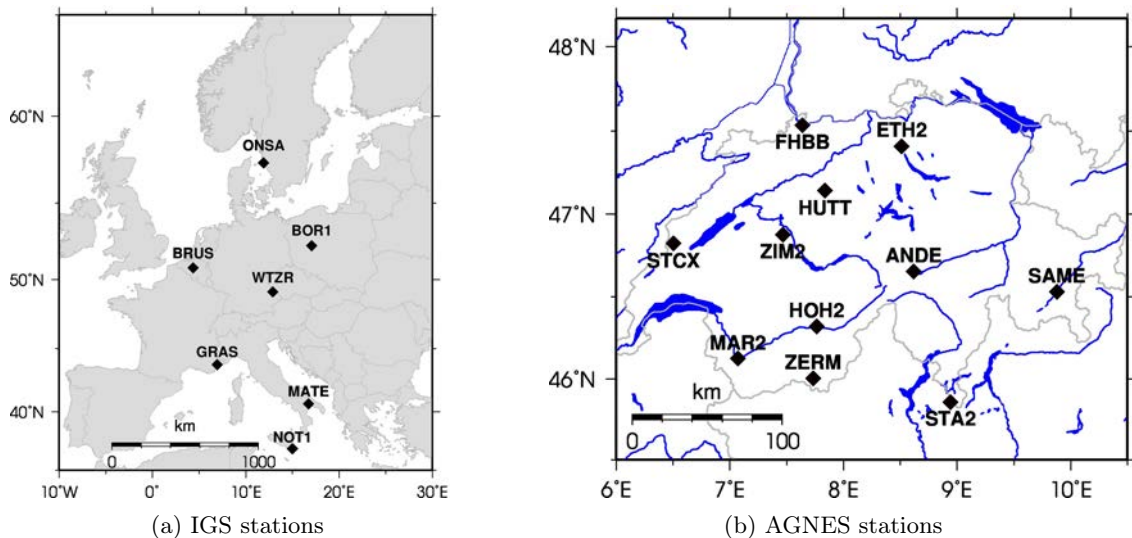


Figure 5.8: GPS stations chosen for datum definition with a minimum constraint condition put on these stations. (a) IGS stations (b) AGNES stations.

Table 5.7: Summary of the settings for the final double-difference network solution of the Zermatt campaign data.

Parameter	Settings
processing mode	<ul style="list-style-type: none"> daily coordinates of IGS, AGNES and Zermatt campaign stations from double-difference processing in a network solution using the ionosphere-free L_3 combination, GPS-only solution.
cutoff angle, weighting	<ul style="list-style-type: none"> 3°, elevation-dependent weighting ($1/\cos^2(\text{elev})$)
orbit and clock products	<ul style="list-style-type: none"> IGS final orbits and clocks
sampling rate	<ul style="list-style-type: none"> 180 seconds
baseline strategy	<ul style="list-style-type: none"> maximum number of observations
a priori troposphere	<ul style="list-style-type: none"> dry GMF, hydrostatic delay with values from the GPT model
estimated troposphere	<ul style="list-style-type: none"> piecewise-linear wet path delays using wet GMF with 2 hours resolution
datum definition	<ul style="list-style-type: none"> minimum constraint solution, allowing a Helmert transformation of the IGS and AGNES stations. A no-net-translation condition is imposed. Net rotation and net scaling are left free.
ambiguity resolution	<ul style="list-style-type: none"> ambiguities resolved with the Quasi-Ionosphere-Free (QIF) strategy
ocean tides	<ul style="list-style-type: none"> GOT00.2 ocean tide model, long-period tides from FES99 (see Tab. 5.6)
phase center variation	<ul style="list-style-type: none"> absolute antenna phase center variation file derived from I08.ATX
reference frame	<ul style="list-style-type: none"> IGS station coordinates are based on ITRF08
campaign a priori coordinates	<ul style="list-style-type: none"> from PPP solution (Tab. 5.6)
IGS a priori coordinates	<ul style="list-style-type: none"> station coordinates were given by their ITRF08 solution.
AGNES a priori coordinates	<ul style="list-style-type: none"> daily AGNES coordinates were determined in a network solution keeping IGS stations fixed to the ITRF08 solution. Then, the average of daily coordinates of the entire campaign period were calculated for each AGNES station.

Table 5.8: Summary of the settings for the 7-day gliding window double-difference network solution of the Zermatt campaign data. Only information different from Tab. 5.7 is included.

Parameter	Settings
processing mode	<ul style="list-style-type: none"> 7-day coordinates with a gliding window strategy. Normal equations of 7 consecutive days were stacked and troposphere parameters at day boundaries were combined.
estimated troposphere	<ul style="list-style-type: none"> concurrent troposphere parameters at day boundaries are combined within the 7-day gliding window.

5.1.6 Station coordinate repeatability

The coordinates of the campaign stations were estimated according to the PPP processing described in Sect. 5.1.5. Their daily coordinate repeatabilities in the east, north, and up component are presented in Figs. 5.9–5.11 and summarized in Tab. 5.9. Similarly, the network solution is included in the same table and corresponding figures are shown in Figs. E.1–E.3 in Appendix E.

The north component repeatability in the PPP solution is generally better than the east component. From the GPS constellation with its satellite gap in the north, one would expect the opposite. Even more surprising, most stations in Zermatt have a relatively bad view to the south (Figs. F.1–F.3 in Appendix F). It is likely that the satellite orbit geometry is beneficial for the north component in terms of elevation coverage. The prevalence of north-south trajectories in mid-latitude regions apparently outweighs the bad view to the north and south. In the network solution, the two horizontal components show roughly the same repeatability with a slightly poorer repeatability of the north component. The strong improvement in the east component of the network solution is a known consequence of the ambiguity resolution. The a posteriori RMS reflects the situation in both cases (not shown): The PPP solution has a higher RMS for the east component and the network solution's north component RMS is slightly higher or equal to the easting RMS. Table 5.9 demonstrates the clear improvement in repeatability from the PPP to the network solution. As we will see in sections to follow, the poorer repeatability of the PPP solution does not necessarily lead to less accuracy in troposphere parameters with respect to radiosonde ZTDs.

Two groups of stations show particularly poor repeatability in the up components. These are the stations with the Javad receiver and antenna and those with the LEIAT502 antenna. Relatively poor repeatabilities of the PPP solutions' up component are observed for the Novatel system (NOV600 antenna), the Trimble 5700 system and the LEIATX1230+GNSS antenna (Tab. 5.9). The most consistent solutions were delivered by the LEIAR25.R3, the LEIATX1230GG and the LEIAX1202GG antennas and associated receivers. Except for the antenna LEIAT502, azimuth-dependent phase center variation values are available and have been applied. Additionally, all antennas are absolutely calibrated. What makes the receiver and antenna groupings explain the observed repeatability pattern relatively well? Are different multipath rejection strategies or antenna designs the suspects? It is mentioned in Section 5.1.1 that the site of the investigation creates a funnel like station distribution when viewed from the south. The skyview of lower stations are thus more obstructed by mountains. As a result, the minimum elevation of observed satellites becomes higher and the number of observations is reduced with lower altitude (Tab. 5.10). Equally well as the receiver and antenna groupings, minimum elevation and number of observations explain the individual station repeatabilities in the up component. Take for example the stations HERM, PARK and WINK, all equipped with the LEIAT502 and all being at low altitudes. Their skyviews are heavily obstructed. The situation is more complex for the Javad stations. The station IMHO (Tab. 5.2) has many obstructions and the environment is likely to create a lot of multipath. Probably by mere chance, BLAT gets satellites down to elevations of 5.3° and has an acceptable amount of observations, but is definitely affected by its bad viewing geometry (Fig. F.3 in Appendix F). On the other hand, UFDR has a good and all-around viewing geometry (Fig. F.2 in Appendix F), but loses a large number of observations during the processing. Inspection of the photos from the station's surrounding suggests that the small-scale topography is not well represented in the DHM. This small-scale topography might cause a lot of multipath. Additionally, the Javad antennas seem to be prone to multipath effects. The relatively poor up component results of stations HUBE, ZMUT, GIFT and RECH are likely caused by strong obstructions.

The horizontal components of most stations show little tendency to permanently move in one direction throughout the campaign. A SE movement of the station HOER remains speculative. At least, it would reasonably fit the geological situation. The station was situated on a seemingly solid rock on a SE facing scree slope. In contrast to the stability of the stations in the horizontal, the vertical component of some stations show a downward movement in the course of the campaign (Figs. 5.9–5.11). The tendency is prevalent in the PPP solution, but also shows up in a few network solutions. These trends have been estimated with a simple linear regression and have

been included in Tab. 5.10. Likewise to the vertical coordinate repeatability, the trend is larger in case of high elevation cutoff and low number of available observations. The station WINK builds an interesting exception to the rule. Despite the poor geometry, no statistically significant trend could be determined. The many trees around the station (Tab. 5.3) might cause a lot of diffraction and scattering, producing harsh conditions for the process of coordinate estimation. This is supported by the fact that in addition to the poor up component repeatability, WINK also displays an exceptionally poor east component. Consequently, the conditions might mask the trend. The station GUGL constitutes an exception in the opposite sense. Despite the lack of low-elevation observations, the trend remains in the range of several other stations, which measure observations down to 3° elevation. We should further note that GUGL observes different satellites as for example ZMUT or HUBE. The latter two stations have a similar minimum elevation, but display a pronounced trend. Hence, the number of observations and the minimum elevation are not suitable descriptors to unmask details in performance of station repeatability. More complex descriptors of satellite geometry, such as the a posteriori parameter uncertainties, would yield better explanations. For example, the a posteriori uncertainty of the up component of GUGL is smaller than for HUBE, and the one from HUBE is smaller than for ZMUT (not shown), being consistent with the size of the trend they suffer from.

The reason for the downward trends remains a matter of speculation. In view of the comparatively stable horizontal components of the stations showing strong downward trends, probable causes are multipath and inaccurate antenna phase center variation corrections that left their traces in the up component.

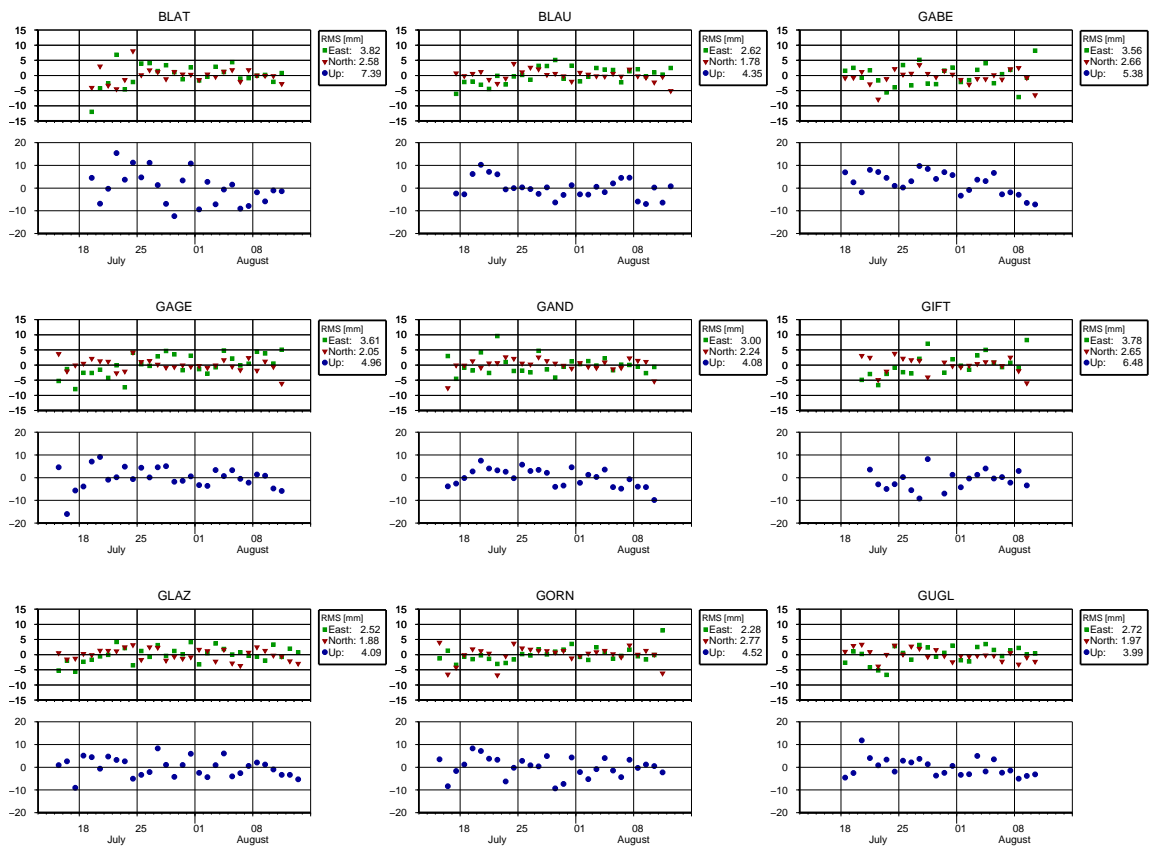


Figure 5.9: Daily coordinate repeatability of the precise point positioning solution of all Zermatt campaign stations. The Zermatt campaign stations are shown in Fig. 5.1 and described in Tabs. 5.1–5.3. Note the change in scaling in the up component of the stations UFDR, IMHO, HERM, WINK and PARK. The processing scheme used: PPP, 300s, daily, GMF, 2h.

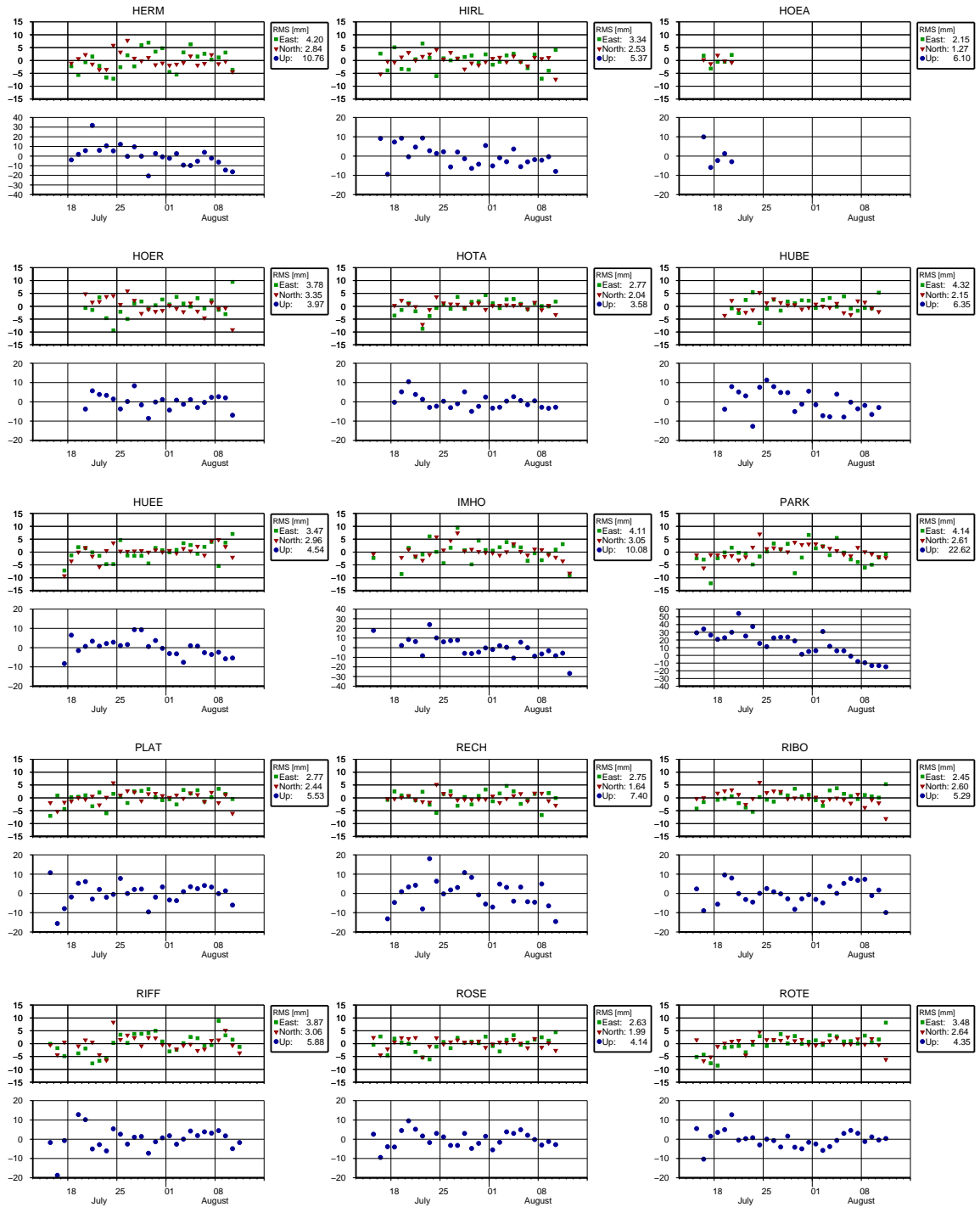


Figure 5.10: Station repeatability continued from Fig. 5.9.

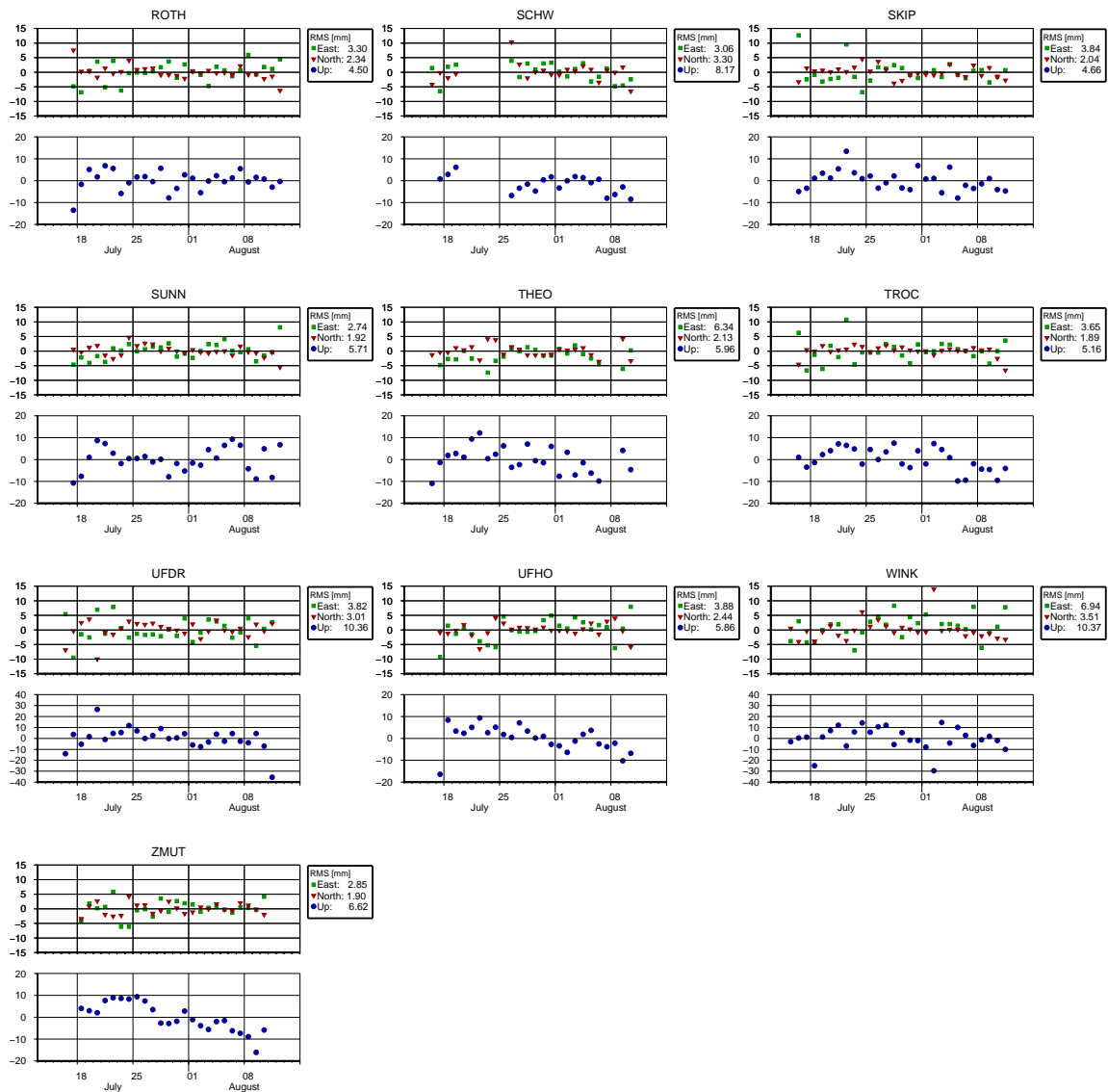


Figure 5.11: Station repeatability continued from Fig. 5.10

Table 5.9: Summary of station repeatabilities from the PPP (PPP, 300s, daily, GMF, 2h) and the network solution (NTW, 180s, daily, GMF, 2h), sorted according to receiver and antenna type. The RMS of each component is given in units of [mm].

Station	Receiver	Antenna	Radome	PPP solution			Network solution		
				East	North	Up	East	North	Up
BLAT				3.82	2.58	7.39	1.38	2.03	6.97
IMHO	JAVAD TRE_G3T DELTA	JAV_GRANT-G3T	NONE	4.11	3.05	10.08	1.65	1.74	6.21
UFDR				3.82	3.01	10.36	2.98	1.69	4.21
BLAU				2.62	1.78	4.35	1.29	1.14	2.96
GORN				2.28	2.77	4.52	1.03	1.90	4.11
RIBO	LEICA GRX1200+GNSS	LEIAR25.R3	LEIT	2.45	2.60	5.29	0.57	1.34	5.92
ROTE				3.48	2.64	4.35	2.20	1.97	5.37
ROTH				3.30	2.34	4.50	2.35	0.86	3.73
SUNN				2.74	1.92	5.71	1.08	1.18	4.42
HERM				4.20	2.84	10.76	1.77	1.98	8.09
PARK	LEICA SR530	LEIAT502	NONE	4.14	2.61	22.62	2.18	2.48	16.62
WINK				6.94	3.51	10.37	1.37	1.64	8.30
GIFT	LEICA RX1250TC	LEIATX1230+GNSS	NONE	3.78	2.65	6.48	0.88	1.85	4.37
HOTA				2.77	2.04	3.58	0.79	2.08	2.19
PLAT	LEICA RX1250TC	LEIATX1230GG	NONE	2.77	2.44	5.53	1.41	1.61	5.84
RIFF				3.87	3.06	5.88	2.19	2.13	6.31
SCHW				3.06	3.30	8.17	1.67	1.83	5.14
GABE				3.56	2.66	5.38	0.98	2.40	4.61
GAGE				3.61	2.05	4.96	1.99	1.33	5.73
GAND				3.00	2.24	4.08	1.63	1.69	3.74
GLAZ				2.52	1.88	4.09	1.22	1.79	3.43
GUGL				2.72	1.97	3.99	0.96	1.48	3.62
HIRL				3.34	2.53	5.37	1.57	1.98	5.19
HOEA				2.15	1.27	6.10	1.45	1.72	7.70
HOER	LEICA GX1230GG	LEIAX1202GG	NONE	3.78	3.35	3.97	2.28	2.17	4.13
HUEE				3.47	2.96	4.54	1.80	2.88	3.36
RECH				2.75	1.64	7.40	1.80	1.22	6.85
ROSE				2.63	1.99	4.14	1.54	1.64	3.85
SKIP				3.84	2.04	4.66	1.89	1.57	2.98
THEO				6.34	2.13	5.96	2.70	1.08	3.98
TROC				3.65	1.89	5.16	1.58	1.20	4.12
UFHO				3.88	2.44	5.86	1.38	2.02	4.23
HUBE	NOV DL4	NOV600	NONE	4.32	2.15	6.35	2.40	1.62	4.90
ZMUT	TRIMBLE 5700	TRM39105.00	NONE	2.85	1.90	6.62	1.76	1.47	5.52

Table 5.10: Minimum elevation and maximum number of observations encountered in the processing for each campaign station. The two major processings from Sect. 5.1.5 are presented: (PPP, 300s, daily, GMF, 2h) and (NTW, 180s, daily, GMF, 2h). Exemplary, the day 23 Jul 2010 was taken. All other days show very similar values. Additionally, a trend line in $\text{cm}/(30\text{days})$ and the trend's standard deviation (SD) of the up component was calculated for each station.

PPP solution					Network solution					
Sta.	Min. elev.	# of obs.	Trend	SD	Sta. 1	Sta. 2	Min. elev.	# of obs.	Trend	SD
BLAT	5.3°	2032	-1.3	0.6	BLAT	ZIM2	6.3°	3042	1.2	0.6
BLAU	3.9°	2302	-0.6	0.3	BLAU	ZIM2	3.8°	3541	-0.2	0.2
GABE	3.1°	2367	-1.1	0.4	GABE	ZIM2	3.0°	3590	-0.2	0.4
GAGE	3.3°	2401	-0.0	0.4	GAGE	ZIM2	3.1°	3543	0.6	0.4
GAND	3.1°	2553	-0.8	0.3	GAND	ZIM2	3.0°	3913	-0.2	0.3
GIFT	3.2°	2387	-0.6	0.7	GIFT	ZIM2	3.7°	3438	0.7	0.5
GLAZ	3.1°	1661	-0.3	0.3	GLAZ	HUTT	3.1°	2530	0.6	0.2
GORN	3.0°	2629	-0.2	0.3	GORN	ZIM2	3.1°	4107	0.5	0.3
GUGL	9.9°	2326	-0.7	0.3	GUGL	ZIM2	8.9°	3610	0.4	0.3
HERM	14.8°	2063	-2.7	0.8	HERM	ZIM2	13.9°	3001	-1.6	0.6
HIRL	3.1°	2542	-1.0	0.4	HIRL	ZIM2	3.1°	3980	-0.7	0.4
HOER	3.1°	2071	-0.4	0.4	HOER	ZIM2	3.3°	2878	0.8	0.4
HOTA	3.1°	2568	-0.7	0.3	HOTA	ZIM2	3.1°	3961	0.4	0.2
HUBE	7.4°	2098	-1.2	0.6	HUBE	ZIM2	6.4°	3300	0.2	0.5
HUEE	3.1°	2398	-0.7	0.4	HUEE	ZIM2	3.4°	3666	-0.2	0.3
IMHO	8.8°	1447	-2.5	0.6	IMHO	ZIM2	9.8°	2814	-0.7	0.5
PARK	15.1°	1684	-5.4	0.7	PARK	ZIM2	14.3°	2375	-4.6	0.8
PLAT	3.3°	2172	0.4	0.4	PLAT	ZIM2	3.0°	3346	0.7	0.4
RECH	5.0°	2309	-0.6	0.6	RECH	ZIM2	4.6°	3587	-0.4	0.6
RIBO	5.1°	2203	0.3	0.4	RIBO	ZIM2	5.5°	3361	0.8	0.4
RIFF	3.5°	772	0.3	0.5	RIFF	ZIM2	4.8°	1110	0.9	0.4
ROSE	3.2°	2447	0.0	0.3	ROSE	ZIM2	3.2°	3733	0.8	0.2
ROTE	3.2°	2194	-0.1	0.3	ROTE	ZIM2	4.3°	3405	0.7	0.4
ROTH	3.1°	2501	0.1	0.3	ROTH	HUTT	3.2°	3901	0.4	0.3
SKIP	3.3°	2431	-0.6	0.3	SKIP	ZIM2	3.0°	3664	0.1	0.2
SUNN	5.1°	2248	0.2	0.4	SUNN	ZIM2	5.8°	3499	0.3	0.3
THEO	3.3°	1495	-0.6	0.5	THEO	ZIM2	3.0°	2204	0.3	0.3
TROC	3.3°	2318	-1.0	0.3	TROC	ZIM2	3.0°	3597	-0.3	0.3
UFDR	5.3°	1672	-1.5	0.7	UFDR	ZIM2	5.3°	2798	0.3	0.3
UFHO	3.1°	2411	-0.9	0.5	UFHO	ZIM2	3.4°	3639	-0.8	0.3
WINK	15.0°	1832	-0.5	0.8	WINK	ZIM2	14.3°	2732	1.1	0.6
ZERM	5.0°	2103	0.1	0.4	ZERM	ZIM2	4.8°	3262	0.5	0.3
ZMUT	7.4°	1945	-2.3	0.3	ZMUT	ZIM2	7.4°	2826	-1.0	0.4

5.2 Troposphere results

The estimated ZWDs from the Bernese processing described in Sect. 5.1.5 and the a priori ZDD were added to form the ZTD. The ZTD time series of the PPP solution (PPP, 300s, daily, GMF, 2h) of the campaign stations are shown in Figs. G.1, G.2 and G.3 of Appendix G. The ZTDs are analysed and validated in the following paragraphs. The results from different processing strategies will be compared to the radiosonde data and to data from the NWP model. The calculation of ZTDs from radiosonde data has been outlined in Sect. 2.1 by Eq. (2.1) and (2.6). The integration of the radiosonde refractivities is pursued till the maximum recording height of each radiosonde. In some cases, heights above 20 km are reached (Tab. 5.4). The last meteo values measured at profile top serve as basis to calculate the contribution of the remaining atmosphere to the ZTD value using Eq. (2.11). The same procedure is applied to the NWP model fields, integrating along the zenith direction. Only stations whose coordinates lie within the NWP model domain are calculated. No extrapolation below model orography has thus been attempted. Additionally, GPS stations situated below the sonde starting height have not been compared to the radiosonde.

5.2.1 Time resolution of the troposphere parameter

If one processes GPS data with the aim to obtain troposphere parameters, one is immediately faced with the question of parameter spacing of the ZTDs. At what interval should the zenith delays be estimated? Can one truly recover temporal fluctuations in the ZTDs at scales of 30 minutes? Fig. 5.12 shows the ZTD time series for selected campaign stations at a coarse 3-hour parameter spacing. The radiosonde integrated values are shown as filled circles. In general, the time variations are well represented by the GPS solution. A more detailed inspection reveals several deficiencies caused by the coarse spacing. Exemplary, we discuss 4 cases with clear deviations of the GPS solution from the radiosonde solution:

- (a) launch 5 of 20 Jul 2010
- (b) launch 6 of 21 Jul 2010
- (c) launch 5 of 22 Jul 2010
- (d) launch 2 of 23 Jul 2010.

The parameter spacing has been decreased to 2 hours in Fig. 5.13. A huge improvement has been achieved for launch (b), (c) and (d), whereas (a) had no gain from the finer spacing. In cases (b) and (d), the GPS solution does still not satisfactorily follow the marked peak suggested by the radiosonde. Since Tab. 5.4 tells us that the sonde usually reaches the troposphere after less than an hour and has passed the lower troposphere containing most water vapour after half an hour, one would expect an improvement from decreasing the spacing even further. The 1-hour solution in Fig. 5.13 hints at an improved representation of the peak on the evening of 21 Jul 2010, i.e. of case (b). The difference of the GPS solution to the last launch (d) of the campaign has also decreased. This very last flight is instructive: A sonde was launched 10:00 a.m., but some error happened in the recording unit. No data could be recovered from that flight. At the time of flight, it was slightly raining. A new sonde had to be started half an hour later at 10:30 a.m., when the rain had ceased. There must have been very rapid changes in the troposphere, which seem to be represented in the 1-hour solution. Figure 5.14 hints at the possibility that shifting the radiosonde on the time axis by only half an hour in one or the other direction would often result in markedly better agreement with GPS. Is GPS indeed capable of reproducing such sharp changes in the atmosphere? With respect to the sensing of sharp atmospheric changes, the 30-minute parameter spacing was hoped to perform even better than the 1-hour solution. This notion could not be confirmed, as shown in Fig. 5.15. None of the discussed peaks has gained from the finer spacing of 30 minutes. More noise seems to have entered the solution. Somehow disturbing is the fact that station ZERM being the closest GPS station to the radiosonde does not show the fast fluctuations during launch (d). Two influences might affect the GPS to radiosonde comparison: Either the radiosonde measurements are not capable to resolve the temporal and spatial heterogeneities due to their one-dimensionality

or GPS is affected by errors from unmodeled delays such as multipath.

In an attempt to quantify the performance of the time series solutions, boxplots have been generated for the 2-hour (Fig. 5.16a), the 1-hour (Fig. 5.16b) and the 30-minute solution (Fig. 5.16c). From a statistical point of view, the GPS solution does not gain from a finer spacing. The quartiles and the minimum and maximum values slightly increase from the 2-hour to the 1-hour spacing and become clearly worse in case of the 30-minute spacing. In conjunction with the launches (b) and (d) from the time series, the boxplots suggest that the radiosonde was not always able to depict very sharp temporal changes. Even though one would favour the 2-hour solution from the statistics, the 1-hour solution is likely to perform best in terms of temporal representativity.

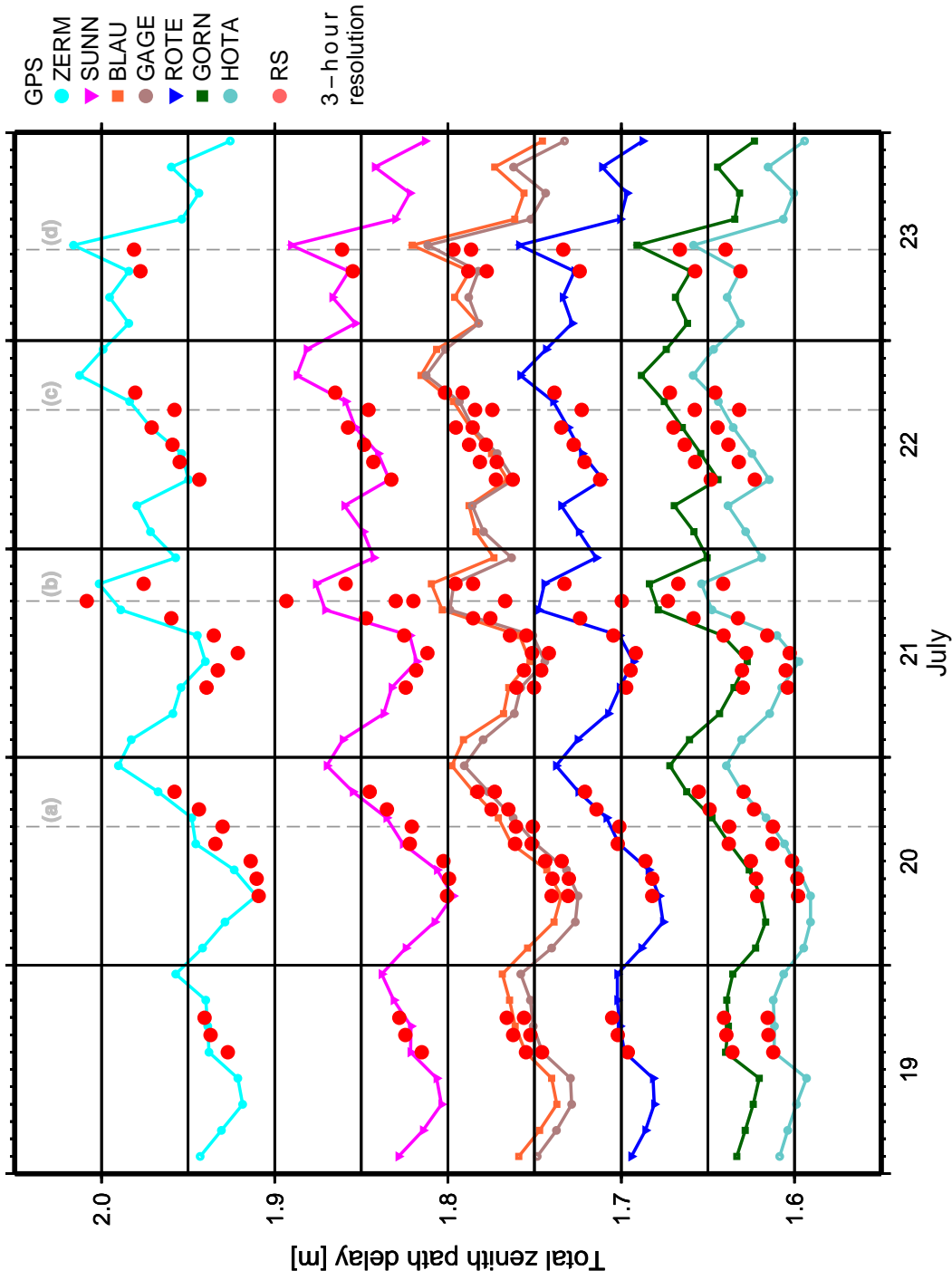


Figure 5.12: Time series of ZTDs of selected campaign stations which cover a wide height range. The ZTD parameters were calculated at 3-hour resolution and the coordinates were estimated daily (NTW, 180s, daily, GMF, 3h). Results from radiosonde integration are shown as red dots. The time system is kept in local DST, which is approximately UTC + 2 hours. Due to the 3-hour resolution of the GPS ZTDs, the first GPS data point of each day starts at 2 a.m. and the last at 11 p.m. The dashed lines mark the launches that are discussed in Sect. 5.2.1.

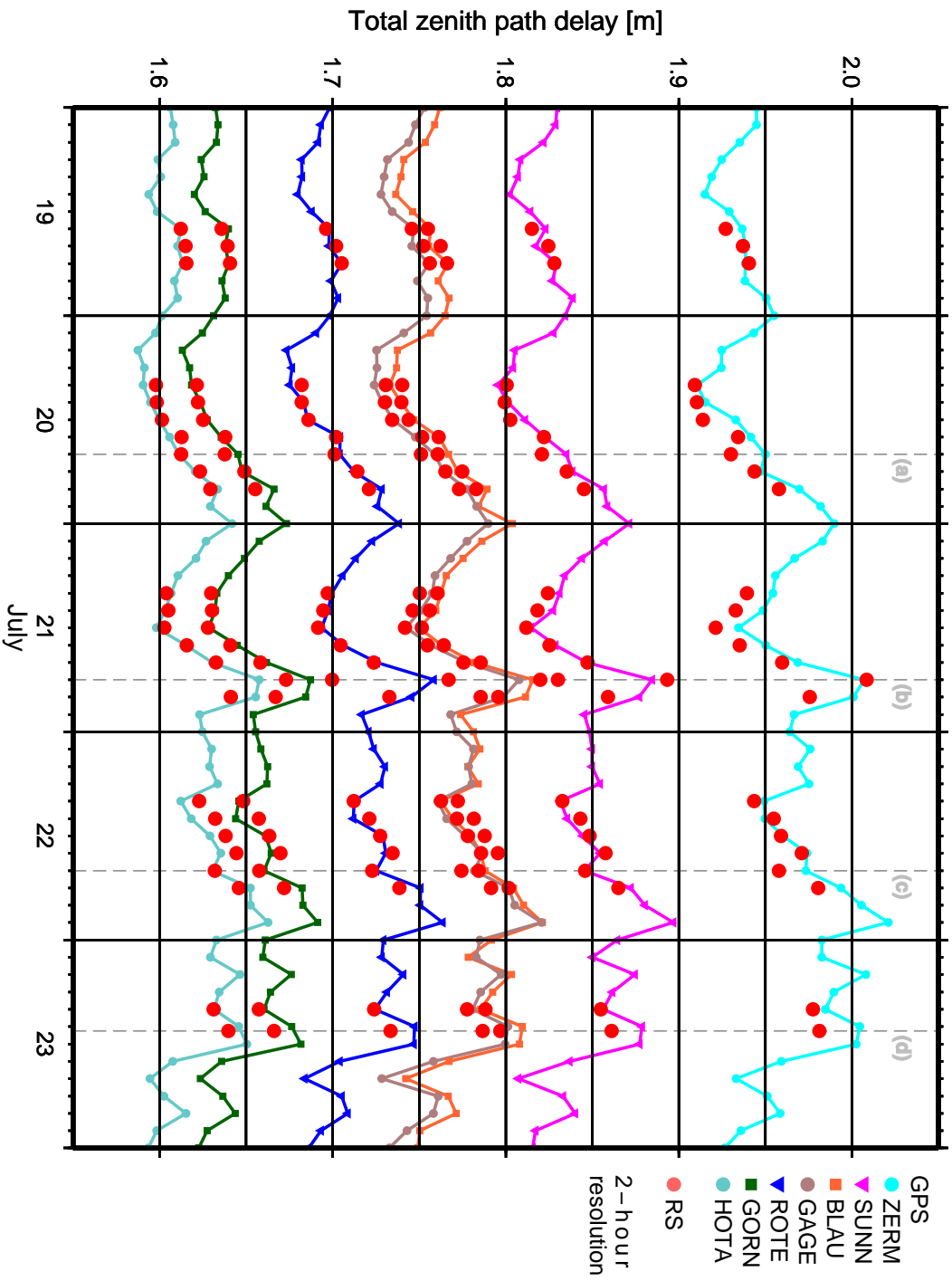


Figure 5.13: Time series of ZTDs of selected campaign stations. The ZTD parameters were calculated at 2-hour resolution (NTW, 180s, daily, GMF, 2h). All other information as for Fig. 5.12.

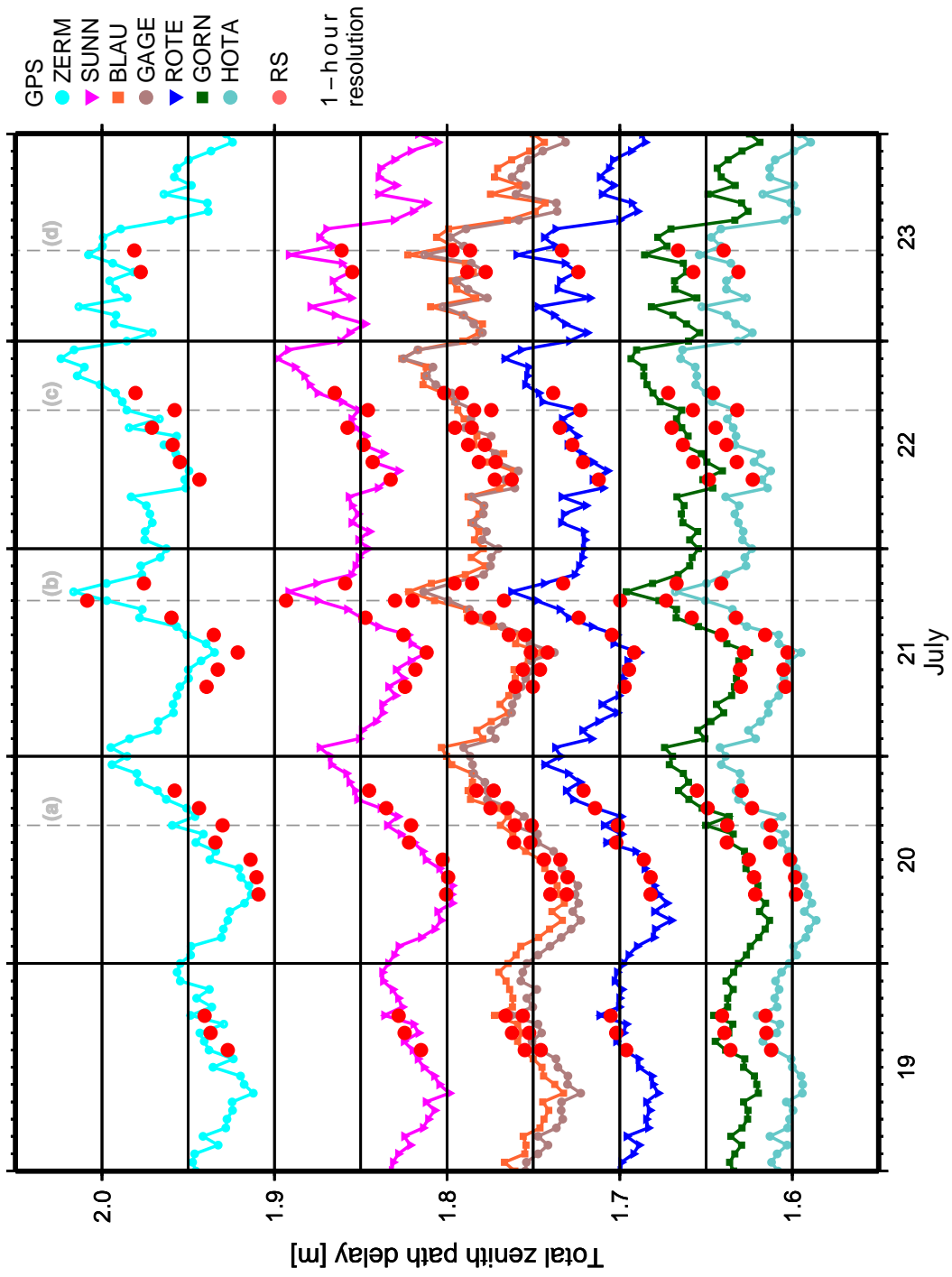


Figure 5.14: Time series of ZTDs of selected campaign stations. The ZTD parameters were calculated at 1-hour resolution (NTW, 180s, daily, GMF, 1h). All other information as for Fig. 5.12.

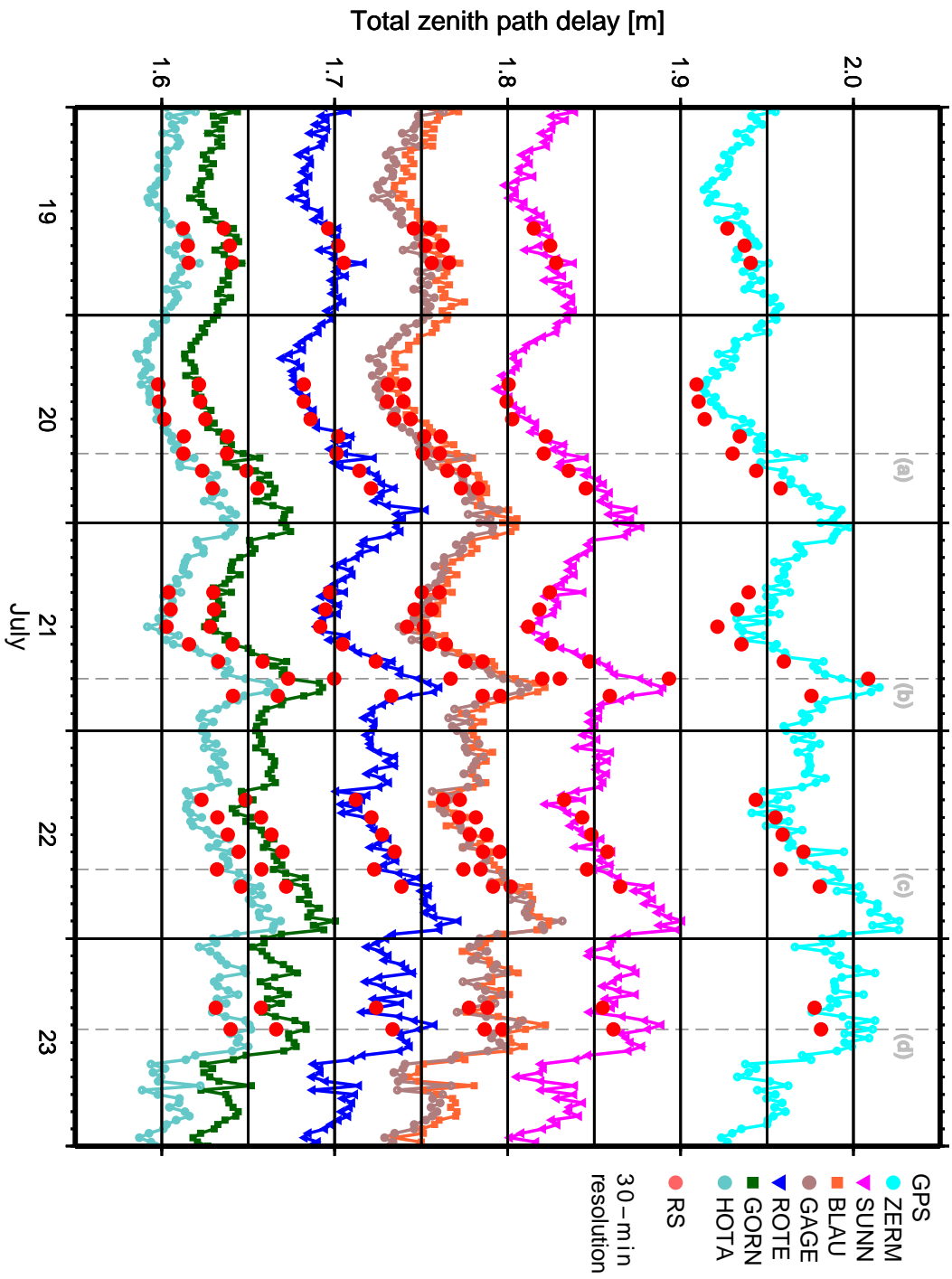


Figure 5.15: Time series of ZTDs of selected campaign stations. The ZTD parameters were calculated at 30-minute resolution (NTW, 180s, daily, GMF, 30min). All other information as for Fig. 5.12.

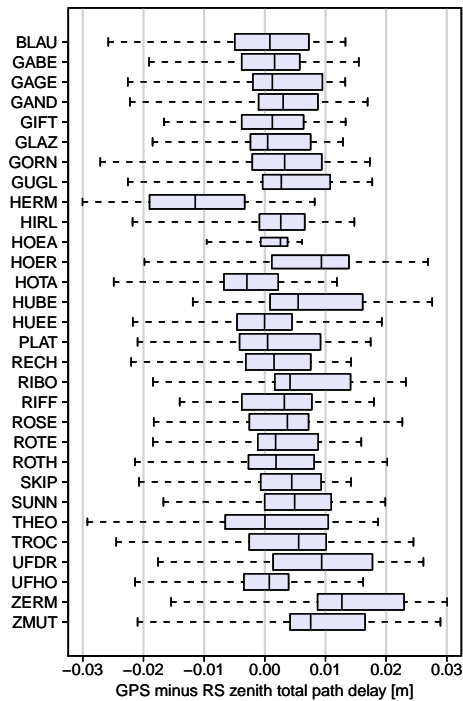
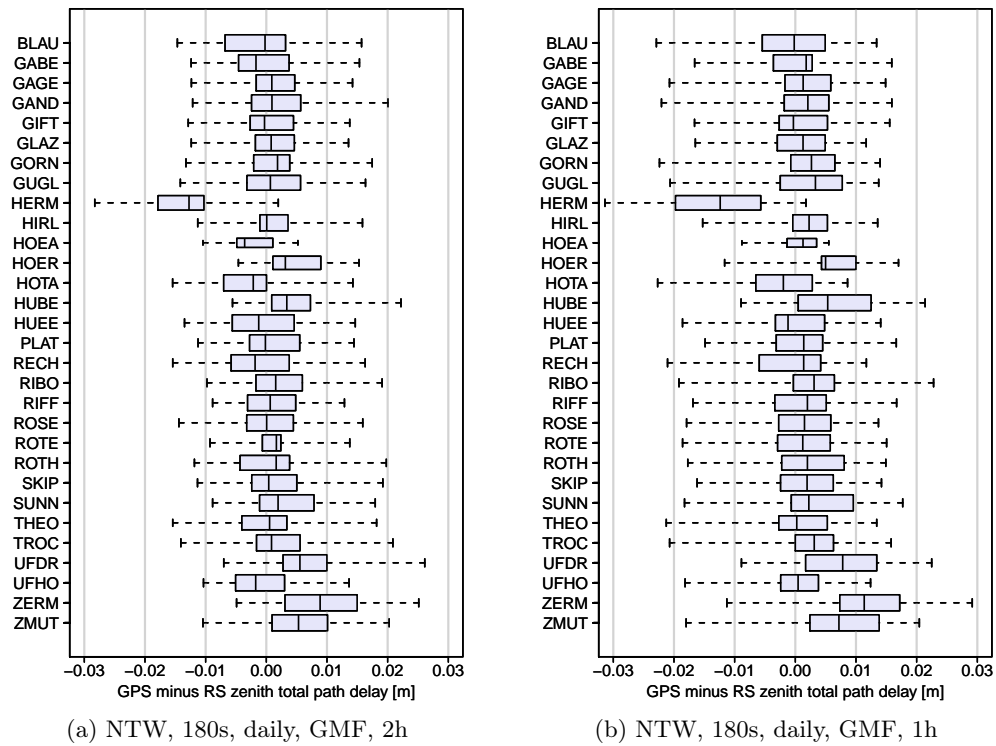


Figure 5.16: Boxplots comparing total zenith path delays estimated with GPS to path delays calculated from radiosonde launches (RS). The GPS path delays were calculated at different time resolutions. The width of the boxes along the ordinate is proportional to the square-root of the number of data points to create the statistics of each box. The number of values is given in the last column of Tab. D.1 and has a maximum of 25, which is the number of radiosonde launches. The maximum number was not always reached due to lacking GPS data or due to a formal GPS standard deviation from the GPS processing of > 5 mm, which was considered an outlier.

5.2.2 Network versus Precise Point Positioning solution

The radiosonde comparisons of the previous section have been carried out for many processing strategies (Tab. D.1 in Appendix D.1). In the following, we will analyse summary histograms of the differences between the GPS and the radiosonde solutions of the various processing strategies listed in Appendix D.1. The median histograms of Figs. 5.17a–j show only few differences between the strategies. A general overestimation of the GPS ZTDs with respect to the radiosonde is obvious. If the offset stems from a systematic component in the GPS processing or from the radiosonde measurements and processing remains debatable. Even the influence of both can not be precluded, as was demonstrated in Chap. 3. A different humidity sensor can easily change the sign of the bias between GPS and radiosonde (Tab. 3.4). Similarly, changing the phase center variations of GPS antennas causes antenna specific offsets of several millimeters in their height coordinates and, eventually in their ZTDs (Tab. 3.5).

We will turn our attention to the question, if atmospheric ZTDs of the campaign stations are more accurate when processed in network instead of PPP mode. Due to the following reasons, a better estimation of the ZTDs is to be expected from the network solution:

- The coarse sampling interval of the basic PPP processing (Tab. 5.10) resulted in less observations than for the network solution.
- Coordinate repeatabilities were on average better for the network solution.
- Contrary to the PPP solution, the network solution included ambiguity resolution.

Comparison of Figs. 5.18a and 5.19a with corresponding Figs. 5.18f and 5.19f reveals, however, superior accuracy of the PPP ZTDs, despite the lower number of observations. One could argue that the double-differencing removes many low elevation observations not being common to both stations of a baseline. Table 5.10 disproves the argument. This is due to the favourable sky visibility of ZIM2, making the horizons of the campaign stations being the limiting factor. The PPP solution also performs better in case of higher observation sampling. The network sampling interval has been decreased from 180s to 30s (compare Fig. 5.18a to 5.18e and Fig. 5.19a to 5.19e) and the PPP sampling interval from 300s to 30s (compare Fig. 5.18f to 5.18g and Fig. 5.19f to 5.19g). It should be noted that the increased sampling was not particularly useful. The formal uncertainty of the ZTD parameters was lowered by a factor of $\approx \sqrt{10} = 3.2$ and $\approx \sqrt{6} = 2.4$ for the PPP and NTW solution, respectively. The actual accuracy remained virtually the same for 300s and 30s sampling of the PPP or 180s and 30s of the NTW solution.

Even though the parameter spacing changes the statistical pattern of the network and the PPP solution, the PPP solution remains always superior (e.g., compare Fig. 5.19e to Figure 5.19h). It is interesting to note that the finer parameter spacing affects the network solutions more than the PPP solutions (e.g., Figs. 5.19a and b versus Figs. 5.19g and h). The weekly network solution (Figs. 5.18j, 5.19j) is of similar accuracy as its daily counterpart and remains thus of lower quality than the PPP. We conclude that the common mode removal characteristics of the double-differencing improves coordinate repeatability, but degrades the troposphere estimation accuracy. In summary, the 2-hour parameter spacing results in a GPS minus radiosonde standard deviation of 6–8 mm for the network solution. The PPP solution achieves a standard deviation of 4–6 mm.

5.2.3 Mapping function

The influence of the applied tropospheric mapping function has been investigated with two network solutions using 1-hour troposphere parameter spacing. First, the Global Mapping Function was switched on for the a priori dry part and the estimated wet part. Secondly, dry Niell constituted the a priori and wet Niell the estimated part. The medians of the difference between the GPS and the radiosonde solution show hardly any change in quality. There are some more medians in the 2–4 mm range in the GMF solution (Fig. 5.17b), while the Niell solution has an increased amount of 0–2 mm medians (Fig. 5.17d). The dominant part resides in the 0–2 mm bin in either case. Similarly, the Inter Quartile Range (IQR) with Niell (Fig. 5.18d) has less entries in the

6–8 mm bin, but more in the 4–6 mm than GMF (Fig. 5.18a). The histograms of the standard deviations are almost identical (Figs. 5.19a and d). Differences between the standard deviations are of the order of sub-millimeter (Tab. D.1 in Appendix D). These findings are in accordance with previous studies. In mid-latitude Europe, the effect of the hydrostatic GMF compared to the hydrostatic Niell mapping function onto the mean height is approximately 0–2 mm in July (Boehm et al., 2006a). Correspondingly small differences are to be expected in the zenith total delay. The estimation process of the non-hydrostatic part mitigates the differences even further.

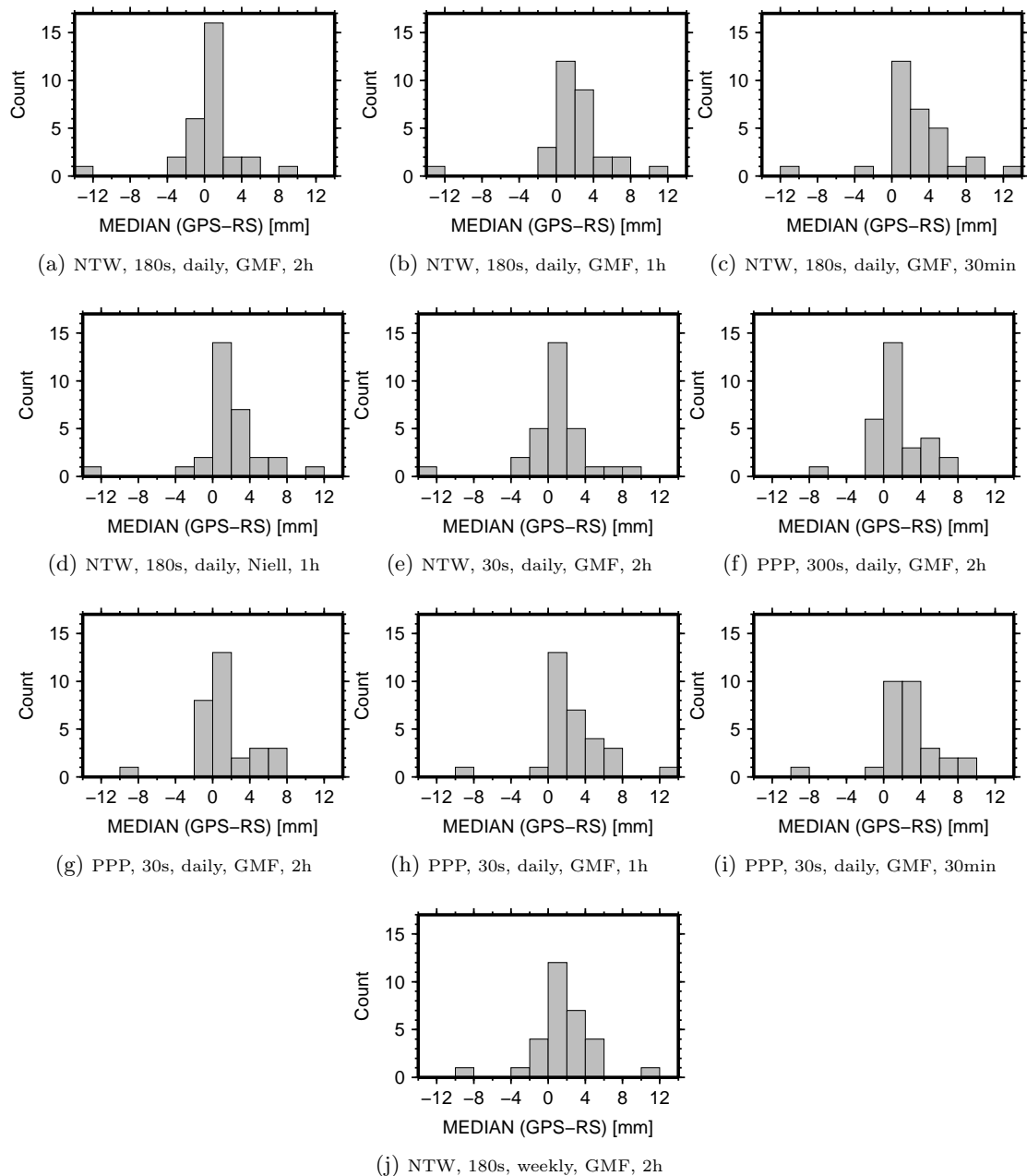


Figure 5.17: Histograms summarizing the medians of the GPS minus radiosonde differences (Tab. D.1 in Appendix D).

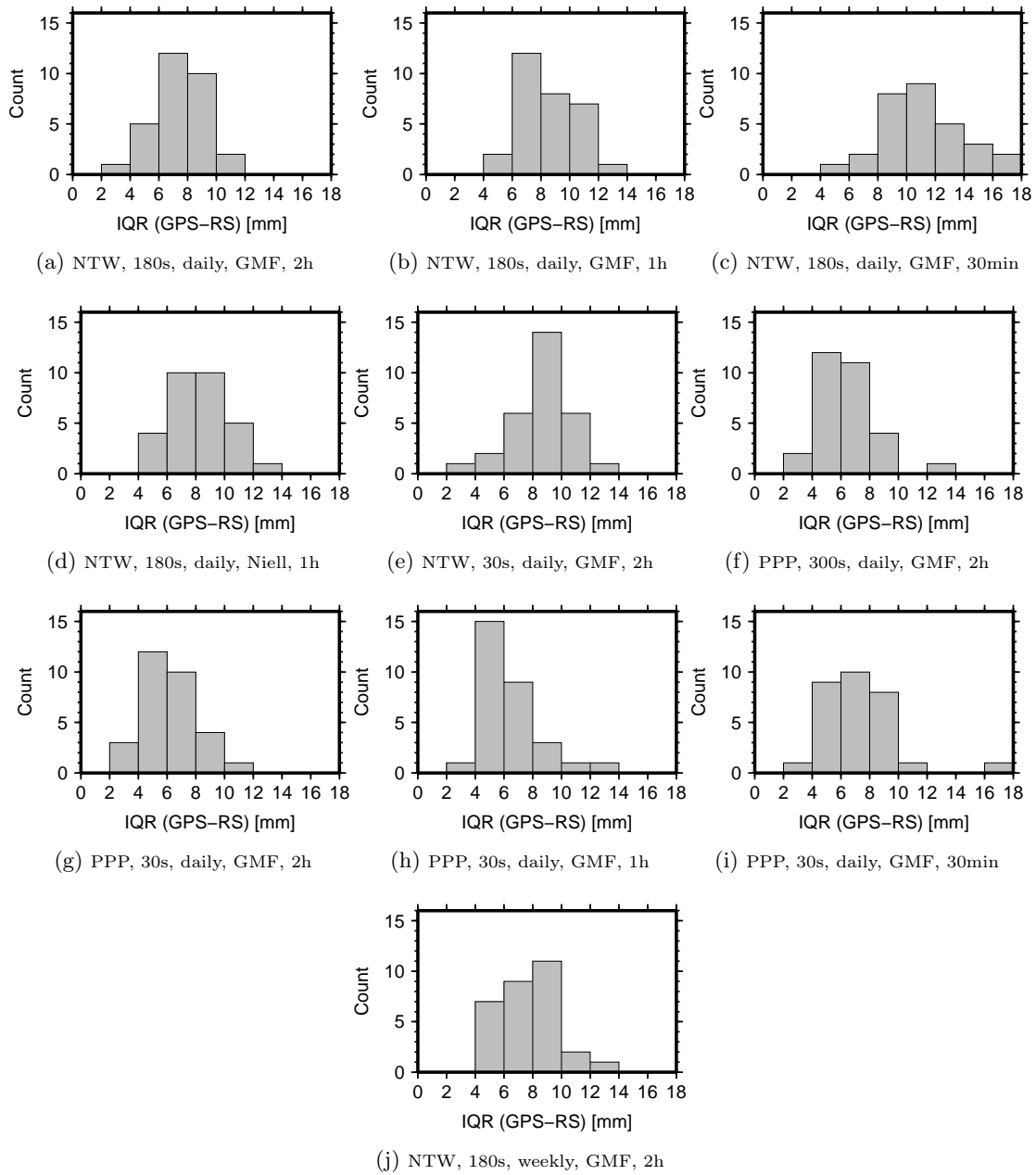


Figure 5.18: Histograms summarizing the interquartile ranges ($Q_{75\%} - Q_{25\%}$) of the GPS minus radiosonde differences (Tab. D.1 in Appendix D).

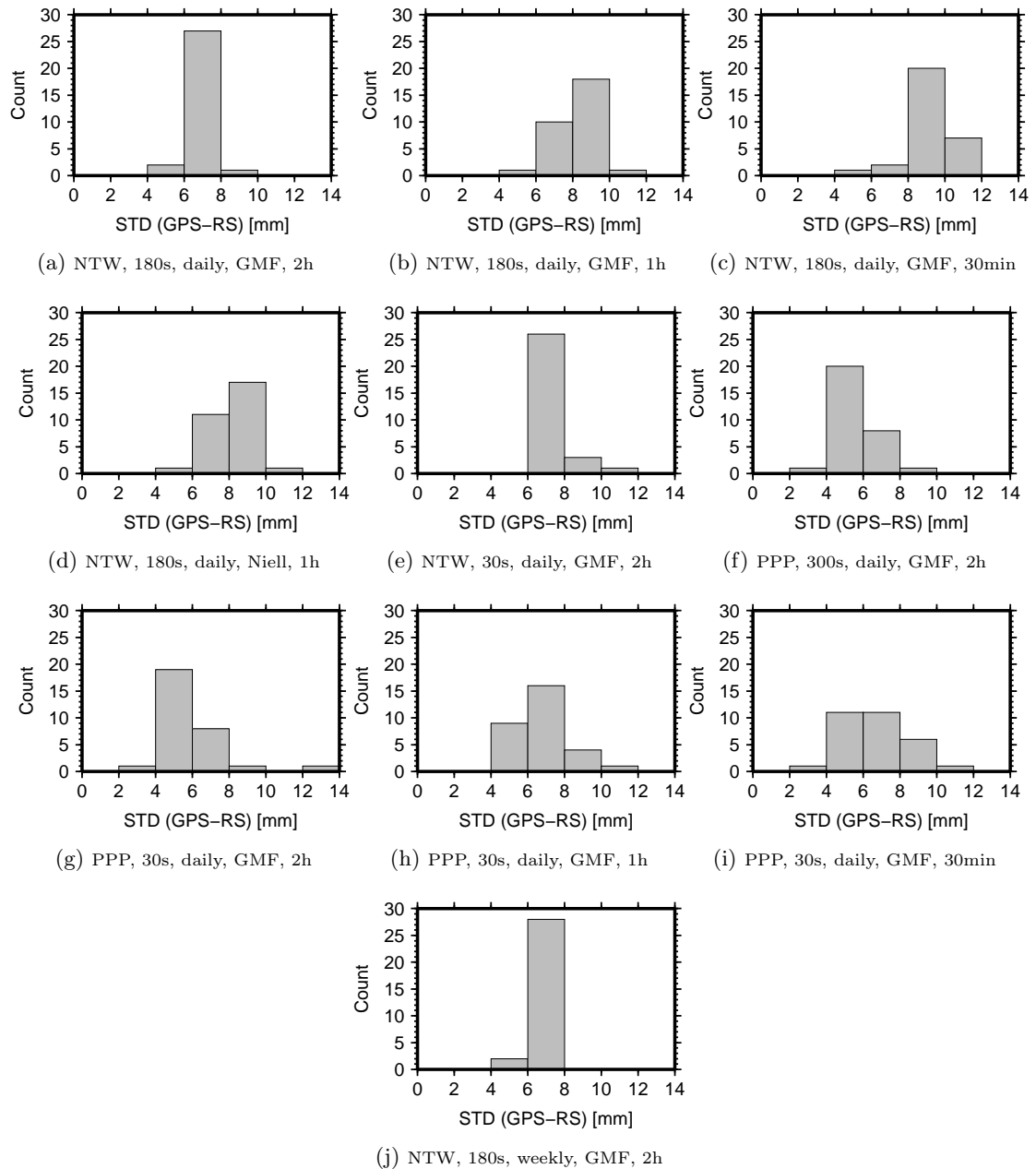


Figure 5.19: Histograms summarizing the standard deviations of the GPS minus radiosonde differences (Tab. D.1 of Appendix D).

5.2.4 ZTD accuracy and up component repeatability

Poorer station repeatability was observed for stations of more obstructed satellite view. How strongly do the obstructions affect the troposphere results? Figure 5.20 shows a height-sorted boxplot. We observe a larger positive bias for stations at lower altitudes. Additionally, the IQR has visibly increased towards the bottom of the network. There is only station HERM showing a markedly negative bias. The negative bias is likely to be attributed to the antenna's Phase Center Variation (PCV) and Phase Center Offset (PCO) correction. The antenna LEIAT502 has probably a poorly determined phase center variation pattern. Inspection of the phase center variation file reveals that this is the only campaign antenna without azimuth-dependent antenna pattern. The lack of azimuth-dependent values does obviously not explain the bias, but tells us something about the quality of the PCV correction, which is definitely of minor quality compared to the other antenna types. A more direct comparison between up component repeatability and troposphere RMS is represented in Fig. 5.21. We observe a general increase in the ZTD RMS for worse station repeatabilities. Hence, unmodeled delays likewise affect the up component and the ZTD. On the basis of Eq. (3.20) in Sec. 3.9, one would expect to see less influence of the unmodeled delays on the ZTD than on the up component. This notion is not confirmed by Fig. 5.21. A possible explanation results from the fact that uncertainties in the radiosonde ZTDs and the dissimilar spatial and temporal resolution of the GPS and radiosonde measurements add to the ZTD RMS.

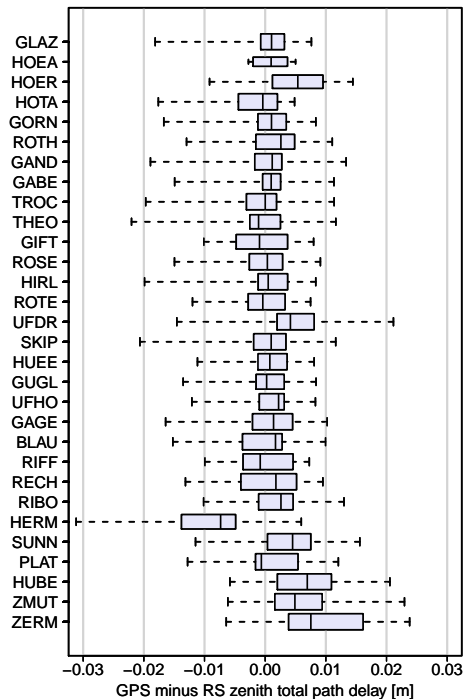


Figure 5.20: Boxplot comparing total zenith path delays from GPS (PPP, 300s, daily, GMF, 2h) minus path delays calculated from radiosondes (RS) sorted according to increasing station height from bottom to top. All other information as for Figs. 5.16a–c.

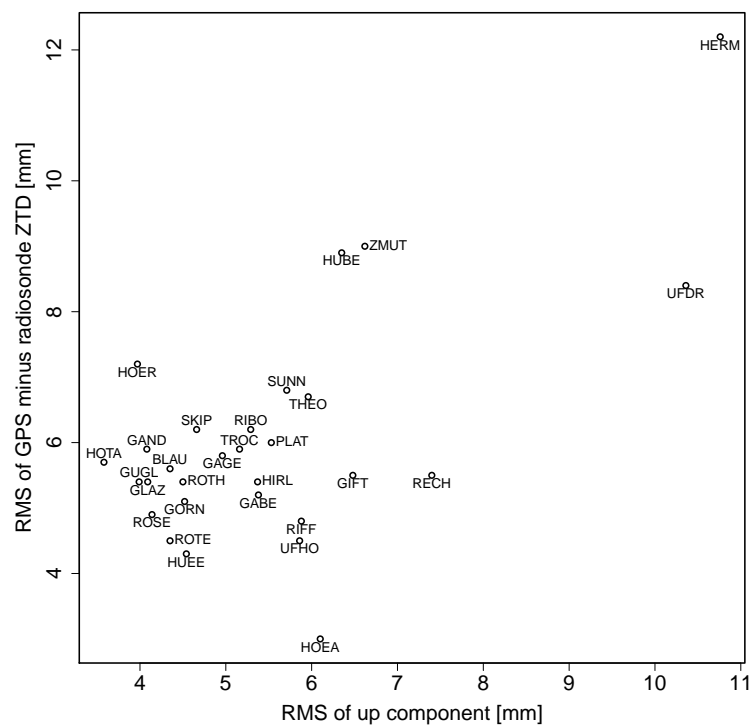


Figure 5.21: Comparison between the up component repeatability of the campaign stations and the ZTD difference between GPS (PPP, 300s, daily, GMF, 2h) and radiosonde. Both values are given as RMS. Only stations above radiosonde launch height are considered.

In order to better separate between the influence of obstructions or of low-quality antenna PCV and PCO corrections on the ZTD, we need to estimate systematic ZTD offsets of stations with the same antenna type. Some interesting stations in that respect are below the radiosonde starting height. With the help of an exponential model fitted to the radiosonde ZTDs and subsequent comparison to GPS ZTDs, station-specific offsets were derived:

$$B(s_j) = \text{MEDIAN}_{k=1\dots 25} \left(ZTD(t_k, s_j) - ZTD_{0,RS}(t_k) \cdot \exp \left(-\frac{h(s_j)}{H_{0,RS}(t_k)} \right) \right) \quad (5.1)$$

- $B(s_j)$: station-specific systematic offset of station s_j
- $ZTD(t_i, s_j)$: zenith total delay from GPS processing at time t_i and of station s_j
- $h(s_j)$: height of station s_j above reference height
- $ZTD_{0,RS}(t_k)$: zenith total delay at reference height of radiosonde-based layer model, estimated for each radiosonde launch
- $H_{0,RS}(t_k)$: scale height of radiosonde-based model, estimated for each radiosonde launch
- k : numbering of radiosonde launches during the campaign

The systematic offsets $B(s_j)$ are shown in Fig. 5.22, sorted according to height to be consistent with the boxplot in Fig. 5.20. A first inspection of the figure reveals very good agreement between the $B(s_j)$ and the medians from Fig. 5.20. Hence, the exponential model fitted to the radiosonde is a sufficiently good approximation to determine extrapolated medians. We can now confidently look at the $B(s_j)$ terms below radiosonde start height. If we trust the Javad stations BLAT and IMHO to be mostly affected by the obstructions and having relatively accurate antenna phase centers, Fig. 5.22 suggests that PARK and WINK experience a negative systematic offset underlying the large positive offset visible for stations BLAT and IMHO. Accordingly, the negative offset caused by the LEIAT502 antenna is of the order of $\approx 10\text{--}15$ mm and seems to affect all three stations (PARK, WINK, HERM) with the LEIAT502 antenna.

5.2.5 Horizontal spatial variability of GPS ZTDs

In addition to the systematic offset of Sect. 5.2.4, the troposphere ZTDs from the precise point positioning (PPP, 300s, daily, GMF,2h) were reduced by a layer model consisting of an exponential function fitted to the offset-corrected GPS ZTDs:

$$\rho^*(t_i, s_j) = ZTD(t_i, s_j) - B(s_j) \quad (5.2)$$

$$\rho(t_i, s_j) = \rho^*(t_i, s_j) - ZTD_{0,GPS}(t_i) \cdot \exp \left(-\frac{h(s_j)}{H_{0,GPS}(t_i)} \right) \quad (5.3)$$

where we have:

- $\rho^*(t_i, s_j)$: preliminary residual at time t_i and of station s_j after reduction of a station-specific offset
- $ZTD(t_i, s_j)$: zenith total delay from GPS processing
- $B(s_j)$: station-specific systematic offset, see Eq. (5.1)
- $\rho(t_i, s_j)$: final residual at time t_i and station s_j with an additional exponential layer model removed
- $h(s_j)$: height of station s_j above reference height
- $ZTD_{0,GPS}(t_i)$: zenith total delay at reference height of GPS-based layer model, estimated for each time step t_i
- $H_{0,GPS}(t_i)$: scale height of GPS-based layer model, estimated for each time step t_i

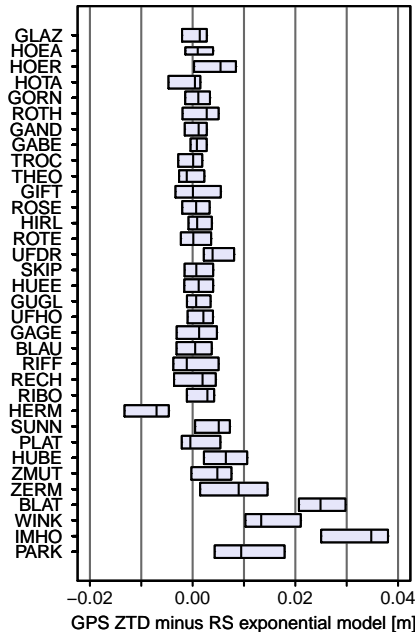


Figure 5.22: Station-specific systematic offsets $B(s_j)$ as boxplot. A measure of accuracy of the medians is given by the quartiles. The bias was calculated as shown in Eq. (5.1). GPS configuration: PPP, 300s, daily, GMF, 2h. They are sorted according to height with the highest station first. For the station SCHW, no bias correction can be calculated from the radiosonde data, since the station was not running during the launches (Fig. 5.3). The exponential fit to the radiosonde-derived ZTDs allows extrapolation to stations below radiosonde launch site (BLAT, WINK, IMHO, PARK).

In the following, we will have a close look at the residuals $\rho(t_i, s_j)$. We ask the question if the residuals display horizontal variability with spatial correlations or if they are of random nature. If they are of random nature, one can consider the profile of the radiosonde to describe the vertical structure of the entire campaign area. The radiosonde would be the perfect validation method for GPS ZTDs.

The residuals are deliberately produced from a PPP solution. Any correlations produced from double-differencing of a network solution can thus be avoided. The alternative to produce residuals without station-specific offset reduction has shown to be impractical. A lot of the horizontal variability has been masked. In the meantime, we should be aware that the offset correction $B(s_j)$ (Fig. 5.22) might also have reduced some of the station-specific climatologies. Exemplary, the final residuals $\rho(t_i, s_j)$ are shown for the 20 Jul 2010 (Figs. 5.23a–l). It is astonishing to see that even on scales of a few kilometers, the averaging nature of ZTDs does not even out all horizontal heterogeneity. Clear patterns and clusters demonstrate correlations between adjacent stations with those patterns moving in time over the investigation area. In Sects. 5.1.6 and 5.2.4, we have observed a strong relationship between satellite geometry and ZTD quality. This relationship must likewise apply to time-varying constellation changes. We should therefore check, if the patterns observed in Figs. 5.23a–l are to a large degree representing actual atmospheric heterogeneity or if they are mostly an image of the underlying constellation. The clear dominance of the constellation effect can be ruled out with Figs. 5.24a–d, showing consecutive days at the same hour of day. The four figures present a large degree of variability, which would otherwise not be visible if equal constellation caused most horizontal variability. The argument obviously presupposes that the constellation repeatability of four sidereal days is sufficiently represented by four solar days. The effect onto the

2-hour spacing of the ZTD parameter is assumed to be negligible.

Despite the possible influence from the satellite constellation, spatial correlations due to atmospheric fluctuations on scales of a few kilometers are observed in the campaign data. Further support for the plausibility of several millimeters fluctuation between stations a few kilometers apart comes from the publication by Nilsson et al. (2007b). For a definite answer, one could envisage a simulation study with the correct obstruction geometries incorporated into synthetic GPS data. Subsequent parameter estimation with Bernese might yield at least some qualitative measure of spatial patterns in the ZTDs. Without a simulation study, Figs. 5.23a-1 still indicate that a portion of the differences between the GPS- and radiosonde-derived ZTDs in Sect. 5.2.1 originate from actual atmospheric variability and not from inaccurate ZTDs.

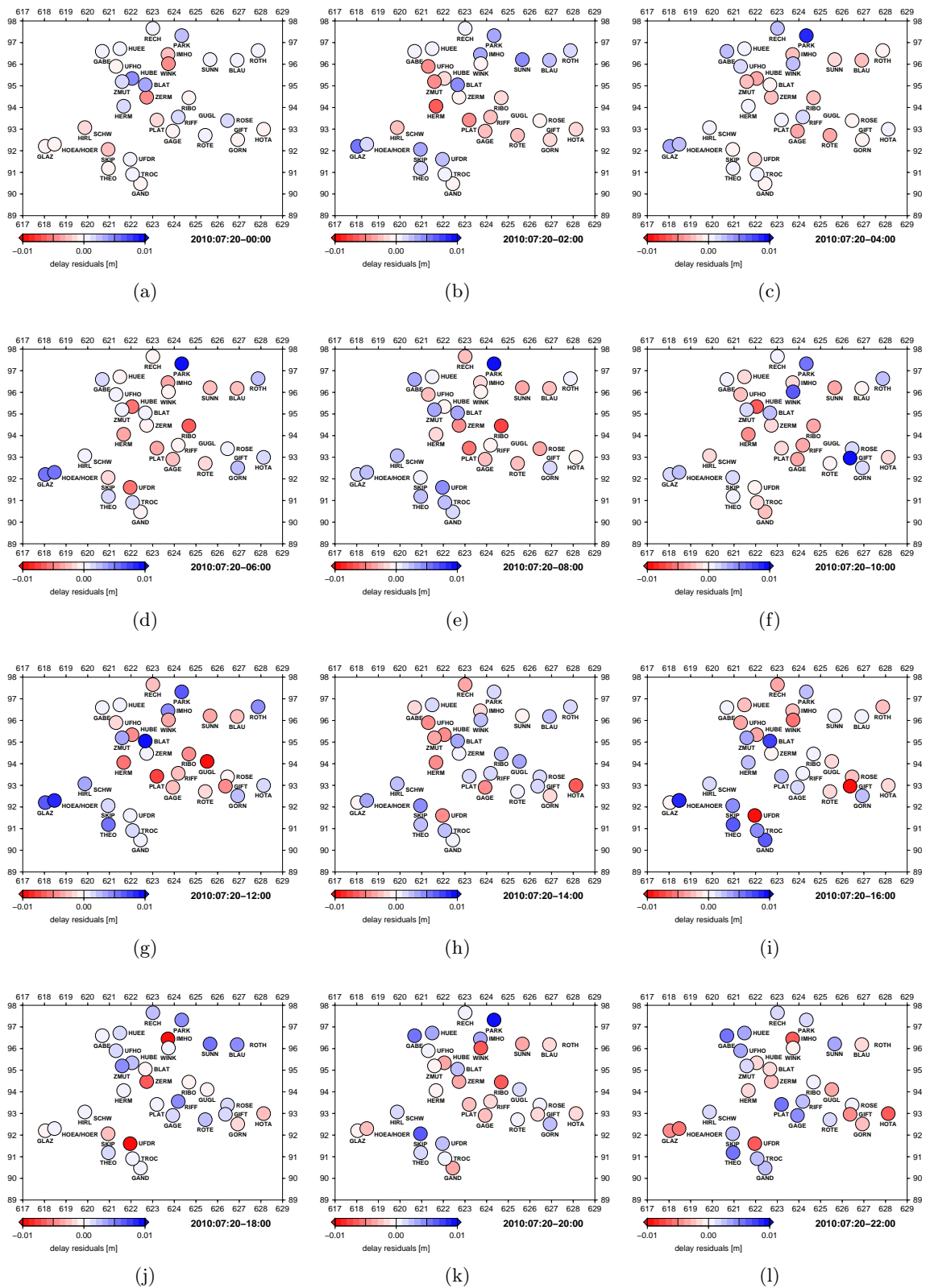


Figure 5.23: Sequence of ZTD maps reduced by the layer model Eq. (5.3) for one day of the campaign (20 Jul 2010). Processing of the GPS data was carried out with the configuration: PPP, 300s, daily, GMF, 2h. Station SCHW is lacking data for the entire day and ROTH lacks data for the last 6 hours of the day (Fig. 5.3).

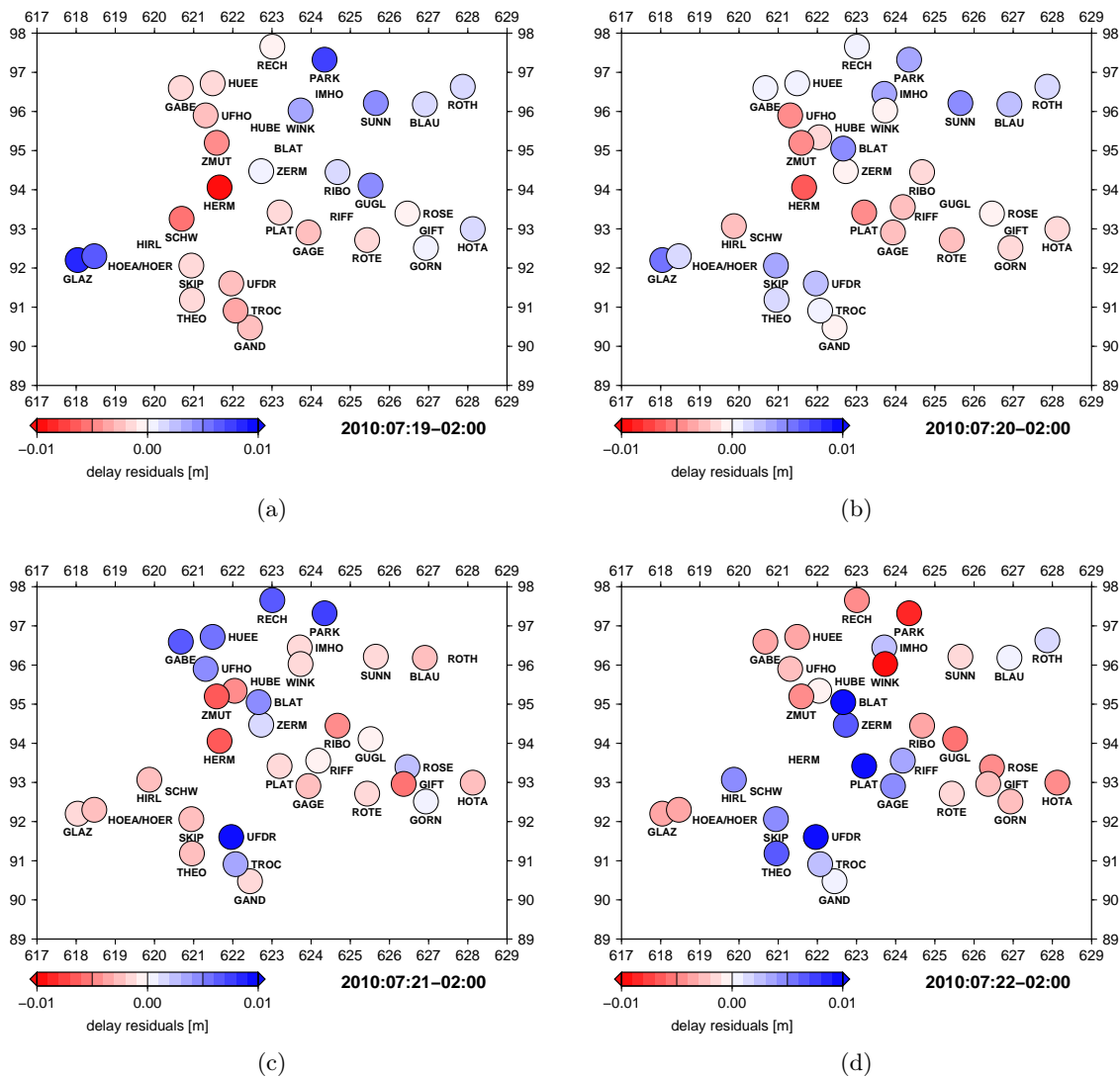


Figure 5.24: ZTD maps of four consecutive days and the same hour of day reduced by the layer model Eq. (5.3) with the GPS configuration: PPP, 300s, daily, GMF, 2h. If the influence of the GPS constellation caused the spatial patterns observed in Figs. 5.23a–l, we would expect roughly the same pattern after one sidereal day. However, distinctly different patterns are observed.

5.2.6 Comparison to NWP models

NWP model analyses provide us with a detailed 4D view of atmospheric state variables. Since the model equations basically describe the changes of these states and not the states themselves, the quality of the outcome heavily relies on observations of the state variables at certain times and positions. The weather model is more accurate, where more observations are assimilated. Additionally, regions of rugged topography are obviously more difficult to model than flatlands. Hence, an apparent proposal would be to densify the measurements in regions of high complexity. It is unfortunate that problems of numerical stability and computational burden force the modelers to flatten the actual rugged topography in exactly these complex regions. The resulting surface is then called the model orography. For the campaign region, the orography of COSMO-2 is shown in Fig. 5.25a and the difference to the actual topography in Fig. 5.25b. We immediately see a strong smoothing in the orography. Side valleys virtually disappear. The smoothing almost completely precludes the assimilation of ground measurements from the regions of the Alps. In case the station is below the model orography, extrapolation might introduce systematic errors. Even if a

meteorological ground station were inside the model domain, the variability of the measurement conditions close to the ground would sometimes prohibit the use of the measurements.

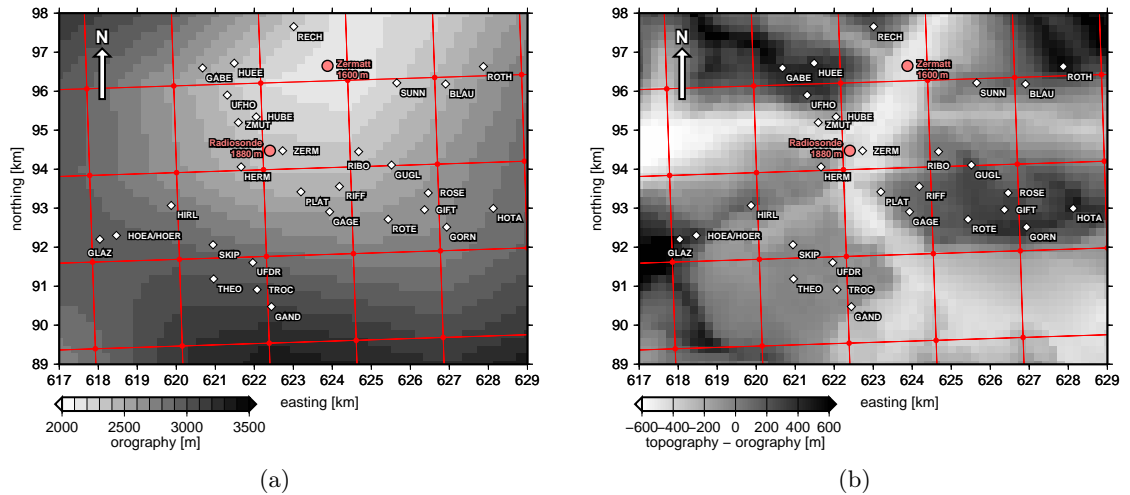


Figure 5.25: (a) Model orography linearly interpolated from the COSMO-2 grid points. (b) Difference between actual topography and linearly interpolated model orography. The COSMO-2 grid points shown in red are at the intersections of the slightly tilted lines in both figures (a) and (b).

In view of the presented difficulties to assimilate ground meteo data, the representativity of NWP model ZTDs is investigated. We would like to know, how well the NWP model ZTDs are represented in a region of high topographic complexity and if GPS meteorology has the potential to improve the NWP model state field.

The model fields of pressure, temperature and humidity are vertically integrated at the campaign station coordinates. For this purpose, AWATOS2 is used in the simulation mode. Refractivities are linearly interpolated from the model grid to where they are needed by the integration. The statistical results from the comparison of the GPS with the radiosonde and the corresponding NWP comparison are shown in Figs. 5.26a and b, respectively. The medians of the 25 NWP comparisons with radiosondes show stronger deviations from zero for almost all stations than the medians from the GPS comparisons. Furthermore, the IQR is clearly larger. The strong negative offsets of the stations GABE, HUEE, RECH and UFHO in Fig. 5.26b arouse suspicion about some hidden pattern. To clarify this issue, the NWP model ZTDs were determined at each topography position that was inside the model domain. At times of radiosonde launches, these ZTD values are compared to ZTDs from corresponding radiosonde heights. The medians of the comparison are plotted in Fig. 5.27 as a map. The figure nicely demonstrates that the difference of the model to the radiosonde is strongly region-dependent, whereas medians of the GPS minus radiosonde differences, shown as filled diamonds in the same figure, are much more homogeneous throughout the campaign domain. The findings suggest region-dependent biases in the NWP model on scales of a few kilometers. The complete GPS minus radiosonde and NWP minus radiosonde values from the investigation area are summarized in their respective histograms in Figs. 5.28a and b. The statistics are given in Tab. 5.11. The low mean difference between the NWP model and the radiosonde indicates that ZTDs of the NWP model COSMO-2 are extremely representative on averaging scales of $\approx 10 \text{ km} \times 10 \text{ km}$. A seemingly obvious reason for the small-scale biases might be the discrepancy between actual topography and smoothed model orography. Visual comparison of the median map (Fig. 5.27) to the topography minus orography map (Fig. 5.25b) does not point at a direct correlation between the two. The huge number of interactions in a NWP model would require an elaborate analysis to determine the dominant factors of these biases. As long as the factors are not known, we run the risk to destabilize the model when we introduce “raw” GPS ZTDs. Although the medians are small for almost all GPS stations (Fig. 5.26a), some of the stations have been demonstrated to produce considerable systematic offsets. Their influence upon assimilation

is hardly possible to foresee. Consequently, a bias correction with respect to the weather model is highly recommended and only stations viewing favourable satellite geometries should be used. With these corrections, the better IQR could then be exploited.

The temporal evolution of the NWP ZTD is tested in Fig. 5.29. The NWP model and the GPS ZTD accurately catch the fluctuations as measured by the radiosonde. For example, both methods observe the strong increases on the 20 and the 21 Jul 2010. Also the decrease between those two days is well represented. An interesting case is shown at 10 a.m. on 23 Jul 2010. The radiosonde seems to miss the sharp peak, whereas NWP model and GPS both depict such a change. It has been discussed in Sect. 5.2.1 that radiosonde launch (d) is probably incapable to show such fast fluctuations. With respect to the NWP model, superior results of GPS are shown on the afternoon of the 22 Jul 2010 (launch (c) in Sect. 5.2.1). The NWP model does not detect the sudden decrease at 4 p.m. at all. In addition to the ZTD time series, the figure includes the temperature and rainfall measured at the station. A strong increase in the ZTD value, a generally high ZTD and a preceding decrease in temperature lead to rainfall events. The typical characteristics of these cold frontal passages can therefore be detected in the GPS data, suggesting that GPS could be an important data source for nowcasting of heavy rain events.

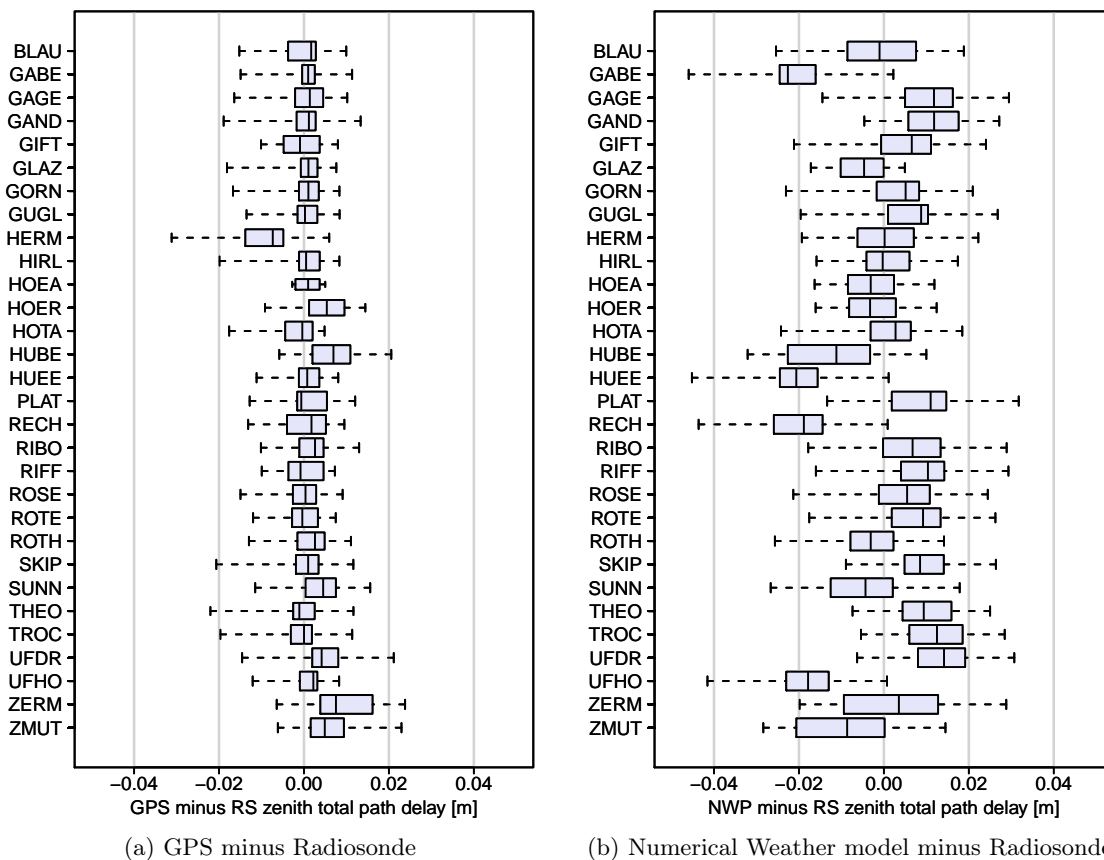


Figure 5.26: Boxplots comparing total zenith path delays from: a) GPS (PPP, 300s, daily, GMF, 2h) minus path delays calculated from radiosondes (RS) and b) path delays from numerical weather prediction (NWP) model data minus radiosonde data. Note that the PPP solution was used for this figure and that the x-axis scaling is different to Figs. 5.16a–c and 5.20.

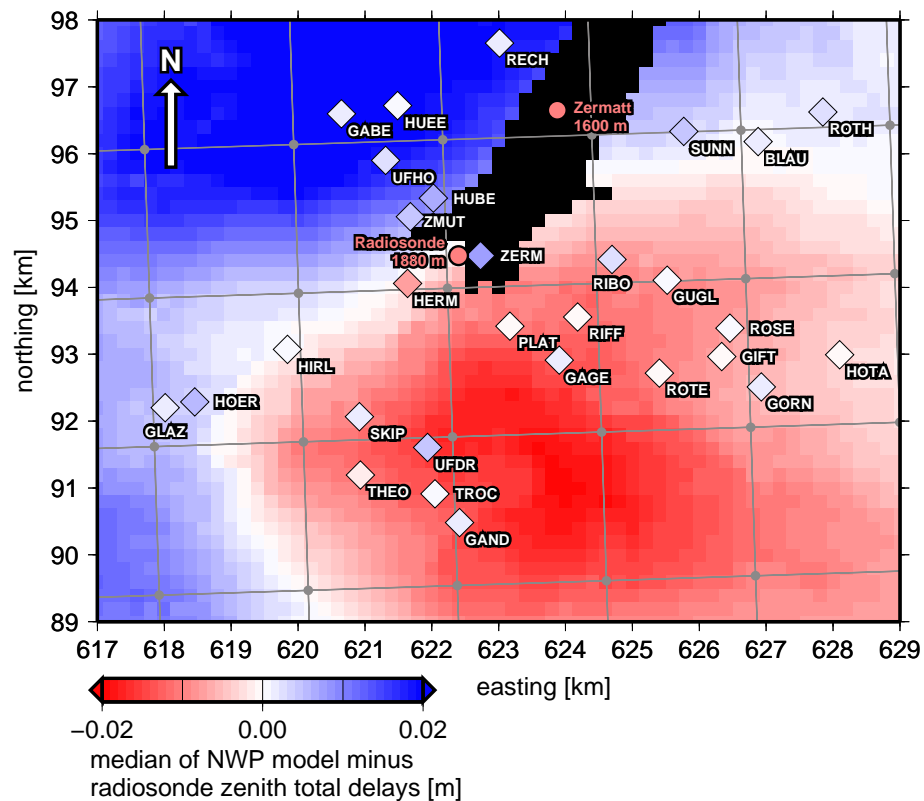


Figure 5.27: GPS minus radiosonde medians of Figs. 5.26a plotted in map view as shaded diamonds (PPP, 300s, daily, GMF, 2h). The difference of the numerical weather prediction model to the radiosonde solution is calculated for the entire campaign domain and shown as shading of the investigation area. The black region around the village of Zermatt denotes the area that is below the height of the radiosonde launch site. The gray lines are the bird's eye view of the NWP model grid.

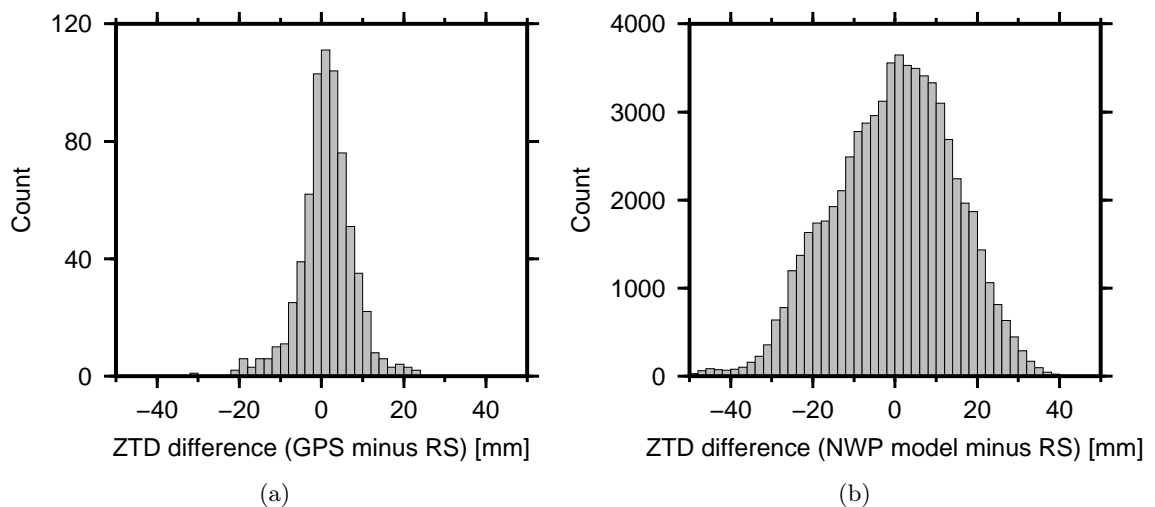


Figure 5.28: Summary histograms of all the differences between (a) GPS (PPP, 300s, daily, GMF, 2h) and, (b) NWP model ZTDs and the data from the 25 radiosonde launches. Note that the NWP model field was interpolated and sampled to a resolution of approximately 180 m, as shown in Fig. 5.27.

Table 5.11: Statistics of the histograms in Figs. 5.28a and b.

Data description	min [mm]	$Q_{25\%}$ [mm]	$Q_{50\%}$ [mm]	$Q_{75\%}$ [mm]	max [mm]	IQR [mm]	mean [mm]	stdev [mm]	# [-]
GPS minus RS	-31.2	-2.0	1.4	4.7	23.8	6.7	1.2	6.5	699
NWP model minus RS	-53.2	-10.3	0.6	10.1	40.8	20.4	-0.3	14.5	66450

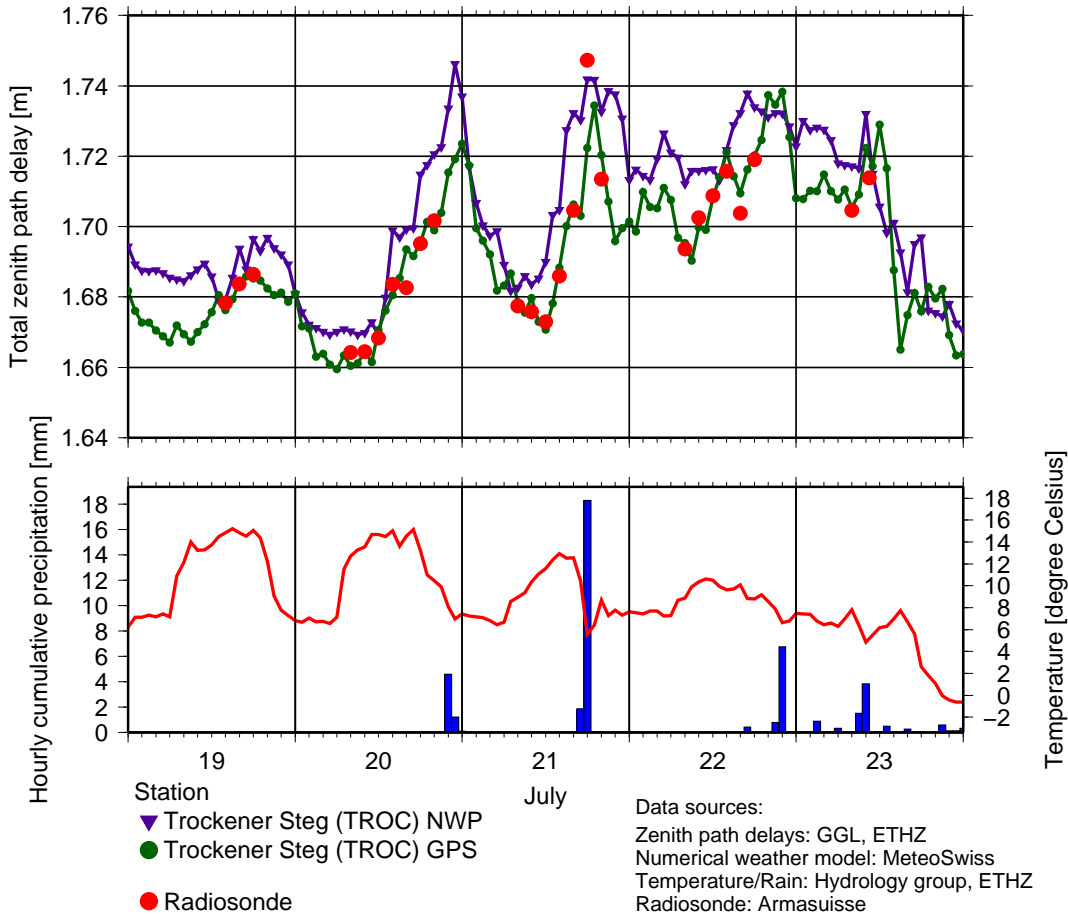


Figure 5.29: Time series of total zenith path delays from the NWP model and the GPS processing (PPP, 30s, daily, GMF, 1h) at 1-hour resolution for the station TROC. Additionally, the 25 radiosonde ZTDs are shown. The bottom plot displays concurrent air temperature 2m above ground as 1-hour averages and rain as 1-hourly cumulative precipitation.

5.3 Conclusions

The campaign GPS stations show many site-specific influences in their coordinate and ZTD time series. Among these influences are inaccurate phase center variations, multipath and satellite obstructions from trees, buildings and mountains. The complex topography created individual satellite views for each station. Additionally, many different antenna and receiver types were used. Despite the various site conditions, we observe stable coordinates with consistently good repeatabilities in the horizontal. The up component is shown to be much more influenced by the site conditions and shows a downward trend for some stations. Stations with satellite visibility down to elevations of 3° were less affected by the trend than heavily obstructed sites. It is demonstrated that the double-differencing with baselines between the campaign stations and ZIM2 from

AGNES removed much of the up component trend observed in the PPP solution. Furthermore, the double-difference solution is successful in improving station repeatabilities in the east, north and up component. We note that the AGNES station ZERM shows a large IQR and median bias in ZTD with respect to the radiosonde. Our campaign station WINK was based on a Swisstopo campaign point. Its coordinate time series shows poor repeatabilities. Moving the point to some more trustworthy site such as Rothorn or Gornergrat might be considered in the future.

Even though the coordinate time series from the network solution have better repeatabilities, the ZTD from the PPP solution proves to be more accurate with respect to radiosonde validation data. It is further demonstrated that the data sampling of the GPS data is not critical for accurate determination of the ZTD. Mid-latitude stations are known to be weakly affected by the choice of the mapping function. The GMF and Niell solutions are confirmed to differ at the submillimeter level.

Clear differences in performance are visible for various parameter spacings of the ZTD parameter. From a statistical point of view, the 2-hour resolution is slightly better than the 1-hour resolution. Analysis of time series in comparison with the 25 radiosonde solutions from the campaign hint at a better temporal performance of the 1-hour solution. No improvement in that respect is observed with the 30-minute solution and more noise seems to govern the solution. Future analysis of this seeming noise is needed. The temporal and spatial heterogeneity of the ZTD might be better represented by the 30-minute solution than by the 1-hour GPS solution, but might be partly absent from the radiosonde ZTD. On average over all campaign stations, the best PPP achieved an accuracy of 4–6 mm standard deviation and a small wet median bias of 0–2 mm with respect to the radiosonde.

After removing a station-specific systematic offset and a simple exponential model from the GPS delays, we still observe several millimeters of horizontal variability across the campaign area. Strong indications are given that the observed patterns are indeed due to atmospheric influences. The degree of influence coming from satellite constellation effects still needs to be investigated. We can already conclude that parts of the discrepancies between GPS and radiosonde ZTDs are due to horizontal variabilities. They are not perceived by the one-dimensionality of the radiosonde profiles.

With respect to ZTDs calculated from the COSMO-2 weather model, we observe clearly superior performance of the GPS ZTDs. At scales of 2–3 km, the model displays systematic offsets of the order of 1–2 cm. Creating the statistics of the NWP ZTDs over the entire campaign area results in a negligible bias with respect to the radiosonde. Hence, the weather model's ZTDs can be considered nearly bias-free at scales of approximately 10 km, even in highly complex regions of the Alps. To make sure that the weather model benefits from the better accuracy of GPS ZTDs and is not disturbed by systematic GPS errors, bias corrections are indispensable and should take the weather model's actual representativity into account. The correction should thus be based on a long-term statistics between the GPS ZTD and a spatial average of the NWP ZTD. The bias corrections should be accompanied by a simulation study that quantifies the influence of satellite geometry and multipath on the GPS ZTD's uncertainties. Corresponding accuracy indicators should be delivered to the modelers. This is also true, if slant delays are assimilated, since the GPS biases enter the slant delays via the ZTDs.

Chapter 6

Conclusions

The ZTD from GNSS processing is a broadly accepted descriptor of the integrated atmospheric state. Its assimilation into NWP models as ZTD has become a very common application of GNSS meteorology (Chap. 1). As such, it is treated like any other measurement of the atmosphere. It is bias-corrected and gets some uncertainty assigned in the form of a standard deviation. The quantification of the standard deviation of GNSS ZTDs requires accurate reference measurements. The radiosonde is usually considered to be the reference of choice. Additionally, we have to distinguish between systematic effects and so-called random measurement uncertainties. Systematic effects are caused by incomplete, inaccurate and missing models for the many influences affecting the GNSS signal. Both, the accuracy of the reference measurements and the separation between systematic and random contributions to the ZTD uncertainty have been attempted with data from the Payerne radiosonde and the adjacent GNSS station (Chap. 3). The systematic part of the GNSS ZTD uncertainty amounts to a few millimeters of station-specific mean offset and 1–2 mm annual fluctuation. The mean offset and the annual systematic fluctuation are likely to contain radiosonde contributions of millimeter magnitude. The random measurement uncertainties of GNSS ZTDs are determined to be 2.5 mm–3.5 mm in winter and 3.5–5.0 mm in summer. The study demonstrates a similar accuracy for the ZTDs calculated with the radiosonde data and thus, questions the radiosonde as a reference for ZTD measurements.

Despite several objections to assimilate GNSS ZTDs in topographically complex areas of NWP models, the ZTDs from the Zermatt campaign stations exposed local-scale biases in the NWP model (Chap. 5). It is also demonstrated that ZTDs catch horizontal spatial variabilities down to a few kilometers. Furthermore, these variabilities are clearly better representing the changing atmosphere than one of the present-day highly resolved regional weather model (COSMO-2). Especially in the Alps, where little data is assimilated and where accurate assimilation data is most needed, a benefit is expected to result from sophisticated use of ZTDs. We could utilise the fact that the NWP model is shown to be quasi bias-free on scales of 10×10 km with respect to radiosondes launched in the Swiss Alps. Spatially averaged NWP ZTD values would serve as basis for bias corrections.

The campaign data in Zermatt provide a detailed look at the systematic components of GNSS ZTD uncertainties. The data emphasize the need to select GNSS station locations for use in meteorology very carefully. It is absolutely essential to set up and use only stations with favourable satellite view. Viewing satellites down to elevations of 3° is considered to be a prerequisite. The all-around view is obviously beneficial. The use of stations with PPP repeatabilities of up component RMS ≥ 10 mm are not recommended. These are usually stations with heavy obstructions or poor PCV and PCO corrections. Thus, the quality of the antenna and its associated corrections are very important. Accurate antenna corrections also reduce the ZTD differences to the radiosonde ZTDs, as is demonstrated in the Payerne radiosonde study (Chap. 3).

For local studies, the network approach is demonstrated to yield less accurate ZTD values than a PPP solution (Chap. 5). The better coordinate repeatability of the network solution is somehow deceiving. We further note that the lower accuracy of the network solution is not due to a loss of

observations by the double-differencing and the interaction of two viewing horizons. A more likely cause is the common-mode removal inherent to double-differencing. If this is true, the inclusion of the AGNES stations into the network is not only needless, but also a bad choice. Baselines between campaign stations and other stations in Switzerland should then have been completely avoided.

The Zermatt campaign data yields ZTD values from PPP that reach standard deviations of 4–6 mm with respect to the radiosondes. The radiosonde’s profiling nature is shown to miss some of the horizontal variability. A few millimeters of horizontal variability is present at scales of roughly 5 km. Consequently, the standard deviations of the campaign’s ZTDs are likely to be < 5 mm.

Before assimilation of slant or zenith delays into NWP models, it is important to investigate the delays’ ability for imaging atmospheric state (Chap. 4). Usually, a tomographic approach is employed for this purpose. Here, a different route is chosen. ZWDs are interpolated with collocation in 3D space and time. The derivative of the ZWD with height yields wet refractivity. Together with radiometer temperature profiles at Payerne, humidity profiles are reconstructed and compared to the operational radiosonde. The reconstructed wet refractivity fields are more accurate than tomography results from the same region and with a similar station network. With additional ground meteorological data or radio occultations, the refractivity and the humidity field are heavily improved. The relatively simple approach of collocation has proven to provide a robust tool for the data combination. Horizontal scale lengths of 35 km have yielded satisfactory interpolation results for ZWDs. The Zermatt campaign suggests the presence of ≈ 5 km horizontal scale lengths of the ZTD. These small-scale variabilities are probably due to the heterogeneities in the ZWD. The presence of various scales in the atmosphere does not come as a surprise. Hence, with the inclusion of even more data sets and the densification of measurement networks, the use of 2–3 scales should be considered in the collocation or in any other stochastic modeling approach.

Chapter 7

Outlook

The benefit of data combination has been long known. Nonetheless, its use for a better tropospheric modeling in GNSS processing has not been fully exploited. The combination of many data sets related to meteorology in one tropospheric model that is incorporated into a state of the art GNSS software would create a large progress in geodesy. This tropospheric model could be an entire NWP model or a model such as COMEDIE, the tomography AWATOS2, or some elaborate stochastic model with correlations at multiple scales. Especially, the support from independent meteorological data sets would decorrelate the ZTD estimation from the height and receiver clock estimation. Possible data types to include are radar refractivities, ground meteorology, radio occultations, satellite-based measurements of water vapour and temperature, or water vapour measurements from wireless communication networks. But also radiosonde measurements, radiometer IWV or raman lidar profiles are possible candidates to incorporate. The combination of a tropospheric model with a GNSS software would also provide consistent estimations of delay gradients. Their physical reality would be directly manifest in the troposphere model and thus, would not be the kind of “garbage” collector it plays in today’s GNSS processing algorithms. Two features would ease the combination:

1. The model should have separate pressure, temperature and water vapour fields. For the NWP model, this goes without saying. The tomography or the collocation approach would still require some adaptations.
2. The PPP approach would simplify the program structure. Regional or even local investigations could easily be carried out without datum definition procedures or incorporation of base stations. Since the PPP modeling has strongly progressed in recent years, even the combination of all European GNSS stations into one inversion process could be envisaged.

At present, some research groups are implementing the assimilation operator for GNSS slant delays in their NWP models for research purposes. In line with the above considerations, one should also take into account to use the GNSS “raw” phase measurements and a complete GNSS model as assimilation operator. Problematic in that respect is the discrepancy between the “real” and the NWP model world. Obviously, the weather modelers work hard at getting the two worlds closer together. By doing that, the modelers consider the model equations to be the backbone. The equations have become more complicated to take more influences into account. The assimilated data only supports the model physics. In my personal view, I think that for short-term forecasts, the physics should support the data and not vice versa. Highly resolved models should go with heavily simplified model equations. Many problems of bias corrections would become obsolete. Unfortunately, the weather modelers I have talked to so far have not acquired a taste for this approach.

Bibliography

- Anthes, R. A.: Exploring Earth's atmosphere with radio occultation: contributions to weather, climate and space weather, *Atmospheric Measurement Techniques*, 4, 1077–1103, doi:10.5194/amt-4-1077-2011, URL <http://www.atmos-meas-tech.net/4/1077/2011/>, 2011.
- Aster, R. C., Borchers, B., and Thurber, C.: *Parameter Estimation and Inverse Problems*, Academic Press, Elsevier Inc., 2nd edn., 2011.
- Ball, W. T., Unruh, Y. C., Krivova, N. A., Solanki, S., Wenzler, T., Mortlock, D. J., and Jaffe, A. H.: Reconstruction of total solar irradiance 1974–2009, *Astronomy & Astrophysics*, 541, A27, doi:10.1051/0004-6361/201118702, URL <http://dx.doi.org/10.1051/0004-6361/201118702>, 2012.
- Bastin, S., Champollion, C., Bock, O., Drobinski, P., and Masson, F.: Diurnal Cycle of Water Vapor as Documented by a Dense GPS Network in a Coastal Area during ESCOMPTE IOP2, *Bull. Am. Meteorol. Soc.*, 46, 167–182, 2007.
- Bender, M., Dick, G., Wickert, J., Schmidt, T., Song, S., Gendt, G., Ge, M., and Rothacher, M.: Validation of GPS slant delays using water vapour radiometers and weather models, *Meteorologische Zeitschrift*, 17, 807–812, URL <http://dx.doi.org/10.1127/0941-2948/2008/0341>, 2008.
- Bender, M., Dick, G., Wickert, J., Ramatschi, M., Ge, M., Gendt, G., Rothacher, M., Raabe, A., and Tetzlaff, G.: Estimates of the information provided by GPS slant data observed in Germany regarding tomographic applications, *Journal of Geophysical Research: Atmospheres*, 114, doi:10.1029/2008JD011008, URL <http://dx.doi.org/10.1029/2008JD011008>, 2009.
- Bender, M., Dick, G., Ge, M., Deng, Z., Wickert, J., Kahle, H.-G., Raabe, A., and Tetzlaff, G.: Development of a GNSS water vapour tomography system using algebraic reconstruction techniques, *Advances in Space Research*, 47, 1704–1720, 2011.
- Bennitt, G. V. and Jupp, A.: Operational Assimilation of GPS Zenith Total Delay Observations into the Met Office Numerical Weather Prediction Models, *Mon. Wea. Rev.*, 140, 2706–2719, URL <http://dx.doi.org/10.1175/MWR-D-11-00156.1>, 2012.
- Besson, L. and Parent du Châtelet, J.: Solutions for Improving the Radar Refractivity Measurement by Taking Operational Constraints into Account, *J. Atmos. Oceanic Technol.*, 30, 1730–1742, URL <http://dx.doi.org/10.1175/JTECH-D-12-00167.1>, 2013.
- Bevis, M., Businger, S., Herring, T. A., Rocken, C., Anthes, R. A., and Ware, R. H.: GPS Meteorology: Remote Sensing of Atmospheric Water Vapor Using the Global Positioning System, *J. Geophys. Res.*, 97, 15 787–15 801, 1992.
- Bevis, M., Businger, S., Chiswell, S., Herring, T. A., Anthes, R. A., Rocken, C., and Ware, R. H.: GPS Meteorology: Mapping Zenith Wet Delays onto Precipitable Water, *J. Appl. Meteor.*, 33, 379–386, 1994.
- Boehm, J., Niell, A., Tregoning, P., and Schuh, H.: Global Mapping Function (GMF): A new empirical mapping function based on numerical weather model data, *Geophys. Res. Lett.*, 33, L07 304, doi:10.1029/2005GL025546, 2006a.

- Boehm, J., Werl, B., and Schuh, H.: Troposphere mapping functions for GPS and very long baseline interferometry from European Centre for Medium-Range Weather Forecasts operational analysis data, *J. Geophys. Res.*, 111, B02406, doi:10.1029/2005JB003629, 2006b.
- Boehm, J., Heinkelmann, R., and Schuh, H.: A Global Model of Pressure and Temperature for Geodetic Applications, *Journal of Geodesy*, 81, 679–683, doi:10.1007/s00190-007-0135-3, 2007.
- Bolton, D.: The Computation of Equivalent Potential Temperature, *Monthly Weather Review*, 108, 1046–1053, 1980.
- Bosy, J., Rohm, W., Borkowski, A., Kroszczynski, K., and Figurski, M.: Integration and verification of meteorological observations and NWP model data for the local GNSS tomography, *Atmospheric Research*, 96, 522 – 530, doi:10.1016/j.atmosres.2009.12.012, URL <http://www.sciencedirect.com/science/article/pii/S0169809509003676>, 2010.
- Bosy, J., Kaplon, J., Rohm, W., Sierny, J., and Hadas, T.: Near real-time estimation of water vapour in the troposphere using ground GNSS and the meteorological data, *Annales Geophysicae*, 30, 1379–1391, doi:10.5194/angeo-30-1379-2012, URL <http://www.ann-geophys.net/30/1379/2012/>, 2012.
- Brenot, H., Neméghaire, J., Delobbe, L., Clerbaux, N., De Meutter, P., Deckmyn, A., Delcloo, A., Frappez, L., and Van Roozendael, M.: Preliminary signs of the initiation of deep convection by GNSS, *Atmospheric Chemistry and Physics*, 13, 5425–5449, doi:10.5194/acp-13-5425-2013, URL <http://www.atmos-chem-phys.net/13/5425/2013/>, 2013a.
- Brenot, H., Walpersdorf, A., Reverdy, M., van Baelen, J., Ducrocq, V., Champollion, C., Masson, F., Doerflinger, E., Collard, P., and Giroux, P.: A GPS network for tropospheric tomography in the framework of the Mediterranean hydrometeorological observatory Cévennes-Vivarais (South-Eastern France), *Atmospheric Measurement Techniques Discussions*, 6, 9513–9578, doi:10.5194/amtd-6-9513-2013, URL <http://www.atmos-meas-tech-discuss.net/6/9513/2013/>, 2013b.
- Brocard, E., Philipona, R., Haeefe, A., Romanens, G., Ruffieux, D., Simeonov, V., and Calpini, B.: Raman Lidar for Meteorological Observations, RALMO - Part 2: Validation of water vapor measurements, *Atmospheric Measurement Techniques Discussions*, 5, 6915–6948, doi:10.5194/amtd-5-6915-2012, URL <http://www.atmos-meas-tech-discuss.net/5/6915/2012/>, 2012.
- Brockmann, E. and Ineichen, D.: National Report of Switzerland and Processing Combined GPS/GLONASS Data at Swisstopo’s Local Analysis Center, EUREF’08: Paper contributions to the EUREF-Symposium in Brussels, 18-20 june, 2008., Swisstopo, 2008.
- Brockmann, E., Ineichen, D., Kistler, M., Marti, U., Schaer, S., Schlatter, A., Vogel, B., Wiget, A., and Wild, U.: National Report of Switzerland: Geodetic activities at Swisstopo presented to the EUREF2012-Symposium, National report 12-07, Swisstopo, EUREF’12: Paper contributions to the EUREF-Symposium in Paris, June 6-8, 2012., 2012.
- Champollion, C., Masson, F., Bouin, M.-N., Walpersdorf, A., Doerflinger, E., Bock, O., and van Baelen, J.: GPS water vapour tomography: preliminary results from the ESCOMPTE field experiment, *Atmos. Res.*, 74, 253–274, doi:10.1016/j.atmosres.2004.04.003, 2005.
- Champollion, C., Drobinski, P., Haeffelin, M., Bock, O., Tarniewicz, J., Bouin, M. N., and Vautard, R.: Water vapour variability induced by urban/rural surface heterogeneities during convective conditions, *Quarterly Journal of the Royal Meteorological Society*, 135, 1266–1276, doi:10.1002/qj.446, URL <http://dx.doi.org/10.1002/qj.446>, 2009a.
- Champollion, C., Flamant, C., Bock, O., Masson, F., Turner, D., and Weckwerth, T.: Mesoscale GPS tomography applied to the 12 June 2002 convective initiation event of IHOP_2002, *Quarterly Journal of the Royal Meteorological Society*, 135, 645–662, doi:10.1002/qj.386, URL <http://dx.doi.org/10.1002/qj.386>, 2009b.

- Chatfield, C.: The Analysis of Time Series: An Introduction, Sixth Edition, Chapman & Hall/CRC Texts in Statistical Science, Taylor & Francis, URL <http://books.google.ch/books?id=qKzyAbdaDFAC>, 2003.
- Chen, G. and Herring, T. A.: Effects of atmospheric azimuthal asymmetry on the analysis of space geodetic data, *Journal of Geophysical Research: Solid Earth*, 102, 20 489–20 502, doi: 10.1029/97JB01739, URL <http://dx.doi.org/10.1029/97JB01739>, 1997.
- CIMO Guide, 2008: WMO Guide to Meteorological Instruments and Methods of Observation, Tech. Rep. WMO-No. 8, 7th edition, World Meteorological Organization, Geneva, Switzerland, 2008.
- Courant, R. and Hilbert, D.: *Methoden der Mathematischen Physik I*, Springer Verlag, Berlin, Heidelberg, New York, 3. edition edn., 1968.
- Dach, R., Hugentobler, U., Fridez, P., and Meindl, M.: Bernese GPS Software Version 5.0, Astronomical Institute, University of Berne, 2007.
- David, N., Alpert, P., and Messer, H.: Technical Note: Novel method for water vapour monitoring using wireless communication networks measurements, *Atmospheric Chemistry and Physics*, 9, 2413–2418, doi:10.5194/acp-9-2413-2009, URL <http://www.atmos-chem-phys.net/9/2413/2009/>, 2009.
- de Haan, S.: Measuring Atmospheric Stability with GPS, *J. Appl. Meteor. and Climatol.*, 45, 467–475, 2006.
- de Haan, S. and van der Marel, H.: Observing three dimensional water vapour using a surface network of GPS receivers, *Atmospheric Chemistry and Physics Discussions*, 8, 17 193–17 235, doi:10.5194/acpd-8-17193-2008, URL <http://www.atmos-chem-phys-discuss.net/8/17193/2008/>, 2008.
- Deng, Z.: GPS meteorology with single frequency receivers, Ph.D. thesis, Hannover: Fachrichtung Geodäsie und Geoinformatik der Leibniz-Univ., 2012.
- Deng, Z., Bender, M., Dick, G., Ge, M., Wickert, J., Ramatschi, M., and Zou, X.: Retrieving tropospheric delays from GPS networks densified with single frequency receivers, *Geophysical Research Letters*, 36, n/a–n/a, doi:10.1029/2009GL040018, URL <http://dx.doi.org/10.1029/2009GL040018>, 2009.
- Doms, G. and Schättler, U.: A Description of the Nonhydrostatic Regional Model LM. Part I: Dynamics and Numerics, COSMO, 2002.
- Duan, J., Bevis, M., Fang, P., Bock, Y., Chiswell, S., Businger, S., Rocken, C., Solheim, F., van Hove, T., Ware, R., McClusky, S., Herring, T. A., and King, R. W.: GPS Meteorology: Direct Estimation of the Absolute Value of Precipitable Water, *J. Appl. Meteor.*, 35, 830–838, 1996.
- Eckert, V., Cocard, M., and Geiger, A.: COMEDIE (Collocation of Meteorological Data for Interpretation and Estimation of Tropospheric Pathdelays), Teil I: Konzepte, Teil II: Resultate, Tech. Rep. 194, ETH Zürich, Grauer Bericht, 1992a.
- Eckert, V., Cocard, M., and Geiger, A.: COMEDIE (Collocation of Meteorological Data for Interpretation and Estimation of Tropospheric Pathdelays), Teil III: Software, Tech. Rep. 195, ETH Zürich, Grauer Bericht, 1992b.
- Elósegui, P. and Davis, J. L.: Accuracy assessment of GPS slant-path determinations., in: Proceedings of the International Workshop on GPS Meteorology, Tsukuba, Japan, 14.-17. Jan 2003., edited by Iwabuchi, T. and Shoji, Y., 2004.
- Essen, L. and Froome, K. D.: The Refractive Indices and Dielectric Constants of Air and its Principal Constituents at 24,000 Mc/s, in: Proceedings of the Physical Society, Section B, vol. 64/10, pp. 862–875, 1951.

- Fabry, F.: The Spatial Variability of Moisture in the Boundary Layer and Its Effect on Convection Initiation: Project-Long Characterization, *Monthly Weather Review*, 134, 79, 2006.
- Fabry, F., Frush, C., Zawadzki, I., and Kilambi, A.: On the extraction of near-surface index of refraction using radar phase measurements from ground targets, *J. Atmos. Oceanic Technol.*, 14, 978–987, 1997.
- Foelsche, U. and Kirchengast, G.: Tropospheric water vapor imaging by combination of ground-based and spaceborne GNSS sounding data, *Journal of Geophysical Research: Atmospheres*, 106, 27 221–27 231, doi:10.1029/2001JD900230, URL <http://dx.doi.org/10.1029/2001JD900230>, 2001.
- Foelsche, U., Syndergaard, S., Fritzer, J., and Kirchengast, G.: Errors in GNSS radio occultation data: relevance of the measurement geometry and obliquity of profiles, *Atmospheric Measurement Techniques*, 4, 189–199, doi:10.5194/amt-4-189-2011, URL <http://www.atmos-meas-tech.net/4/189/2011/>, 2011.
- Fritsche, M., Dietrich, R., Knöfel, C., Rülke, A., Vey, S., Rothacher, M., and Steigenberger, P.: Impact of higher-order ionospheric terms on GPS estimates, *Geophysical Research Letters*, 32, doi:10.1029/2005GL024342, URL <http://dx.doi.org/10.1029/2005GL024342>, 2005.
- Furumoto, J.-i., Imura, S., Tsuda, T., Seko, H., Tsuyuki, T., and Saito, K.: The Variational Assimilation Method for the Retrieval of Humidity Profiles with the Wind-Profiling Radar, *J. Atmos. Oceanic Technol.*, 24, 1525–1545, URL <http://dx.doi.org/10.1175/JTECH2074.1>, 2007.
- Gamma, E., Helm, R., Johnson, R., and Vlissides, J.: Design patterns: elements of reusable object-oriented software, Addison-Wesley Longman Publishing Co., Inc., Boston, MA, USA, 1995.
- Geiger, A.: Einfluss richtungsabhängiger Fehler bei Satellitenmessungen, Bericht 130, Inst. of Geodesy and Photogrammetry, ETH Zurich, 1987.
- Gerlach, U. H.: Linear Mathematics in Infinite Dimensions: Signals, Boundary Value Problems, and Special Functions, Columbus, Ohio, weblink: <https://people.math.osu.edu/gerlach.1/math/BVtypset/>, 2009.
- Gschwend, F.: GPS-Zeitreihenanalyse, Master-projekt thesis, ETH Zürich, Switzerland, Institute for Geodesy and Photogrammetrie., spring semester, 2012.
- Hajj, G. A., Kursinski, E. R., Romans, L. J., Bertiger, W. I., and Leroy, S. S.: A technical description of atmospheric sounding by GPS occultation, *J. Atmos. Solar-Terr. Phys.*, 64, 451–469, 2002.
- Hirter, H.: Mehrdimensionale Interpolation von Meteorologischen Feldern zur Berechnung der Brechungsbedingungen in der Geodäsie, Mitteilung 64, Inst. of Geodesy and Photogrammetry, ETH Zurich, 1998.
- Ho, S.-p., Kirchengast, G., Leroy, S., Wickert, J., Mannucci, A. J., Steiner, A., Hunt, D., Schreiner, W., Sokolovskiy, S., Ao, C., Borsche, M., von Engeln, A., Foelsche, U., Heise, S., Iijima, B., Kuo, Y.-H., Kursinski, R., Pirscher, B., Ringer, M., Rocken, C., and Schmidt, T.: Estimating the uncertainty of using GPS radio occultation data for climate monitoring: Intercomparison of CHAMP refractivity climate records from 2002 to 2006 from different data centers, *Journal of Geophysical Research: Atmospheres*, 114, doi:10.1029/2009JD011969, URL <http://dx.doi.org/10.1029/2009JD011969>, 2009.
- Hurter, F. and Maier, O.: Tropospheric profiles of wet refractivity and humidity from the combination of remote sensing datasets and measurements on the ground, *Atmospheric Measurement Techniques Discussions*, 6, 4895–4940, doi:10.5194/amtd-6-4895-2013, URL <http://www.atmos-meas-tech-discuss.net/6/4895/2013/>, 2013.

- Hurter, F., Geiger, A., Perler, D., and Rothacher, M.: GNSS water vapor monitoring in the Swiss Alps, in: IEEE International Geoscience and Remote Sensing Symposium proceedings (2012), pp. 1972–1975, IEEE, Piscataway, NJ, 2012.
- Hyland, R. W. and Wexler, A.: Formulations for the Thermodynamic Properties of the saturated Phases of H₂O from 173.15K to 473.15K, ASHRAE Trans, 89(2A), 500–519, 1983.
- Ineichen, D., Brockmann, E., and Schaer, S.: Enhancing the Swiss Permanent GPS Network (AGNES) for GLONASS, in: EUREF Publication No. 17, Mitteilungen des Bundesamtes für Kartographie und Geodäsie, Band 42, edited by Torres, J. A. and Hornik, H., Subcommission for the European Reference Frame (EUREF), London, 2007.
- Iske, A.: Scattered data approximation by positive definite Kernel functions, Rendiconti del seminario matematico Vol. 69, 3, Universita e Politecnico di Torino, Italy, 217–246, 2011.
- Iwabuchi, T., Miyazaki, S., Heki, K., Naito, I., and Hatanaka, Y.: An impact of estimating tropospheric delay gradients on tropospheric delay estimations in the summer using the Japanese nationwide GPS array, Journal of Geophysical Research: Atmospheres, 108, n/a–n/a, doi: 10.1029/2002JD002214, URL <http://dx.doi.org/10.1029/2002JD002214>, 2003.
- Jacobson, M., Z.: Fundamentals of atmospheric modeling, Cambridge Uni. Press, 2 edn., 2005.
- Kačmařík, M., Douša, J., and Zapletal, J.: Comparison of GPS slant Wet delays acquired by different techniques, Acta Geodynamica et Geomaterialia, 9, 427–433, 2012.
- Kleijer, F., Elósegui, P., and Davis, J. L.: Characterizing atmospheric turbulence with GPS, in: 16th Symposium on Boundary Layers and Turbulence, American Meteorological Society, extended abstract, 2004.
- Kräuchi, A.: Experiments to investigate the radiation error on radiosonde temperature measurements., Master thesis, ETH Zürich, Institute for Atmospheric and Climate Science., 2011.
- Kuo, Y.-H., Wee, T.-K., Sokolovskiy, S., Rocken, C., Schreiner, W., Hunt, D., and Anthes, R.: Inversion and Error Estimation of GPS Radio Occultation Data, Journal of the Meteorological Society of Japan. Ser. II, 82, 507–531, 2004.
- Labbouz, L., Van Baelen, J., Tridon, F., Reverdy, M., Hagen, M., Bender, M., Dick, G., Gorgas, T., and Planche, C.: Precipitation on the lee side of the Vosges Mountains: Multi-instrumental study of one case from the COPS campaign, Meteorologische Zeitschrift, 22, 413–432, doi:doi: 10.1127/0941-2948/2013/0413, URL <http://www.ingentaconnect.com/content/schweiz/mz/2013/00000022/00000004/art00004>, 2013.
- Lin, L., Zhao, Z., Zhu, Q., and Zhang, Y.: Profiling tropospheric refractivity in real time, based on a relevance vector machine and single ground-based GPS receiver, International Journal of Remote Sensing, 33, 4044–4058, doi:10.1080/01431161.2011.639403, URL <http://www.tandfonline.com/doi/abs/10.1080/01431161.2011.639403>, 2012.
- Löhnert, U. and Maier, O.: Operational profiling of temperature using ground-based microwave radiometry at Payerne: prospects and challenges, Atmospheric Measurement Techniques, 5, 1121–1134, doi:10.5194/amt-5-1121-2012, URL <http://www.atmos-meas-tech.net/5/1121/2012/>, 2012.
- Lowry, A. R., Rocken, C., Sokolovskiy, S. V., and Anderson, K. D.: Vertical profiling of atmospheric refractivity from ground-based GPS, Radio Science, 37, 13–1–13–19, doi:10.1029/2000RS002565, URL <http://dx.doi.org/10.1029/2000RS002565>, 2002.
- Lutz, S.: High-resolution GPS tomography in view of hydrological hazard assessment, vol. 76 of *Geodätisch-geophysikalische Arbeiten in der Schweiz*, Swiss Geodetic Commission, 2009.
- Lutz, S., Troller, M., Perler, D., Geiger, A., and Kahle, H. G.: Better Weather Prediction Using GPS, GPS World, 21, 40–47, 2010.

- Manning, T., Zhang, K., Rohm, W., Choy, S., and Hurter, F.: Detecting Severe Weather using GPS Tomography: An Australian Case Study, *Journal of Global Positioning Systems*, 11, 58–70, doi:10.5081/jgps.11.1.58, 2012.
- Manning, T., Rohm, W., Zhang, K., Hurter, F., and Wang, C.: Determining the 4D dynamics of wet refractivity using GPS tomography in the Australian region, in: *Earth on the Edge: Science for a Sustainable Planet*, edited by Rizos, C. and Willis, P., Proceedings of the IAG General Assembly, Melbourne, Australia, 28 June-2 July, 2011, IAG Symp. 139, ISBN 978-3-642-37221-6, 2013.
- Masiello, G., Serio, C., Deleporte, T., Herbin, H., Di Girolamo, P., Champollion, C., Behrendt, A., Bossler, P., Bock, O., Wulfmeyer, V., Pommier, M., and Flamant, C.: Comparison of IASI water vapour products over complex terrain with COPS campaign data, *Meteorologische Zeitschrift*, 22, 471–487, URL <http://dx.doi.org/10.1127/0941-2948/2013/0430>, 2013.
- Mercer, J.: Functions of Positive and Negative Type, and their Connection with the Theory of Integral Equations, *Philosophical Transactions of the Royal Society of London. Series A, Containing Papers of a Mathematical or Physical Character*, 209, pp. 415–446, URL <http://www.jstor.org/stable/91043>, 1909.
- Meteolabor: SRS-C34, Digital Radiosonde, Published by meteolabor, www.meteolabor.ch, www.meteolabor.ch/fileadmin/user_upload/pdf/meteo/UpperAir/srs-c34_e.pdf, last visited: 16 Aug 2013, 2010.
- Miyazaki, S., Iwabuchi, T., Heki, K., and Naito, I.: An impact of estimating tropospheric delay gradients on precise positioning in the summer using the Japanese nationwide GPS array, *Journal of Geophysical Research: Solid Earth*, 108, doi:10.1029/2000JB000113, URL <http://dx.doi.org/10.1029/2000JB000113>, 2003.
- Moritz, H.: Least-squares collocation, *Rev. Geophys.*, 16(3), 421–430, 1978.
- Moritz, H.: *Advanced Physical Geodesy*, no. 13 in *Sammlung Wichmann:N.F.:Buchreihe*, Herbert Wichmann Verlag, Karlsruhe, Germany, ISBN 3-87907-106-3, 1980.
- Nash, J., Oakley, T., Vömel, H., and Wei, L.: WMO Intercomparison of high quality radiosonde systems Yanjiang, China, 12 July - 3 August 2010, Tech. Rep. WMO/TD-No. 1580, World Meteorological Organization, Geneva, Switzerland, 2011.
- Nef, W.: *Lehrbuch der linearen Algebra*, no. 31 in *Mathematische Reihe*, Birkhäuser Verlag, Basel und Stuttgart, 1966.
- Nicol, J. C., Bartholomew, K., Darlington, T., Illingworth, A. J., and Kitchen, M.: Operational radar refractivity retrieval for numerical weather prediction, in: *8th International Symposium on Weather Radar and Hydrology*, Exeter, UK, 2011.
- Niell, A. E.: Improved atmospheric mapping functions for VLBI and GPS, *Earth Planets Space*, 52, 699–702, 2000.
- Nilsson, T. and Gradinarsky, L.: Water Vapor Tomography Using GPS Phase Observations: Simulation Results, *IEEE Transactions on Geoscience and Remote Sensing*, 44, 2927–2941, doi:10.1109/TGRS.2006.877755, 2006.
- Nilsson, T., Gradinarsky, L., and Elgered, G.: Water vapour tomography using GPS phase observations: Results from the EXCOMPTE experiment, *Tellus*, 59A, 674–682, doi:10.3402/tellusa.v59i5.15150, 2007a.
- Nilsson, T., Haas, R., and Elgered, G.: Simulations of atmospheric path delays using turbulence models, in: *Proc. of the 18th Working Meeting on European VLBI for Geodesy and Astrometry*, edited by Böhm, J., Pany, A., and Schuh, H., pp. 175–180, Technische Universität Wien, Vienna, Austria, 2007b.

- Nilsson, T., Davis, J. L., and Hill, E. M.: Using ground-based GPS to characterize atmospheric turbulence, *Geophysical Research Letters*, 36, doi:10.1029/2009GL040090, URL <http://dx.doi.org/10.1029/2009GL040090>, 2009.
- Notarpietro, R., Cucca, M., Gabella, M., Venuti, G., and Perona, G.: Tomographic reconstruction of wet and total refractivity fields from GNSS receiver networks, *Advances in Space Research*, 47, 898–912, doi:<http://dx.doi.org/10.1016/j.asr.2010.12.025>, URL <http://www.sciencedirect.com/science/article/pii/S0273117711000561>, 2011.
- Park, S. and Fabry, F.: Simulation and Interpretation of the Phase Data Used by the Radar Refractivity Retrieval Algorithm, *J. Atmos. Oceanic Technol.*, 27, 1286–1301, URL <http://dx.doi.org/10.1175/2010JTECHA1393.1>, 2010.
- Park, S. and Fabry, F.: Estimation of Near-Ground Propagation Conditions Using Radar Ground Echo Coverage, *J. Atmos. Oceanic Technol.*, 28, 165–180, URL <http://dx.doi.org/10.1175/2010JTECHA1500.1>, 2011.
- Perler, D.: Water Vapor Tomography using Global Navigation Satellite Systems, ETH Zürich, doi:<http://dx.doi.org/10.3929/ethz-a-006875504>, diss., Eidgenössische Technische Hochschule ETH Zürich, Nr. 20012, 2011.
- Perler, D., Geiger, A., and Hurter, F.: 4D GPS water vapor tomography: new parameterized approaches, *J. Geod.*, 85, 539–550, 2011.
- Philipona, R., Levrat, G., Romanens, G., Jeannet, P., Ruffieux, D., and Calpini, B.: Transition from VIZ/Sippican to ROTRONIC - A new humidity sensor for the SWISS SRS 400 Radiosonde, *Fachberichte 229, MeteoSchweiz*, pages 37pp, 2009.
- Pougatchev, N., August, T., Calbet, X., Oduleye, O., Schlüssel, P., Stiller, B., Germain, K., S., and Bingham, G.: IASI temperature and water vapor retrievals – error assessment and validation, *Atmos. Chem. Phys.*, 9, 6453–6458, 2009.
- Rohm, W.: The ground GNSS tomography - unconstrained approach, *Advances in Space Research*, 51, 501 – 513, doi:10.1016/j.asr.2012.09.021, URL <http://www.sciencedirect.com/science/article/pii/S0273117712005935>, 2013.
- Rohm, W. and Bosy, J.: The verification of GNSS tropospheric tomography model in a mountainous area, *Advances in Space Research*, 47, 1721–1730, doi:10.1016/j.asr.2010.04.017, URL <http://www.sciencedirect.com/science/article/pii/S0273117710002784>, 2011.
- Rohm, W., Zhang, K., and Bosy, J.: Unconstrained, robust Kalman filtering for GNSS troposphere tomography, *Atmospheric Measurement Techniques Discussions*, 6, 9133–9162, doi:10.5194/amtd-6-9133-2013, URL <http://www.atmos-meas-tech-discuss.net/6/9133/2013/>, 2013.
- Rothacher, M.: Estimation of Station Heights with GPS, in: *Vertical Reference Systems*, edited by Drewes, H., Dodson, A., Fortes, L., Sánchez, L., and Sandoval, P., vol. 124 of *International Association of Geodesy Symposia*, pp. 81–90, Springer Berlin Heidelberg, doi:10.1007/978-3-662-04683-8_17, URL http://dx.doi.org/10.1007/978-3-662-04683-8_17, 2002.
- Rüeger, J. M.: Refractive Index Formulae for Radio Waves, in: *Integration of Techniques and Corrections to Achieve Accurate Engineering*, 2002.
- Saastamoinen, J.: Contributions to the theory of atmospheric refraction: Part II. Refraction corrections in satellite geodesy, *J. Geod.*, 47, 13–34, 1973.
- Schaer, S.: Mapping and predicting the Earth’s ionosphere using the global positioning system, vol. 59 of *Geodätisch-geophysikalische Arbeiten in der Schweiz*, Schweizerische Geodätische Kommission, 1999.

Schaer, S. and Meindl, M.: Consideration of Station-Specific Intersystem Translation Parameters at CODE, National report 11-11, swisstopo, in EUREF'11: Paper contributions to the EUREF-Symposium in Chisinau, May 25-28, 2011., 2011.

Schäppi, B.: Measurement and analysis of rainfall gradients along a hillslope transect in the Swiss Alps, ETH Zürich, Zürich, diss., Eidgenössische Technische Hochschule ETH Zürich, Nr. 21084, 2013.

Scherllin-Pirscher, B., Steiner, A. K., Kirchengast, G., Kuo, Y.-H., and Foelsche, U.: Empirical analysis and modeling of errors of atmospheric profiles from GPS radio occultation, *Atmospheric Measurement Techniques*, 4, 1875–1890, doi:10.5194/amt-4-1875-2011, URL <http://www.atmos-meas-tech.net/4/1875/2011/>, 2011.

Shalloway, A. and Trott, J.: *Design Patterns Explained: A New Perspective on Object-Oriented Design* (2nd Edition) (Software Patterns Series), Addison-Wesley Professional, 2004.

Sharma, N., Jagadheesha, D., Joshi, P. C., and Pal, P. K.: Atmospheric stability estimation using radio occultation data over India and surrounding region, *Indian Journal of Radio & Space Physics*, 38, 317–325, 2009.

Shoji, Y., Nakamura, H., Iwabuchi, T., Aonashi, K., Seko, H., Mishima, K., Itagaki, A., Ichikawa, R., and Ohtani, R.: Tsukuba GPS Dense Net Campaign Observation: Improvement in GPS Analysis of Slant Path Delay by Stacking One-way Postfit Phase Residuals, *J. Meteor. Soc. Japan*, 82, 301–314, 2004.

Smirnov, W.: *Lehrgang der höheren Mathematik - Teil IV*, VEB Deutscher Verlag der Wissenschaften, Berlin, 6. edition edn., 1973.

Steigenberger, P., Rothacher, M., Dietrich, R., Fritsche, M., Rülke, A., and Vey, S.: Reprocessing of a global GPS network, *J. Geophys. Res.*, 111, doi:10.1029/2005JB003747, 2006.

Swisstopo: Automatic Geodetic Network of Switzerland (AGNES) History, URL: <http://www.swisstopo.admin.ch/swisstopo/geodesy/pnac/html/de/statpaye.html>, last visited: May 2014, 2014a.

Swisstopo: DHM25, URL: <http://www.swisstopo.admin.ch/internet/swisstopo/en/home/products/height/dhm25.html>, last visited: Aug 2014, 2014b.

Swisstopo: Automatic Geodetic Network of Switzerland (AGNES): Official Website, URL: www.swisstopo.admin.ch/internet/swisstopo/de/home/topics/survey/permnet/agnes.html, last visited: May 2014, 2014c.

Troller, M.: GPS based Determination of the Integrated and Spatially Distributed Water Vapor in the Troposphere, vol. 67 of *Geodätisch-geophysikalische Arbeiten in der Schweiz*, Swiss Geodetic Commission, 2004.

Urquhart, L., Nievinski, F., and Santos, M.: Ray-traced slant factors for mitigating the tropospheric delay at the observation level, *Journal of Geodesy*, 86, 149–160, doi:10.1007/s00190-011-0503-x, URL <http://dx.doi.org/10.1007/s00190-011-0503-x>, 2012.

Vaisala: Vaisala Radiosonde RS92-SGP, Published by Vaisala, www.vaisala.com, www.vaisala.com/Vaisala%20Documents/Brochures%20and%20Datasheets/RS92SGP-Datasheet-B210358EN-F-LOW.pdf, last visited: 16 Aug 2013, 2013a.

Vaisala: Vaisala Radiosonde RS92-SGP, website to datasheet: [http://www.vaisala.com/Vaisala/Documents/Brochures and Datasheets/](http://www.vaisala.com/Vaisala/Documents/Brochures%20and%20Datasheets/), last visited: April 2013, 2013b.

Van Baelen, J., Aubagnac, J.-P., and Dabas, A.: Comparison of Near-real Time Estimates of Integrated Water Vapor Derived with GPS, Radiosondes, and Microwave Radiometer, *J. Atmos. Oceanic Technol.*, 22, 201–210, URL <http://dx.doi.org/10.1175/JTECH-1697.1>, 2005.

- Van Baelen, J., Reverdy, M., Tridon, F., Labbouz, L., Dick, G., Bender, M., and Hagen, M.: On the relationship between water vapour field evolution and the life cycle of precipitation systems, *Quarterly Journal of the Royal Meteorological Society*, 137, 204–223, doi:10.1002/qj.785, URL <http://dx.doi.org/10.1002/qj.785>, 2011.
- VARS Documentation: Variational Atmospheric Retrieval Scheme (VARS) for GPS Radio Occultation Data, COSMIC Project Office, University Corporation for Atmospheric Research, version 1.1: <http://cdaac-www.cosmic.ucar.edu/cdaac/doc/documents/1dvar.pdf> (last access: 27 May 2013), 2005.
- Walpersdorf, A., Calais, E., Haase, J., Eymard, L., Desbois, M., and Vedel, H.: Atmospheric gradients estimated by GPS compared to a high resolution numerical weather prediction (NWP) model, *Phys. Chem. Earth*, 26, 147–152, 2001.
- Wang, B.-R., Liu, X.-Y., and Wang, J.-K.: Assessment of COSMIC radio occultation retrieval product using global radiosonde data, *Atmospheric Measurement Techniques*, 6, 1073–1083, doi:10.5194/amt-6-1073-2013, URL <http://www.atmos-meas-tech.net/6/1073/2013/>, 2013a.
- Wang, J., Zhang, L., Dai, A., Immler, F., Sommer, M., and Vömel, H.: Radiation Dry Bias Correction of Vaisala RS92 Humidity Data and Its Impacts on Historical Radiosonde Data, *J. Atmos. Oceanic Technol.*, 30, 197–214, URL <http://dx.doi.org/10.1175/JTECH-D-12-00113.1>, 2013b.
- Wilhelm, M.: COSMO-2 Model Performance in Forecasting Foehn: a Systematic Process-Oriented Verification., *Veröffentlichungen der MeteoSchweiz*, 89, 64pp, MeteoSchweiz, 2012.
- Wu, X., Wang, X., and Lü, D.: Retrieval of vertical distribution of tropospheric refractivity through ground-based GPS observation, *Advances in Atmospheric Sciences*, 31, 37–47, doi:10.1007/s00376-013-2215-z, URL <http://dx.doi.org/10.1007/s00376-013-2215-z>, 2014.
- Wu, Y.-Y., HONG, Z.-J., GUO, P., and ZHENG, J.: Simulation of Atmospheric Refractive Profile Retrieving from Low-Elevation Ground-Based GPS Observations, *Chinese Journal of Geophysics*, 53, 639–645, doi:10.1002/cjg2.1533, URL <http://dx.doi.org/10.1002/cjg2.1533>, 2010.
- Xia, P., Cai, C., and Liu, Z.: GNSS troposphere tomography based on two-step reconstructions using GPS observations and COSMIC profiles, *Annales Geophysicae*, 31, 1805–1815, doi:10.5194/angeo-31-1805-2013, URL <http://www.ann-geophys.net/31/1805/2013/>, 2013.

Appendix A

Design of AWATOS2

A.1 An introductory example

A typical task for AWATOS2 would be the simulation of zero-difference path delays across a refractivity field. Figure A.1 is a flowchart of what the software does and what data sets it needs to achieve the task. The refractivity field's source are the pressure p , temperature T and relative humidity f data from a NWP model output. Usually, these data are given in netcdf file format. The NWP model output belongs to certain grid nodes whose coordinates are also defined in a netcdf file. The p, T and f values in combination with the NWP model grid coordinates define a refractivity field. Furthermore, AWATOS2 needs to know the GNSS ground station coordinates and the satellites' positions at the time period under investigation. They are read by the software from corresponding coordinate and orbit files. Now that the geometry of the problem is set, the zero-difference path delays can be calculated, integrating across the refractivity field from the satellites to the GNSS ground stations. An output of the delays in ascii format concludes the processing chain.

A.2 Modular layout

Each subtask of Fig. A.1 is handled with a module. The AWATOS2 modules need input data and give an output as shown in Fig. A.2. For example, the `mod_semistructured_grid_file` takes the netcdf file with NWP model grid coordinates as its input and creates an AWATOS2 representation of the grid definition. Together with the refractivity values from `mod_refractivity_field_file`, they provide the input for `mod_data_refractivity_field` that assigns the coordinates to their corresponding values. The output refractivity field and the output from the orbit and ground station file readers become the input to the zero-difference path delay simulation module (`mod_sim_zero_difference`), which in turn, hands its output to the writer module `mod_zero_difference_observation_writer`. The software's language is C++, where the modules are written as shared libraries that are dynamically loaded at runtime. Modules with identical inputs are interchangeable and allow flexible use of the individual modules. The module options are configured with a file in xml-format. Figure A.3 displays the configuration file of our introductory example with comments on the structure of the file. The topmost lines give the xml parser some xml-version information and a file that specifies the structure of the read xml-file. With the structure information, the parser is able to check the correctness of the file. That is, what attribute names are admissible and what is the correct order of xml-elements the AWATOS2 configuration file should comply with. The `<global>` section includes information that becomes important to a number of processing modules. It includes AWATOS2 internal grid definitions and voxel parameterizations (none, constant, linear, spline). Other `<global>`s might include the definition of the initial Kalman filter setup or, a so-called diagnostics module that serves as a kind of diary, into which processing modules can write intermediate results. The `<modules>` section contains four different types of modules:

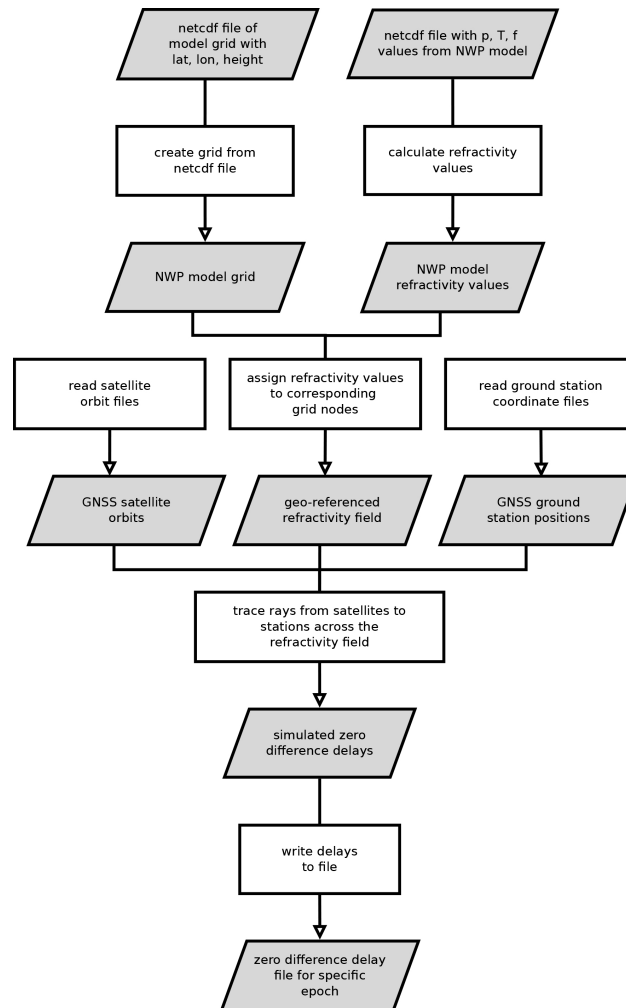


Figure A.1: Flowchart showing an example of the processing steps needed to simulate zero-difference path delays with AWATOS2. White boxes denote actual processing steps and grey boxes are the sources or products of these steps.

1. reading modules get the correct refractivity field, satellite orbits and ground station coordinate files
2. processing modules are responsible for calculating intermediate or final results
3. writing modules write the processing results to files in ascii format
4. the interval iterator is a kind of internal clock of the software that mimics time

As presented in Fig. A.2, some output become input for other modules. The `<connections>` part of the configuration file in Fig. A.3 handles the data flow with slots that have a source (output of a module) and a destination (input to a module). In case of multiple slots, naming is required, otherwise no slot name needs to be stated. The last module in the processing chain is always connected to the interval iterator. Its responsibility as starting module is marked in the bottom line of the xml-file as runnable id. As the `<global>` modules do not connect to other modules through the `<connections>`, the processing modules fetch the `<global>` data from the environment (an AWATOS2 object). In the environment, the `<global>` modules' data is registered and can be accessed with characteristic names. For example, the grid created in our example is registered and accessed under the name `my_grid`.

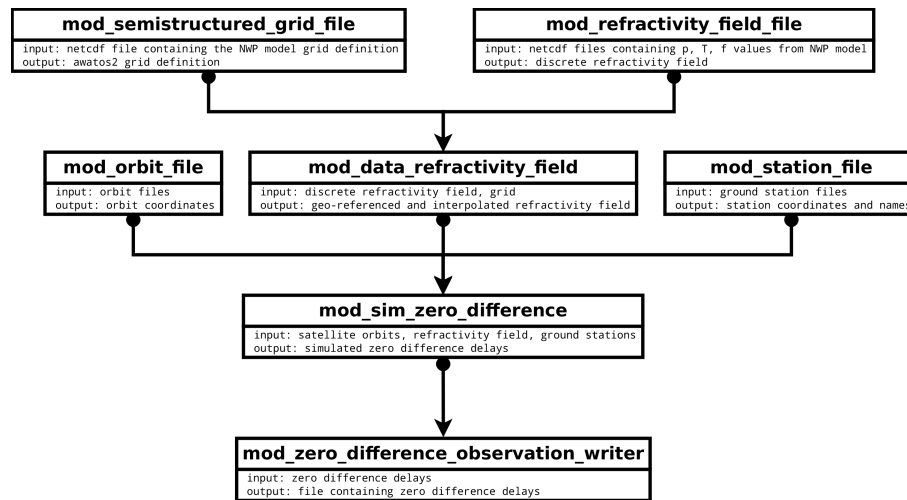


Figure A.2: AWATOS2 modules and their dependencies to simulate zero-difference delays from NWP model pressure, temperature and relative humidity fields. It shows the processing chain of Fig. A.1 at the specification level.

A.3 General object-oriented design

The configuration file in Fig. A.3 contains already an important principle of the AWATOS2 software design: The software acts as a kind of lazy evaluator of data. Imagine, the interval iterator states a change in its internal clock. It passes this change to the writer module whose writing task of the previous time interval has just finished. As it receives the new interval, it notes that there is no up-to-date results available to write to file. In our example, `mod_zero_difference_observation_writer` would then ask `mod_sim_zero_difference` to provide updated data. Also `mod_sim_zero_difference` would realize that it needs updated data and asks its inputs to provide their part. This chain reaction continues to the file readers. They will then read a new set of files and hand this information on to their destination modules, till all modules are satisfied with updated data and the interval iterator can continue with another time step.

How is this program logic transferred into an object-oriented software design? AWATOS2 makes heavy use of the observer pattern. Its structure is given in Fig. A.4 (see e.g., Gamma et al., 1995). A subject, whose state has changed, notifies its registered observers about the change. The observers react to it with an update procedure. In our example, the observers react with the calculation of an updated data set to the notification of the subject. As they need updated input to calculate their updated output, the observers act themselves as subjects for other observers, too. In AWATOS2, the subject's and the observers' responsibilities are thus unified using multiple inheritance. For the four module types presented in Sect. A.2, there are slight differences in implementations of the observer pattern (Fig. A.5): The timer is not a source of data for any other module and does not need to inherit from the observer. It is just a subject for the writer module or any other module that follows. The writers do need input data, but there is no need for a place to store their attained data. They will write data directly to file. The `data_file_sink` therefore does not inherit from a source class that is a derived class of the observer containing a data member. The processors require all the functionality of the observer and subject plus a data member. As there are different ways to carry out the update procedure (either requiring all data from the new interval or only the data parts that have actually changed), there is another abstraction layer for the processors. Presently in use is the `simple_interval_operator` only. The readers inherit from the same classes as the processors. They act as subjects for file list sources that inherit only from the source class (not shown in Fig. A.5). The file list sources act as the tail of the processing chain, whereas the interval iterator is the head or starting point. The file access sources themselves get

file lists where each filename is assigned to a specific date/time (`time_file_source`) or to a time interval (`interval_file_source`).

There are data files that contain measurements of an entire interval, as for example daily GNSS ZTD files, and there are files, where each file contains measurements of one specific date/time only, as is the case for NWP model files (Fig. A.6). The way, reader modules determine which files to access and read for a requested time interval, is specified in either the `abstract_time_access_file_source` or the `interval_access_file_source`.

Many specific writers, processors and readers derive from `data_file_sink`, `simple_interval_operator`, `abstract_time_access_file_source` and `interval_access_file_source`, respectively (Fig. A.5). They make up the sources and destinations in the `<connections>` section of Fig. A.3, whereas the modules are responsible for the setup, assignment and management of these sources and destinations. The modules themselves get set up and managed by the main-program and the `module_manager`.

A.4 Other design patterns used

Beside the observer pattern, many other object-oriented design patterns have been realized in AWATOS2. A number of source-code file names have been sorted according to their affiliation to a pattern. Furthermore, the patterns' purpose and consequences in AWATOS2 and some notes on their specific participants and implementations are outlined in this section. Names of patterns and abstract names of their participants correspond to the naming in Gamma et al. (1995).

- **FactoryMethod**

- **purpose and consequences:** Defines an interface to create file readers, since there will be a lot of variation in the readers. The modules (being the readers' clients) should be as unaffected as possible by the addition of a new reader.

- **participants:**

Product:

`fstream_reader`

`netcdf_reader`

ConcreteProduct:

- * `fstream`: `atab_meteo_field_reader`, `atab_radar_field_reader`,
`awatos_apriori_reader`, `awatos_dd_residuum_reader`,
`awatos_zpd_reader`, `bernese_station_reader`,
`illh_station_reader`, `kalman_filter_info_field_reader`, `point_meteo_reader`,
`sp3_reader`, `tabulated_meteo_reader`

- * `netcdf`: `netcdf_meteo_field_reader`

Creator:

`fstream_reader_factory`

`netcdf_reader_factory`

ConcreteCreator:

- * `fstream`: `atab_meteo_field_reader_factory`, `atab_radar_field_reader_factory`,
`awatos_apriori_reader_factory`, `awatos_dd_residuum_reader_factory`,
`awatos_zpd_reader_factory`, `bernese_station_reader_factory`,
`illh_station_reader_factory`, `kalman_filter_info_field_reader_factory`,
`point_meteo_reader_factory`, `sp3_reader_factory`, `tabulated_meteo_reader_factory`
- * `netcdf`: `netcdf_meteo_field_reader_factory`

- **implementation notes:**

Reading method:

* `fstream`:

`operator()(istream)`

* `netcdf`:

`operator()(filename)`

Factory method:

`operator>()()`

- **purpose and consequences:** AWATOS2 offers different grid structures where the height is meshed differently. The FactoryMethod allows further height parameterizations to be added without changing the modules considerably. Small changes are needed in the initialize_module method of the client modules, where the module configurations are handled.
- **participants:**
 - Product:*
(grid)
 - ConcreteProduct:*
structured_grid
 - Creator:*
abstract_structured_grid_creator
 - ConcreteCreator:*
exponential_structured_grid_creator, geometric_series_structured_grid_creator, swiss_grid_structured_grid_creator
- **implementation notes:**
 - FactoryMethod:
operator()
 - Clients that use the FactoryMethod are the structured_swiss_grid_creator_module and the structured_grid_creator_module. The created grid is directly assigned to structured_grid and not to the interface of the structure_grid (which would be the *Product*), since the modules do not provide any other grid types than the one *ConcreteProduct*.

- **Strategy**

- **purpose and consequences:** Determines how options from the xml-configuration file should be handled, i.e. if they should be input into the environment or directly assigned to a specific module.
- **participants:**
 - Context:*
option_xml_state
 - Strategy:*
option_strategy
 - ConcreteStrategy:*
environment_option_strategy, module_option_strategy
- **implementation notes:** Either an option is a normal module option inserted into the module or it is an environment option that is inserted into the environment. The clients that configure the context are global_xml_state and module_xml_state.
 - AlgorithmInterface:
operator()(key,value)
- **purpose and consequences:** Depending on the order of the Kalman filter (zeroth_order means that the Kalman filter state vector does not include refractivity changes in time), the boundaries have to be set. These possibilities are encapsulated in the boundary condition strategies.
- **participants:**
 - Context:*
boundary_condition_source
 - Strategy:*
abstract_boundary_condition_strategy
 - ConcreteStrategy:*
zeroth_order_boundary_condition_strategy, first_order_boundary_condition_strategy

- **implementation notes:** The client that configures the context with a *ConcreteStrategy* is the `boundary_condition_module`.

AlgorithmInterface:

`operator()(grid_id, time, field)`

`compute_ids()`

The parameter field combines the grid with its associated refractivity values. The operator then returns the refractivity value corresponding to a given `grid_id`, time, and field. `Compute_ids` gets all grid ids that belong to a certain boundary.

- **purpose and consequences:** Get the coefficients of grid nodes for the model matrix from either a point, a slant or a zenith path observation for the three voxel parameterization modes `const/linear/spline`.

- **participants:**

Context:

`station_indexed_observation_source`, `double_difference_observation_source`,

`point_observation_source`, `zenith_path_delay_observation_source`,

`zero_difference_observation_source`

Strategy:

`coeff_calculator`

ConcreteStrategy:

`const_voxel_line_strategy`, `const_voxel_point_strategy`,

`const_voxel_zenith_strategy`, `linear_voxel_line_strategy`,

`linear_voxel_point_strategy`, `linear_voxel_zenith_strategy`,

`spline_voxel_line_strategy`, `spline_voxel_point_strategy`,

`spline_voxel_zenith_strategy`

- **implementation notes:**

Clients that configure the context with the correct strategy:

`cont_id_meteo_module`, `double_difference_module`, `id_meteo_module`,

`point_observation_module`, `zenith_path_delay_module`,

`zero_difference_creator_module`, `zero_difference_module`

AlgorithmInterface:

`coeff_type operator()(voxel id, point within voxel or start-/end-point`

`on voxel boundary)`

The operator only calculates grid node coefficients for one voxel.

- **Adapter (class adapter)**

- **purpose and consequences:** Treat strings, as for example grid type strings, like any other object that can be added to the environment. This makes it possible that beside several different types of objects, also strings can be added to the environment. The following object types are accepted by the environment: `grid`, `diagnostics_dictionary`, `grid_adaptor`, `zpd_model_info_object`, `kalman_filter_info`, `zenith_path_delay_model_info`, `module_manager`, any string adapted by the `object_wrapper`

- **participants:**

Target:

`abstract_object`

Client:

`environment`

Adaptee:

`string`

Adapter:

`object_wrapper`

- **implementation notes:** The `grid_type` string and any other option string that is inserted into the environment needs to be adapted to look like an abstract object. This adaptor does not adapt a specific request, but adapts type. The `<global>` options from the xml-configuration are set into the environment by means of the `object_wrapper`.

- **Adapter (object adapter)**

- **purpose and consequences:** Allows a common treatment of the grid parameterizations linear, spline or voxel. The two presently implemented adapters are `structured_grid_adaptor` and `semistructured_grid_adaptor` for the corresponding structured and semistructured grids.
- **participants:**
 - Client:*
modules that use a `structured_grid`, e.g., `data_refractivity_field_module`
 - Target:*
`structured_grid`
 - Adaptee:*
a voxel field
 - Adapter:*
`voxel_structured_grid_adaptor`
- **implementation notes:** Example of adapted request in `voxel_structured_grid_adaptor`:
Request:
 `get_nbr_ids()`
Specific request:
 `get_nbr_voxels()`

- **Observer**

- **purpose and consequences:** Coordinating the modules such that if the state of a module changes to `CHANGED` or `DELETED`, the observer pattern takes care of the rebuilding or destruction of the module chain. It works similarly to a double-linked list since each module serves as subject and observer.
- **participants:**
 - Subject:*
subject
 - Observer:*
observer
 - ConcreteSubject:*
module
 - ConcreteObserver:*
module
- **implementation notes:** The four states a module can have are `NONE`, `CHANGED`, `DELETED`, `CREATED`. The update procedure has only an effect in cases of `CHANGED` or `DELETED`. For example, the `xml_config_module` gets deleted after having parsed the xml configuration file.

- **TemplateMethod**

- **purpose and consequences:** Defer the task of getting the *ConcreteFactory* to the subclasses of `interval_access_file_module`. All other parts in `initialize_module` of `interval_access_file_module` remain the same for the subclass reader modules. Thus, the TemplateMethod avoids code duplication.
- **participants:**
 - AbstractClass:*
`interval_access_file_module`
 - ConcreteClass:*

apriori_file_module, cont_id_meteo_file_module,
double_difference_residuum_file_module, id_meteo_file_module,
orbit_file_module, point_meteo_file_module, station_file_module

– **implementation notes:**

TemplateMethod:

 initialize_module(environment)

PrimitiveOperation:

 get_factory_method(environment)

Usually, a TemplateMethod should not be overridden, but in `zenith_path_delay_file_module` there is an `initialize_module` that overrides the version from the *AbstractClass*. However, it calls the TemplateMethod and adds additional information to the environment. This added information is not known in the *AbstractClass*. (An option would have been to add another PrimitiveOperation in the *ConcreteClass*: `add_info_to_environment`).

```

<?xml version="1.0"?>
<!DOCTYPE configuration SYSTEM "/awatos2/xmlconfig/config.dtd">
<configuration>
  <module_path>./awatos2/modules</module_path>
  <global>
    <option name="voxel_parametrization">none</option>
    <module id="1" name="mod_semistructured_grid_file">
      <option name="grid_file">./cosmo2/tomo_c2_ana_cnc</option>
      <option name="grid_name">my_grid</option>
      <option name="max_lat">55.0</option>
      <option name="max_lon">20.0</option>
      <option name="min_lat">35.0</option>
      <option name="min_lon">0.0</option>
      <option name="lat_rot">43.0</option>
      <option name="lon_rot">-170.0</option>
      <option name="off_lat">0</option>
      <option name="off_lon">0</option>
      <option name="reader">netcdf</option>
    </module>
  </global>
  <modules>
    <module id="201" name="mod_refractivity_field_file">
      <option name="delta_time">0.0</option>
      <option name="mapper">year_month_day_hour</option>
      <option name="path">./cosmo2/2010/07/</option>
      <option name="reader">netcdf</option>
      <option name="max_relative_humidity">100.0</option>
      <option name="refractivity_type">total</option>
      <option name="regex">.*tomo_c2_ana_[0-9]+.nc</option>
      <option name="renew">>false</option>
    </module>
    <module id="202" name="mod_orbit_file">
      <option name="mapper">gpsweek_weekday</option>
      <option name="max_time_span">6.0</option>
      <option name="path">/orbits</option>
      <option name="regex">.*igs_*.sp3</option>
      <option name="renew">>false</option>
    </module>
    <module id="203" name="mod_station_file">
      <option name="mapper">gpsweek_week</option>
      <option name="max_time_span">7.0</option>
      <option name="path">/station_files/</option>
      <option name="reader">bernese</option>
      <option name="regex">.*STATS[0-9]+.CRD</option>
      <option name="renew">>false</option>
    </module>
    <module id="204" name="mod_data_refractivity_field">
      <option name="grid_name">my_grid</option>
      <option name="interpolation">linear</option>
      <option name="rot_lat">43.0</option>
      <option name="rot_lon">-170.0</option>
      <option name="scale_height">7821.0</option>
      <option name="ch_adapt">>false</option>
    </module>
    <module id="301" name="mod_sim_zero_difference">
      <option name="cutoff_angle">1.0</option>
      <option name="slant_delay_bias">0.0</option>
      <option name="slant_delay_integration_height">22992.2</option>
      <option name="slant_delay_nbr_int_steps">12</option>
      <option name="slant_delay_nbr_layers">8</option>
      <option name="slant_delay_noise_variance">0.0</option>
      <option name="slant_delay_reported_variance">0.0</option>
      <option name="slant_delay_scale_height">3500.0</option>
      <option name="zero_difference_start_time">55395.0</option>
      <option name="zero_difference_time_step">30.0</option>
      <option name="station_ids">1, 2, 3, 8, 9, 10</option>
    </module>
    <module id="302" name="mod_zero_difference_observation_writer">
      <option name="filename_pattern">matrix_%05d_%05d.txt</option>
      <option name="offset">0.0</option>
      <option name="step">3600</option>
    </module>
    <module id="303" name="mod_interval_iterator">
      <option name="interval_size">3640.0</option>
      <option name="start_time">55396.0</option>
      <option name="stop_time">55401.0</option>
      <option name="step_size">3600.0</option>
    </module>
  </modules>
  <connections>
    <connect src="201" dst="204" slot="atmosphere"/>
    <connect src="202" dst="301" slot="orbit"/>
    <connect src="203" dst="301" slot="station"/>
    <connect src="204" dst="301" slot="atmosphere"/>
    <connect src="301" dst="302"/>
    <connect src="302" dst="303"/>
  </connections>
  <runnable id="303"/>
</configuration>

```

configuration information for xml-reader

modules and parameters used by multiple processing modules

file reading modules

processing modules

writing modules

module mimicking running time

connection between modules with source and destination number and slot

number of starting module

Figure A.3: Example of an AWATOS2 configuration file in xml-format.

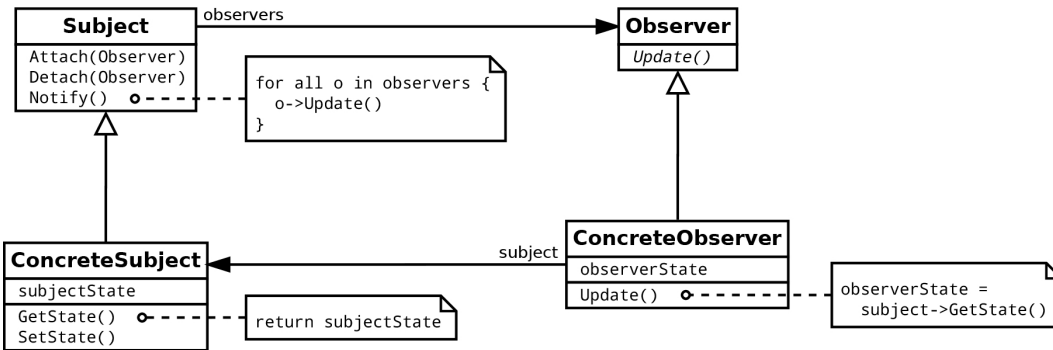


Figure A.4: UML diagram of the observer software design pattern (Gamma et al., 1995; Shalloway and Trott, 2004). Note that italic member functions are abstract.

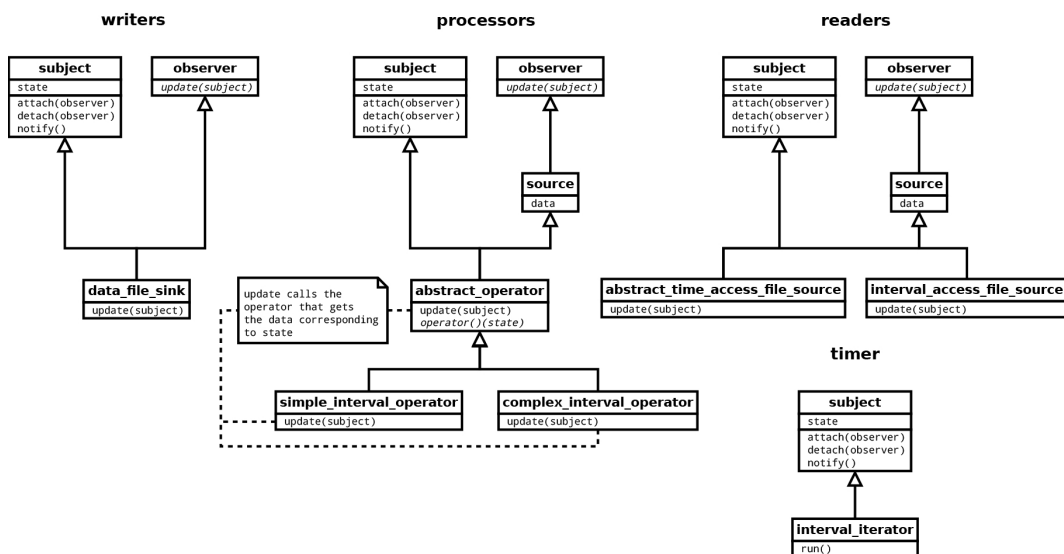


Figure A.5: UML diagram of the solutions implemented in AWATOS2 that combine the subject and observer capabilities with multiple inheritance. The timer being the starting point of the observer pattern only inherits from the subject.

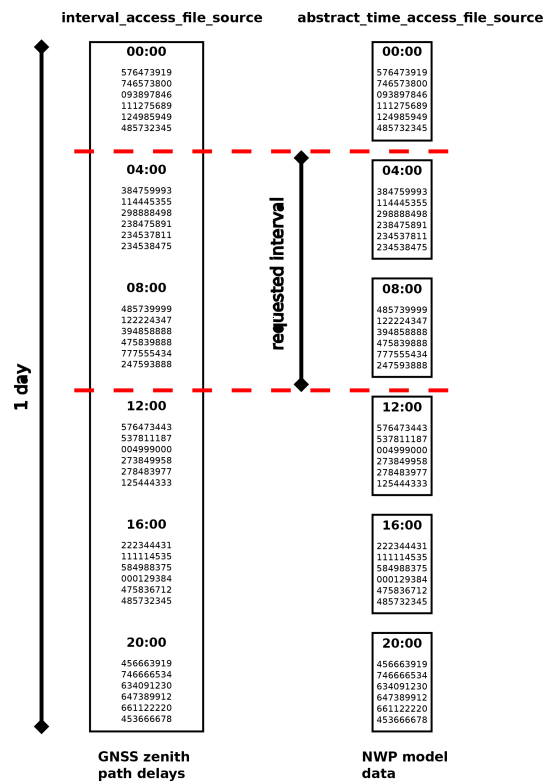


Figure A.6: Sketch showing the two different file access sources. They decide on the basis of the filename-to-interval or the filename-to-date mapping, which files need to be read and what data is kept in the specific storage. They also call the corresponding readers in their update procedures.

Appendix B

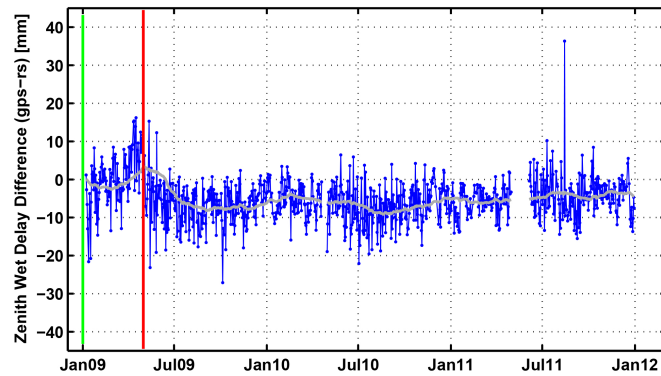
Model fits to empirical autocorrelation functions

Table B.1: Estimated model parameters and their 1σ standard deviations from fits of Eq. (2.100) to empirical autocorrelation functions. Other information as for Tab. 2.1, but with a horizontal ordering according to the number of sample stations instead of spatial extent.

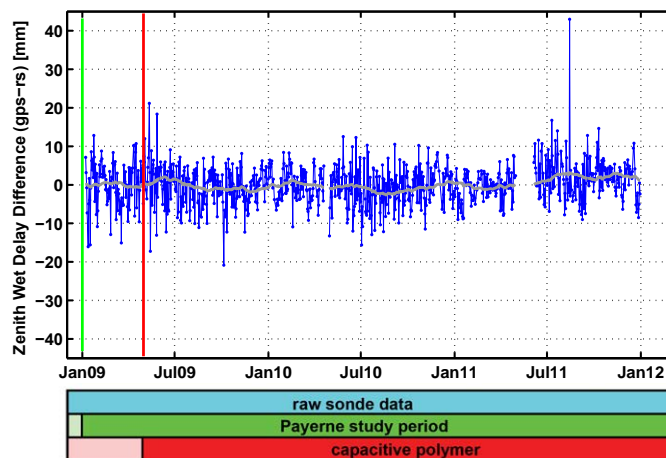
		# of sample stations												
		8000	4000	2000	1333	1000	500	333	250	200	100	60	50	
sample spacing [m]	0.5	$l_{x,data}$	3.943 \pm 0.045			4.045 \pm 0.036		3.474 \pm 0.071			2.739 \pm 0.214	2.590 \pm 0.195	1.894 \pm 0.211	
		a	0.798 \pm 0.003			0.828 \pm 0.002		0.820 \pm 0.006			0.777 \pm 0.028	0.797 \pm 0.029	0.748 \pm 0.045	
		σ_{signal}	2.010			2.199		2.029			1.801	2.055	1.779	
		σ_{noise}	1.012			1.003		0.950			0.964	1.036	1.032	
	1.0	$l_{x,data}$		3.817 \pm 0.039			3.945 \pm 0.054	3.067 \pm 0.189				2.627 \pm 0.288		3.230 \pm 0.029
		a		0.805 \pm 0.005			0.837 \pm 0.007	0.859 \pm 0.036				0.793 \pm 0.060		0.746 \pm 0.003
		σ_{signal}		2.009			2.197	2.072				1.943		2.145
		σ_{noise}		0.989			0.968	0.839				0.994		1.252
	2.0	$l_{x,data}$			3.784 \pm 0.077			4.628 \pm 0.370		3.213 \pm 0.175				
		a			0.809 \pm 0.014			0.797 \pm 0.049		0.881 \pm 0.042				
		σ_{signal}			2.047			2.207		2.140				
		σ_{noise}			0.994			1.114		0.785				
3.0	$l_{x,data}$				4.361 \pm 0.504			5.801 \pm 0.991						
	a				0.747 \pm 0.080			0.619 \pm 0.087						
	σ_{signal}				1.947			1.914						
	σ_{noise}				1.134			1.501						

Appendix C

Zenith Wet Delay comparison to Payerne radiosonde

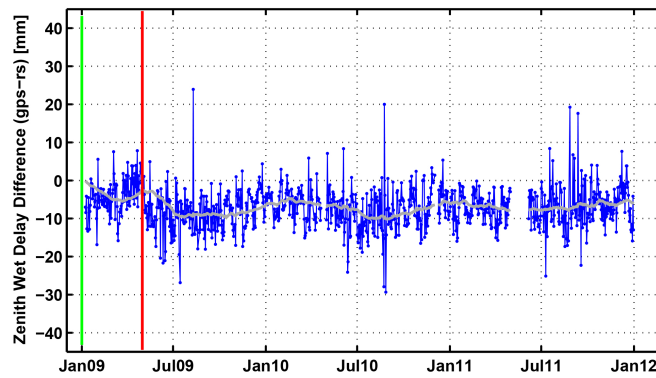


(a) original

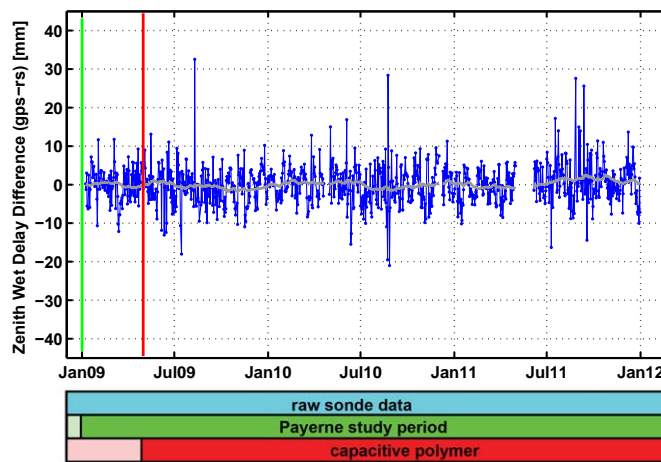


(b) filtered

Figure C.1: (a) Original day (gps-rs) ZWD time series. (b) Filtered day (gps-rs) ZWD time series. Other information as for Figs. 3.2a and b.



(a) original



(b) filtered

Figure C.2: (a) Original night (gps-rs) ZWD time series. (b) Filtered night (gps-rs) ZWD time series. Other information as for Figs. 3.2a and b.

Appendix D

Statistics of Zermatt troposphere results

Table D.1: Results from ZTD comparisons between GPS and Radiosonde with different Bernese processing configurations. The interquartile range is defined as $IQR = Q_{75\%} - Q_{25\%}$.

station	processing mode	tropo map	param. spacing	min [mm]	$Q_{25\%}$ [mm]	$Q_{50\%}$ [mm]	$Q_{75\%}$ [mm]	max [mm]	IQR [mm]	mean [mm]	stdev [mm]	# [-]
BLAU	NTW, 180s, daily	GMF	2 h	-14.7	-6.8	-0.2	3.2	15.7	10.0	-0.9	7.2	25
	NTW, 180s, daily	GMF	1 h	-22.9	-5.4	-0.2	4.9	13.4	10.4	-0.7	8.1	25
	NTW, 180s, daily	GMF	30 min	-25.8	-4.9	0.8	7.2	13.3	12.2	0.8	8.7	25
	NTW, 180s, daily	Niell	1 h	-22.8	-5.2	0.2	4.2	21.8	9.4	-0.3	8.8	25
	NTW, 30s, daily	GMF	2 h	-14.8	-6.6	0.5	3.8	13.8	10.4	-0.4	7.2	25
	PPP, 300s, daily	GMF	2 h	-15.2	-3.7	1.7	2.8	10.0	6.5	-0.1	5.7	25
	PPP, 30s, daily	GMF	2 h	-15.1	-3.0	1.2	2.9	10.4	5.9	0.1	5.6	25
	PPP, 30s, daily	GMF	1 h	-15.2	-0.5	1.8	4.2	13.6	4.7	1.1	5.6	25
	PPP, 30s, daily	GMF	30 min	-13.7	-1.1	1.9	4.2	22.2	5.3	2.1	6.5	25
	NTW, 180s, weekly	GMF	2 h	-13.7	-3.9	0.5	4.3	15.4	8.2	0.6	6.7	25
GABE	NTW, 180s, daily	GMF	2 h	-12.4	-4.6	-1.7	3.7	15.4	8.3	-0.4	7.1	25
	NTW, 180s, daily	GMF	1 h	-16.6	-3.6	1.8	2.8	15.9	6.4	0.6	8.0	25
	NTW, 180s, daily	GMF	30 min	-19.1	-3.8	1.6	5.8	15.5	9.5	1.5	8.3	25
	NTW, 180s, daily	Niell	1 h	-15.3	-3.2	1.7	3.0	18.2	6.2	0.9	8.2	25
	NTW, 30s, daily	GMF	2 h	-12.2	-5.2	-0.3	5.3	11.9	10.5	-0.0	7.0	25
	PPP, 300s, daily	GMF	2 h	-14.9	-0.4	1.0	2.5	11.3	2.9	0.9	5.3	25
	PPP, 30s, daily	GMF	2 h	-14.8	-0.1	1.4	2.8	10.0	2.9	1.0	5.0	25
	PPP, 30s, daily	GMF	1 h	-15.0	0.6	2.9	5.0	9.1	4.4	2.1	5.4	25
	PPP, 30s, daily	GMF	30 min	-7.3	0.5	3.7	5.4	16.0	5.0	3.1	4.6	25
	NTW, 180s, weekly	GMF	2 h	-11.3	-4.7	-0.4	5.6	16.4	10.3	0.6	7.2	25
GAGE	NTW, 180s, daily	GMF	2 h	-12.3	-1.7	0.9	4.7	14.2	6.3	1.5	6.3	25
	NTW, 180s, daily	GMF	1 h	-20.7	-1.7	1.3	5.8	14.9	7.5	1.6	7.3	25
	NTW, 180s, daily	GMF	30 min	-22.6	-1.9	1.2	9.5	13.3	11.4	2.1	7.9	25
	NTW, 180s, daily	Niell	1 h	-19.5	-1.6	1.4	6.2	22.8	7.8	1.9	8.0	25
	NTW, 30s, daily	GMF	2 h	-12.2	-0.4	1.7	7.3	15.1	7.7	2.3	6.3	25
	PPP, 300s, daily	GMF	2 h	-16.4	-2.1	1.4	4.5	10.2	6.6	0.7	5.9	25
	PPP, 30s, daily	GMF	2 h	-14.7	-1.6	0.6	4.2	10.7	5.8	0.9	5.7	25
	PPP, 30s, daily	GMF	1 h	-15.5	-0.6	1.3	6.4	16.1	7.0	2.1	6.5	25
	PPP, 30s, daily	GMF	30 min	-11.3	-0.3	2.2	6.6	21.1	7.0	2.7	7.3	25
	NTW, 180s, weekly	GMF	2 h	-13.7	-1.3	1.5	5.9	15.6	7.2	1.8	6.3	25
GAND	NTW, 180s, daily	GMF	2 h	-12.1	-2.4	0.9	5.7	20.0	8.1	1.5	6.5	25
	NTW, 180s, daily	GMF	1 h	-22.1	-1.8	2.1	5.3	15.9	7.1	1.4	7.3	24
	NTW, 180s, daily	GMF	30 min	-22.2	-1.0	3.0	8.3	16.9	9.3	2.9	8.6	24
	NTW, 180s, daily	Niell	1 h	-18.1	-1.6	2.1	4.9	17.4	6.6	1.8	7.2	24
	NTW, 30s, daily	GMF	2 h	-12.1	-1.6	2.7	6.7	16.2	8.3	2.1	6.3	25
	PPP, 300s, daily	GMF	2 h	-18.9	-1.7	1.2	2.7	13.3	4.4	0.8	5.9	25
	PPP, 30s, daily	GMF	2 h	-18.3	-2.1	1.3	3.4	13.8	5.5	0.9	5.8	25
	PPP, 30s, daily	GMF	1 h	-23.6	-0.7	2.1	3.7	17.6	4.4	1.4	6.9	25
	PPP, 30s, daily	GMF	30 min	-15.6	-0.9	2.8	4.6	21.2	5.4	2.8	6.5	24
	NTW, 180s, weekly	GMF	2 h	-12.8	-2.4	1.4	4.9	18.9	7.2	1.7	6.4	25

D Statistics of Zermatt troposphere results

GIFT	NTW, 180s, daily	GMF	2 h	-12.9	-2.4	-0.3	4.1	13.8	6.5	0.6	6.8	20
	NTW, 180s, daily	GMF	1 h	-16.6	-2.5	-0.3	5.1	15.6	7.6	1.0	7.2	20
	NTW, 180s, daily	GMF	30 min	-16.6	-3.8	1.2	6.4	13.3	10.2	1.4	8.0	19
	NTW, 180s, daily	Niell	1 h	-16.2	-3.0	-0.5	5.6	24.5	8.6	1.5	8.3	20
	NTW, 30s, daily	GMF	2 h	-11.1	-2.2	-0.4	6.8	13.7	9.0	1.5	6.8	21
	PPP, 300s, daily	GMF	2 h	-10.1	-4.5	-0.9	3.1	8.0	7.6	-0.5	5.6	20
	PPP, 30s, daily	GMF	2 h	-10.6	-3.9	-1.5	3.2	7.5	7.0	-0.7	5.2	21
	PPP, 30s, daily	GMF	1 h	-7.1	-3.1	-0.4	3.6	10.3	6.7	0.4	5.0	20
	PPP, 30s, daily	GMF	30 min	-4.7	-2.9	0.8	5.0	25.4	8.0	2.3	6.9	20
	NTW, 180s, weekly	GMF	2 h	-12.9	-1.7	1.7	5.7	15.2	7.4	1.6	6.9	20
GLAZ	NTW, 180s, daily	GMF	2 h	-12.4	-1.6	0.4	3.9	13.5	5.6	1.2	6.1	25
	NTW, 180s, daily	GMF	1 h	-16.5	-2.6	1.3	4.9	12.0	7.5	1.3	6.8	25
	NTW, 180s, daily	GMF	30 min	-18.5	-2.4	0.7	7.9	15.1	10.2	1.5	8.2	25
	NTW, 180s, daily	Niell	1 h	-16.0	-2.4	1.6	5.2	19.0	7.7	1.5	7.3	25
	NTW, 30s, daily	GMF	2 h	-14.0	-2.4	1.3	3.9	12.2	6.2	1.1	6.2	25
	PPP, 300s, daily	GMF	2 h	-18.1	-0.7	1.1	3.2	9.5	3.9	0.9	5.4	25
	PPP, 30s, daily	GMF	2 h	-18.2	-0.4	1.3	3.9	9.2	4.3	1.0	5.3	25
	PPP, 30s, daily	GMF	1 h	-19.6	0.1	1.5	4.6	7.4	4.4	1.3	5.2	25
	PPP, 30s, daily	GMF	30 min	-13.7	-0.2	2.2	4.9	10.2	5.1	1.9	5.0	25
	NTW, 180s, weekly	GMF	2 h	-11.8	-0.8	2.2	4.7	13.9	5.5	2.1	6.2	25
GORN	NTW, 180s, daily	GMF	2 h	-13.2	-2.1	1.9	3.9	17.4	5.9	1.6	6.9	25
	NTW, 180s, daily	GMF	1 h	-22.4	-0.7	2.7	6.5	14.0	7.2	2.3	7.7	25
	NTW, 180s, daily	GMF	30 min	-27.1	-2.1	3.3	9.4	17.3	11.4	2.6	9.0	25
	NTW, 180s, daily	Niell	1 h	-21.9	-0.6	2.0	6.2	17.6	6.8	2.4	7.9	25
	NTW, 30s, daily	GMF	2 h	-12.8	-1.9	1.6	3.8	14.3	5.6	1.6	6.7	25
	PPP, 300s, daily	GMF	2 h	-16.7	-1.2	1.0	3.5	8.3	4.6	0.3	5.2	25
	PPP, 30s, daily	GMF	2 h	-17.5	-1.0	1.0	3.4	8.2	4.4	0.4	5.2	25
	PPP, 30s, daily	GMF	1 h	-18.1	-0.4	1.5	4.3	14.1	4.7	1.1	5.6	25
	PPP, 30s, daily	GMF	30 min	-10.2	-0.7	0.8	3.6	15.6	4.3	1.8	4.7	25
	NTW, 180s, weekly	GMF	2 h	-12.8	-1.2	1.7	3.9	17.0	5.2	1.9	6.7	25
GUGL	NTW, 180s, daily	GMF	2 h	-14.2	-3.2	0.7	5.6	16.4	8.8	0.5	7.6	21
	NTW, 180s, daily	GMF	1 h	-20.6	-2.4	3.3	7.7	13.7	10.1	1.7	8.4	20
	NTW, 180s, daily	GMF	30 min	-22.6	-0.1	2.7	10.6	17.7	10.7	3.1	9.2	20
	NTW, 180s, daily	Niell	1 h	-20.3	-2.9	3.0	6.8	19.9	9.8	1.8	8.9	20
	NTW, 30s, daily	GMF	2 h	-20.7	-2.8	-0.0	6.0	13.9	8.8	0.1	8.2	22
	PPP, 300s, daily	GMF	2 h	-13.5	-1.5	0.2	3.1	8.4	4.6	-0.0	5.5	21
	PPP, 30s, daily	GMF	2 h	-13.3	-2.2	0.4	3.8	8.9	6.0	-0.1	5.5	22
	PPP, 30s, daily	GMF	1 h	-14.1	0.0	2.2	4.0	15.0	4.0	1.8	5.8	21
	PPP, 30s, daily	GMF	30 min	-13.2	-1.5	4.4	7.4	19.2	8.9	3.0	7.2	20
	NTW, 180s, weekly	GMF	2 h	-14.6	-2.1	1.1	6.2	15.9	8.3	1.1	7.6	21
HERM	NTW, 180s, daily	GMF	2 h	-28.3	-16.8	-12.7	-10.5	2.0	6.3	-13.5	8.0	20
	NTW, 180s, daily	GMF	1 h	-31.4	-19.1	-12.4	-6.0	1.8	13.1	-13.0	9.7	20
	NTW, 180s, daily	GMF	30 min	-30.0	-19.0	-11.5	-3.3	8.2	15.7	-11.6	10.8	19
	NTW, 180s, daily	Niell	1 h	-31.6	-19.1	-12.4	-5.5	3.5	13.6	-12.8	10.0	20
	NTW, 30s, daily	GMF	2 h	-33.3	-17.8	-13.0	-9.5	3.2	8.3	-13.9	8.8	20
	PPP, 300s, daily	GMF	2 h	-31.2	-13.4	-7.3	-5.0	6.0	8.4	-8.9	8.5	20
	PPP, 30s, daily	GMF	2 h	-25.9	-12.5	-9.2	-6.5	10.5	6.0	-9.5	8.7	20
	PPP, 30s, daily	GMF	1 h	-29.0	-15.5	-9.1	-4.8	13.1	10.8	-9.5	10.2	20
	PPP, 30s, daily	GMF	30 min	-29.9	-18.9	-10.1	-3.3	11.6	15.6	-10.1	11.0	20
	NTW, 180s, weekly	GMF	2 h	-24.6	-17.7	-9.7	-6.8	5.0	10.9	-11.2	7.7	20
HIRL	NTW, 180s, daily	GMF	2 h	-11.3	-1.0	0.1	3.6	15.8	4.6	1.2	6.1	25
	NTW, 180s, daily	GMF	1 h	-15.3	-0.4	2.3	5.3	13.6	5.7	2.4	6.2	25
	NTW, 180s, daily	GMF	30 min	-21.8	-0.9	2.6	6.6	14.8	7.5	2.7	7.9	25
	NTW, 180s, daily	Niell	1 h	-14.6	0.6	2.1	5.2	18.4	4.7	2.6	6.6	25
	NTW, 30s, daily	GMF	2 h	-11.4	-1.5	-0.2	2.9	13.3	4.4	1.1	6.1	25
	PPP, 300s, daily	GMF	2 h	-19.9	-1.1	0.5	3.7	8.3	4.8	0.7	5.4	25
	PPP, 30s, daily	GMF	2 h	-19.0	-1.0	0.6	2.9	8.8	3.9	0.7	5.4	25
	PPP, 30s, daily	GMF	1 h	-21.6	-0.1	1.6	5.3	11.5	5.4	1.5	6.1	25
	PPP, 30s, daily	GMF	30 min	-14.6	-1.2	1.4	5.4	12.5	6.6	2.0	5.7	25
	NTW, 180s, weekly	GMF	2 h	-11.6	-0.8	2.0	4.1	15.7	5.0	2.0	6.3	25
HOEA	NTW, 180s, daily	GMF	2 h	-10.4	-4.6	-3.6	-0.4	5.2	4.2	-2.5	5.1	8
	NTW, 180s, daily	GMF	1 h	-8.8	-1.4	1.3	3.5	5.5	4.9	0.3	4.8	7
	NTW, 180s, daily	GMF	30 min	-9.6	-0.7	2.6	3.7	6.1	4.4	0.8	5.2	7
	NTW, 180s, daily	Niell	1 h	-9.0	-1.4	1.3	3.1	5.4	4.5	0.2	4.8	7
	NTW, 30s, daily	GMF	2 h	-11.8	-6.0	-1.4	2.2	10.0	8.1	-1.4	7.0	8
	PPP, 300s, daily	GMF	2 h	-2.8	-1.9	1.0	3.2	5.0	5.1	0.9	3.1	8
	PPP, 30s, daily	GMF	2 h	-2.5	-1.4	1.3	2.8	4.8	4.2	1.0	2.8	8
	PPP, 30s, daily	GMF	1 h	-1.9	2.8	4.4	5.2	15.7	2.4	4.9	5.0	8
	PPP, 30s, daily	GMF	30 min	-1.2	1.0	3.3	4.7	5.2	3.7	2.7	2.6	7
	NTW, 180s, weekly	GMF	2 h	-10.1	-4.2	-3.4	-0.1	5.4	4.2	-2.2	5.2	8

HOER	NTW, 180s, daily	GMF	2 h	-4.6	1.1	3.1	9.0	15.3	7.9	4.7	6.1	17
	NTW, 180s, daily	GMF	1 h	-11.7	4.3	5.0	10.0	17.0	5.7	5.6	7.0	17
	NTW, 180s, daily	GMF	30 min	-19.8	1.2	9.3	13.9	26.9	12.7	6.7	11.7	17
	NTW, 180s, daily	Niell	1 h	-11.3	4.1	5.6	9.2	19.5	5.1	6.3	7.7	17
	NTW, 30s, daily	GMF	2 h	-7.3	0.6	2.6	9.3	15.2	8.7	4.3	6.1	18
	PPP, 300s, daily	GMF	2 h	-9.2	1.2	5.4	9.5	14.4	8.3	4.7	5.6	17
	PPP, 30s, daily	GMF	2 h	-8.4	2.3	6.0	10.0	22.8	7.6	6.0	6.8	18
	PPP, 30s, daily	GMF	1 h	-11.0	3.5	5.9	9.4	11.9	5.8	5.6	5.5	17
	PPP, 30s, daily	GMF	30 min	-5.8	3.2	5.3	10.1	16.6	6.9	6.3	6.7	17
	NTW, 180s, weekly	GMF	2 h	-3.0	2.7	5.7	10.8	16.2	8.1	6.6	6.1	17
HOTA	NTW, 180s, daily	GMF	2 h	-15.4	-7.0	-2.1	0.0	14.3	7.0	-2.5	6.6	25
	NTW, 180s, daily	GMF	1 h	-22.7	-6.5	-2.0	2.8	8.6	9.3	-2.4	6.9	25
	NTW, 180s, daily	GMF	30 min	-24.9	-6.7	-2.9	2.2	11.9	8.9	-2.2	8.1	25
	NTW, 180s, daily	Niell	1 h	-22.2	-6.2	-2.3	2.9	12.6	9.0	-2.2	7.1	25
	NTW, 30s, daily	GMF	2 h	-15.4	-6.2	-2.2	1.3	10.3	7.5	-2.1	6.4	25
	PPP, 300s, daily	GMF	2 h	-17.6	-4.4	-0.4	2.0	4.8	6.4	-2.0	5.4	25
	PPP, 30s, daily	GMF	2 h	-17.6	-4.0	-0.1	1.6	4.7	5.6	-2.1	5.4	25
	PPP, 30s, daily	GMF	1 h	-17.1	-5.3	-1.1	2.7	11.1	8.0	-1.4	5.6	25
	PPP, 30s, daily	GMF	30 min	-12.5	-4.8	-1.0	1.6	11.9	6.4	-1.2	5.2	25
	NTW, 180s, weekly	GMF	2 h	-14.3	-5.2	-1.3	0.7	14.8	5.9	-1.4	6.4	25
HUBE	NTW, 180s, daily	GMF	2 h	-5.6	1.4	3.4	7.2	22.2	5.8	5.2	7.1	24
	NTW, 180s, daily	GMF	1 h	-8.9	0.6	5.3	12.2	21.4	11.7	6.8	8.3	24
	NTW, 180s, daily	GMF	30 min	-11.9	1.0	5.5	14.8	27.6	13.8	8.1	9.8	24
	NTW, 180s, daily	Niell	1 h	-8.6	0.6	5.1	10.6	24.2	10.0	6.9	8.5	24
	NTW, 30s, daily	GMF	2 h	-3.9	1.6	3.7	7.7	48.2	6.2	6.9	11.1	25
	PPP, 300s, daily	GMF	2 h	-5.8	2.1	6.9	10.8	20.6	8.7	6.5	6.2	24
	PPP, 30s, daily	GMF	2 h	-6.2	0.9	6.9	10.9	27.1	9.9	7.0	7.5	25
	PPP, 30s, daily	GMF	1 h	-8.5	3.3	7.1	13.0	21.1	9.7	7.3	7.8	24
	PPP, 30s, daily	GMF	30 min	-7.9	3.8	8.0	12.8	26.2	9.0	8.2	8.6	24
	NTW, 180s, weekly	GMF	2 h	-4.4	1.5	4.4	8.1	21.0	6.6	5.2	6.7	24
HUEE	NTW, 180s, daily	GMF	2 h	-13.5	-5.6	-1.2	4.6	14.7	10.2	-0.6	7.1	25
	NTW, 180s, daily	GMF	1 h	-18.6	-3.3	-1.2	4.8	14.1	8.1	-0.2	8.1	25
	NTW, 180s, daily	GMF	30 min	-21.8	-4.6	-0.0	4.5	19.3	9.0	0.2	9.1	25
	NTW, 180s, daily	Niell	1 h	-17.1	-4.0	-1.4	6.0	16.2	10.0	0.2	8.3	25
	NTW, 30s, daily	GMF	2 h	-12.0	-5.9	-1.9	4.1	13.1	10.0	-0.9	7.2	25
	PPP, 300s, daily	GMF	2 h	-11.2	-1.2	0.8	3.6	8.1	4.8	1.0	4.3	25
	PPP, 30s, daily	GMF	2 h	-11.6	-0.8	1.7	3.2	7.1	4.0	0.9	4.2	25
	PPP, 30s, daily	GMF	1 h	-10.9	-0.7	3.7	4.8	10.6	5.6	2.0	4.7	25
	PPP, 30s, daily	GMF	30 min	-8.0	-0.0	2.1	4.7	12.4	4.7	2.1	4.8	25
	NTW, 180s, weekly	GMF	2 h	-11.2	-4.3	-0.6	5.2	14.8	9.5	0.2	7.0	25
PLAT	NTW, 180s, daily	GMF	2 h	-11.2	-2.8	-0.1	5.5	14.4	8.2	0.8	6.7	25
	NTW, 180s, daily	GMF	1 h	-14.9	-3.1	1.4	4.5	16.6	7.6	0.8	7.5	25
	NTW, 180s, daily	GMF	30 min	-21.0	-4.2	0.5	9.2	17.4	13.3	1.1	9.4	25
	NTW, 180s, daily	Niell	1 h	-14.2	-3.0	1.4	4.9	17.8	7.9	1.0	7.8	25
	NTW, 30s, daily	GMF	2 h	-13.2	-3.3	0.5	5.4	14.5	8.6	0.4	6.8	25
	PPP, 300s, daily	GMF	2 h	-12.8	-1.6	-0.6	5.4	12.1	7.0	0.5	6.1	25
	PPP, 30s, daily	GMF	2 h	-12.9	-2.9	-0.6	4.6	11.1	7.5	0.3	6.3	25
	PPP, 30s, daily	GMF	1 h	-12.9	-3.0	1.3	4.7	18.9	7.7	1.5	7.8	25
	PPP, 30s, daily	GMF	30 min	-14.1	-3.4	0.6	6.9	20.5	10.4	2.0	8.9	25
	NTW, 180s, weekly	GMF	2 h	-12.4	-2.7	0.4	5.4	14.2	8.1	0.8	6.6	25
RECH	NTW, 180s, daily	GMF	2 h	-15.4	-5.8	-1.9	3.8	16.3	9.6	-1.0	7.1	25
	NTW, 180s, daily	GMF	1 h	-21.1	-5.9	1.4	4.2	11.7	10.1	-0.7	7.4	25
	NTW, 180s, daily	GMF	30 min	-22.0	-3.1	1.5	7.6	14.2	10.7	0.9	7.8	25
	NTW, 180s, daily	Niell	1 h	-20.6	-5.9	0.6	4.2	14.0	10.1	-0.8	7.4	25
	NTW, 30s, daily	GMF	2 h	-15.4	-5.9	-0.7	4.3	13.2	10.3	-0.9	7.2	25
	PPP, 300s, daily	GMF	2 h	-13.1	-4.0	1.8	5.2	9.5	9.1	0.7	5.6	25
	PPP, 30s, daily	GMF	2 h	-13.2	-4.4	2.1	5.1	8.7	9.4	0.6	5.7	25
	PPP, 30s, daily	GMF	1 h	-15.6	-1.8	2.8	4.4	11.1	6.2	1.4	5.8	25
	PPP, 30s, daily	GMF	30 min	-11.6	-1.5	2.7	4.7	14.2	6.3	2.3	5.6	25
	NTW, 180s, weekly	GMF	2 h	-16.1	-6.0	0.0	3.7	16.6	9.7	-0.6	7.7	25
RIBO	NTW, 180s, daily	GMF	2 h	-9.8	-1.7	1.6	5.9	19.1	7.6	2.9	7.4	25
	NTW, 180s, daily	GMF	1 h	-19.2	-0.3	3.1	6.4	22.8	6.7	3.6	8.2	25
	NTW, 180s, daily	GMF	30 min	-18.4	1.7	4.2	14.1	23.2	12.5	6.0	9.1	25
	NTW, 180s, daily	Niell	1 h	-18.4	-0.2	3.4	5.3	26.6	5.5	4.0	8.9	25
	NTW, 30s, daily	GMF	2 h	-10.3	-1.0	1.9	7.2	19.0	8.2	3.1	7.2	25
	PPP, 300s, daily	GMF	2 h	-10.1	-1.1	2.6	4.6	13.0	5.7	2.0	6.0	25
	PPP, 30s, daily	GMF	2 h	-10.1	-2.3	2.7	5.4	12.6	7.7	1.8	5.8	25
	PPP, 30s, daily	GMF	1 h	-10.5	0.5	5.0	7.1	18.4	6.6	3.9	7.2	25
	PPP, 30s, daily	GMF	30 min	-9.6	0.5	4.8	8.8	27.6	8.2	5.7	9.0	25
	NTW, 180s, weekly	GMF	2 h	-10.8	-1.3	1.6	6.3	18.2	7.6	2.6	7.3	25

D Statistics of Zermatt troposphere results

RIFF	NTW, 180s, daily	GMF	2 h	-8.8	-2.8	0.6	4.8	12.9	7.6	1.3	5.9	24
	NTW, 180s, daily	GMF	1 h	-16.9	-3.0	2.0	5.0	16.7	8.0	1.7	7.2	24
	NTW, 180s, daily	GMF	30 min	-14.0	-3.6	3.2	7.6	18.0	11.2	2.8	8.0	24
	NTW, 180s, daily	Niell	1 h	-16.5	-2.9	1.7	4.8	16.3	7.7	1.6	7.2	24
	NTW, 30s, daily	GMF	2 h	-11.1	-2.1	0.9	6.9	10.4	8.9	1.5	5.8	24
	PPP, 300s, daily	GMF	2 h	-9.9	-3.5	-0.8	4.6	7.3	8.1	-0.3	4.9	24
	PPP, 30s, daily	GMF	2 h	-12.4	-3.7	-0.6	3.0	8.9	6.6	-0.6	5.0	24
	PPP, 30s, daily	GMF	1 h	-13.1	-3.9	0.6	4.5	16.2	8.4	1.0	6.7	24
	PPP, 30s, daily	GMF	30 min	-11.5	-3.8	1.2	5.0	17.6	8.8	1.4	6.9	24
	NTW, 180s, weekly	GMF	2 h	-10.8	-2.9	1.1	5.3	11.0	8.2	0.8	5.6	24
ROSE	NTW, 180s, daily	GMF	2 h	-14.4	-3.2	0.1	4.5	15.9	7.7	0.5	7.2	25
	NTW, 180s, daily	GMF	1 h	-17.9	-2.7	1.5	5.8	13.7	8.6	1.5	7.0	25
	NTW, 180s, daily	GMF	30 min	-18.3	-2.5	3.7	7.2	22.7	9.7	2.9	8.7	25
	NTW, 180s, daily	Niell	1 h	-17.5	-2.9	1.3	5.7	20.4	8.6	1.7	7.6	25
	NTW, 30s, daily	GMF	2 h	-15.6	-2.6	0.2	5.3	13.5	7.9	1.1	7.2	25
	PPP, 300s, daily	GMF	2 h	-14.9	-2.6	0.4	2.9	9.1	5.5	-0.5	5.0	25
	PPP, 30s, daily	GMF	2 h	-14.8	-2.9	0.9	2.5	9.0	5.4	-0.4	4.9	25
	PPP, 30s, daily	GMF	1 h	-11.7	-2.4	1.1	4.5	10.1	7.0	0.8	5.0	25
	PPP, 30s, daily	GMF	30 min	-5.1	-2.1	1.0	4.5	16.2	6.7	2.0	5.4	25
	NTW, 180s, weekly	GMF	2 h	-14.0	-3.4	0.2	4.7	16.0	8.1	1.0	7.1	25
ROTE	NTW, 180s, daily	GMF	2 h	-9.3	-0.6	1.7	2.4	13.8	3.0	1.4	5.8	25
	NTW, 180s, daily	GMF	1 h	-18.6	-2.9	1.2	5.8	15.0	8.7	1.7	6.8	25
	NTW, 180s, daily	GMF	30 min	-18.4	-1.1	1.8	8.8	15.9	9.9	3.4	7.5	25
	NTW, 180s, daily	Niell	1 h	-18.2	-2.8	1.0	5.7	22.5	8.5	1.9	7.5	25
	NTW, 30s, daily	GMF	2 h	-9.2	-0.7	1.5	3.1	15.2	3.8	1.7	6.2	25
	PPP, 300s, daily	GMF	2 h	-12.0	-2.8	-0.4	3.3	7.5	6.1	-0.1	4.6	25
	PPP, 30s, daily	GMF	2 h	-11.5	-2.8	-0.2	4.2	7.6	7.0	-0.0	4.6	25
	PPP, 30s, daily	GMF	1 h	-10.0	-1.0	1.4	3.9	12.0	4.9	1.3	4.8	25
	PPP, 30s, daily	GMF	30 min	-4.3	0.4	2.9	4.8	16.0	4.4	3.1	4.5	25
	NTW, 180s, weekly	GMF	2 h	-10.7	-0.6	1.7	4.2	12.8	4.9	1.7	5.7	25
ROTH	NTW, 180s, daily	GMF	2 h	-11.8	-4.3	1.6	3.8	19.8	8.2	1.2	7.6	21
	NTW, 180s, daily	GMF	1 h	-17.7	-1.9	2.0	7.9	14.9	9.8	2.2	7.7	20
	NTW, 180s, daily	GMF	30 min	-21.4	-2.7	1.9	8.1	20.2	10.8	2.3	9.1	19
	NTW, 180s, daily	Niell	1 h	-17.4	-2.1	1.8	7.4	20.2	9.5	2.5	8.2	20
	NTW, 30s, daily	GMF	2 h	-12.9	-3.3	2.7	6.0	17.6	9.4	1.6	7.6	21
	PPP, 300s, daily	GMF	2 h	-13.0	-1.5	2.6	4.8	11.1	6.4	1.3	5.4	21
	PPP, 30s, daily	GMF	2 h	-13.2	-1.8	1.7	4.9	8.7	6.7	1.0	5.3	21
	PPP, 30s, daily	GMF	1 h	-11.7	-0.6	3.0	5.8	9.5	6.4	2.0	5.0	21
	PPP, 30s, daily	GMF	30 min	-8.6	-2.0	3.2	5.4	9.5	7.5	2.3	5.0	19
	NTW, 180s, weekly	GMF	2 h	-10.9	-1.8	2.1	4.0	19.7	5.7	1.9	7.0	21
SKIP	NTW, 180s, daily	GMF	2 h	-11.3	-2.4	0.4	5.0	19.2	7.4	1.4	6.5	25
	NTW, 180s, daily	GMF	1 h	-16.2	-2.4	1.9	6.2	14.2	8.7	1.9	7.0	25
	NTW, 180s, daily	GMF	30 min	-20.7	-0.7	4.4	9.3	14.2	9.9	2.4	8.3	25
	NTW, 180s, daily	Niell	1 h	-15.6	-1.6	1.5	7.0	13.5	8.6	1.9	7.0	25
	NTW, 30s, daily	GMF	2 h	-11.5	-2.5	1.6	5.6	15.9	8.1	1.6	6.6	25
	PPP, 300s, daily	GMF	2 h	-20.6	-1.9	1.0	3.4	11.6	5.3	0.5	6.3	25
	PPP, 30s, daily	GMF	2 h	-19.7	-2.8	-0.8	2.7	9.3	5.5	-0.1	5.7	25
	PPP, 30s, daily	GMF	1 h	-22.4	-1.9	1.2	3.4	13.7	5.4	0.4	6.3	25
	PPP, 30s, daily	GMF	30 min	-16.4	-2.3	2.8	5.1	12.9	7.4	1.7	6.0	25
	NTW, 180s, weekly	GMF	2 h	-11.5	-1.5	2.8	6.3	18.6	7.8	2.4	6.5	25
SUNN	NTW, 180s, daily	GMF	2 h	-8.8	-1.1	1.9	7.8	17.9	8.9	3.1	7.4	25
	NTW, 180s, daily	GMF	1 h	-18.3	-0.7	2.2	9.5	17.7	10.2	3.4	8.1	25
	NTW, 180s, daily	GMF	30 min	-16.7	-0.0	4.9	10.9	19.9	10.9	5.2	8.5	25
	NTW, 180s, daily	Niell	1 h	-17.5	-0.5	2.0	9.5	26.1	9.9	3.7	8.8	25
	NTW, 30s, daily	GMF	2 h	-10.3	-2.0	2.4	8.9	19.2	10.9	3.3	7.9	25
	PPP, 300s, daily	GMF	2 h	-11.5	0.4	4.5	7.5	15.6	7.1	3.8	5.8	25
	PPP, 30s, daily	GMF	2 h	-9.8	0.5	4.0	6.7	17.5	6.2	3.9	5.7	25
	PPP, 30s, daily	GMF	1 h	-9.1	2.6	5.5	7.9	20.7	5.3	5.8	5.5	25
	PPP, 30s, daily	GMF	30 min	-3.9	4.2	7.3	10.5	23.8	6.3	7.4	6.0	25
	NTW, 180s, weekly	GMF	2 h	-7.3	0.7	2.8	9.4	18.1	8.7	4.3	7.1	25
THEO	NTW, 180s, daily	GMF	2 h	-15.4	-4.0	0.5	3.4	18.2	7.4	-0.1	7.3	19
	NTW, 180s, daily	GMF	1 h	-21.3	-2.7	0.2	5.3	13.4	8.0	0.3	8.3	19
	NTW, 180s, daily	GMF	30 min	-29.2	-6.5	0.0	10.4	18.6	17.0	0.8	11.7	19
	NTW, 180s, daily	Niell	1 h	-20.2	-2.1	0.2	4.9	14.1	7.0	0.5	8.2	19
	NTW, 30s, daily	GMF	2 h	-14.9	-2.4	0.9	6.1	15.4	8.5	0.9	7.6	20
	PPP, 300s, daily	GMF	2 h	-22.0	-2.5	-1.1	2.5	11.7	5.0	-0.8	6.8	19
	PPP, 30s, daily	GMF	2 h	-32.6	-2.4	-0.8	1.4	11.3	3.9	-2.4	9.9	20
	PPP, 30s, daily	GMF	1 h	-28.8	-2.6	0.1	1.7	14.1	4.4	-1.3	7.9	19
	PPP, 30s, daily	GMF	30 min	-28.7	-2.0	0.7	2.3	19.8	4.2	-0.3	9.3	19
	NTW, 180s, weekly	GMF	2 h	-14.4	-3.4	2.1	4.2	19.0	7.6	0.3	7.5	19

TROC	NTW, 180s, daily	GMF	2 h	-14.1	-1.6	0.9	5.5	20.9	7.2	1.4	7.2	25
	NTW, 180s, daily	GMF	1 h	-20.7	0.0	3.1	6.3	15.8	6.3	2.4	7.3	25
	NTW, 180s, daily	GMF	30 min	-24.5	-2.6	5.6	10.1	24.5	12.7	4.2	10.0	25
	NTW, 180s, daily	Niell	1 h	-20.0	-0.0	3.3	6.3	16.3	6.3	2.4	7.2	25
	NTW, 30s, daily	GMF	2 h	-13.2	-2.0	1.2	6.2	16.1	8.2	1.3	6.8	25
	PPP, 300s, daily	GMF	2 h	-19.7	-3.1	0.0	1.9	11.4	4.9	0.0	6.0	25
	PPP, 30s, daily	GMF	2 h	-20.8	-2.2	-0.1	2.3	12.6	4.5	0.2	6.1	25
	PPP, 30s, daily	GMF	1 h	-24.9	-2.1	0.8	2.4	10.9	4.4	0.3	6.3	25
	PPP, 30s, daily	GMF	30 min	-16.6	-0.9	2.0	4.1	16.0	5.0	1.9	6.2	25
	NTW, 180s, weekly	GMF	2 h	-14.0	-1.3	0.9	6.3	19.8	7.6	1.9	7.2	25
UFDR	NTW, 180s, daily	GMF	2 h	-7.0	2.8	5.5	10.0	26.1	7.2	5.9	7.1	25
	NTW, 180s, daily	GMF	1 h	-8.9	1.7	7.8	13.4	22.5	11.7	7.3	7.3	25
	NTW, 180s, daily	GMF	30 min	-17.6	1.4	9.4	17.7	26.1	16.4	9.9	10.8	25
	NTW, 180s, daily	Niell	1 h	-8.1	2.0	6.9	13.8	23.0	11.8	7.5	7.5	25
	NTW, 30s, daily	GMF	2 h	-6.5	1.7	6.5	9.1	21.9	7.4	6.0	6.7	25
	PPP, 300s, daily	GMF	2 h	-14.6	2.0	4.2	8.1	21.1	6.1	4.3	7.3	25
	PPP, 30s, daily	GMF	2 h	-12.6	0.0	4.5	8.5	22.3	8.5	4.3	7.5	25
	PPP, 30s, daily	GMF	1 h	-6.7	2.6	6.1	8.0	17.7	5.4	5.3	6.0	25
	PPP, 30s, daily	GMF	30 min	-8.2	3.1	6.1	11.7	26.1	8.6	6.8	7.8	25
	NTW, 180s, weekly	GMF	2 h	-7.8	2.5	5.6	10.2	24.2	7.7	5.9	6.9	25
UFHO	NTW, 180s, daily	GMF	2 h	-10.3	-5.0	-1.8	3.0	13.6	8.1	-0.4	6.5	25
	NTW, 180s, daily	GMF	1 h	-18.2	-2.4	0.5	3.8	12.4	6.2	0.3	7.2	25
	NTW, 180s, daily	GMF	30 min	-21.4	-3.4	0.7	3.9	16.2	7.3	1.2	8.3	25
	NTW, 180s, daily	Niell	1 h	-16.8	-2.7	-0.3	3.8	16.4	6.4	0.4	7.4	25
	NTW, 30s, daily	GMF	2 h	-11.2	-4.7	-2.1	3.4	12.8	8.2	-0.1	6.4	25
	PPP, 300s, daily	GMF	2 h	-12.1	-1.0	2.2	3.1	8.3	4.1	0.7	4.5	25
	PPP, 30s, daily	GMF	2 h	-12.8	-1.4	1.9	2.9	8.8	4.3	0.6	4.7	25
	PPP, 30s, daily	GMF	1 h	-14.5	-0.2	2.5	4.1	10.1	4.3	1.5	5.3	25
	PPP, 30s, daily	GMF	30 min	-9.8	-0.7	1.6	4.8	13.5	5.5	1.8	5.0	25
	NTW, 180s, weekly	GMF	2 h	-10.4	-4.6	-0.2	3.7	14.3	8.3	0.8	6.5	25
ZERM	NTW, 180s, daily	GMF	2 h	-4.9	3.1	8.9	15.0	25.1	11.9	9.3	8.1	25
	NTW, 180s, daily	GMF	1 h	-11.3	7.3	11.4	17.2	29.2	9.9	12.0	9.1	25
	NTW, 180s, daily	GMF	30 min	-15.5	8.7	12.7	22.9	30.0	14.2	14.4	10.5	25
	NTW, 180s, daily	Niell	1 h	-10.8	7.8	11.4	16.2	29.0	8.4	12.0	9.1	25
	NTW, 30s, daily	GMF	2 h	-5.2	2.2	9.8	14.4	23.3	12.2	8.9	8.2	25
	PPP, 300s, daily	GMF	2 h	-6.4	3.9	7.5	16.1	23.8	12.3	9.3	7.6	25
	PPP, 30s, daily	GMF	2 h	-4.8	4.7	7.5	15.7	26.0	11.0	9.6	7.8	25
	PPP, 30s, daily	GMF	1 h	-8.0	8.0	12.8	20.1	37.0	12.1	13.6	9.7	25
	PPP, 30s, daily	GMF	30 min	-6.7	10.4	16.1	22.0	35.2	11.6	16.4	9.7	25
	NTW, 180s, weekly	GMF	2 h	-3.9	4.4	10.0	14.0	24.6	9.6	9.9	7.4	25
ZMUT	NTW, 180s, daily	GMF	2 h	-10.4	1.0	5.3	10.1	20.2	9.1	5.3	7.6	25
	NTW, 180s, daily	GMF	1 h	-18.0	2.4	7.2	13.8	20.4	11.4	7.1	8.8	25
	NTW, 180s, daily	GMF	30 min	-21.0	4.2	7.6	16.5	28.9	12.3	9.0	11.6	25
	NTW, 180s, daily	Niell	1 h	-17.6	3.6	6.5	13.8	20.5	10.1	7.2	8.8	25
	NTW, 30s, daily	GMF	2 h	-10.1	0.1	4.9	10.5	14.9	10.4	4.5	7.1	25
	PPP, 300s, daily	GMF	2 h	-6.2	1.6	4.9	9.4	23.0	7.8	6.0	6.9	25
	PPP, 30s, daily	GMF	2 h	-10.9	2.0	6.0	10.7	22.2	8.7	5.8	7.5	25
	PPP, 30s, daily	GMF	1 h	-18.4	5.0	7.9	9.7	26.1	4.7	6.6	8.3	25
	PPP, 30s, daily	GMF	30 min	-25.4	3.6	8.0	11.7	28.1	8.1	7.3	9.8	25
	NTW, 180s, weekly	GMF	2 h	-14.1	-0.4	4.9	12.5	18.6	12.9	5.0	7.8	25

Appendix E

Station repeatability of network solution

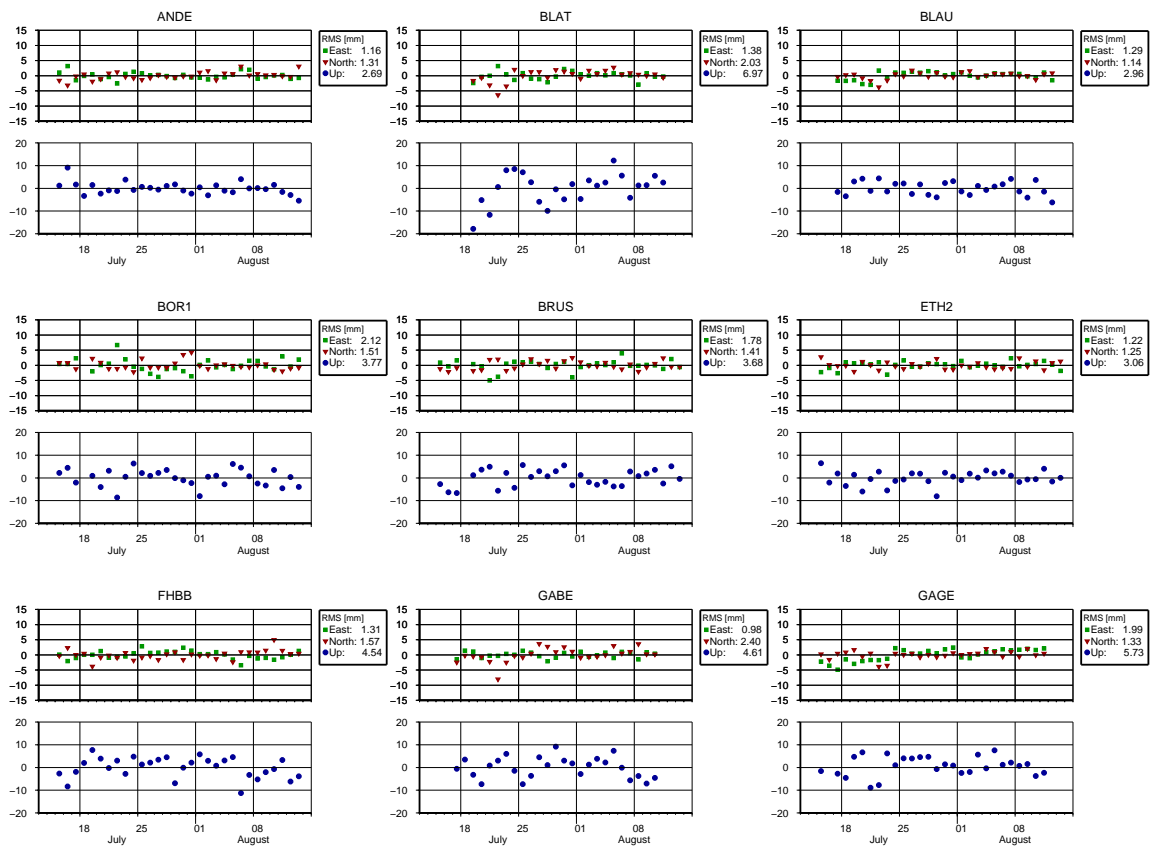


Figure E.1: Daily coordinate repeatability of the network solution in mm including some IGS, some AGNES and all Zermatt campaign stations. The Zermatt campaign stations are shown in Fig. 5.1 and described in Tabs. 5.1–5.3. Note the change in scaling in the up component of the stations UFDR, IMHO, HERM, WINK and PARK.

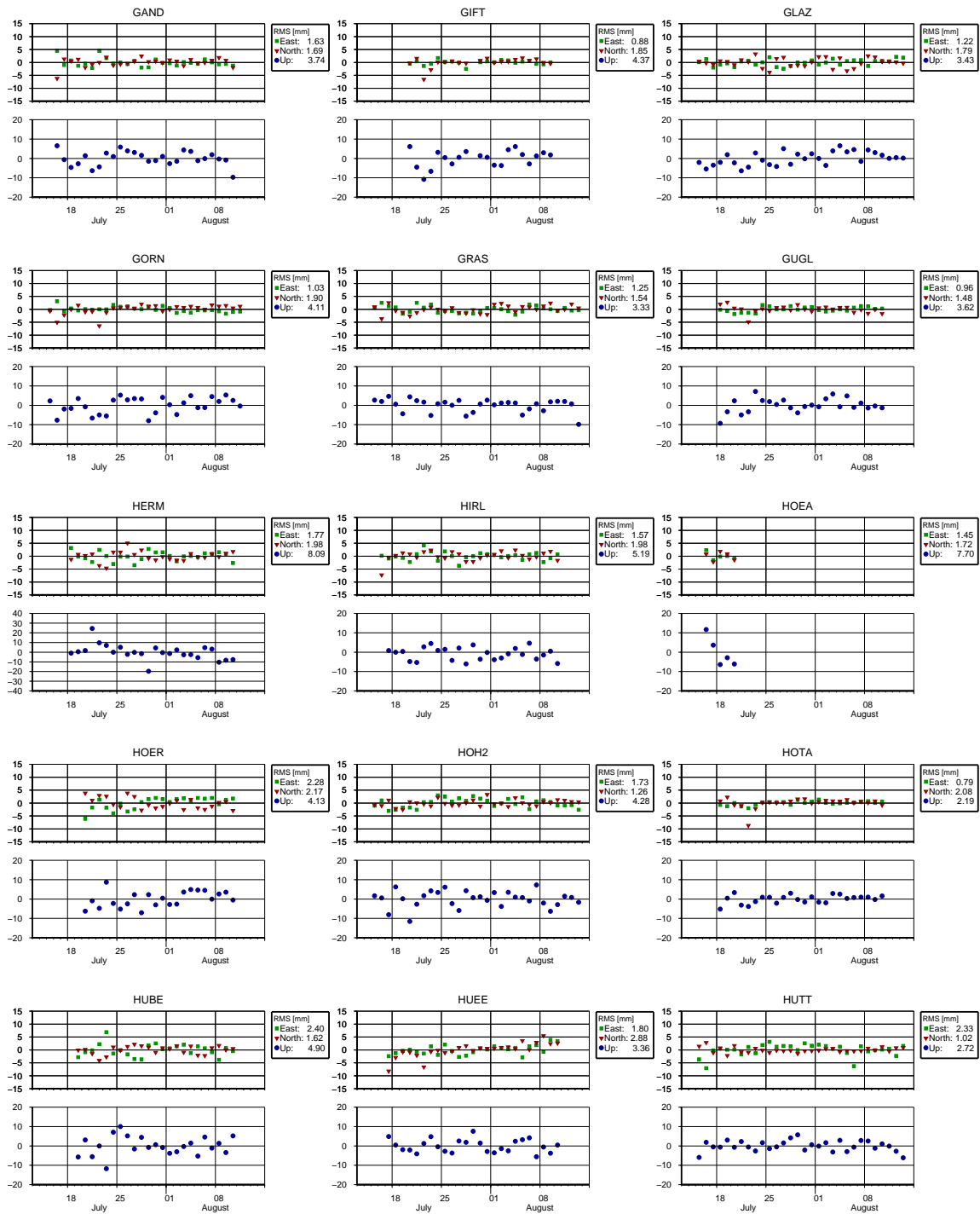


Figure E.2: Coordinate repeatabilities continued from Fig. E.1.

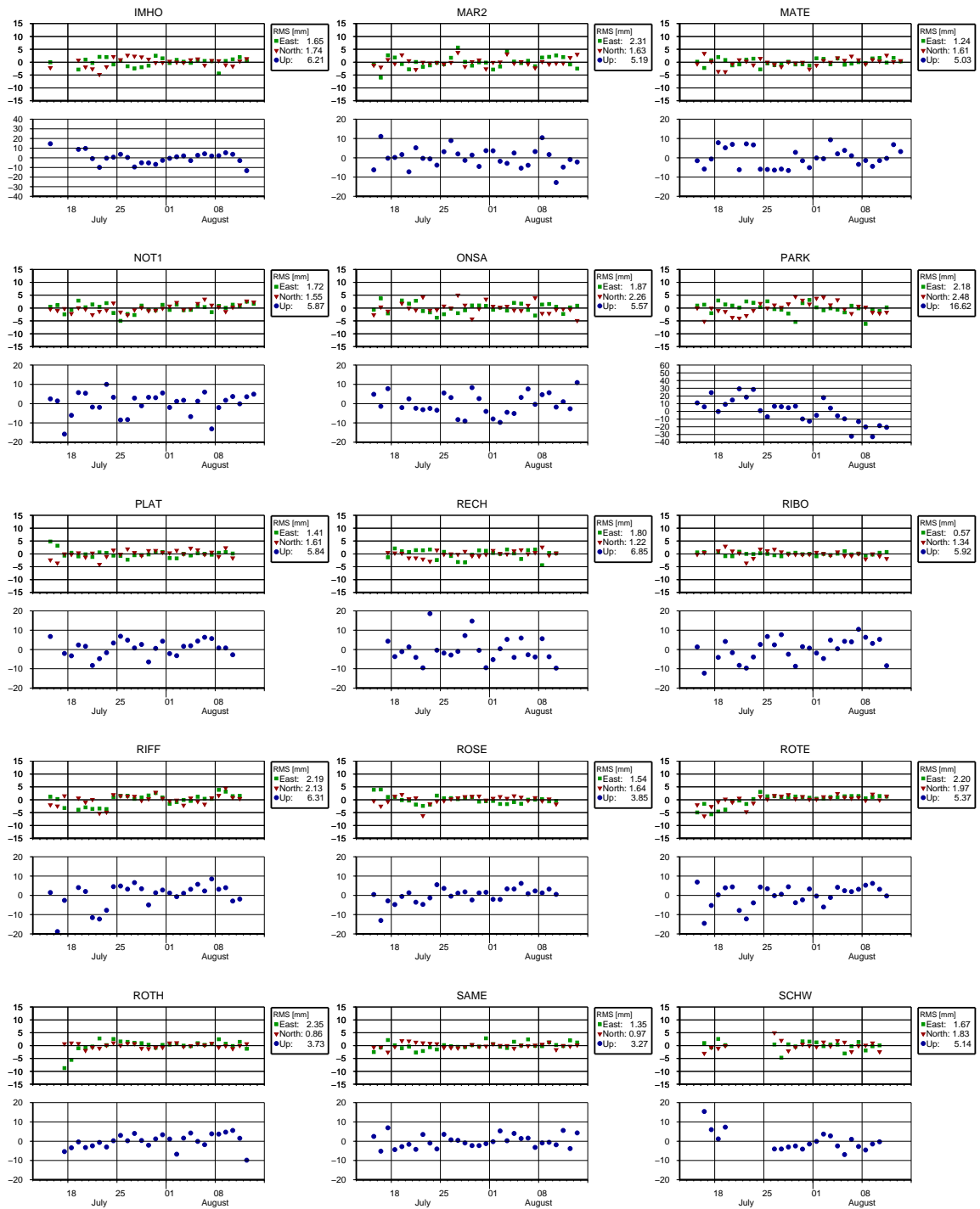


Figure E.3: Coordinate repeatabilities continued from Fig. E.2.

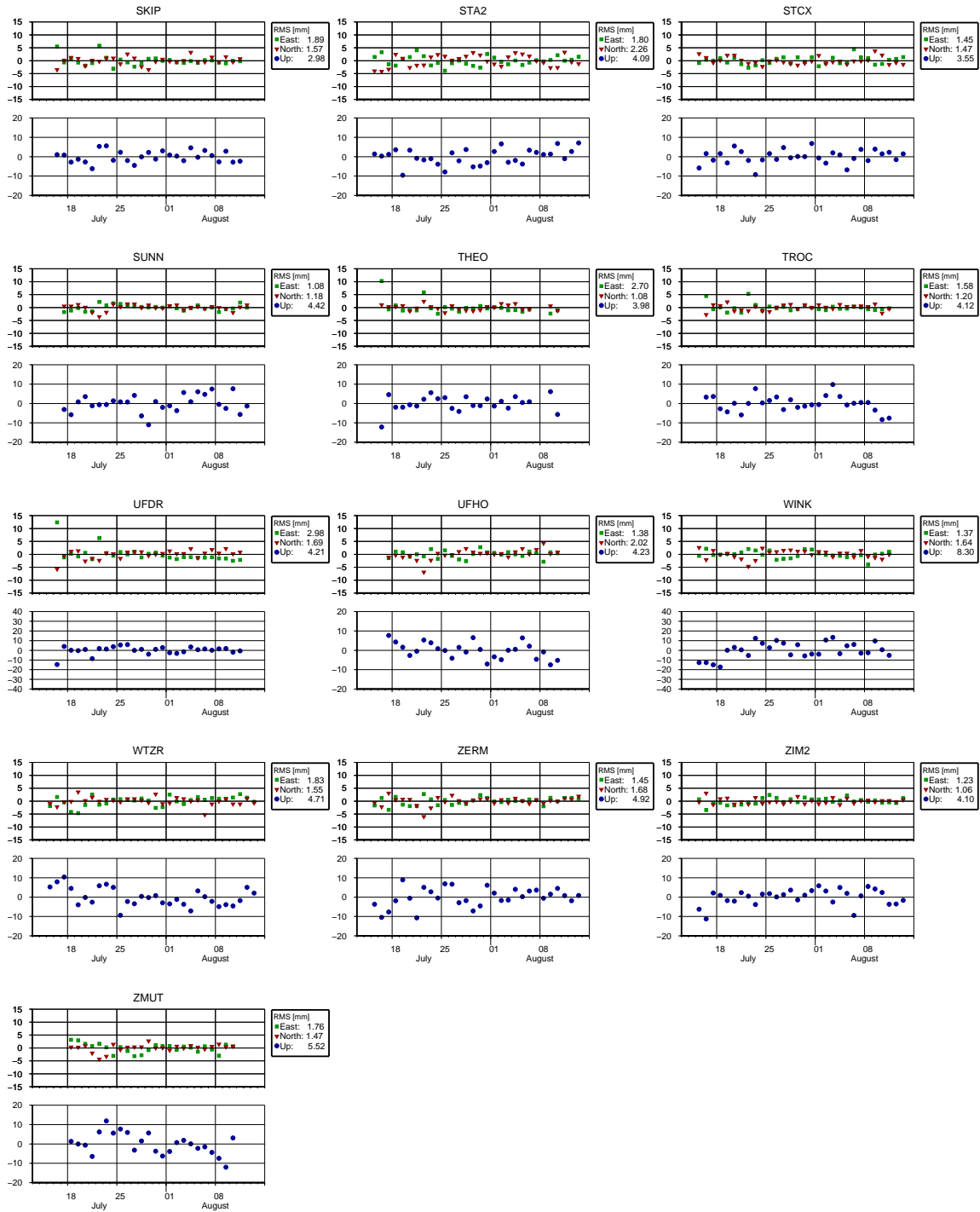


Figure E.4: Coordinate repeatabilities continued from Fig. E.3.

Appendix F

Skyplots of Zermatt campaign stations

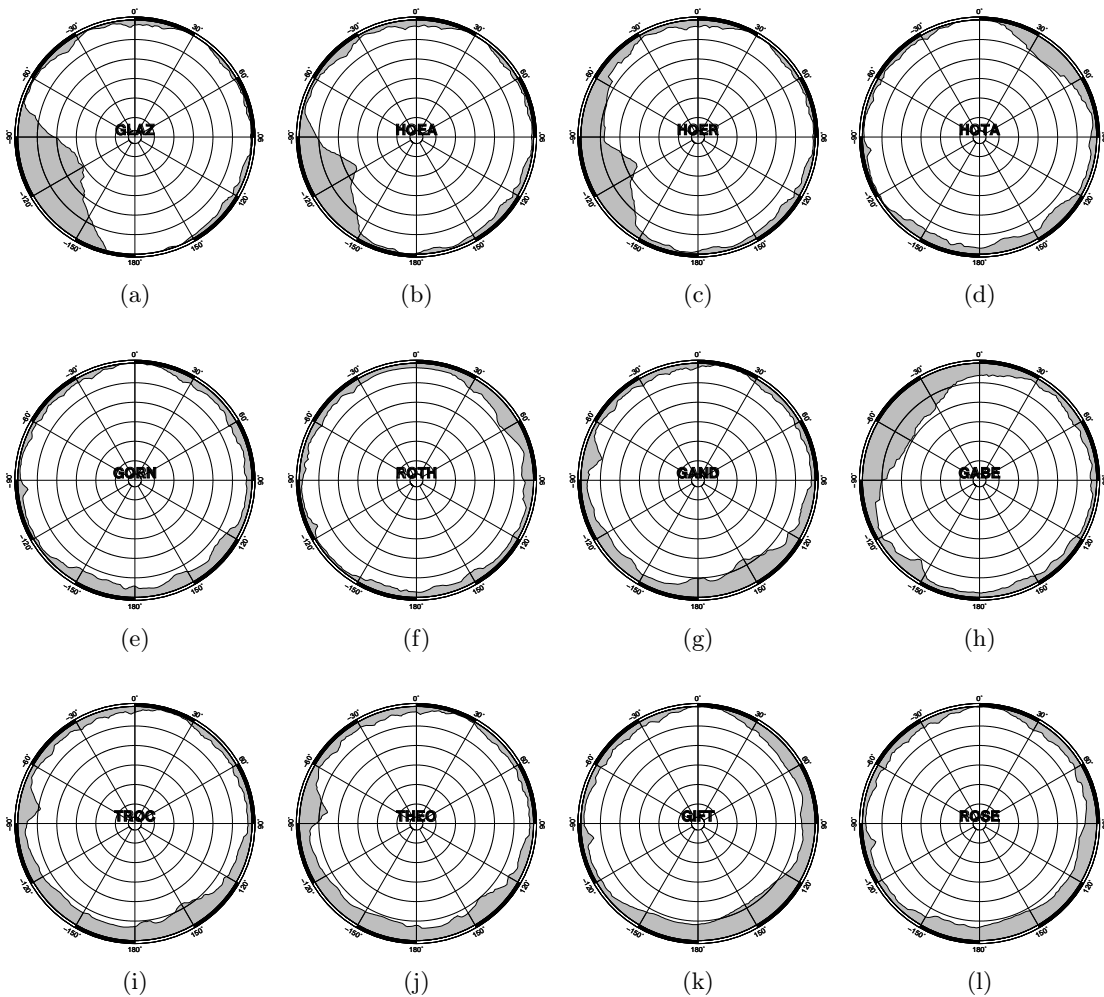


Figure F.1: Visibility skyplots of the campaign stations, calculated from a digital height model DHM25 (Swisstopo, 2014b). Obstructions caused by buildings or vegetation such as trees are not included. The stations are sorted according to their heights.

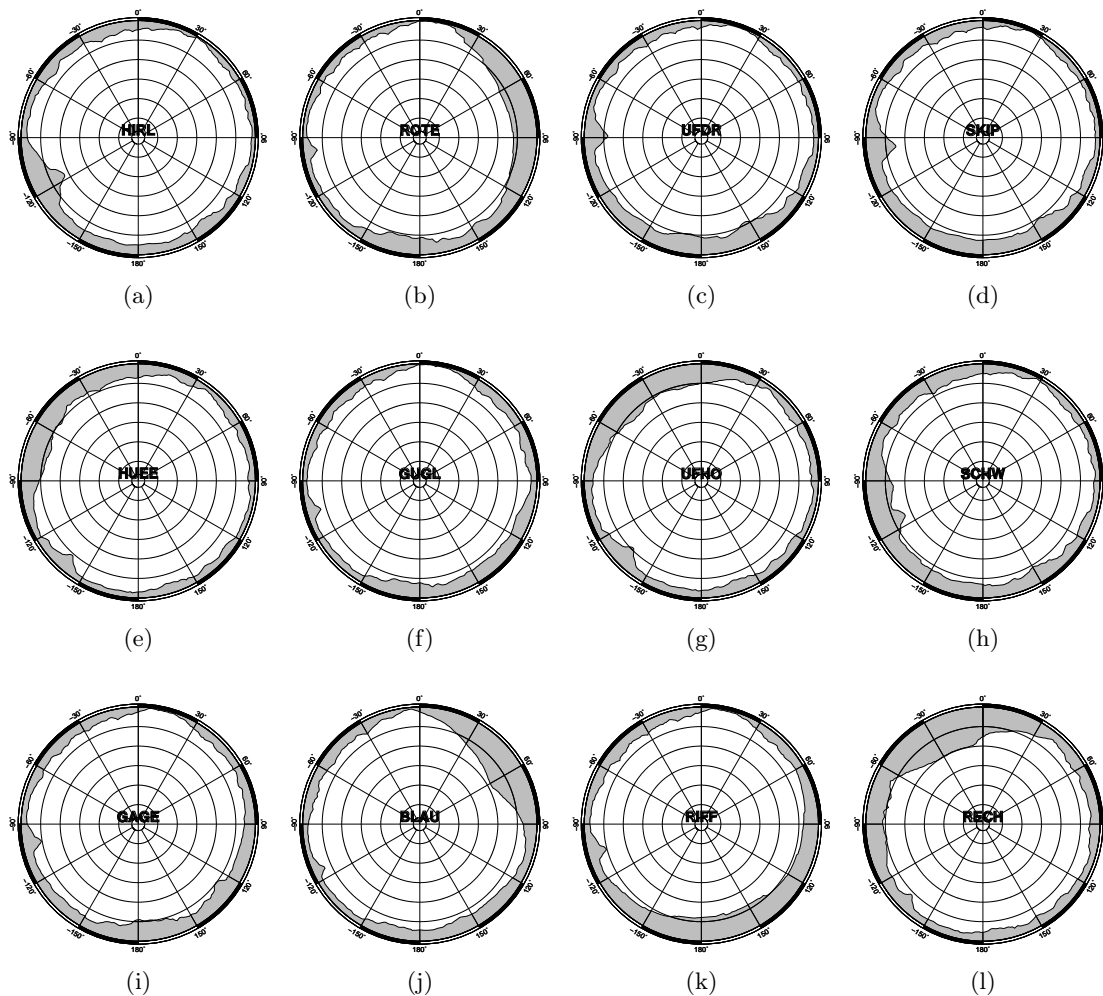


Figure F.2: Skyplots continued.

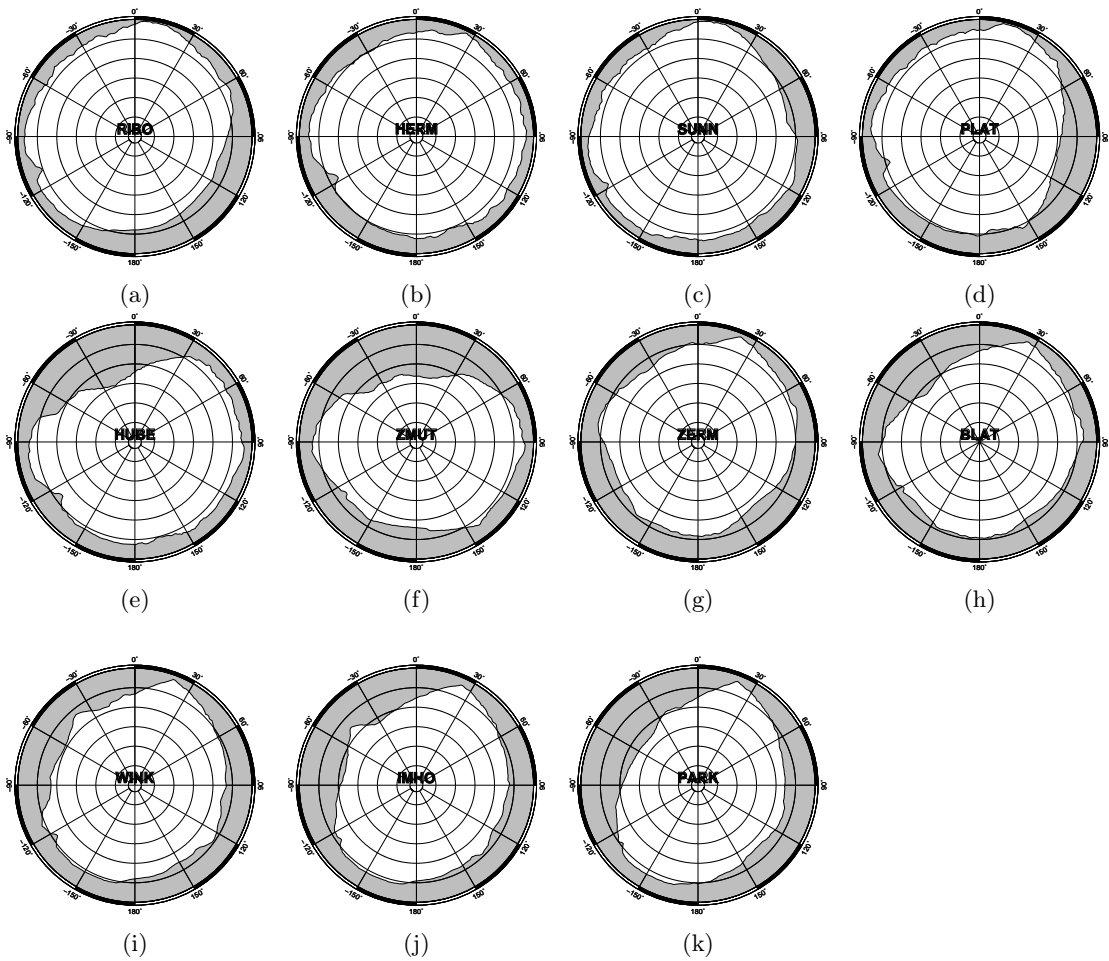


Figure F.3: Skyplots continued.

Appendix G

ZTD time series of campaign stations

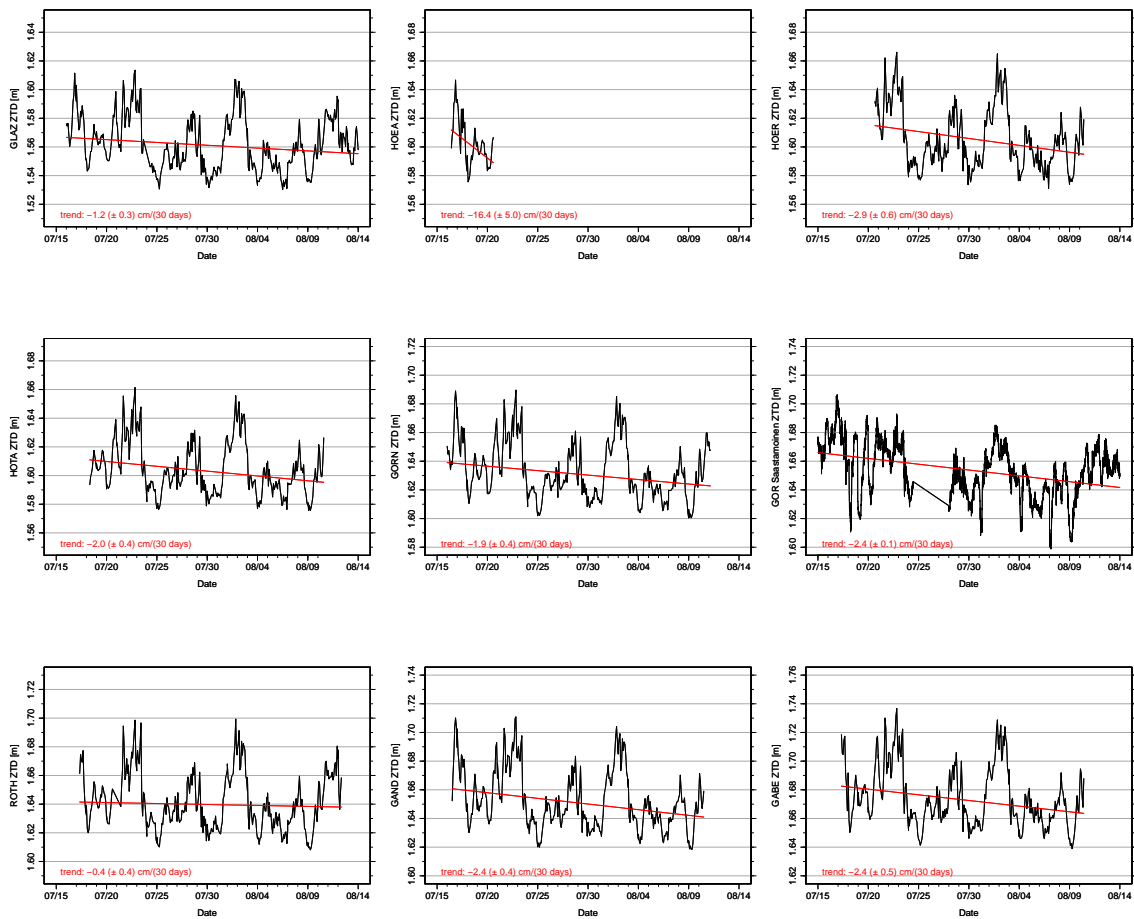


Figure G.1: Time series of the ZTD solution (PPP, 300s, daily, GMF, 2h) of all campaign stations. They are sorted according to decreasing height. See Fig. 5.2 for their heights. Additionally, Saastamoinen ZTDs (Eq. (2.11)) calculated from meteo data of the SwissMetNet stations Zermatt (ZER), Monte Rosa-Plattje (MRP) and Gornergrat (GOR) are also included at their respective heights. The trend line has been estimated with an ordinary least-squares algorithm.

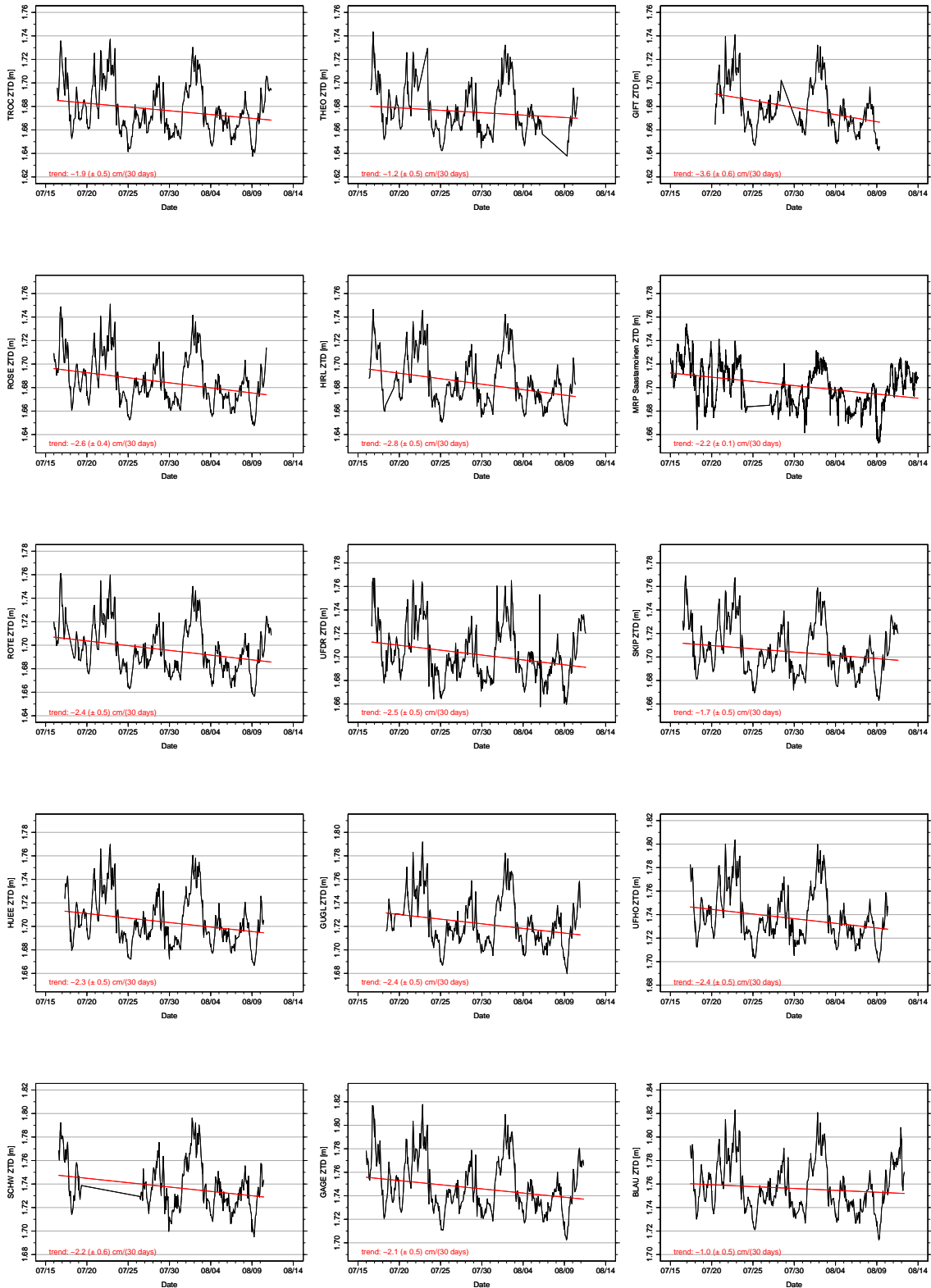


Figure G.2: Time series continued.

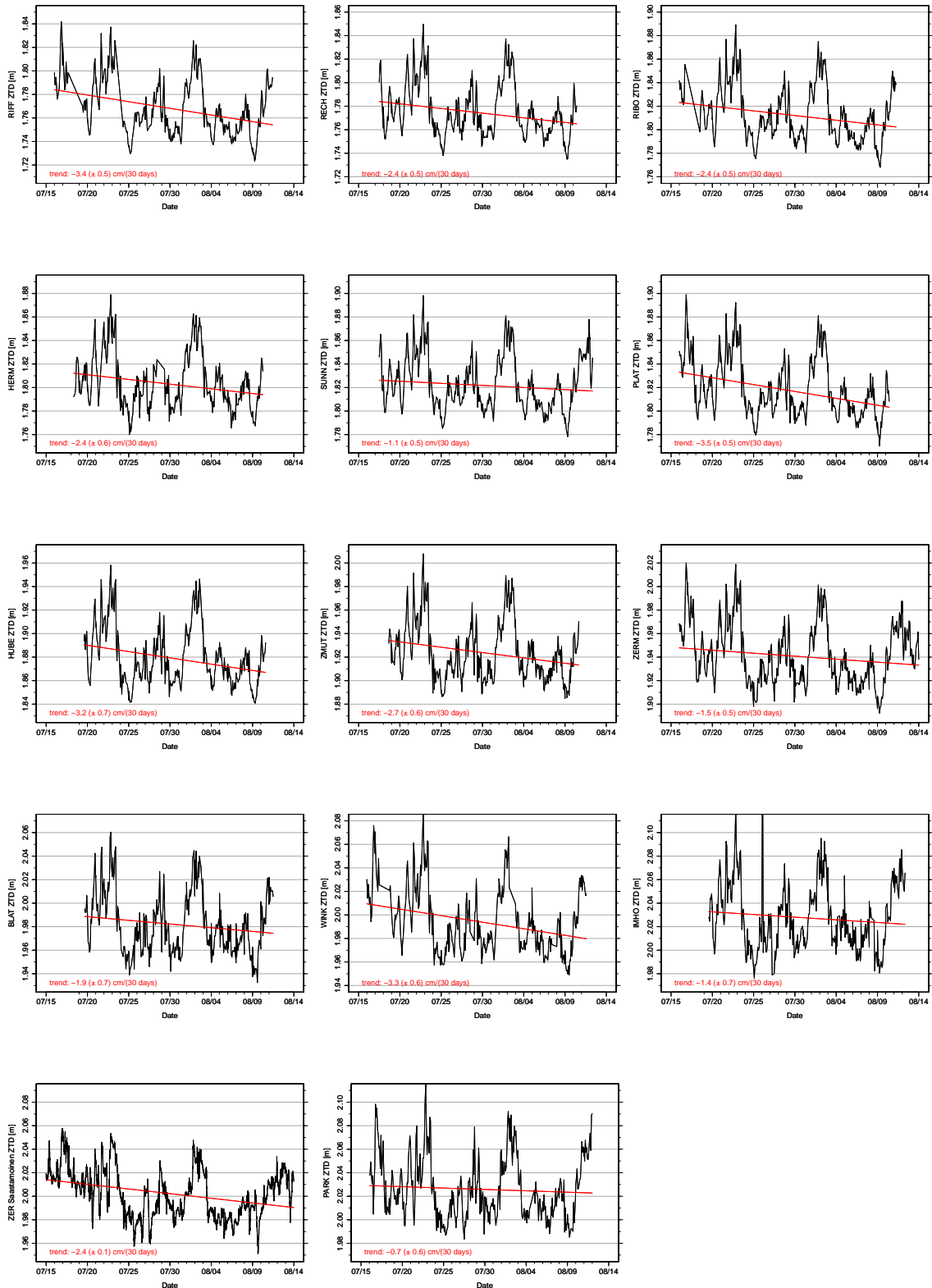


Figure G.3: Time series continued.